Numerical Modelling of Stretched Smectic Elastomer Sheets: Mechanical Properties and Microstructure

Andrew William Brown

September 2013

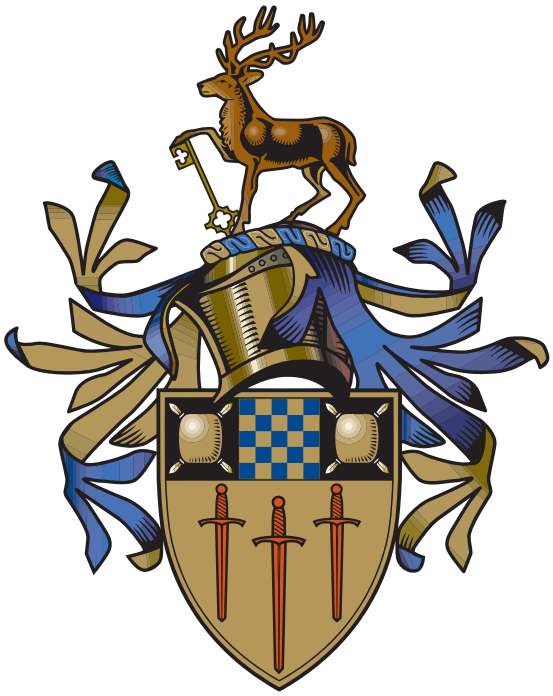

Submitted for the degree of Doctor of Philosophy

SEPnet and the Department of Physics,
Faculty of Engineering and Physical Sciences,
University of Surrey.

Numerical Modelling of Stretched Smectic Elastomer Sheets: Mechanical Properties and Microstructure

Contents

Abstract

This thesis explores the non-linear elasticity of smectic-A and smectic-C liquid crystal elastomers. These materials consist of "rod-like" liquid crystal mesogens arranged in a layered phase, cross-linked into a polymer matrix. The alignment direction of the mesogens is termed the director, and in the smectic-A phase the director and layer normal are parallel, whereas in the smectic-C phase the director is tilted at an angle to the layer normal. For smectic-C elastomers deformations that rotate the director in a conical path around the layer normal are ideally perfectly soft. Realistically non-idealities destroy perfect softness, and the resulting elasticity is termed semi-softness.

The semi-soft elasticity of monodomain smectic-C elastomer is investigated; starting from a model consisting of smectic layering and nematic elasticity terms, and a penalty for changing the tilt angle. A semi-soft elasticity term is then added to this energy. The elastic response to uniaxial deformation in various stretching geometries is calculated using an energy minimization routine. The stress-strain curves are diverse and depend strongly on the orientation of the layer normal, director and stretch axis. Remarkably, for an elongation parallel to the layer normal the stress-strain curve is non-monotonic, and the sample expands laterally in one direction over a range of strains.

The stretching of monodomain smectic-A elastomer sheet is studied under realistic clamping conditions; examining the effects of stretching angle and sample aspect ratio on microstructure formation. Results generated by finite element analysis show that stretching parallel to the director the sample bulk forms bidirectionally buckled microstructure, with unidirectional buckling near the clamped edges. The aspect ratio significantly affects the microstructure distribution, but weakly influences the stress-strain behaviour. It is shown that existing smectic models require an additional energy term, related to the energy of deforming buckled layers or non-Gaussian effects, to reproduce the experimentally observed Poisson's ratios.

Preface

Firstly I would like to thank my supervisors for giving me the opportunity to study smectic liquid crystal elastomers in so much depth. In particular I would like to thank Dr James Adams for his helpful and patient guidance, and Dr James Busfield for his instruction on finite element modelling.

The topic of smectic elastomers has proven to be an interesting introduction to both the physics of liquid crystals and the solid mechanics of rubbery materials. The macroscopic deformation properties of these materials, such as the stress-strain behaviour and Poisson's ratios, are intimately related to the behaviour of the smectic layers at the nano-scale, which can in turn lead to microstructure formation at the micron-scale. The complexity of these deformation mechanisms, and the sometimes surprising outcomes of experiments has provided thought-provoking material. The work of this thesis was performed as part of my PhD training, kindly funded by SEPnet, and hopefully it serves as a useful extension to the understanding of smectic elastomers.

Chapter 1 of this thesis is an introduction to past experimental work on smectic elastomers, and the existing theoretical models. Chapter 2 is a study of the deformation of monodomain semisoft smectic-C elastomer, which was first presented as a poster at the 6th International Liquid Crystal Elastomers Conference in Lisbon, and published in *Phys. Rev. E* as "Negative Poisson's ratio and semisoft elasticity of smectic-C liquid-crystal elastomers". This work benefited from short discussions with Dr Daniel Corbett and Prof. Mark Warner on theoretical issues, and with Dr Antoni Sánchez-Ferrer on the interpretation of mechanical experiments.

Chapters 3 and 5 form an investigation into the deformation of monodomain smectic-A elastomer sheets using finite element modelling. Chapter 4 serves as a brief introduction to the methodology of finite element modelling. The results of this investigation were first presented at the 24th International Liquid Crystal Conference in Mainz, and form the *Phys. Rev. E* paper "A numerical study of stretched smectic-A elastomer sheets". An epilogue to this thesis is provided by chapter 6, which summarizes the research findings and suggests possible future avenues of enquiry.

Declaration of Originality

This thesis and the work to which it refers are the results of my own efforts. Any ideas, data, images or text resulting from the work of others (whether published or unpublished) are fully identified as such within the work and attributed to their originator in the text, bibliography or in footnotes. This thesis has not been submitted in whole or in part for any other academic degree or professional qualification. I agree that the University has the right to submit my work to the plagiarism detection service TurnitinUK for originality checks. Whether or not drafts have been so-assessed, the University reserves the right to require an electronic version of the final document (as submitted) for assessment as above.

Andrew William Brown
September 2013

List of Publications

A. W. Brown and J. M. Adams. Negative Poisson's ratio and semisoft elasticity of smectic-C liquid-crystal elastomers. *Phys. Rev. E* 85(1):011703, Jan 2012.

A. W. Brown and J. M. Adams. Numerical study of stretched smectic-A elastomer sheets. *Phys. Rev. E* 88(1):012512, Jul 2013.

Chapter 1

Introduction

This chapter contains some background material on liquid crystals, their phases, and liquid crystal elastomers. There is then a literature survey of the synthesis of smectic elastomers, their alignment into monodomains, their mechanical properties, and some applications. The theoretical background of smectic elastomer models is then discussed with reference to experimental work.

1.1 Liquid Crystals

Liquid crystals (LCs) are liquids comprised of highly anisotropic molecules, e.g. rod-like or disc-like molecules [1]. At high temperatures the positional order of the molecules is liquid like, and the orientations are isotropic. As the temperature is lowered the attractive force between rods causes their orientations to align, forming the nematic phase [2]. If the temperature is lowered further then the molecules assemble into lamellae known as the smectic phase. These different LC mesophases are illustrated in figure 1.1.

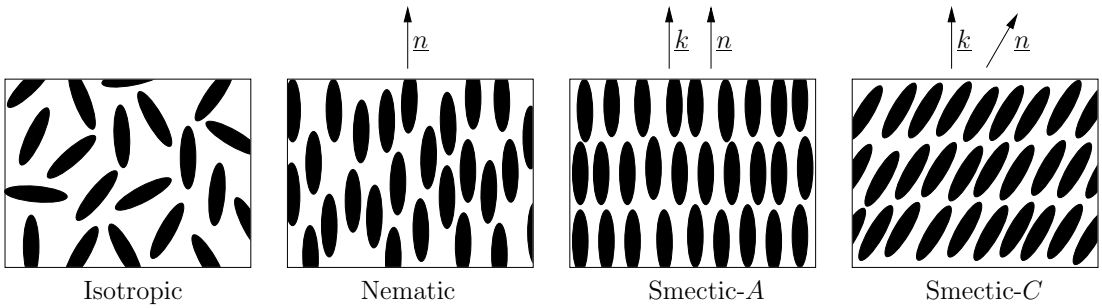

Figure 1.1: Schematic drawing of some LC phases. The high temperature isotropic phase is shown on the left, followed by increasingly ordered lower temperature phases. The alignment direction of the molecules is denoted by the director $\underline{n}$ and layer normal by $\underline{k}$.

LCs exhibit a broad variety of differently ordered phases, but this thesis will focus on the following phases:

- Isotropic Phase. The LC mesogens have liquid like positional order, and are randomly oriented. This is the most disordered state and occurs at high temperatures.
- Nematic Phase. The LC mesogens are uniaxially aligned, but still have liquid like order of their centers of mass. The average alignment direction of the rod-like molecules is called the director, denoted by the unit vector $\underline{n}$.
- Smectic-A Phase. The LC mesogens are arranged in a layered structure, with the director and layer normal parallel [3]. The unit vector $\underline{k}$ denotes the layer normal.

- Smectic-C Phase. The LC mesogens are arranged in a layered structure, with the director at an angle θ_0 to the layer normal, called the tilt angle.
- Smectic-C^* Phase. This is the chiral version of the smectic-C phase, formed by using chiral mesogens which have an electric dipole moment [4]. The chirality creates a tendency for the director to twist slightly between neighbouring layers, which creates a helical director pattern. Consequently the dipole moments cancel out over one rotation period. If the helical structure is untwisted the molecular dipole moments align, and a macroscopic electrical polarization vector exists in the direction $\underline{n} \times \underline{k}$.

The degree of ordering in a phase can be quantified by an order parameter. For example the nematic orientational order can be described by the order parameter $Q = \langle \frac{3}{2}\cos^2\theta - \frac{1}{2} \rangle$. The average is taken over all mesogens within a region of space, and θ is the polar angle each mesogen makes with $\underline{n}$. The parameter $Q = 0$ in the isotropic phase, and $Q = 1$ for a perfectly aligned distribution. Similar order parameters can be defined to encode the orientation of the layer normal, and the perfection of the smectic layers, but they will not be used here. We will assume that when LCs are deep in an ordered phase the magnitude of the order parameter is fixed.

Deformations of Nematic Liquid Crystal

The deformation behaviour of LCs can be investigated by deforming them between two initially parallel glass plates. At the interface of the LC and the glass the surface forces are strong, and the mesogens are effectively anchored at a fixed orientation to the surface. Experimental techniques can align the mesogens to be fixed parallel or perpendicular to the surface. Typically this is achieved by rubbing the glass surface with a cloth. Unidirectional rubbing creates nanoscale grooves running in one direction, and the rod-like mesogens tend to lie in these grooves, i.e. the mesogens are aligned parallel to the surface and point in the rubbing direction [5]. Whereas inducing surface roughness in two directions causes the mesogens to align end on to the surface.

The three principal deformation modes of nematic LC are splay, twist and bend.

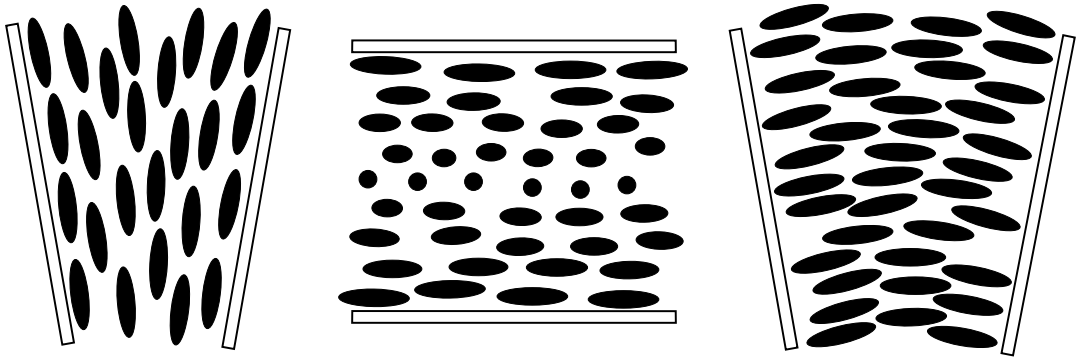

Figure 1.2: Splay, twist and bend deformations in a nematic liquid crystal.

The splay and bend deformations illustrated in figure 1.2 are performed by altering the separation of the plates, so that the plates are no longer parallel. Whereas the twist deformation is achieved by rotating the plates relative to each other, whilst maintaining a constant spacing. The Frank free energy [6] describes the elastic free energy per unit volume of a nematic LC, and has contributions from each of the deformation modes,

$$F_{Fr} = \underbrace{\frac{1}{2}K_1(\nabla \cdot \underline{n})^2}_{\text{Splay}} + \underbrace{\frac{1}{2}K_2(\underline{n} \cdot \nabla \times \underline{n})^2}_{\text{Twist}} + \underbrace{\frac{1}{2}K_3(\underline{n} \times \nabla \times \underline{n})^2}_{\text{Bend}}. \tag{1.1}$$

The elastic constants K_1, K_2 and K_3 penalize splaying, twisting and bending of the director field respectively. Typically the three elastic constants have a similar magnitude $K \sim 10^{-11}\,\text{N}$ [7].

Deformations of Smectic-A Liquid Crystal

In smectic LC the energetic cost of changing the layer spacing is very high, so the layer spacing varies only slightly from its equilibrium value. Bending of the layers is compatible with maintaining the layer spacing, so layer bending is a low energy deformation mode. Whereas any significant splaying or twisting of the layers would not maintain the layer spacing, and so can not occur unless layer defects provide the deformation as illustrated in figure 1.3.

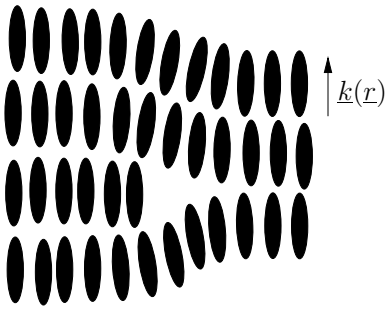

Figure 1.3: Layer splay can occur due to the presence of edge dislocations [8].

Typically the effect of defects is small, so layer splaying and twisting can be entirely neglected. For a set of defect-free, incompressible layers the integral $\oint \underline{k}(\underline{r}) \cdot \underline{dl}$ is zero for any path choice, which implies by Stoke's theorem that $\nabla \times \underline{k} = 0$ holds everywhere [9]. In the case of the smectic-A phase $\underline{k} = \underline{n}$, which implies that $\nabla \times \underline{n} = 0$ holds everywhere. Consequently the smectic-A energy does not include contributions from the K_2 or K_3 Frank elasticity terms, as these are zero.

The two principal deformation modes of smectic-A LC are layer stretching and layer bending.

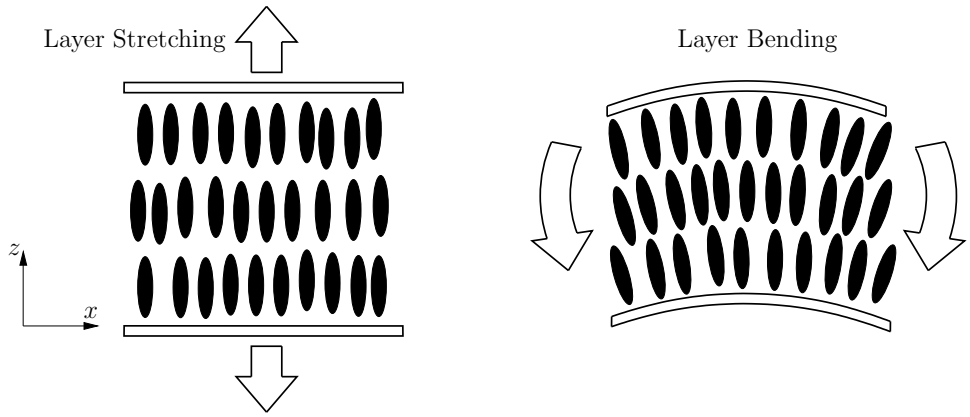

Figure 1.4: The deformation modes of smectic-A LC are layer stretching and layer bending.

The stretching of layers is penalized by the smectic layer modulus B, which typically has a magnitude of 10^6 Pa [10]. The bending of layers results in the splaying of the director field, as illustrated in figure 1.4, so layer bending is penalized by the splay elastic coefficient K_1. The continuum model of smectic-A LC describes the elastic free energy in terms of the layer stretching and bending energies [9]. The displacement of the layers along the direction of the initial layer normal is described by a scalar field $\mathcal{U}(x, y, z)$. For a sample with the layer normal initially oriented in the z direction the smectic-A energy to leading order is

$$F_{Sm-A} = \underbrace{\frac{1}{2}B\left(\frac{\partial \mathcal{U}}{\partial z} - \frac{1}{2}\left(\frac{\partial \mathcal{U}}{\partial x}\right)^2 - \frac{1}{2}\left(\frac{\partial \mathcal{U}}{\partial y}\right)^2\right)^2}_{\text{Layer Stretching}} + \underbrace{\frac{1}{2}K_1\left(\frac{\partial^2 \mathcal{U}}{\partial x^2} + \frac{\partial^2 \mathcal{U}}{\partial y^2}\right)^2}_{\text{Layer Bending}}. \tag{1.2}$$

This model provides a description of the smectic-A buckling instability that occurs when stretching parallel to the director, which was first reported by Clark and Meyer [11].

Smectic-A Buckling Instability

When a uniform sample of smectic-A LC is strained in dilation parallel to the layer normal the deformation is initially accommodated by an increase in the layer spacing. This deformation is penalized by the smectic layer modulus B and is consequently energetically very expensive. A far softer deformation mechanism is for the layers to periodically buckle and then to deform by rotating the layers, as illustrated in figure 1.5.

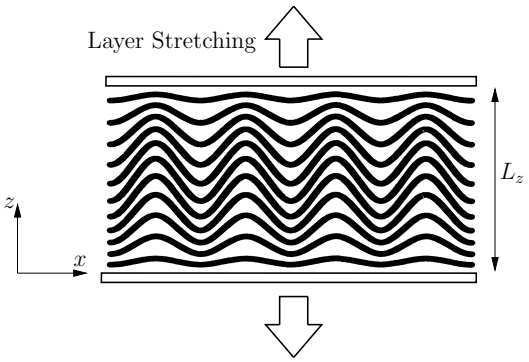

Figure 1.5: A buckling instability occurs when dilating smectic-A liquid crystal parallel to the layer normal [12]. The glass plates prohibit undulations from occurring at the boundaries.

The buckling of layers is penalized by the layer bending modulus K, and is therefore much softer than layer stretching. The buckling instability occurs at threshold strain $\epsilon_{th} = 2\pi\sqrt{K/B}/L_z$ [11], which is typically a very low strain as K is very small. The buckling instability can be relaxed away via the movement of edge dislocations to relieve the strain, i.e. additional layers are locally added to relax highly buckled or dilated regions [11].

1.2 What is Smectic Liquid Crystal Elastomer?

A liquid crystalline polymer (LCP) is formed by connecting the LC mesogens onto a polymer chain. The LC mesogens can be linked onto the side of a polymer chain, or be directly incorporated into the polymer backbone; respectively these are called i) side-chain LCP and ii) main-chain LCP.

The LC mesogens influence the conformation of the polymer backbone. In the isotropic phase the chain shape is spherical, whereas in the more ordered LC phases the chain shape is a prolate or oblate spheroid. Crosslinking these LCPs produces a rubbery solid called a Liquid Crystal Elastomer (LCE), here we will focus on smectic LCEs. The result of cross-linking LC mesogens in the smectic-C phase into a rubbery polymer network, is illustrated in figure 1.6.

LCEs are unusual materials because applying a macroscopic strain can alter the microscopic orientation of the LC molecules. Just like LCs, LCEs undergo temperature dependent transitions between phases. However in LCEs a phase transition can alter the macroscopic shape of the sample, as the polymer chain conformation depends on the phase. In some systems it is possible to transition directly from the isotropic phase to the smectic-C phase [13].

Liquid Crystal Elastomer Chemistry

There are several different methods of synthesizing LCEs. For example smectic main-chain LCE (MLCE) is commonly synthesized by using a one-pot, platinum-catalyzed, hydrosilylation polyaddition reaction, as outlined by Donnio *et al.* (2000) [14]. A uniformly thick film is achieved by the

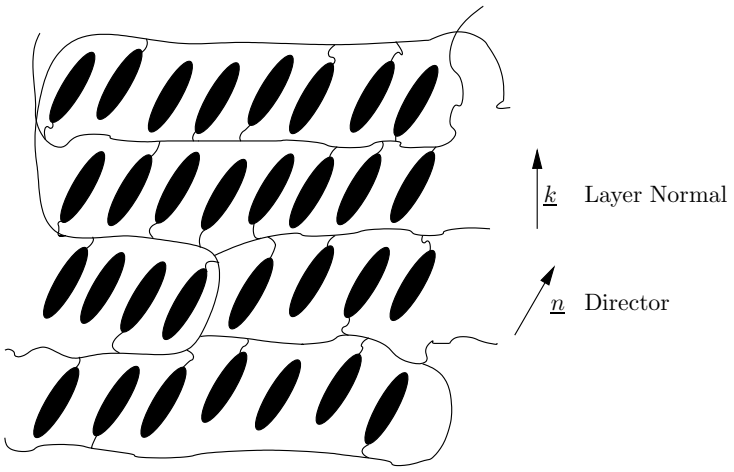

Figure 1.6: Schematic Drawing of side-chain smectic-C LCE. The mesogens are shown attached end-on to the polymer network, but side-on attachment is also possible.

spin-casting technique. The constituents of a typical photoactive smectic-C MLCE, MCEB7Azo2-2.5, are shown in figure 1.7.

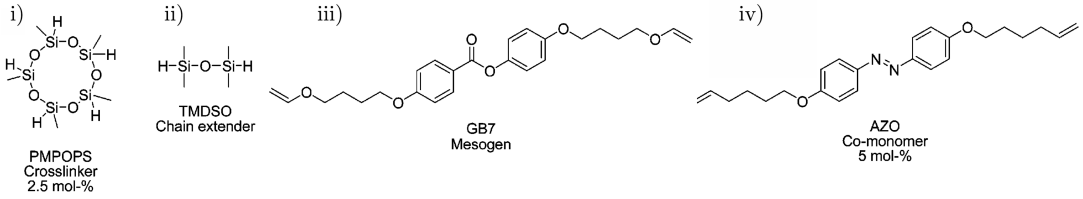

Figure 1.7: Constituents of a typical photoactive smectic-C MLCE. i) PMPOPS is a pentafunctional cross-linker, ii) TMDSO, tetramethydisiloxane is a siloxane rubber, iii) GB7 is a LC mesogen of length 34 Å, and iv) AZO is a photoactive azobenzene derivative monomer [15].

The choice of chain chemistry strongly influences the resultant mesophases, for example aliphatic acid chains and epoxy resin rigid monomers tend to result in smectic phases. This is because the aliphatic chains sit between the smectic layers and the rigid monomers stay within the layers.

The "physicists view" of LCEs ignores the chemical details of the system, instead focusing on more generic properties. This coarse grained approach will be adopted throughout the rest of this work.

Smectic LCE Domain Structure

When a high temperature phase is cooled to an ordered phase the symmetry of the system is broken. For example when a ferromagnet is cooled below its Curie temperature it spontaneously develops a magnetization. The direction in which the magnetization points is random, and may be different in spatially separated parts of the ferromagnet. As a result a polydomain structure forms. A similar process occurs in LCEs, for example when the isotropic phase is cooled into the smectic-C phase two new directions, $\underline{n}$ and $\underline{k}$, are introduced to the sample. As there is no preferred direction, a randomly oriented domain structure is formed, as illustrated in figure 1.8.

Obraztsov *et al.* [16] found the domain size of a side-chain, Sm-A elastomer was 0.7 μm without cross-links and 3.4 μm when cross-linked. The main-chain Sm-C elastomers studied by de Jeu *et al.* [17] had domain sizes of approximately 100 nm. It is typical that side-chain systems have much larger domains than main-chain systems, as in main-chain systems the folding of the polymer chain will reduce the coherence of the smectic layers.

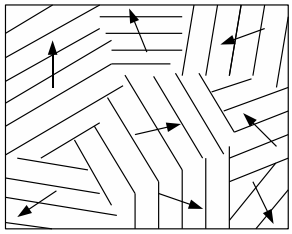

Figure 1.8: A 2-D slice through a **randomly oriented polydomain** of smectic-C LCE. Layers are represented by lines and the arrows represent local directors.

To produce a monodomain sample a preferred direction can be created by applying a uniaxial load during the sample manufacture (whilst chemical cross-linking is still ongoing). In the nematic phase uniaxial stretching causes the directors within different domains to orient along the stretch axis. This technique was developed by Küpfer and Finkelmann [18], and results in well ordered, transparent monodomain LCEs.

A similar technique can be used in smectic-A LCEs for example Nishikawa *et al.* (1999) [19]. However in smectic-C LCE this process only aligns the director, and leaves a domain structure of layer normals, $\underline{k}$, each at an angle θ_0 to $\underline{n}$. A sample that has a uniform director and a conical distribution of layer normals is termed a pseudo-monodomain [20], and is illustrated in figure 1.9.

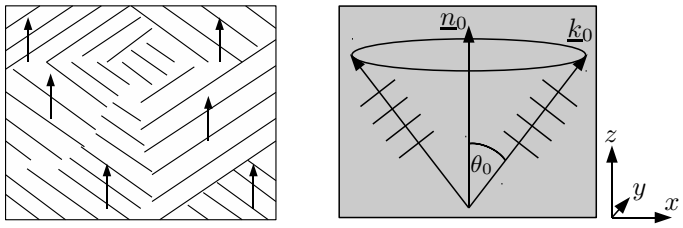

Figure 1.9: (left) A 2-D slice through a **pseudo-monodomain** of smectic-C LCE. The director is globally aligned, and the layer normals are conically distributed. (right) A representation of a smectic-C pseudo-monodomain.

A smectic-C LCE monodomain has a globally aligned director *and* aligned layer normal, as shown in figure 1.10. Various experimental techniques are employed to create a monodomain, which will be discussed in section 1.4.

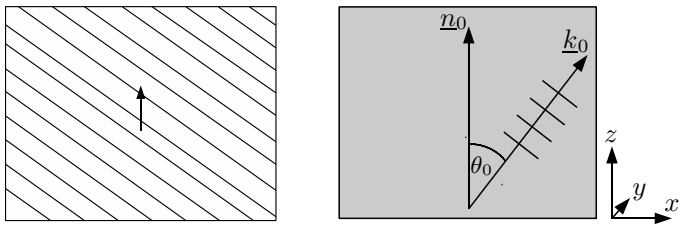

Figure 1.10: (left) A 2-D slice through a smectic-C LCE **monodomain**. (right) A representation of a smectic-C monodomain.

1.3 Mechanical Experiments on Smectic-A LCE

Nishikawa & Finkelmann (side-chain)

The first single domain smectic-A elastomer was reported by Nishikawa *et al.* [21], and based on side chain liquid crystalline polymers. A single domain was obtained by subjecting the elastomer to a uniaxial mechanical stress during cross-linking, which serves to align the layers. The single crystal elastomer formed by this process is highly optically transparent, see figure 1.11(a). Whereas polydomain elastomers appear opaque, due to the scattering of light at domain interfaces [22].

When stretching parallel to $\underline{n}_0$ the sample undergoes a layer buckling instability analogous to the buckling transition found in smectic-A liquid crystals. The stress-strain curve for this stretch is shown in figure 1.11. The deformation is initially stiff with an elastic modulus of $\sim 3\,\mathrm{MPa}$, which is characteristic of the smectic layer modulus B. At a threshold strain ϵ_{th} of approximately 3% the layers buckle, and the sample become opaque due to the newly formed microstructure. Above the threshold the elastic modulus is only $\sim 0.1\,\mathrm{MPa}$, which is characteristic of the rubber elastic modulus μ. This deformation is reversible and the microstructure clears within seconds of the strain being removed [21].

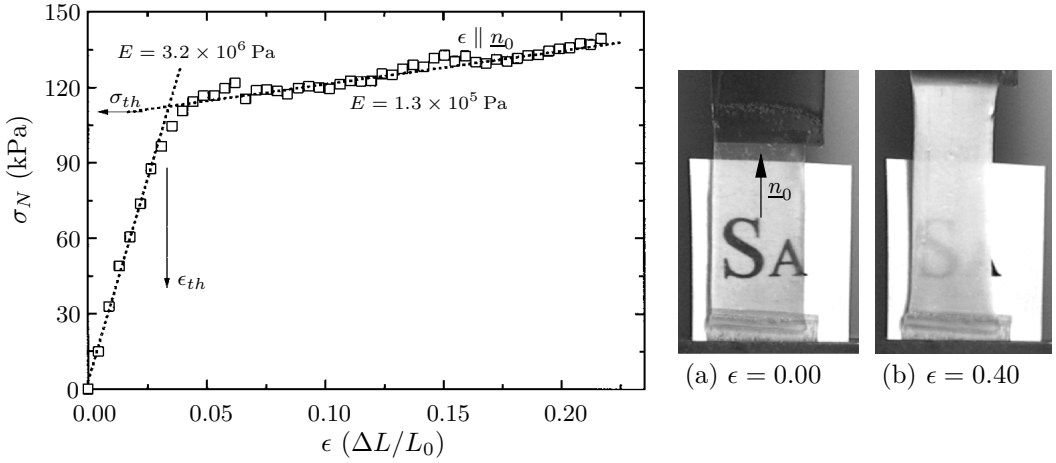

Figure 1.11: Stress-strain curve stretching parallel to $\underline{n}_0$ of a smectic-A monodomain. The sample is shown (a) undeformed, and (b) at a strain of $\epsilon = 0.4$ parallel to $\underline{n}_0$ [19].

The reorientation of the smectic layers is revealed by the x-ray scattering patterns of figure 1.12. The small angle x-ray scattering (SAXS) corresponds to the orientation of layer normals that lie in the scattering plane. The buckling instability causes the SAXS pattern to split into four maxima, which are oriented at an angle ϕ to the stretch axis. The layer normals rotate away from the stretch axis with increasing strain, resulting in a conical distribution of layer normals.

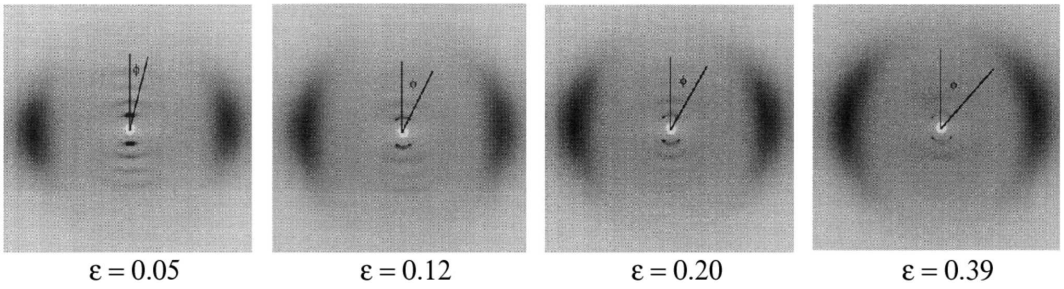

Figure 1.12: X-ray scattering patterns at various strains applied parallel to $\underline{n}_0$ [19].

The wide angle x-ray scattering (WAXS) patterns of figure 1.12 correspond to the orientation of directors that lie in the scattering plane. A uniform director field results in two broad WAXS maxima, and a line connecting these maxima is normal to the director orientation. The two WAXS peaks become increasingly broad with strain but cannot be resolved into four separate maxima, due to their high intrinsic width.

Nishikawa and Finkelmann assert that at high strains the layers breakdown and the smectic phase melts into the nematic. However later authors argue that the elastic energy is too small to melt the system [23]. More detailed x-ray studies of similar side chain systems reveal that the layers behave as if they are embedded in the rubber matrix [24].

When stretching perpendicular to $\underline{n}_0$ the layer planes maintain their original orientation. The stretch does not alter the layer spacing, instead the deformation is accommodated within the plane of the layers. Consequently the width of the sample is unchanged by the stretch and all the contraction occurs in thickness direction, as shown in figure 1.13(b). The Poisson's ratios stretching perpendicular to $\underline{n}_0$ are $(0, 1)$, which contrasts with $(\frac{1}{2}, \frac{1}{2})$ for the parallel case. The stress-strain curve of figure 1.13 shows that the elastic modulus stretching perpendicular to $\underline{n}_0$ is $\sim 0.1\,\mathrm{MPa}$, which is characteristic of the rubber modulus μ.

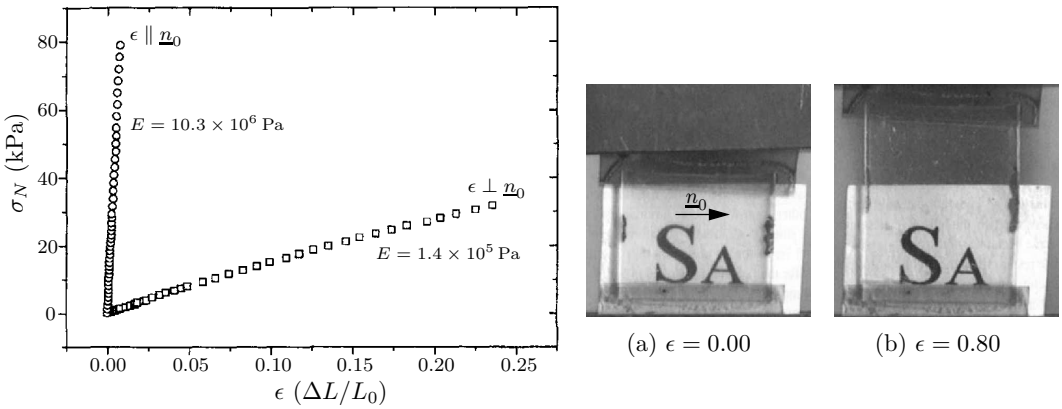

(a) $\epsilon = 0.00$ (b) $\epsilon = 0.80$

Figure 1.13: Stress-strain curve stretching perpendicular and parallel to $\underline{n}_0$. The sample is shown (a) undeformed, and (b) at a strain of $\epsilon = 0.8$ perpendicular to $\underline{n}_0$ [21].

Komp & Finkelmann (side-chain)

Later experiments on side chain systems with different chemistry have found a similar stress-strain threshold behaviour when stretching parallel to the director [25]. The stress-strain curve of figure 1.14 shows that at a strain of $\sim 5\%$ the stiffness reduces from $\sim 14\,\mathrm{MPa}$ to $\sim 0.4\,\mathrm{MPa}$, which is similar to the behaviour found by Nishikawa *et al.*. The Poisson's ratios stretching parallel to the layer normal are $(\frac{1}{2}, \frac{1}{2})$, and in the perpendicular case they are approximately $(0, 1)$. The sample has an elastic modulus of $\sim 3.8\,\mathrm{MPa}$ when stretching perpendicular to the layer normal, which is surprisingly stiff as this is an order of magnitude larger than the rubber elasticity modulus in the isotropic phase.

Unexpectedly the sample remains transparent when stretching parallel to the layer normal, as shown in figure 1.14(b). Also the x-ray scattering shown, in figure 1.15, does not indicate a reorientation of the smectic layers, as the SAXS peaks remain parallel to the stretch axis. The interpretation of Komp and Finkelmann is that no buckling instability or microstructure formation occurs. They attribute the behaviour to defects in the smectic layer structure, as their sample has a low smectic layer correlation length $\xi = 300\,\text{Å}$, compared to $\xi \sim 1.4\,\mu\mathrm{m}$ found by Nishikawa *et al.*. They argue that in order to achieve the deformation the number of layers in the sample to increases, which is possible due to the rearrangement of defects in the sample. The poorly correlated layers may prohibit the typical in-plane fluidity of the layers, resulting in an increased stiffness when stretching perpendicular to the layer normal.

An alternative explanation is that the sample is buckling only in its thickness direction. The sample might still appear transparent because it is only 100 μm thick. The x-ray scattering data could be consistent with this scenario, as unidirectional buckling would rotate the layers out of the scattering plane rather than around the scattering plane. Consequently the absolute scattering intensity would drop sharply at the threshold, and the SAXS peaks would remain parallel to the stretch axis. Unfortunately absolute scattering intensity measurements are unavailable. However the observed Poisson's ratio of $(\frac{1}{2}, \frac{1}{2})$ are not consistent with a deformation mode of unidirectional buckling, which would only cause contraction in the thickness direction. Other possible explanations such as the influence of the sample aspect ratio and a small misalignment of the layer normal with the stretch axis are considered in the finite element modelling work of chapter 5.

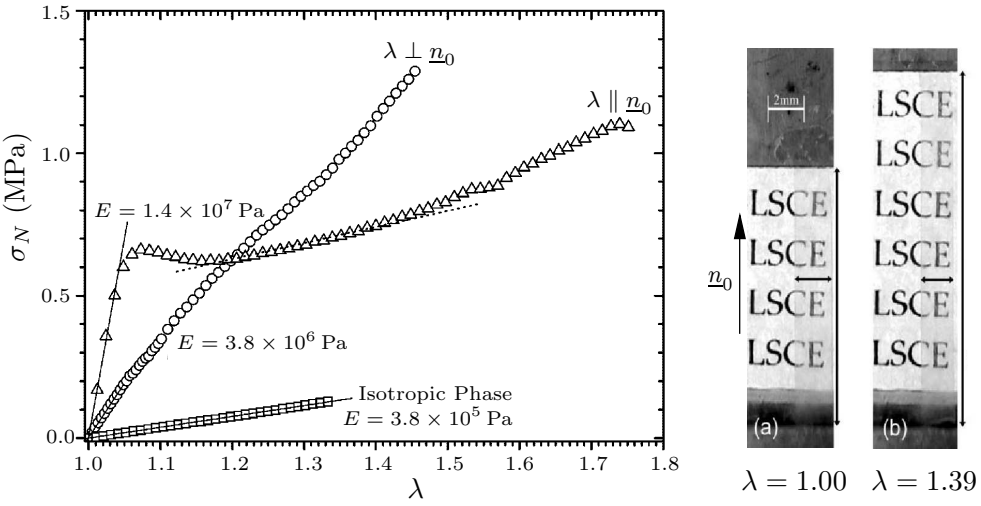

Figure 1.14: Stress-strain curves stretching monodomain Sm-A LCE parallel and perpendicular to $\underline{n}_0$, and stretching the high temperature elastomer in the isotropic phase. The Sm-A monodomain sample is shown (a) undeformed and (b) stretched by $\lambda = 1.39$ parallel to $\underline{n}_0$ [25].

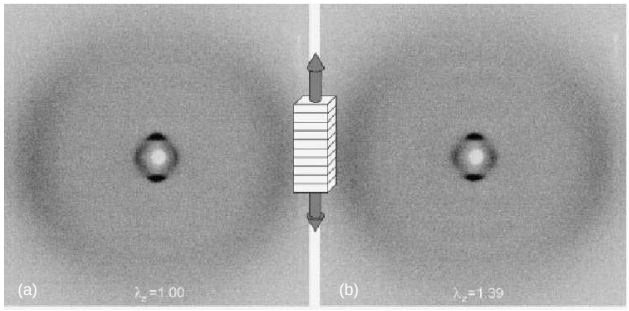

Figure 1.15: X-ray scattering patterns for (a) $\lambda = 1.00$ and (b) $\lambda = 1.39$ parallel to $\underline{n}_0$ [25].

A side-chain smectic-A elastomer with a high concentration of defects was investigated by Kramer and Finkelmann [26]. Chemically the sample included two different mesogens of slightly different sizes, resulting in a layer correlation length $\xi = 400$ Å. When stretching parallel to the layer normal there was a smeared out stress-strain threshold at $\sim 3\%$, and the sample remained optically transparent above the threshold, which is qualitatively similar to the behaviour found by Komp and Finkelmann. The behaviour of smectic elastomer is also known to depend on the degree of crosslinking in the elastomer [27], as heavy cross-linking induces disorder in the layers.

Kramer & Finkelmann - Shear experiment (side-chain)

Kramer and Finkelmann investigated the shearing of monodomain smectic-A elastomer [28]. The sample was identical in chemical composition to that of Nishikawa *et al.* (1999). Imposing a shear strain perpendicular to the initial layer normal resulted in a non-zero tilt angle in the smectic-A phase. A shear strain of 21° is shown applied in figure 1.16. The corresponding x-ray scattering data demonstrates that the layers do not reorient, as the SAXS peaks are fixed in orientation. Whereas the director has rotated by 6°, as the WAXS peaks have rotated by this amount, thus there there is an induced tilt of 6°.

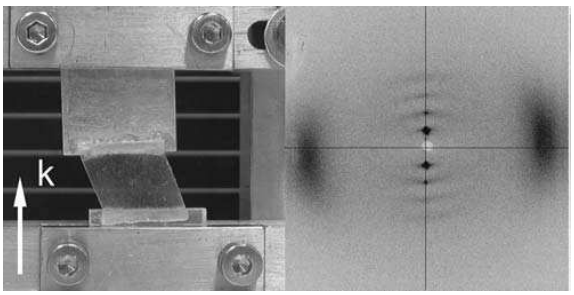

Figure 1.16: (left) A smectic-A monodomain sheared perpendicular to the layer normal to angle of 21°, and (right) the corresponding SAXS and WAXS shows an induced tilt of 6° [28].

Beyer, Terentjev & Zentel (main-chain)

A smectic elastomer with a main chain polymer architecture (where the mesogens are incorporated directly into the backbone) was investigated by Beyer, Terentjev & Zentel [29] . This system and other main-chain systems have contrasting behaviour to side chain systems [30, 31]. The stress-strain curves for main-chain monodomain smectic-A elastomer, shown in figure 1.17, only exhibit a threshold behaviour when stretching at low temperatures. At higher temperatures the initial elastic modulus is less than 1 MPa, which is smaller than the expected smectic modulus. This suggests that network crosslinks may be free to move between the smectic layers in these systems, whereas in the samples of Nishikawa *et al.* the cross-links are thought to be constrained by the layers. Consequently the difference between the elastic moduli in the parallel and perpendicular directions is relatively low.

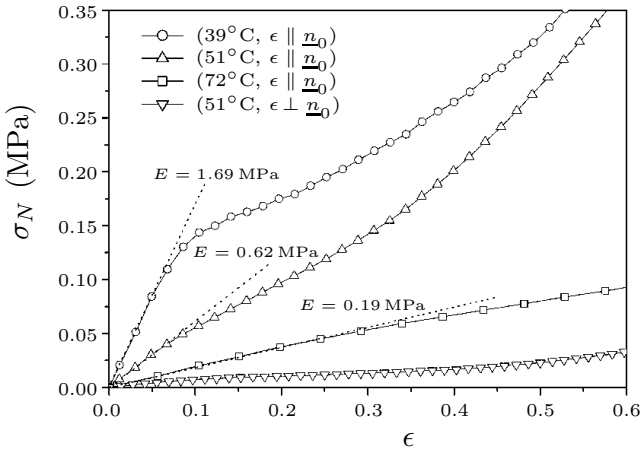

Figure 1.17: Stress-strain curves stretching a smectic-A monodomain parallel to $\underline{n}_0$ of at 39°C, 51°C and 72°C and stretching perpendicular to $\underline{n}_0$ at 51°C [29].

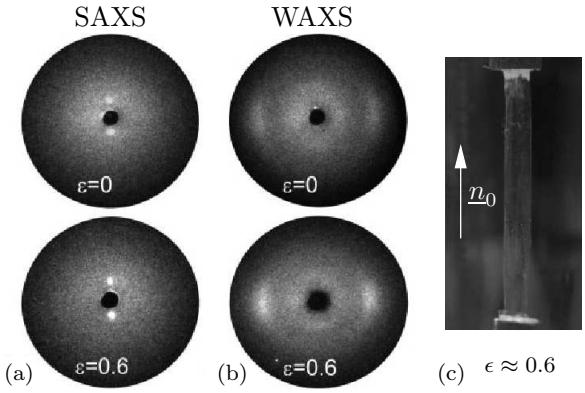

Figure 1.18: (a) SAXS and (b) WAXS patterns stretching a smectic-A monodomain parallel to $\underline{n}_0$ at strains of $\epsilon = 0$ and $\epsilon = 0.6$, at room temperature, and (c) the sample at $\epsilon \approx 0.6$ [29].

The x-ray scattering patterns, shown in figure 1.18(a) and (b), demonstrate an increase in ordering when stretching parallel to the layer normal [29]. The sample, shown in figure 1.18(c), remains transparent when stretched parallel to the layer normal. It is thought that hairpin defects – sharp reversals in the chain orientation – play a crucial role in the softening behaviour rather than layer buckling [29, 30, 32], hence no rotation of the layers or microstructure formation is observed. The smectic layers do not seem to be strongly coupled to the rubber matrix, and hence do not behave as embedded planes. Experiments on main chain smectic-C elastomers layers also show that layers are weakly coupled to the rubber matrix [33, 34].

1.4 Mechanical Experiments on Smectic-C LCE

Experimentally Aligning a Smectic-C LCE Monodomain

On crosslinking smectic-C LCE forms with a randomly-oriented, polydomain structure if there is no preferred direction. The creation of uniformly-ordered monodomain samples was a significant experimental development, and there are two principal experimental methods for their creation. These experiments are based on applying two deformations (one after the other) during crosslinking, to align both the director and layer normal in a sample.

Method 1. Reorientation by two sequential uniaxial stretches

Semmler and Finkelmann [35] demonstrated that two uniaxial stretches can be used to align a smectic-C^* sample. The first stretch aligns the director just as in a nematic, which results in a pseudo-monodomain described earlier. The second stretch is at an angle ϕ to the first stretch, where $\phi = 90° - \theta_0$ as illustrated in figure 1.19. This second stretch does not reorient layer normals that are already perpendicular to the stretch axis. All the other layer normals are reoriented to become perpendicular to the stretch axis.

Method 2. One uniaxial stretch followed by a shear deformation

Hiraoka and Finkelmann [36] demonstrated that a uniaxial stretch followed by a shear deformation can be used to align a smectic-C^* sample. The first stretch is achieved by applying a uniaxial stress of 25 kPa for 1 hour, and produces a pseudo-monodomain. The shear deformation is used to align the layer normals and is through an angle of approximately 20° applied for 3 hours, until the cross-linking reactions are complete. The apparatus used to apply this shear is shown in figure 1.20.

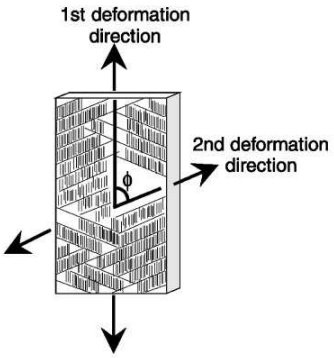

Figure 1.19: Geometry of the two uniaxial deformations. ϕ is 90° minus the Sm-C tilt angle [35].

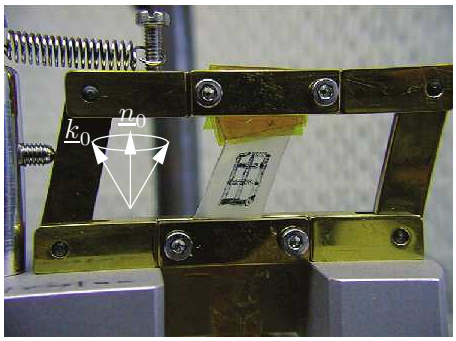

Figure 1.20: Geometry of shearing a Sm-C pseudo-monodomain to produce a monodomain [36].

Hiraoka and Finkelmann - Reversible thermal deformation

The quality of a smectic-C monodomain can be illustrated by demonstrating the coupling between the microscopic orientation of the director and the macroscopic shape of the rubber. Hiraoka *et al.* [37] took a smectic-C^* monodomain and heated it into the smectic-A phase, which causes a spontaneous shear as a result of the tilt angle going to zero. When cooled back to the smectic-C^* phase the sample recovers its initial shape, as illustrated in figure 1.21.

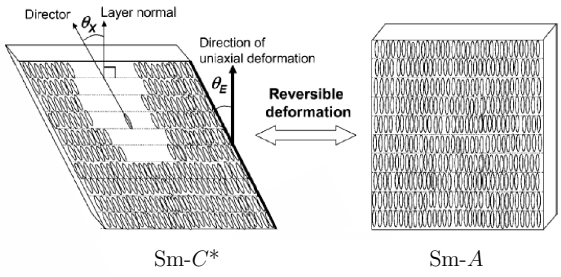

Figure 1.21: Model of the molecular realignment of Sm-C^* LCE film on heating to the Sm-A phase. The shear angle, θ_E, is not in general equal to the induced tilt angle, θ_X, due to the polymer chain anisotropy [37].

Pseudo-Monodomain Samples

Despite the existence of these methods to produce a monodomain, there are no mechanical experiments characterizing the stress strain behaviour of smectic-C monodomains. Experimentally it is easier to produce a pseudo-monodomain, and hence mechanical experiments have focussed on them. However, the reorientation of the director and layer normal in each domain results in a more complicated deformation process than for a monodomain. This process has been studied through x-ray scattering [15], but the scattering patterns can be difficult to interpret as they are the sum of many, differently oriented domains. Unfortunately they are the only mechanical data available to probe current theoretical models, so the main results of these experiments are presented here.

Sánchez-Ferrer & Finkelmann - Stretching a pseudo-monodomain (main-chain)

The uniaxial stretching and shearing experiments of Sánchez-Ferrer and Finkelmann [15] are performed on smectic-C, main-chain LCE with a pseudo-monodomain microstructure described earlier. The samples are highly anisotropic; stretching parallel to the director is much stiffer than stretching perpendicular to the director and much larger deformations are possible when stretching perpendicular to the director, see figure 1.22. The sample relaxation proceeded slowly, so 1 hour of relaxation time was given between deformation increments.

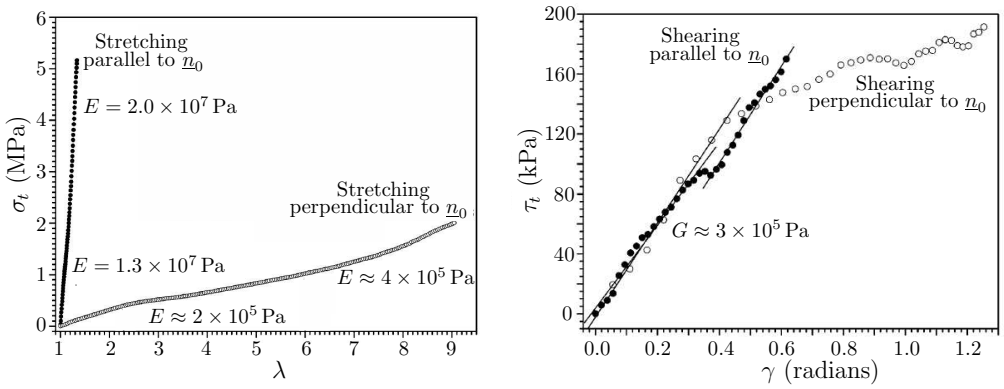

Figure 1.22: (left) True stress versus deformation, for stretching parallel and perpendicular to the director, and (right) shear stress versus shear strain, parallel and perpendicular to the director in a smectic-C LCE pseudo-monodomain [15].

When stretching parallel to the director the initial elastic modulus is ~ 13 MPa, but at a deformation of $\lambda \approx 1.2$ the modulus increases to ~ 20 MPa. The x-ray scattering patterns for the initial part of this stretch are shown in figure 1.23.

The WAXS patterns appear to show that the director remains parallel to the stretch axis, and this is further supported by a corresponding increase in the WAXS order from S = 0.82 to 0.89. The SAXS peaks can be seen to reorient from an angle of 31° to 40° relative to the stretch axis, i.e. the layer normals rotate away from the stretch axis. If the director is parallel to the stretch axis, then the smectic-C tilt angle must be increasing. For deformations greater than $\lambda \approx 1.2$ no further reorientation is observed, and the corresponding stiffness is slightly higher. The deformations applied parallel to the director are reversible.

The stretching of a pseudo-monodomain parallel to the director provokes a number of questions;

1. *Why does the rotation of the layers stop at a certain strain?*

   If the smectic layers deform like embedded planes then the layer normals would rotate away from the stretch axis with the director following at the tilt angle. This is because when a

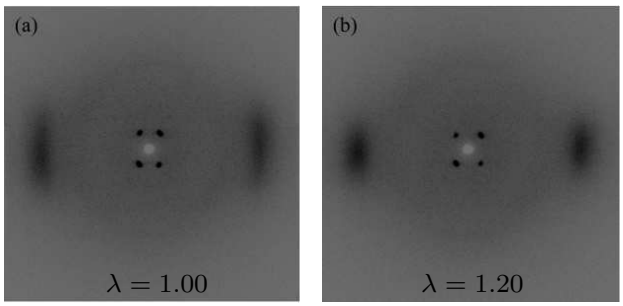

Figure 1.23: X-ray scattering patterns for (a) $\lambda = 1.00$ and (b) $\lambda = 1.20$ parallel to $\underline{n}_0$ [15].

strain is imposed at an angle to the layer normal of a layered material, the elongation and contraction of the sample naturally rotate the layer normal. It seems surprising that no buckling instability like that found by Nishikawa *et al.* occurs in this geometry, as this would allow deformation at the rubber shear modulus.

Sánchez-Ferrer and Finkelmann assert that the director is not able to rotate when strain is applied parallel to the director, due to the main-chain chemistry of the system. They argue that as the mesogens are incorporated directly into the polymer backbone there is a torque which prevents the mesogens rotating. This explanation seems to contradict the classical understanding of liquid crystal elastomers, which argues that the anisotropic polymer chain distribution created by the broken symmetry of the liquid crystal director is free to rotate.

2. *Why is stretching parallel to the director so stiff?*

   The observed stiffness is characteristic of the smectic layer modulus and only limited layer rotation occurs, but theoretically a layer instability seems favourable. One possible explanation is that it is difficult to rotate the layers and deform neighbouring domains in a compatible way. The problem of compatibility may be exacerbated by the initial domain structure present in a smectic-C pseudo-monodomain, i.e. the interlocking domains are irregularly shaped and possess different initial orientations of the layer normal.

   The layer correlation length in this sample is 400 Å, which is typical for main-chain systems. In main-chain smectic-A systems such poorly correlated [26] or weakly coupled layers [38] result in a low elastic modulus when stretching parallel to the director. But these mechanism do not seem to allow for a low elastic modulus here.

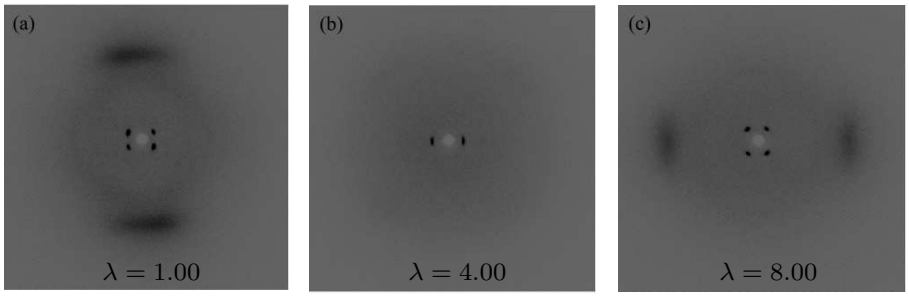

Figure 1.24: X-ray scattering patterns for deformations (a) $\lambda = 1.00$, (b) $\lambda = 4.00$ and (c) $\lambda = 8.00$ perpendicular to $\underline{n}_0$ [15].

When stretching perpendicular to the director the initial modulus is ~ 0.3 MPa, but a reduction in the modulus occurs at a deformation of $\lambda \sim 2.3$. This coincides with the initiation of a reorientation process, where the layers reorient to become perpendicular to the stretch axis. The x-ray scattering patterns, shown in figure 1.24, demonstrate that the layer normals are oriented perpendicular to the stretch axis when $\lambda = 4$. Surprisingly at deformations above $\lambda \sim 6$ the layers rotate towards the stretch axis, as the director becomes aligned with the stretch axis. The x-ray scattering shows

that at $\lambda = 8$ the sample has reoriented into a pseudo-monodomain with the director parallel to the stretch axis. The modulus corresponding to the last phase of deformation is $\sim 0.4\,\mathrm{MPa}$, which seems low considering that a pseudo-monodomain is being stretched parallel to the director. All the deformation associated with reorientation (i.e. $\lambda > 2.3$) is irreversible.

The stretching of a pseudo-monodomain perpendicular to the director also provoke questions;

1. *When stretching perpendicular to the director why does reorientation form a pseudo-monodomain?*

   At very large strains the layer normals rotate towards the stretch axis, which indicates that the layers are not behaving like embedded planes It is possible that at large strains the smectic layers are no longer strongly coupled to the rubbery matrix, which allows the director to align with the stretch axis.

2. *Why are the deformations that result in reorientation irreversible?*

   It might be expected that layer and director reorientation would correspond to elastic processes, so the deformations would be able to reverse themselves when the strain is removed.

When shearing parallel and perpendicular to the director the initial elastic modulus is identical for both geometries, see figure 1.22, The modulus of $\sim 0.3\,\mathrm{MPa}$ is characteristic of the rubber modulus. For the case of shearing perpendicular to the director there is a reduction in the shear modulus above a shear angle of around 19°. Both shear deformations cause reorientation towards a monodomain state, but the order parameter data indicates that shearing perpendicular creates a more uniform monodomain.

Modelling the mechanical deformations of smectic-C elastomer in various geometries may be able to resolve some of the questions raised by this experiment.

Sánchez-Ferrer & Finkelmann: Polydomain to Pseudo-Monodomain Transition (main-chain)

Sánchez-Ferrer and Finkelmann also studied the stretching of main-chain, smectic-C polydomain [34]. The strain causes a reorientation process, which eventually produces a pseudo-monodomain with the director parallel to the stretch axis. Increasing the crosslink density resulted in a shorter soft plateau and a shorter extension to breaking point. Once reorientation is complete the sample deforms nearly as stiffly as the pseudo-monodomain sample stretched parallel to the director, see figure 1.25.

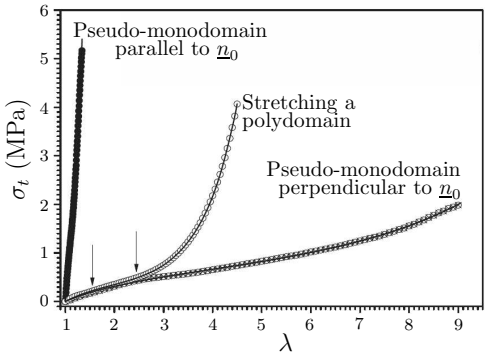

Figure 1.25: True stress versus strain. The stiffness of stretching a polydomain is intermediate to the two cases of stretching a pseudo-monodomain shown. The arrows indicate the strain region where the polydomain sample undergoes a reorientation towards a Sm-C pseudo-monodomain [34].

Patil, Lentz and Hedden: Polydomain to Pseudo-Monodomain Transition (main-chain)

Hedden *et al.* investigated the stretching of a main-chain smectic-C polydomain, prepared in a similar way to that of Sánchez-Ferrer *et al.* but with different chemical constituents. The polydomain undergoes a necking process, which produces a pseudo-monodomain with the director aligned with the stretch axis. The necking transition occurs at $\lambda \sim 1.2$, with the necked pseudo-monodomain region eventually consuming the non-necked polydomain region. The authors attribute the necking transition to the unfolding of hairpin chains, and the irreversibility of the deformation to the formation of new smectic domains. The stress-strain curve, shown in figure 1.26, indicates that the sample initially deforms at the smectic modulus.

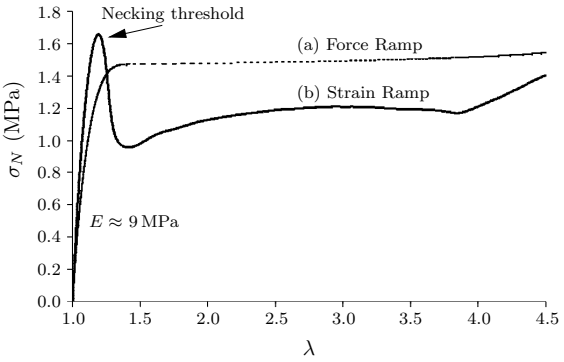

Figure 1.26: Nominal stress versus strain of main-chain smectic-C polydomain imposed by (a) a force ramp and (b) a strain ramp [33].

Ren, McMullan, and Griffin: Various Systems (main-chain)

Griffin *et al.* measured the strains-ratio (the negative ratio of the width strain to elongation strain) for polydomain and pseudo-monodomain smectic-C elastomer [39], as shown in figure 1.27. The stress behaviour is similar to that found by Sánchez-Ferrer and Finkelmann. However stretching a pseudo-monodomain perpendicular to $\underline{n}_0$ resulted in necking at a strain of $\sim 30\%$ after which the strains-ratio measurements were discontinued.

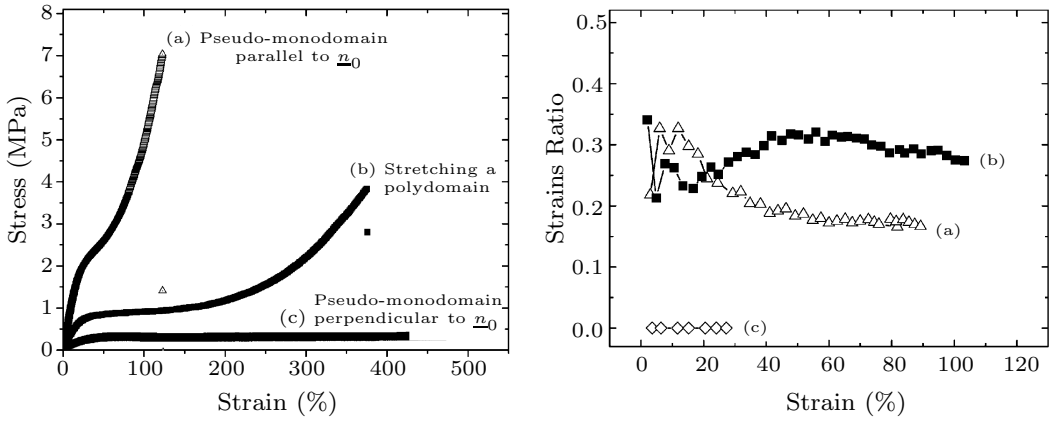

Figure 1.27: (left) Stress-strain and (right) the strains ratio for stretching (a) a pseudo-monodomain parallel to $\underline{n}_0$, (b) a polydomain, and (c) pseudo-monodomain perpendicular to $\underline{n}_0$ [39].

Griffin *et al.* then incorporated transverse rods into a main-chain smectic-C polydomain [40]. The intention was to create an auxetic effect (lateral expansion perpendicular to the stretch axis) by increasing the packing density when the transverse rods rotate, as illustrated in figure 1.28.

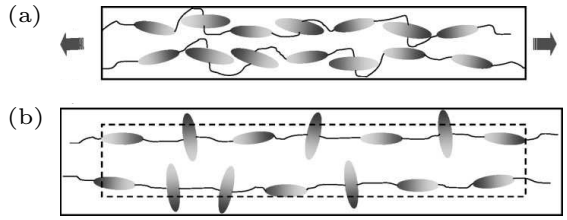

Figure 1.28: Illustration of the auxetic effect mechanism, achieved through the incorporation of transverse rods, shown (a) in the undeformed state, and (b) once a deformation is applied [40].

The stress-strain behaviour is largely unchanged by the transverse rods, and the mechanism failed to achieve a negative stress-strain ratio, as shown in figure 1.29. The authors attribute this to the smectic layers preventing rotation of the transverse rods, and argue that longer transverse rods with shorter spacing between rods might realize auxetic effects in main-chain LCE. However in elastomeric materials a non-volume conserving deformation mode would be penalized by the bulk modulus $\sim 1\,\text{GPa}$ [41]. This greatly exceeds the energetic cost of all other deformation modes in main-chain LCE, e.g. layer stretching $\sim 10\,\text{MPa}$ or entropic elasticity $\sim 0.1\,\text{MPa}$, so these deformation modes will occur rather than a volume expansion. Consequently the proposed auxetic mechanism is unlikely to be achievable in LCE, but a glassy system where the volume is not ordinarily conserved may render it possible.

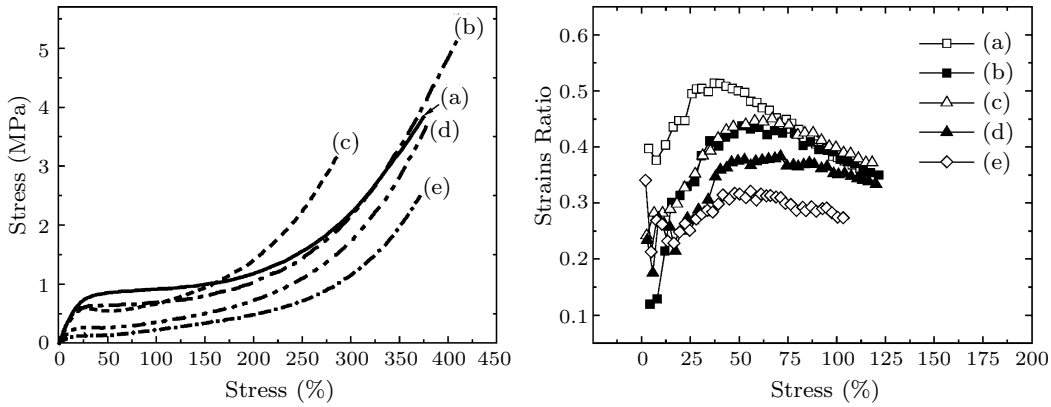

Figure 1.29: (left) Stress-strain and (right) the strains ratio for stretching a smectic-C polydomain with (a) 0mol% (b) 10mol% (c) 20mol% (d) 30mol% and (e) 40mol% of transverse rods [40].

Smectic-C LCE Balloon Experiments (side-chain)

Schüring *et al.* [42] demonstrated that a planar film of smectic melt can be inflated into a spherical bubble and then photocross-linked to form a smectic-C LCE balloon, see figure 1.30. The melt was blown and UV cross-linked whilst in the smectic-A phase and the biaxial elongation flow aligned the layer normals parallel to the radius of the balloon. In order to blow a bubble low viscosities and therefore high temperatures are required. Measuring the air pressure and balloon radius determined the elastic modulus in the isotropic, smectic-A and smectic-C phases.

It was not possible to blow a balloon with a radius much larger than the capillary tube, meaning that the balloon is not perfectly spherical. A uniform thickness of a balloon could not be exper-

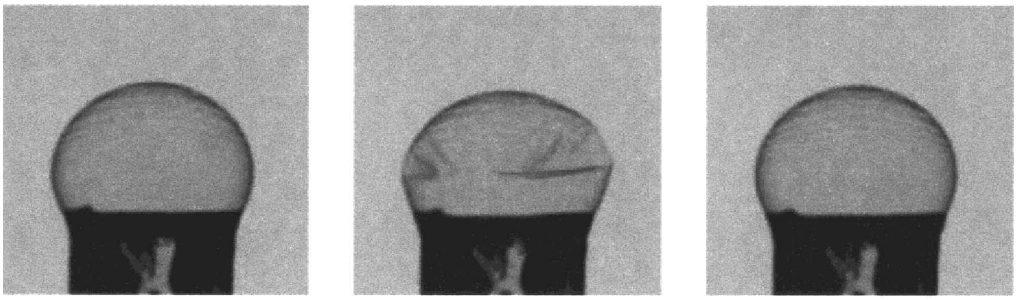

$P = 91.7\,\mathrm{Pa}$ $P = -0.25\,\mathrm{Pa}$ $P = 1.15\,\mathrm{Pa}$

Figure 1.30: Shape of an LCE balloon with different internal excess pressures. The diameter is approximately 5 mm. The balloon is stable at negative pressure differences because of elastic forces (the crinkles are fully reversible). The balloon had an equatorial thickness of 2.3 μm [42].

imentally achieved due to the high molecular weight of the polymer melt. The high cross-linking density and dilute concentration of smectic mesogens in the elastomer meant that there was no significant difference between the isotropic and smectic phases [43], which prevented any smectic layer compression or tilt angle effects from being observed.

Similar side-chain systems produced by photo-crosslinking also behave closer to isotropic rubbers [44], and demonstrate interlayer penetration upon stretching parallel to the layers [45].

1.5 Applications of Smectic LCE

Smectic elastomers have a number of potential applications, but are especially interesting as miniaturized-actuators, sensors and shape memory materials [46, 47]. The symmetry properties of the chiral smectic phases allows electrical actuation, which may be more convenient than thermal or photo actuation.

Smectic-C^* LCEs are **piezoelectric**, as they have the correct symmetry properties to possess electric dipoles. The polarization vector points in the direction $\underline{n} \times \underline{k}$. Piezoelectricity is the effect whereby a mechanical strain causes a change in the electrical polarization of the material. A change in electrical polarization can be measured as a change in surface charge density. Smectic-C^* LCE is a soft and highly-deformable material. This is in contrast with ceramic piezoelectric actuators, which are capable of very small deformations at high stress.

Smectic-C^* LCEs also exhibit **ferroelectricity** [20]. This means that the spontaneous electrical polarization can be reversed, for example by an applied electric field.

The **electroclinic effect** was first demonstrated in smectic-A^* LCs by Garoff and Meyer (1977) [48]. It is the direct coupling of the tilt angle to an imposed electric field. In smectic-A^* LCEs this effect induces a macroscopic strain because it modifies the tilt angle away from an initial value of $\theta_0 = 0$, producing a contraction in the layer spacing by a factor $1 - \cos\theta_0$. In LCEs the electroclinic effect is strongest at the smectic-C^* to smectic-A phase transition.

Ferroelectricity in a Pseudo-Monodomain

Heinze and Finkelmann [20] subjected pseudo-monodomain smectic-C^* samples to a simple shear deformation, see figure 1.31. The layer structure was reoriented by the shear, which resulted in a spontaneous polarization.

The layer normal reorientation was tracked using x-ray diffraction and measurements of the spontaneous polarization. The X-ray measurements showed that shear does not create a uniform monodomain sample, which appears to contradict similar experiments e.g. [15], [36].

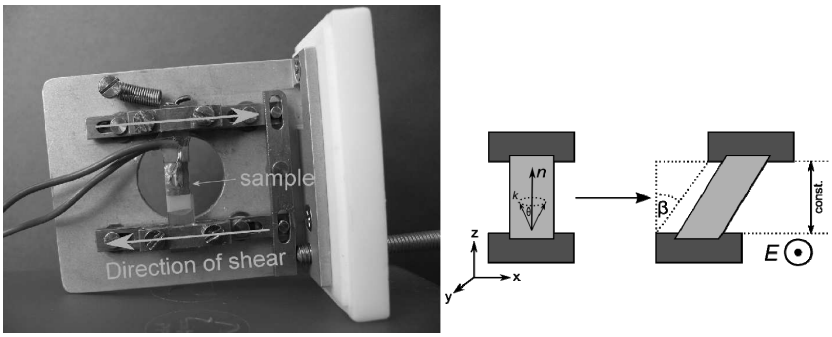

Figure 1.31: Shearing perpendicular to the director of a pseudo-monodomain. Silver grease was used to create electrical contacts on the two sides of the elastomer [20].

At shear angles smaller than the tilt angle there is a splitting of the wide angle scattering distribution, which suggests that there are two different director orientations. At shears greater than the tilt angle the director reorientation process has finished and the scattering peaks are constant.

The layer normals that are initially on the positive half of the x-axis, K_{+x}, behave differently to their negative counterparts, K_{-x}. At small shears the layers K_{-x} migrate to the x-z plane, which can be seen from the increase in scattering intensity. Once shears of around the tilt angle have been reached these layers are finished reorientating. However the layers K_{+x} migrate away from the x-z plane and never realign with the x-z plane. This behaviour qualitatively agrees with the smectic-C model of Warner and Adams [49].

The spontaneous polarization was linearly dependent on the concentration of chiral dopants.

A different realignment method, where the layer reorientation is much less complicated, is required to study the true spontaneous polarization of this material.

Electroclinic Effect in a Monodomain

Hiraoka and Finkelmann demonstrated the electroclinic effect in a monodomain Sm-C^* sample at various temperatures [50]. The electroclinic effect is the direct coupling of the tilt angle to an imposed electric field. Electrodes imposed an electric field across the thickness of the sample, and the resultant deformation was measured with a microscope, see figure 1.32.

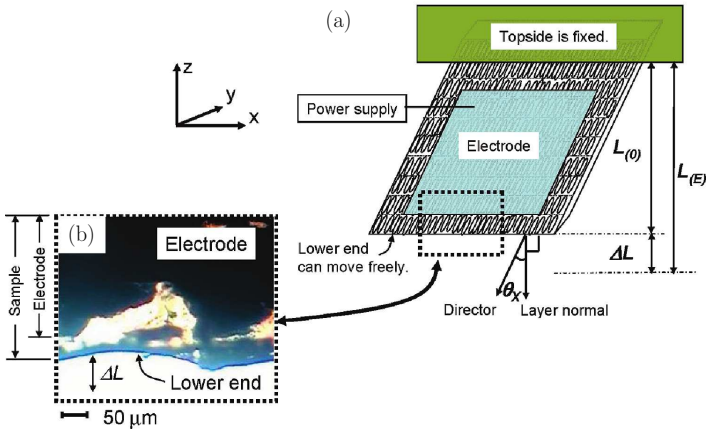

Figure 1.32: Observation of an electric-field-induced deformation; (a) sample geometry and (b) a micrograph image corresponding to the square section dotted within in (a) [50].

By varying the temperature the material was found to be most responsive at the Sm-C^*- Sm-A phase transition. The electroclinic effect can occur in the Sm-A^* phase because an applied electric field can induce a polarization by increasing the tilt angle. The resultant deformation from an imposed electric field is shown in figure 1.33. The greatest strain achieved was $\Delta L/L_0 = 0.6\%$

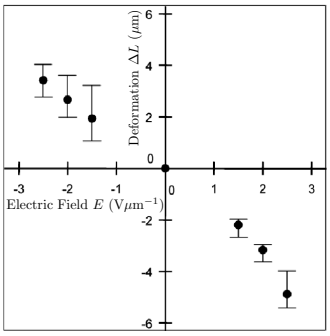

Figure 1.33: Electric field, E, and deformation in the direction ΔL. The temperature was just above the Sm-C^* to Sm-A phase transition. The sample had a residual tilt angle of about 5° in the Sm-A phase, caused by cross-linking the sample in the Sm-C phase [50].

Shape Memory in Smectic-C LCE

Shape memory polymers (SMPs) are materials that have the ability to return from a deformed state (temporary shape) to an original shape, when triggered by an external stimulus e.g. temperature change.

Rousseau and Mather [47] demonstrated that polydomain smectic-C main-chain LCE exhibits a thermomechanical shape memory.

Shape memory polymer works by following the cycle shown in figure 1.34;

(i) Firstly the material is heated to a point above the transition temperature. This starting point is marked in figure 1.34 by the point marked (a).

(ii) **Deformation**. A force is imposed on the material, which deforms it into a temporary shape.

(iii) **Cooling**. The material is cooled beneath the transition temperature. In typical SMPs a crystallization occurs, which forms covalent netpoints that prevent a return to the original shape.

(iv) **Fixing**. The deformation force is removed, with the material retaining its temporary shape.

(v) **Recovery**. The material is activated by heating it above the temperature required to destroy the covalent netpoints. The material returns to the original shape.

In Smectic-C LCE a polydomain microstructure forms on cooling beneath the Iso-Sm-C transition temperature. This polydomain microstructure is responsible for stabilizing the temporary shape. If the sample is heated above the transition temperature the microstructure is destroyed and the initial shape recovered. By comparison natural rubber is not an effective shape memory material, as illustrated by the cycle starting from point (b) in figure 1.34. There is no memory effect here, as after the sample is cooled and the force removed, the strain recovers back to zero.

The transition temperature of the LCE can be fixed by varying the composition of mesogens, which enables body temperature triggering (37°C). There are numerous biomedical applications of shape memory polymer technology foams e.g. scaffolds for tissue engineering, foams for treating aneurysms, stent materials that release embedded drugs and a needle adapter for dialysis patients [51].

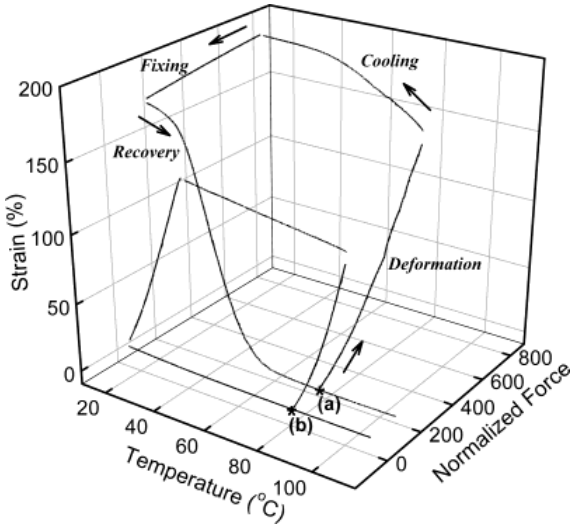

Figure 1.34: Shape memory cycle of (a) Smectic-C LCE (b) Natural rubber [47].

1.6 Theoretical Models of Nematic Elastomer

The reorientation processes and mechanical properties of LCE can be studied by considering the minimization of model free energies. It is useful to introduce the theory of nematic elastomers here, as smectic elastomer models are based on this theory. Numerous nematic free energies have been put forward in the literature and these can successfully describe many observed phenomena, e.g. the rotation of the director towards the stretch axis and the associated stress-strain plateau.

Ideally Soft Nematic Elastomers

Nematic elastomers have an anisotropic polymer chain conformation, due to the liquid crystalline ordering. Typically the polymer chains prefer to run parallel to the director, giving a prolate chain configuration. The polymer anisotropies parallel and perpendicular to the director are $l_{||}$ and $l_{\perp}$, and their ratio is denoted as $r = l_{||}/l_{\perp}$. Deformations that can be achieved by simply rotating the polymer chain anisotropy are in an idealized sense perfectly soft. The elastic energy of an ideally soft nematic elastomer was derived by Bladon, Terentjev and Warner [52] to be,

$$F_{BTW} = F_0(Q, \underline{\underline{\lambda}}) + \frac{k_B T}{2}\left(\frac{1}{l_{||}} - \frac{1}{l_{\perp}}\right) \mathrm{Tr}\left[\underline{\underline{\lambda}} \cdot \underline{\underline{\ell}}_0 \cdot \underline{\underline{\lambda}}^T \cdot \underline{\underline{\ell}}^{-1}\right], \tag{1.3}$$

where the nematic liquid crystal order parameter Q is taken to be unaffected by the deformation. The initial orientation of the director is $\underline{n}_0$, and following deformation the director is $\underline{n}$. The polymer step-length tensor is $\underline{\underline{\ell}}_0 = \underline{\underline{\delta}} + (r-1)\underline{n}_0\,\underline{n}_0^T$ and its inverse is $\underline{\underline{\ell}}^{-1} = \underline{\underline{\delta}} + (\frac{1}{r} - 1)\underline{n}\,\underline{n}^T$. The deformation matrix $\underline{\underline{\lambda}}$ describes affine deformations of the elastomer. A point $\underline{R}_0$ in the reference state is transformed to the target state by $\underline{R} = \underline{\underline{\lambda}} \cdot \underline{R}_0$, as illustrated in figure 1.35.

The components of the deformation matrix describe either shears or elongations, e.g. the λ_{xx} component is an elongation in the x-direction and λ_{xz} is a shear of the planes with a normal in the z-direction into the x-direction.

For an imposed deformation the energy can be minimized with respect to the director orientation. When stretching perpendicular to the initial director there is a director instability at a threshold strain λ_c, provided restrictions on the allowed deformation components are made. The threshold strain is a probe of the initial chain anisotropy as $\lambda_c = \left(l_{||}/l_{\perp}\right)^{\frac{1}{3}}$.

This prediction qualitatively agrees with the experimental findings of Mitchell *et al.* [53], where a monodomain nematic sample underwent a strain-induced discontinuity of the director orientation.

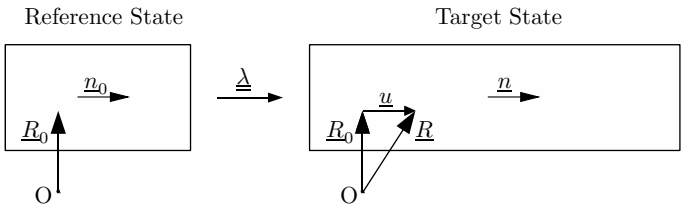

Figure 1.35: The deformation matrix $\underline{\underline{\lambda}}$ transforms points between the reference and target states.

However similar experiments by Kundler and Finkelmann [54] do not observe any discontinuity instead a stripe domain pattern forms at a threshold strain. It was also observed that perfectly soft deformations of nematic elastomers do not occur, as there is a slight elastic stiffness associated with rotations of the director.

Semi-Soft Nematic Elastomers

In order to explain the stiffness associated with director rotations an additional semi-softness term is required, i.e. an energy term that penalizes the soft deformation modes. Verwey, Terentjev and Warner [55] introduced a model of semi-softness caused by compositional fluctuations. Compositional fluctuations are unlikely to be the dominant factor in how softness is actually destroyed, but this energy term is of the correct functional form to describe semi-softness arising from any sample non-ideality.

$$F_{VTW} = \underbrace{\frac{1}{2}\mu \mathrm{Tr}\left[\underline{\underline{\lambda}} \cdot \underline{\underline{\ell}}_0 \cdot \underline{\underline{\lambda}}^T \cdot \underline{\underline{\ell}}^{-1}\right]}_{F_{nematic}} + \underbrace{\frac{1}{2}\alpha\mu \mathrm{Tr}\left[\underline{\underline{\lambda}} \cdot (\underline{\underline{\delta}} - \underline{n}_0\,\underline{n}_0^T) \cdot \underline{\underline{\lambda}}^T \cdot \underline{n}\,\underline{n}^T\right]}_{F_{semi-soft}} \tag{1.4}$$

Theoretical stress-strain curves can be derived from the semi-soft model and compared to the experimental results of Kundler and Finkelmann. A deformation, λ, is imposed perpendicular to the initial director and the remaining deformation components and director orientation are minimized over. The free energies for ideally soft and semi-soft nematic elastomers are shown in figure 1.37. The curves are labelled A, B and C corresponding to different degrees of director rotation: A is no director rotation, along B the director rotates from $\theta = 0$ to $\pi/2$ and C corresponds to $\pi/2$ rotation. Stripe domains are visible when the director is partially rotated, i.e. on curve B.

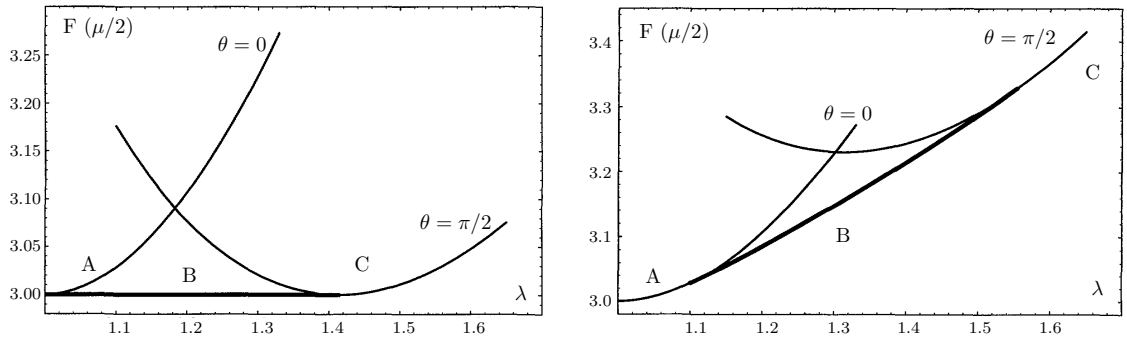

Figure 1.36: Free energy of (left) ideally soft and (right) semi-soft nematic LCE, stretched perpendicular to $\underline{n}_0$ for $r = 2$. [55].

The semi-soft stress-strain response and the corresponding lateral strains are shown in figure 1.37. There is a semi-soft plateau in the stress-strain curve, with a characteristic stiffness $\alpha\mu$, which coincides with the rotation of the director, as shown on the left of figure 1.38. If the clamping conditions deny the required shears, then the following of the softest path is prohibited.

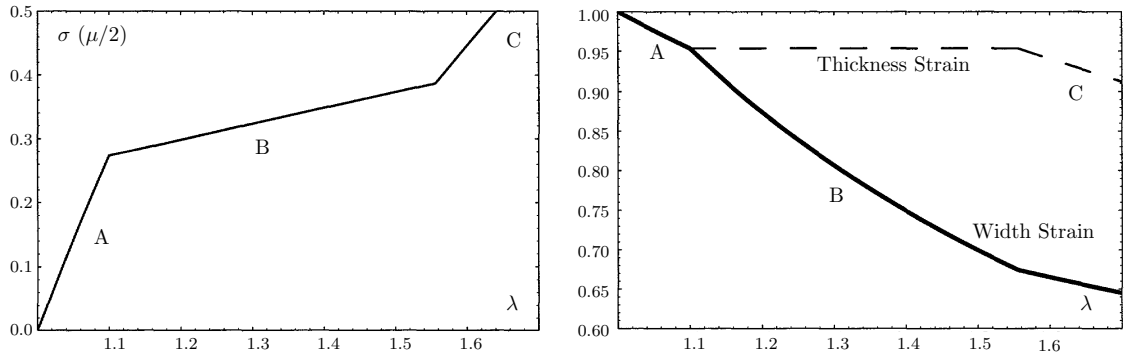

Figure 1.37: (left) Nominal stress versus imposed strain and (right) the corresponding lateral strains for a semi-soft nematic LCE [55].

A wide range of differing nematic elastomers exhibit qualitatively the same pattern of director rotation [56]. This experimental data can be collapsed onto one single master curve given by the semi-soft model, as shown on the right of figure 1.38. The optimal director rotation is, $\theta = \pm \arcsin\left[\frac{r}{r-1}\left(1-\frac{\lambda_1}{\lambda}\right)\right]^{\frac{1}{2}}$, where $\lambda_1 = \left(\frac{r-1}{r-\alpha r-1}\right)^{\frac{1}{3}}$ is the threshold to rotation.

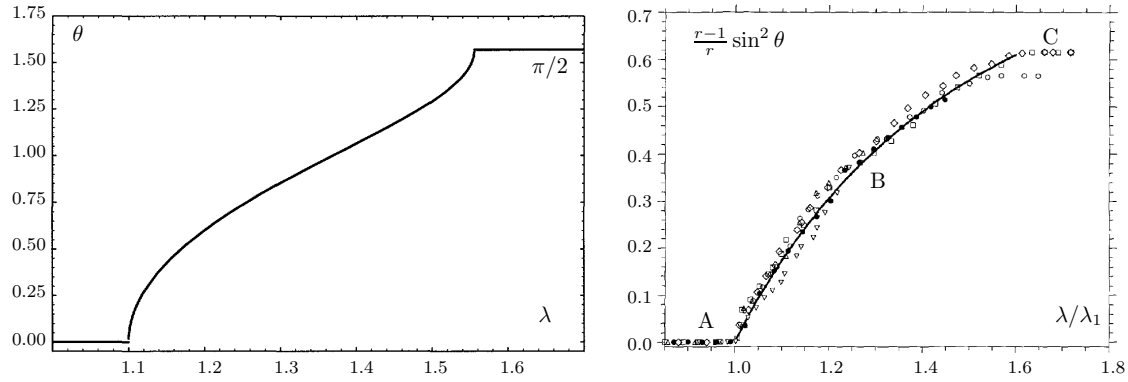

Figure 1.38: (left) The director rotation angle within the stripe domains [55]. (right) Experimental director rotation data collapsed onto a master curve by using λ/λ_1 as a relative deformation. The solid line is $\left(1-(\lambda_1/\lambda)^2\right)$ [56].

Phenomenological Model of Nematic Elastomers

A uniaxial solid has 5 elastic coefficients, but a nematic elastomer can be treated as an approximately isotropic elastic medium characterized by only two moduli; a shear modulus (C_1) and a bulk modulus (C_2). A one-constant approximation can be made for the Frank elasticity, which describes the energy cost of the director field.

The free energy can be written down in terms of the strain field, ϵ_{ij}, and the relative rotation of director and the network, Ω_i. The energy can be written as a sum over a surface if the problem can be simplified to 2D.

$$E = \int ds(\frac{1}{2}C_1\epsilon_{ij}^2 + \frac{1}{2}C_2\epsilon_{ii}^2 + \frac{1}{2}D_1\Omega_i\Omega_j + D_2\Omega_i\epsilon_{jk}n_j\delta_{ik}^{tr}) + \frac{K}{2}((\boldsymbol{\nabla}\cdot\underline{n})^2 + (\underline{n}\times(\boldsymbol{\nabla}\times\underline{n}))^2) \quad (1.5)$$

Minimizing over the free variables gives solutions for the director reorientation.

Weilepp and Brand [57] used this model to provide a description of nematic elastomers, which can be taken as two dimensional phenomenon for sufficiently thin films, i.e. thinner than all than the other length scales in the system.

The mechanism of instability is that the imposed stress gives rise to mechanical strains. The coupling between strains and relative rotations via. D_2 then leads to rotations of the director with respect to the network, which are visible as stripes.

This model was criticized because the threshold strain is predicted to decrease with increasing cross-linking density, which contradicts experimental results [58]. The model also implies values of the threshold strain and elasticity constants that appear to be of the wrong magnitude.

The Weilepp and Brand model can be extended to smectic-A liquid single crystal elastomers [59] to explain the instability found by Nishikawa and Finkelmann [19].

1.7 Theoretical Models of Smectic-A Elastomers

Adams-Warner Model

The Adams-Warner model is an extension of the Bladon, Terentjev, Warner model of nematic elastomers to describe smectic elastomers [23]. The model includes an additional microscopically-justifiable term to describe the elasticity of layers,

$$F_{\text{smectic-}A} = \frac{1}{2}\mu \text{Tr}\left[\underline{\underline{\lambda}} \cdot \underline{\underline{\ell}}_0 \cdot \underline{\underline{\lambda}}^T \cdot \underline{\underline{\ell}}^{-1}\right] + \frac{1}{2}B\left(\frac{d}{d_0} - 1\right)^2, \tag{1.6}$$

where d/d_0 is the change in smectic layer spacing and B is the smectic modulus. The model assumes that the smectic layers are strongly coupled to the polymer matrix, and that the layers deform like embedded planes. Consequently the orientation of the layer normal is simply a slave to the deformation matrix, i.e.

$$\underline{k} = \frac{\underline{\underline{\lambda}}^{-T} \cdot \underline{k}_0}{|\underline{\underline{\lambda}}^{-T} \cdot \underline{k}_0|}, \tag{1.7}$$

and the change in the layer spacing is given by,

$$\frac{d}{d_0} = \frac{1}{|\underline{\underline{\lambda}}^{-T} \cdot \underline{k}_0|}. \tag{1.8}$$

The director is assumed to be fixed along the layer normal, i.e. $\underline{n} = \underline{k}$. The bulk modulus of the sample is much greater than the rubber or smectic moduli, so the elastomer can be taken incompressible, i.e. $\det \underline{\underline{\lambda}} = 1$. The Adams-Warner model successfully describes the Clark-Meyer buckling instability in monodomain smectic-A elastomers, see figure 1.39. The models predicts the instability to occur at a strain $\lambda_c \sim 1 + r\mu/B$ when stretching parallel to the layer normal.

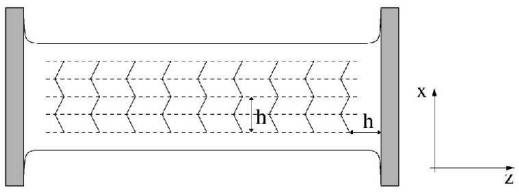

Figure 1.39: Schematic of the Clark-Meyer buckled microstructure. The stripes are shown with width h and in each stripe the layer normal is oriented at $\pm\phi$ to the stretch axis [23].

The instability can be understood to occur due to the relative cost of stretching the layers versus the cost of deforming by a shear λ_{xz} that rotates the layers (and other distortions which leave the layer spacing unchanged). The energy cost of layer stretching is $\sim \frac{1}{2}B\epsilon^2$, whereas for shearing the energy cost is $\sim \mu r\epsilon$ [60]. Consequently the sample deforms by layer stretching for small strains and by shearing the microstructure above the threshold strain, see figure 1.40.

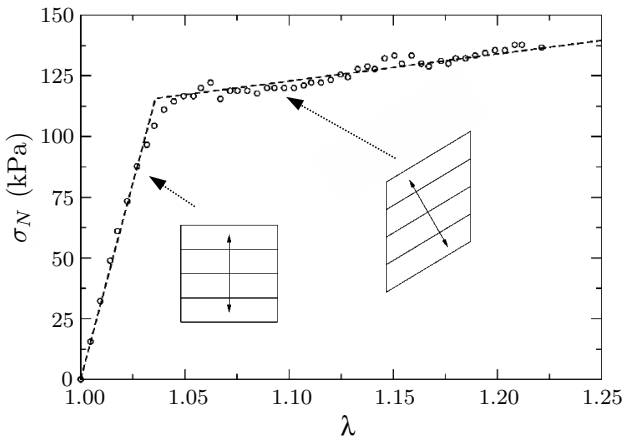

Figure 1.40: Nominal stress versus deformation parallel to $\underline{n}_0$. The solid line is the Adams-Warner model and the points are experimental data from Nishikawa and Finkelmann.

Phenomenological model of Smectic-A elastomers

Stenull and Lubensky produced a phenomenological model of smectic-A elastomers [61]. It is a free energy expansion in terms of the Cauchy-Saint-Venant strain tensor and the director, with the terms chosen to be consistent with the symmetry of the smectic-A phase. The Cauchy-Saint-Venant strain tensor, $\underline{\underline{E}} = \frac{1}{2}(\underline{\underline{\lambda}}^T \cdot \underline{\underline{\lambda}} - \underline{\underline{\delta}})$, has the property of removing rotations of the reference state from $\underline{\underline{\lambda}}$.

The free energy of Stenull-Lubensky can be obtained by considering a slightly more general form of the Adams-Warner model. In particular the tilt angle between director and layer normal is not fixed in the Stenull-Lubensky model. The Stenull-Lubensky model includes a penalty for changing the tilt angle and an additional semi-softness term. The theories become equivalent for small strains once an energy penalty for modifiying the tilt angle is included [28, 62, 63].

1.8 Theoretical Model of Smectic-C Elastomers

Soft elasticity in Smectic-C Elastomers

Adams and Warner [64] introduce an energy model for smectic-C elastomers,

$$F_{smectic-C} = \frac{1}{2}\mu \mathrm{Tr}\left[\underline{\underline{\lambda}} \cdot \underline{\underline{\ell}}_0 \cdot \underline{\underline{\lambda}}^T \cdot \underline{\underline{\ell}}^{-1}\right] + \frac{1}{2}B\left(\frac{d}{d_0} - 1\right)^2, \tag{1.9}$$

where the tilt angle, θ, between $\underline{n}$ and $\underline{k}$ is taken as fixed at the initial value of θ_0.

They show that there is only one non-trivial trajectory of the director that gives soft deformations, which corresponds to the rotation of the director around the layer normal. In the stretching geometry where $\underline{k}_0 = \underline{z}$ and $\underline{n}_0 = (0, \sin\theta_0, \cos\theta_0)$, a soft response exists to an imposed λ_{xx}

deformation. The soft deformation mode, $\underline{\underline{\lambda}}_{\text{soft}}$, is given by,

$$\underline{\underline{\lambda}}_{\text{soft}} = \begin{pmatrix} \frac{1}{a(\phi)} & (1-\frac{\rho}{r})\frac{\sin 2\phi}{2a(\phi)} & \frac{(r-1)\sin 2\theta_0}{2\rho}\left(\sin\phi - (1-\frac{\rho}{r})\frac{\sin 2\phi}{2a(\phi)}\right) \\ 0 & a(\phi) & \frac{(r-1)}{2\rho}\sin 2\theta_0(-a(\phi)+\cos\phi) \\ 0 & 0 & 1 \end{pmatrix} \tag{1.10}$$

where $\mathrm{a}(\phi) = \sqrt{\cos^2\phi + \frac{\rho}{r}\sin^2\phi}$ and $\rho = \sin^2\theta_0 + r\cos^2\theta_0$. The layer normal does not reorient in this stretching geometry, because the imposed strain is perpendicular to $\underline{k}_0$. The angle that the director has rotated around $\underline{k}_0$ is termed ϕ, so $\underline{n} = (\sin\theta_0\sin\phi,\ \sin\theta_0\cos\phi,\ \cos\theta_0)$.

The axial extensions that can be achieved by director rotation in the soft mode are shown in figure 1.41(a). As the director rotates by π the sample width, λ_{yy}, first decreases and then increases back to the original width. The sympathetic shears required to achieve a soft deformation are shown in figure 1.41(b), and the soft-mode is illustrated in figure 1.41(c).

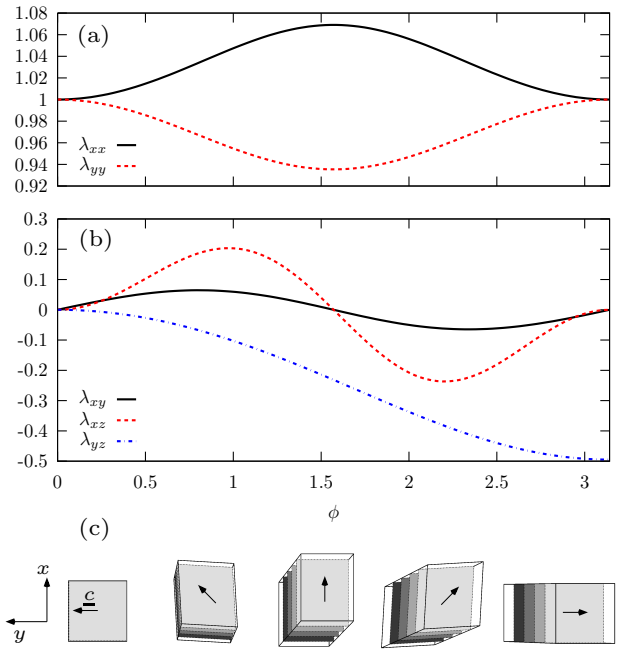

Figure 1.41: (a) The elongation and (b) shear components of the deformation matrix $\underline{\underline{\lambda}}_{\text{soft}}$, for the parameter values $r = 2$ and $\theta_0 = 0.5$ radians. (c) An illustration of these deformations for an initially square LCE. The component of the director perpendicular to the layer normal is $\underline{c}$.

The soft mode of equation (1.10) can be transformed to different starting configurations of the director and layer normal by a set of rotation matrices. Adams and Warner [49] transformed the soft mode to the case of stretching parallel to the layer normal, i.e. $\underline{k}_0 = \underline{x}$, $\underline{n}_0 = \cos\theta_0\underline{x} + \sin\theta_0\underline{y}$ and an imposed λ_{xx}. The components of the upper triangular deformation matrix deformation matrix for this geometry are shown in figures 1.42(a) and (b).

Microstructural considerations are known to rule out soft deformations in some geometries of stretching. Adams, Conti and DeSimone [65] showed that stretching a smectic-C monodomain parallel to the director cannot be soft because there is no compatible deformation scheme of microstructure for this geometry.

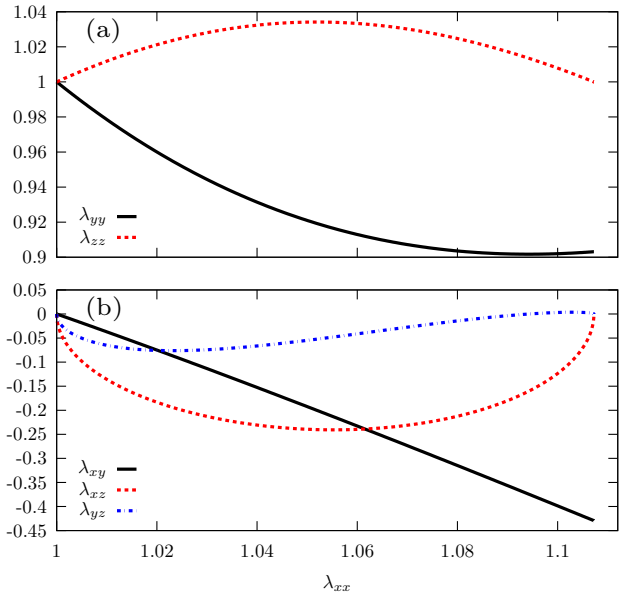

Figure 1.42: (a) The elongation and (b) shear components for the Sm-C soft mode stretching parallel to $\underline{k}_0$, with $r = 2$ and $\theta_0 = 0.5$ radians. Initially $\underline{k}_0 = \underline{x}$ and $\underline{n}_0 = \cos\theta_0\underline{x} + \sin\theta_0\underline{y}$.

1.9 Summary

Smectic elastomers are layered rubbery materials, composed of smectic phase liquid crystal mesogens cross-linked into a polymer matrix. At high temperatures the mesogens are oriented and distributed isotropically, but at lower temperatures the mesogens align and form layers. The alignment direction is termed the director, $\underline{n}$, and the layer normal direction is denoted $\underline{k}$. In main-chain systems the mesogens are incorporated directly into the polymer chains, whereas in side-chain systems the mesogens are attached pendantly. Typically the average path of polymer chains is distorted to be follow the director, resulting in a prolate polymer chain distribution.

In the smectic-A phase the mesogens are arranged in layers, with the director and layer normal parallel. Whereas in the smectic-C phase the director is at an angle θ to the layer normal, termed the tilt angle. Cooling isotropic LCE into a smectic phase results in a randomly oriented polydomain microstructure, because there is no preferred direction for $\underline{n}$ or $\underline{k}$ to form in. Typical the domains are micron-sized for side-chain systems [16], but much smaller for main-chain systems, where the folding of the polymer chain reduces the layer coherence [17].

To produce a macroscopic monodomain sample a preferred direction can be created by applying a uniaxial load during sample manufacture. In smectic-A LCE uniaxial loading aligns the directors with the stretch axis, resulting in a well ordered, transparent smectic-A monodomain [19]. In smectic-C LCE this process aligns the director, but leaves a conical distribution of layer normals; a configuration termed a pseudo-monodomain. To align a smectic-C monodomain an additional stretch or shear can then be applied, which results in a uniform director and layer normal [35].

Nishikawa and Finkelmann observed a buckling instability when stretching a smectic-A monodomain parallel to the director. Initially the elastomer deforms by layer stretching, with a modulus $\sim 10\,\text{MPa}$, but at a threshold strain $\sim 3\%$ a sheared microstructure forms turning the sample opaque [19]. Subsequent deformation rotates the layers and leaves the layer spacing unchanged, so the modulus is much lower $\sim 0.1\,\text{MPa}$. Later experiments on smectic-A monodomains observe a similar stress-strain threshold, but no reorientation of the layers [25].

The Adams-Warner model of smectic elastomers consists of a smectic layer term and a nematic elasticity term, which models the rotation and stretching of an anisotropic polymer chain distribution. The layers are assumed to deform like embedded planes, and the sample is taken as incompressible [23]. This model predicts that for smectic-C elastomers the rotation of the poly-

mer anisotropy gives rise to soft modes, where the director rotates around the layer normal [64]. However in the Stenull-Lubensky model these deformations are no longer perfectly soft due to an additional semi-soft elasticity term, which models the destruction of softness due to defects. Also the Stenull-Lubensky model does not assume the tilt angle is fixed at its initial value, instead there is an energy penalty for changing the tilt angle [61].

The literature of mechanical experiments on monodomain smectic-A LCE is summarized below. Noticeably samples with short layer correlation lengths, ξ, are not well described by current theory.

Smectic-A Elastomers

Experiment	Experiment Description	Fit with theory
Nishikawa and Finkelmann (1999) "Smectic-A LSCE- strain induced breakdown of smectic layering" (side-chain) [19]	**Stretch parallel to $\underline{n}_0$.** A buckling instability is observed at a threshold strain, and the sample becomes optically opaque. Dimensions: 1.6 cm × 1.0 cm × 500 μm. $\xi \approx 1.4\,\mu$m.	**Good**. The buckling instability is described by W-B, A-W and S-L models. The reorientation of the layers is modelled successfully with the assumption that layers behave like embedded planes. The S-L model suggests that the buckling results in a non-zero tilt angle [61].
Komp and Finkelmann (2007) "A New Type of Macroscopically Oriented Smectic-A Liquid Crystal Elastomer"(side-chain) [25]	**Stretch parallel to $\underline{n}_0$.** A strain threshold to a lower modulus is observed, but the sample remains optically transparent. Dimensions: 2 cm × 4 mm ×100 μm. $\xi = 300$ Å.	**Poor.** Is there a small misalignment of the director with the stretch axis? Or is the sample buckling only in its thickness direction? If not then the number of layer must be increasing, which is not described by any model.
Kramer and Finkelmann (2007) "Breakdown of Layering in Frustrated Smectic-A Elastomers." (side-chain) [26]	**Stretch parallel to $\underline{n}_0$.** The smectic structure may have defects, as the two mesogens are differently sized. Dimensions; not stated. $\xi = 400$ Å.	**Poor.** The sample exhibits a smeared out threshold, and is optically transparent above the threshold. The authors attribute this behaviour to defects in the smectic layer structure.
Beyer, Terentjev & Zentel (2007) "Monodomain Liquid Crystal Main Chain Elastomers by Photocrosslinking" (main-chain) [38]	**Stretch parallel to $\underline{n}_0$.** The sample was prepared via a 2 step photo-crosslinking process. Dimensions: 15 mm × 2 mm × 30 μm. ξ is small.	**Poor.** The sample exhibits a weak threshold at low temperatures, and is optically transparent above the threshold. The authors attribute this to the main-chain chemistry giving a short smectic layer correlation length.
Kramer and Finkelmann (2008) "Shear-induced tilt in smectic-A elastomers"(side-chain) [28]	**Shear perpendicular to $\underline{k}_0$.** The sample is identical to Nishikawa *et al.* (1999). Dimensions: 7.4 × 5.0 × 0.45 mm.	**Good with S-L model.** A tilt angle of 6° is induced by a shear of 21°. The assumption of a fixed tilt angle in the A-W model is only approximately true.
Stannarius *et al.* (2006) "Mechanical manipulation of molecular lattice parameters in smectic elastomers" (side-chain) [45]	**Stretch perpendicular to $\underline{k}_0$.** Multiple experimental techniques measure no layer reorientation. Dimensions: 1 mm × 3 mm × 0.5 μm (i.e. very thin)	**Unclear.** The film shrinks normal to the smectic layers, indicating interlayer penetration. The authors attributed this to the UV cross-linking producing a microscopically homogeneous sample.

The literature of experiments on smectic-C LCE is summarized in the following table. Most experiments are performed on pseudo-monodomain and polydomain samples, which are not easily relatable to theoretical descriptions of monodomains. There are no stress-strain curves reported for stretching a monodomain smectic-C elastomer, which would directly probe current theory. The reorientation of the layers observed in these experiments seems to suggest that the layer normal are not strongly coupled to the rubber matrix.

Smectic-C Elastomers

Experiment	Experiment Description	Fit with theory
Sánchez-Ferrer and Finkelmann (2008) "Uniaxial and Shear Deformations in Smectic-C Main-Chain Liquid Crystal Elastomers" (main-chain) [15]	**Pseudo-monodomain stretching parallel and perpendicular to $\underline{n}_0$.** Dimensions: not stated. $\xi \sim 400\,\text{Å}$.	**Poor**. Stretching parallel to $\underline{n}_0$ the high stiffness is surprising, as a monodomain would theoretically deform at the rubber modulus. Stretching perpendicular to $\underline{n}_0$ the director aligns with the stretch axis at high strains, which is not expected if the layers are embedded planes.
Sánchez-Ferrer and Finkelmann (2011) "Polydomain-Monodomain Orientational Process in Smectic-C Main-Chain Liquid-Crystalline Elastomers" (main-chain) [34]	**Polydomain to pseudo-monodomain transition.** Dimensions: not stated. $\xi \sim 380\,\text{Å}$.	**Poor**. Unexpectedly at high strains the director aligns with the stretch axis and the layer normals do not rotate to away from the stretch axis. The cause of the plasticity associated with layer reorientation is not well understood.
Hedden *et al.* (2009) "Necking Instability during Polydomain-Monodomain Transition in a Smectic Main-Chain Elastomer" (main-chain) [33]	**Polydomain to pseudo-monodomain transition.** Initially the sample is stiff, then necking forms a pseudo-monodomain. Dimensions: $7\,\text{mm} \times 1.15\,\text{mm} \times 0.4\,\text{mm}$.	**Poor.** The layer normals do not rotate away from the stretch axis. The authors argue that the necking transition is due to hairpin chains unfolding, and that smectic domains may form.
Ren, McMullan, and Griffin (2008) "Poisson's Ratio of Monodomain Liquid Crystalline Elastomers"(main-chain) [39]	**Pseudo-monodomain stretched parallel to $\underline{n}_0$.** Dimensions: not stated.	**Poor.** The behaviour is similar to that observed by Sánchez-Ferrer *et al.*, except that when stretching pseudo-monodomain perpendicular to $\underline{n}_0$ necking occurs.
Hiraoka *et al.* (2005) "Biaxial Shape Memory Effect Exhibited by Monodomain Chiral Smectic-C Elastomers" (side-chain) [37]	**Thermal cycling of a Sm-C monodomain results in spontaneous shearing.** The sample was 8.5 mm long in the smectic-A phase.	**Good.** The macroscopic shape changes indicate that the polymer chain distribution is influenced by the smectic-A to smectic-C phase transition as expected.
Heinze and Finkelmann (2010) "Shear Deformation and Ferroelectricity in Chiral SmC* Main-chain Elastomers" (main-chain) [20]	**Pseudo-monodomain sheared perpendicular to $\underline{n}_0$.** Dimensions: $\xi \sim 850\,\text{Å}$.	**Good.** The reorientation of the layer normals is a complicated, but qualitatively agree with the A-W model.
Schüring *et al.* (2001) "Liquid Crystal Elastomer Balloons" (side-chain) [42]	**Biaxial stretch perpendicular to $\underline{k}_0$.** Pressure and radius measurements were made in the isotropic and smectic phases. Balloon radius $\sim 2\,\text{mm}$, and thickness $\sim 1 - 5\,\mu\text{m}$.	**Unclear.** The biaxial stretch is expected to reduce the layer spacing, but a characteristic smectic modulus is never observed. This may be result from the UV cross-linking process, and the high cross-linking density.

Chapter 2

Modelling Semi-Soft Smectic-C LCE

In this chapter a constitutive model of a semi-soft, smectic-C LCE monodomain is described. This model is used to investigate stretching of a microscopic monodomain in various geometries, by imposing one deformation component and minimizing the energy with respect to the remaining free components. The minimization of this free energy is not analytically soluble, due to the complication of the constraint on the director. Therefore computational techniques are used to derive stress-strain curves from the constitutive model.

2.1 Smectic-C Monodomain Model

Monodomain smectic-C elastomer has an initial director $\underline{n}_0$ and layer normal $\underline{k}_0$ arranged at a tilt angle θ_0, see figure 2.1. The tilt angle is assumed to vary with strain, so after deformation the director $\underline{n}$ and layer normal $\underline{k}$ are arranged at a tilt angle θ, i.e. $\underline{n} \cdot \underline{k} = \cos\theta$.

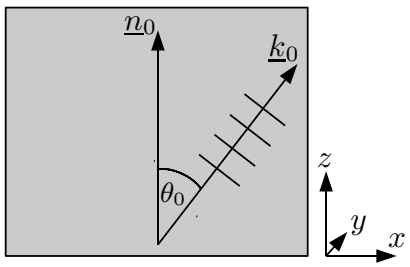

Figure 2.1: A monodomain of smectic-C LCE.

The layers are taken as embedded planes, so the layer normal orientation is simply a slave to the deformation matrix,

$$\underline{k} = \frac{\underline{\underline{\lambda}}^{-T} \cdot \underline{k}_0}{|\underline{\underline{\lambda}}^{-T} \cdot \underline{k}_0|}, \tag{2.1}$$

and the material can be taken as incompressible, i.e. $\det \underline{\underline{\lambda}} = 1$.

The free energy of a monodomain can be modelled as having four contributions;

1) The **smectic layering elasticity**, $F_{smectic}$, is the enthalpic cost of changing the layer spacing. Changing the layer spacing is the stiffest deformation mode by an order of magnitude.

$$F_{smectic} = \frac{1}{2} B \left(\frac{d}{d_0} - \frac{\cos\theta}{\cos\theta_0} \right)^2 \tag{2.2}$$

where d_0 is the initial layer spacing, d is the final layer spacing and $\dfrac{d}{d_0} = \dfrac{1}{|\underline{\underline{\lambda}}^{-T} \cdot \underline{k}_0|}$.

2) The **nematic elasticity**, $F_{nematic}$, is the entropic elastic energy of stretching or rotating an anisotropic chain network,

$$F_{nematic} = \frac{1}{2}\mu \mathrm{Tr}\left[\underline{\underline{\lambda}} \cdot \underline{\underline{\ell}}_0 \cdot \underline{\underline{\lambda}}^T \cdot \underline{\underline{\ell}}^{-1}\right] \tag{2.3}$$

where μ is the rubber shear modulus, $\underline{\underline{\ell}}_0 = \underline{\underline{\delta}} + (r-1)\underline{n}_0\,\underline{n}_0^T$ is the polymer anisotropy tensor and $\underline{\underline{\ell}}^{-1} = \underline{\underline{\delta}} + (\frac{1}{r} - 1)\underline{n}\,\underline{n}^T$ is the inverse of $\underline{\underline{\ell}}_0$.

3) The **semi-softness elasticity**, $F_{semi-soft}$, is a small modification to the nematic energy term due to various non-idealities of the sample. The non-idealities could be any defects that eliminate the isotropy of the undeformed sample, e.g. anisotropy of crosslinking [66]. Biggins *et al.* [67] proposed a completely general semi-soft form up to quadratic order for nematics. The most general energy that is quadratic in $\underline{\underline{\lambda}}$ takes the form,

$$F = \sum_{i,j} \mathrm{Tr}\left[\underline{\underline{A}}_i \cdot \underline{\underline{\lambda}} \cdot \underline{\underline{B}}_j \cdot \underline{\underline{\lambda}}\right], \tag{2.4}$$

where $\underline{\underline{A}}_i$ and $\underline{\underline{B}}_j$ are constructed out of vectors and scalars from the reference and target states respectively. If the reference state is characterized by a single direction $\underline{n}_0$ and the final state by $\underline{n}$ then the most general energy is,

$$F = \mathrm{Tr}\left[\mathrm{H}\,\underline{\underline{\lambda}} \cdot \underline{\underline{\lambda}}^T + \mathrm{J}\,\underline{n}_0\,\underline{n}_0^T \cdot \underline{\underline{\lambda}} \cdot \underline{\underline{\lambda}}^T + \mathrm{K}\,\underline{n}_0\,\underline{n}_0^T \cdot \underline{\underline{\lambda}}^T \cdot \underline{n}\,\underline{n}^T \cdot \underline{\underline{\lambda}} + \mathrm{L}\,\underline{\underline{\lambda}}^T \cdot \underline{n}\,\underline{n}^T \cdot \underline{\underline{\lambda}}\right]. \tag{2.5}$$

Typically these constants are chosen so that the semi-soft energy has the form

$$F_{semi-soft} = \frac{1}{2}\mu\alpha \mathrm{Tr}\left[\underline{\underline{\lambda}} \cdot (\underline{\underline{\delta}} - \underline{n}_0\,\underline{n}_0^T) \cdot \underline{\underline{\lambda}}^T \cdot \underline{n}\,\underline{n}^T\right]. \tag{2.6}$$

In smectic elastomers there are new possible sources of non-ideal behaviour, and new directions in the problem such as the layer normal. However it will be assumed that the semi-soft energy in smectics has the same form as in nematics. Conti *et al.* [68] used a neo-Hookean form of the semi-soft energy, $F = \frac{1}{2}\mathrm{Tr}\left[\underline{\underline{\lambda}} \cdot \underline{\underline{\lambda}}^T\right]$ to regularize the ideal nematic free energy, and a uniaxial neo-Hookean term in [69]. These terms produce similar behaviour to the nematic semi-soft term.

4) The **tilt elastic energy**, F_{tilt}, penalizes deviations of the tilt angle away from θ_0,

$$F_{tilt} = \frac{1}{2}a_t\left[\cos^2\theta_0 - (\underline{n}.\underline{k})^2\right]^2, \tag{2.7}$$

where a_t is the tilt modulus and $\underline{n} \cdot \underline{k} = \cos\theta$. The tilt modulus is typically large compared to the shear modulus $a_t \gg \mu$, so the tilt angle remains close to θ_0 [28]. It is convenient to define the dimensionless tilt modulus $c = a_t/\mu$.

Summation of the four energy contributions yields the smectic-C energy;

$$\begin{aligned} F_{Sm-C} =& \frac{1}{2}\mu \mathrm{Tr}\left[\underline{\underline{\lambda}} \cdot \underline{\underline{\ell}}_0 \cdot \underline{\underline{\lambda}}^T \cdot \underline{\underline{\ell}}^{-1}\right] + \frac{1}{2}\alpha\mu \mathrm{Tr}\left[\underline{\underline{\lambda}} \cdot (\underline{\underline{\delta}} - \underline{n}_0\,\underline{n}_0^T) \cdot \underline{\underline{\lambda}}^T \cdot \underline{n}\,\underline{n}^T\right] \\ &+ \frac{1}{2}B\left(\frac{d}{d_0} - \frac{\cos\theta}{\cos\theta_0}\right)^2 + \frac{1}{2}c\mu\left[\cos^2\theta_0 - (\underline{n}.\underline{k})^2\right]^2. \end{aligned} \tag{2.8}$$

Any correct description of the smectic-C system should be unchanged by the operations $\underline{n} \to -\underline{n}$ and $\underline{k} \to -\underline{k}$. This is because the director and layer normal are quadrupolar objects, i.e. they are double-headed vectors. Also the description should be invariant under rotations of the reference space. The energy, F_{Sm-C}, satisfies these symmetry conditions.

This investigation will ignore the effect of clamping at the boundaries, and focus on the deformation of sheets of Sm-C elastomer whose mechanical properties will be dominated by the deformation of

the material in the middle of the long sheet. The elongations considered will be in the x direction, i.e. imposing the λ_{xx} component, together with the induced shear deformations. The appropriate deformation matrix is

$$\underline{\underline{\lambda}} = \begin{pmatrix} \lambda_{xx} & \lambda_{xy} & \lambda_{xz} \\ 0 & \lambda_{yy} & \lambda_{yz} \\ 0 & 0 & \lambda_{zz} \end{pmatrix}. \tag{2.9}$$

The components λ_{yx} and λ_{zx} are set to zero as they would be resisted by countertorques when applying a load in the x direction. The uniaxial symmetry of the deformation means that $\underline{\underline{\lambda}}$ can be arbitrarily rotated around the extension axis, and this freedom has been used to set λ_{zy} to zero. The constraint of incompressibility can be used to set $\lambda_{yy} = 1/\lambda_{xx}\lambda_{zz}$.

In experiment, imposed stress ensembles are often used, which yield the same results when the stress-strain curve is monotonic. However, some of the stress-strain curves calculated here are non-monotonic; hence there are several strain values for a single stress value. In this case there is a difference between the fixed stress and fixed strain ensembles, and for fixed stress a Maxwell construction must be used to determine the strain. This is described in [63] and briefly in section 2.3.

Auxetic Behaviour

An unusual property of some Sm-C soft modes is their **negative Poisson's ratio**, albeit it in one direction only. The soft mode when stretching parallel to the layer normal is illustrated in figure 2.2. The λ_{zz} component increases with imposed λ_{xx}, i.e. the sample expands in the direction perpendicular to the imposed elongation. This is because the constraint of an approximately fixed tilt angle between the layer normal and director results in the director rotating into the z direction. The sample then laterally expands to accommodate the anisotropic chain shape.

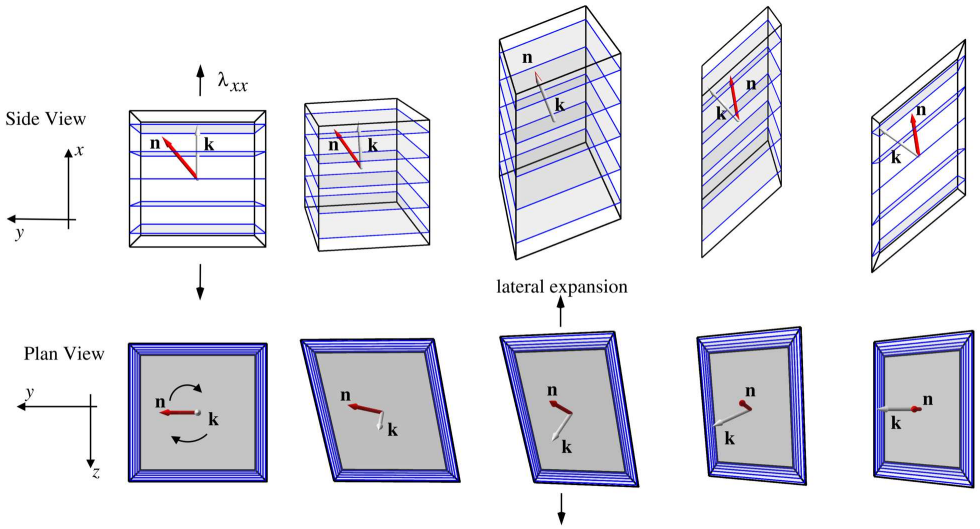

Figure 2.2: Illustration of auxetic behaviour stretching parallel to $\underline{k}_0$. The director (red) moves out into the z direction, causing a lateral expansion of the sample, while maintaining the initial tilt angle with respect to the layer normal (white).

To the author's knowledge this mechanism for negative Poisson's ratio has not been reported before. The microstructure formed by LCEs during deformation may prevent the observation of negative Poisson's ratio for some deformations, and this is discussed further in section 2.3. Alternative mechanisms of producing auxetic behaviour based on modifying the attachment of mesogens to the polymer backbone in smectic LCEs have been proposed and investigated experimentally [40, 70].

For isotropic materials, the Poisson's ratio must be in the range $-1 < \nu < 0.5$. LCEs are anisotropic materials, so have Poisson's ratios outside this range. As the materials considered here are volume conserving, the Poisson's ratio in the y direction is $\nu_{yy} = 1 - \nu_{zz}$. When stretching parallel to the

layer normal, the Poisson's ratio for $\theta_0 > 0$ is given by

$$\nu_{zz} = -\frac{d\lambda_{zz}}{d\lambda_{xx}}\Big|_{\lambda_{xx}=1} = -\frac{1}{(r-1)\cos^2\theta_0}. \tag{2.10}$$

Substituting in typical values of $\theta_0 \sim 0.5$ radians, and $r \sim 2$ for a side chain system produces $\nu \sim -1.3$. When compared with other auxetic materials [71] this is a more negative Poisson's ratio, corresponding to a larger rate of expansion (albeit in only one direction here). The extent of the soft mode in this geometry is

$$\lambda_{xx} = \sqrt{1 + \frac{(r-1)^2}{\rho^2}\sin^2 2\theta_0,}. \tag{2.11}$$

To illustrate the expansion of the LCEs on elongation here, we will use the **incremental Poisson's ratio (IPR)** defined by

$$\nu_{zz} = -\frac{d\lambda_{zz}}{d\lambda_{xx}}, \tag{2.12}$$

where an elongation λ_{xx} is imposed and λ_{zz} is the transverse deformation.

Computational Minimization

The free energy for a monodomain of smectic-C LCE is sufficiently complicated to render analytic minimization impossible. This is in contrast to the case of a semi-soft nematic elastomer where the behaviour is analytically soluble in some geometries. The additional difficulty in smectic-C LCE arises because of the non-linear constraint on the director, i.e. it is constrained to rotate around the layer normal.

The absence of analytical solutions means that computational minimization algorithms are required to minimize the free energy and derive a stress-strain curve. When the elastomer undergoes a deformation step its deformation components relax to find the configuration of the lowest energy, and a minimization algorithm is used to find this configuration. A programming implementation to minimize the smectic-C energy is included as appendix A.

The energy minimization problem for an imposed λ_{xx} is;

$$\begin{aligned} &\underset{\lambda_{xy},\lambda_{xz},\lambda_{yz},\lambda_{zz},\underline{n}}{\text{Minimize}} \; F_{Sm-C}(\lambda_{xx},\lambda_{xy},\lambda_{xz},\lambda_{yz},\lambda_{zz},\underline{n}) \\ &\text{subject to } |\underline{n}| = 1, |\underline{k}| = 1 \text{ and } \underline{n}\cdot\underline{k} = \cos\theta. \end{aligned} \tag{2.13}$$

The constraint of the tilt angle of θ between the layer normal and director can be encoded as

$$\underline{n} = \underline{c}\sin\theta + \underline{k}\cos\theta, \tag{2.14}$$

where $\underline{c}$ is a unit vector perpendicular to $\underline{k}$. A particular basis is required to express $\underline{c}$. It is convenient to use the unit vector $\underline{c}_0$, the starting orientation of $\underline{c}$, and $\underline{c}_0 \times \underline{k}_0$. The vector $\underline{c}$ can be expressed as

$$\underline{c} = \underline{a}\cos\phi + \underline{b}\sin\phi, \tag{2.15}$$

where $\underline{a} \propto \underline{c}_0 - \underline{k}(\underline{c}_0 \cdot \underline{k})$ is a unit vector constructed from the component of $\underline{c}_0$ that is perpendicular to $\underline{k}$. The unit vector $\underline{b} = \underline{k} \times \underline{a}$ is perpendicular to both $\underline{a}$ and $\underline{k}$, see figure 2.3. Hence in the initial configuration $\phi = 0$, and $\underline{a} = \underline{c}_0$.

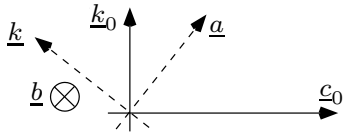

Figure 2.3: An illustration of the vectors $\underline{a}$ and $\underline{b}$ used in the numerical calculations.

2.2 Tensile Deformations of Monodomain Smectic-C Elastomers

Tensile deformations of monodomains in five different geometries were investigated. These were chosen in light of the pseudo-monodomain stretching experiments of Sánchez-Ferrer and Finkelmann [15], and reflect likely choices for future investigations.

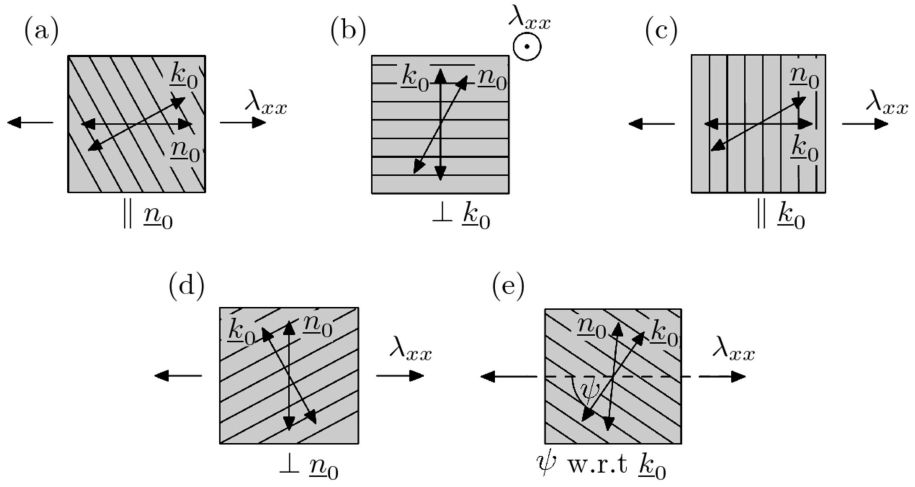

Figure 2.4: The director and layer normal orientations for the five elongations considered: (a) parallel to $\underline{n}_0$, (b) perpendicular to $\underline{k}_0$ and $\underline{n}_0$, (c) parallel to $\underline{k}_0$, (d) perpendicular to $\underline{n}_0$, with $\underline{k}_0$ coplanar, and (e) at an angle ψ to $\underline{k}_0$.

Algorithms

Successful computational minimization requires finding the global energy minimum not just a local minima. The degree of difficulty is strongly dependent on the geometry of deformation. The five geometries investigated here are shown in figure 2.4. A particularly simple case is (b), because the layer normal does not reorient in this geometry. The most difficult case is (d), as the director orientation is discontinuous at a critical strain. This makes reliable minimization challenging, as two energy minima exist that are separated in parameter space by an energy barrier.

A variety of pre-existing algorithms were employed in an attempt to robustly minimize F_{Sm-C}.

i) A **simplex algorithm**, `E04CCF` from the NAG library [72]. This algorithm works for the easy geometry of stretching parallel to the director. For more difficult geometries it is generally unsuccessful in finding a global minimum rather than local minima.

ii) A **sequential quadratic programming algorithm**, `nag_con_nlin_lsq` from the NAG library [73]. This algorithm is designed to solve constrained nonlinear least-squares problems. It directly handles the constraints using Lagrange multipliers. It fails completely for the difficult case of stretching perpendicular to the director, with the layer normal coplanar.

iii) A **genetic algorithm**, `Pikaia` by the High Altitude Observatory [74]. Using default control parameters the algorithm is significantly slower than the NAG algorithms, taking around 1 second to perform a minimization. The algorithm is partially reliable for the case of stretching perpendicular to the director, with the layer normal coplanar.

iv) A **simulated annealing algorithm**, `SIMANN` by Goffe *et al.* [75], can reliably minimize the energy even in difficult cases. Simulated annealing is more robust because it is designed to initially accept moves away from local minima thus exploring the parameter space more thoroughly. The computational results were produced using simulated annealing, then further refined using the sequential quadratic programming algorithm.

Computational Results: Elongations of Smectic-C Elastomers

The model has the parameters μ, a_t, B, r and θ_0. Typically, $\theta_0 \sim 30°$ [20], $B/\mu \sim 60$ in well ordered samples [16, 19, 21], $a_t/\mu = c \gtrsim 1$ in smectics [28, 62], and $r \sim 2$ in side chain liquid crystalline polymers [60, 76]. Petelin *et al.* measured $\alpha \sim 0.1$ in nematic elastomers [77], and similar values are expected in smectics. These parameter values will be used to illustrate the behaviour of the model in the following computational investigation.

A. Elongation Parallel to $\underline{n}_0$

The first deformation considered is stretching parallel to the director, i.e. imposing λ_{xx} with $\underline{n}_0 = \underline{x}$ and $\underline{k}_0 = \cos\theta_0 \underline{x} + \sin\theta_0 \underline{z}$.

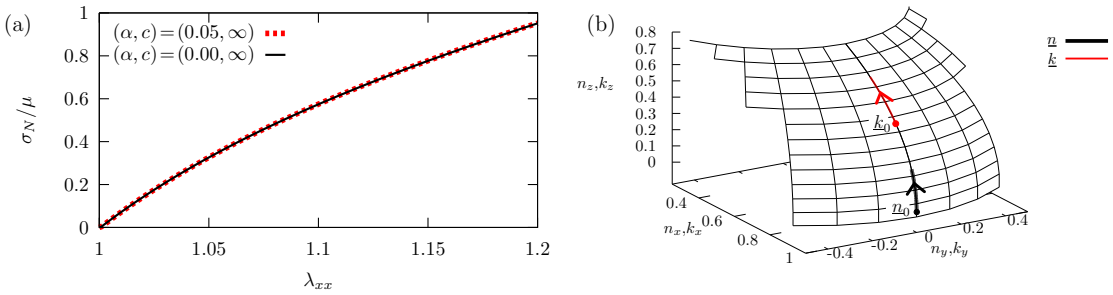

Figure 2.5: (a) The stress-strain response for a semisoft Sm-C elastomer stretched parallel to $\underline{n}_0$. The model parameters are $B/\mu = 60$, $r = 2$, $\theta_0 = 0.5$, and the values of (α, c) shown in the figure. (b) Director and layer normal reorientation, for $(\alpha, c) = (0.05, \infty)$.

The stress-strain response is shown in figure 2.5(a) for the case of a fixed tilt angle. The stiffness is characteristic of the rubber modulus, as the energy is incurred almost entirely by the nematic elasticity term (the layer spacing is unchanged by the stretch). The reorientation of the layer normal and director is shown in figure 2.5(b). Because the layers deform as embedded planes the layer normal reorients to become perpendicular to the stretch direction as $\lambda_{xx} \to \infty$, and the director follows at the tilt angle.

The components of the deformation matrix are shown in figure 2.6(a) and (b). The behaviour in the lateral directions is anisotropic due to the rotation of the polymer anisotropy. Only the λ_{xz} shear component is non-zero.

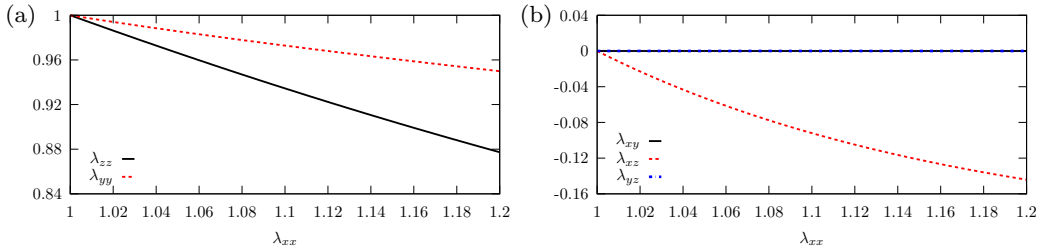

Figure 2.6: (a) The diagonal and (b) shear components of the deformation tensor when stretching parallel to $\underline{n}_0$, for parameter values of $(\alpha, B/\mu, c, \theta_0, r) = (0.05, 60, \infty, 0.5, 2)$.

B. Elongation Perpendicular to $\underline{k}_0$ and $\underline{n}_0$

The deformation considered is stretching perpendicular to the initial layer normal and director, i.e. imposing λ_{xx} with $\underline{k}_0 = \underline{z}$ and $\underline{n}_0 = \cos\theta_0\underline{z} + \sin\theta_0\underline{y}$. The layer normal does not reorient in this geometry, as it is perpendicular to the stretch direction.

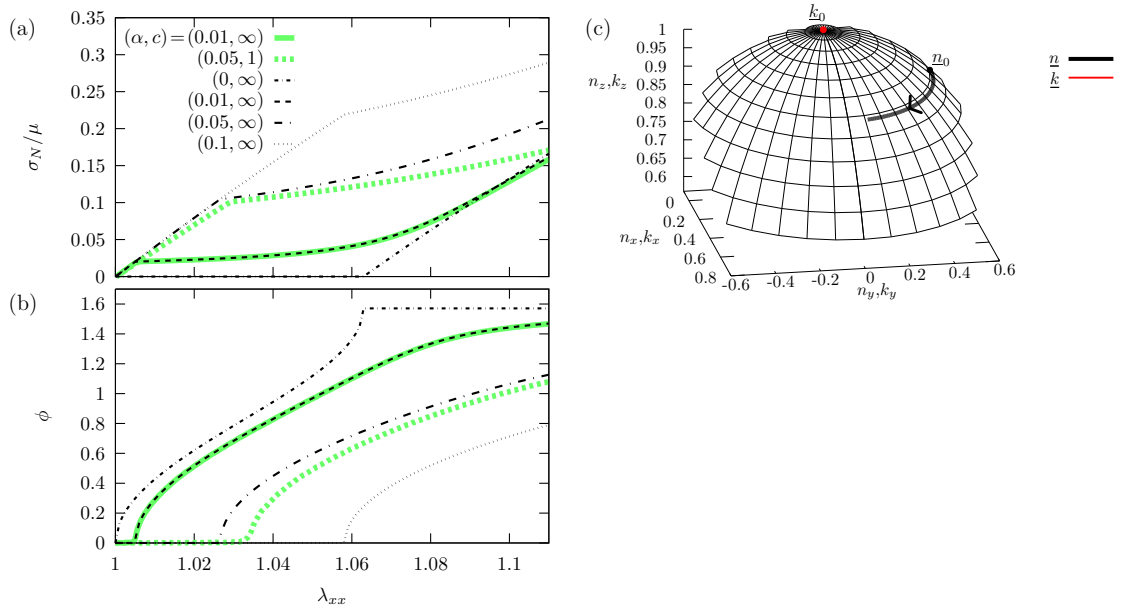

Figure 2.7: (a) The stress and (b) the angle of rotation for a semisoft Sm-C elastomer stretched perpendicular to $\underline{k}_0$ and $\underline{n}_0$. The model parameters are $B/\mu = 60$, $r = 2$, $\theta_0 = 0.5$, and the values of (α, c) shown in the figure. The thick curves (green) are from the more general numerical relaxation, and the black curves are calculated using the decomposition of the deformation matrix. (c) Director and layer normal reorientation for $(\alpha, c) = (0.05, \infty)$.

In the absence of the semi-softness term of equation (2.6) this deformation is a smectic-C soft mode, which is described analytically in section 1.10. However the full free energy can only be minimized numerically. The resulting stress-strain curve, and the orientation of the director of this minimisation are shown in figures 2.7(a) and (b) by the thick (green) lines.

For the ideal Sm-C elastomer, the soft plateau ends at $\lambda_{xx} = \sqrt{r/\rho}$, as can be seen from the soft mode in equation (1.10). The plateau ends when the director has completed a rotation by $\pi/2$ around the layer normal. For non-zero values of α the onset of rotation of the layer normal is delayed, and it never finishes a full $\pi/2$ rotation. This is evident in the stress-strain curve, because the well defined stress plateau for $\alpha = 0$ becomes progressively less sharply defined. For $\alpha \sim 0.01$ there is a pronounced stress plateau, but for larger values of $\alpha \sim 0.1$ there is no plateau, merely a knee in the stress-strain curve. Figures 2.7(a) and (b) also shows the effect of reducing the tilt modulus c. The knee in the stress strain curve becomes less pronounced, and the rubber hardens more slowly for larger values of λ_{xx}.

The retardation of the director rotation may be significant for piezoelectric response of these materials. There would be no piezoelectric response until the strain was above the threshold. The potential difference across the sample would be lower in semi-soft samples because the alignment of the electric dipoles associated with director rotation is spread over a much larger deformation range.

The deformation components when stretching perpendicular to $\underline{k}$ are illustrated in figure 2.8. Note the sympathetic shears that accompany the director rotation are persistent, because the director rotation is never completed if $\alpha > 0$.

Numerically it is clear that with the inclusion of the semi-soft term there is a delay in the rotation of the director. The director rotation path is shown in figure 2.7(c). Some analytical progress

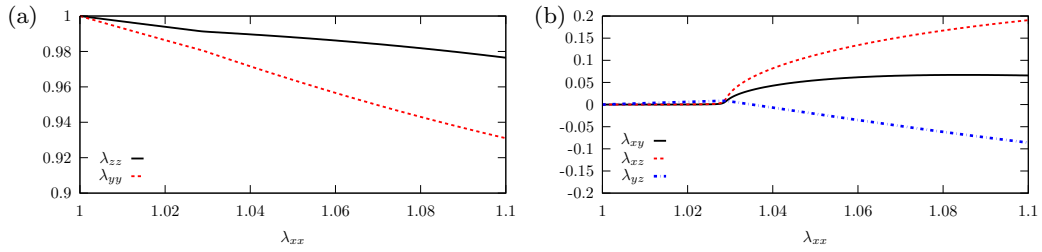

Figure 2.8: (a) The diagonal and (b) shear components of the deformation tensor when stretching perpendicular to $\underline{k}_0$ and $\underline{n}_0$, for $(\alpha, B/\mu, c, \theta_0, r) = (0.05{,}60{,}1{,}0.5{,}2)$. The sympathetic shears persist, as the director rotation never completes its $\pi/2$ rotation.

can be made in this geometry by decomposing the deformation into three parts; the initial hard deformation with fixed director and layer spacing denoted $\underline{\underline{\lambda}}_{\text{hard}}$, the soft mode $\underline{\underline{\lambda}}_{\text{soft}}$ and the subsequent shear and elongation after the soft mode $\underline{\underline{\lambda}}'$ [49],

$$\underline{\underline{\lambda}} = \underline{\underline{\lambda}}' \cdot \underline{\underline{\lambda}}_{\text{soft}} \cdot \underline{\underline{\lambda}}_{\text{hard}}, \tag{2.16}$$

where $\underline{\underline{\lambda}}_{\text{hard}} = \text{diag}(\lambda_1, 1/\lambda_1, 1)$, $\underline{\underline{\lambda}}_{\text{soft}}$ given in equation(1.10), and

$$\underline{\underline{\lambda}}' = \begin{pmatrix} \zeta & 0 & \eta \\ 0 & 1/\zeta & 0 \\ 0 & 0 & 1 \end{pmatrix}. \tag{2.17}$$

This deformation matrix can be substituted into the free energy terms of equation (2.2), (2.3), and (2.6) (assuming that $c \to \infty$, so that $\theta = \theta_0$). The problem is then reduced to a minimization over the variables λ_1, ζ, η and ϕ, with the constraint that the total λ_{xx} is prescribed. The threshold before the onset of director rotation can be calculated by setting $\zeta = 1$ and $\eta = 0$, then performing a series expansion of the free energy in soft mode rotation angle ϕ. The leading term is $\mathcal{O}(\phi^2)$, and when this term becomes negative a non-zero value of ϕ will lower the free energy. To leading order in $(\lambda_1 - 1)$, this coefficient becomes negative when λ_1 is approximately

$$\begin{aligned} \lambda_1 = 1 + 8r^2\alpha/(1 + 29r - 29r^2 - r^3 + r\alpha + 35r^2\alpha \\ +4r^2\alpha\cos 2\theta + (r-1)((r-1)^2 + r\alpha)\cos 4\theta) \end{aligned} \tag{2.18}$$

This value is slightly smaller than the corresponding threshold to director rotation in nematic elastomers of $\lambda_1^3 = \frac{r-1}{r-1-\alpha r}$ [60]. Intuitively this is because in the Sm-C phase the deformation is restricted to two dimensions by the layer spacing constraint. Consequently there is a larger contraction in the direction perpendicular to the stretch which causes the elastic free energy to rise faster, and hence the director rotation to start earlier in Sm-C LCEs as compared to the nematic phase.

The minimization of the free energy over λ_1, ζ, η and ϕ produces results that are in good agreement with the more general numerical method. These results are shown by the black lines in figures 2.7(a) and (b).

C. Elongation Parallel to $\underline{k}_0$

The deformation considered is stretching parallel to the initial layer normal, i.e. imposing λ_{xx} with $\underline{k}_0 = \underline{x}$ and $\underline{n}_0 = \cos\theta_0 \underline{x} + \sin\theta_0 \underline{z}$.

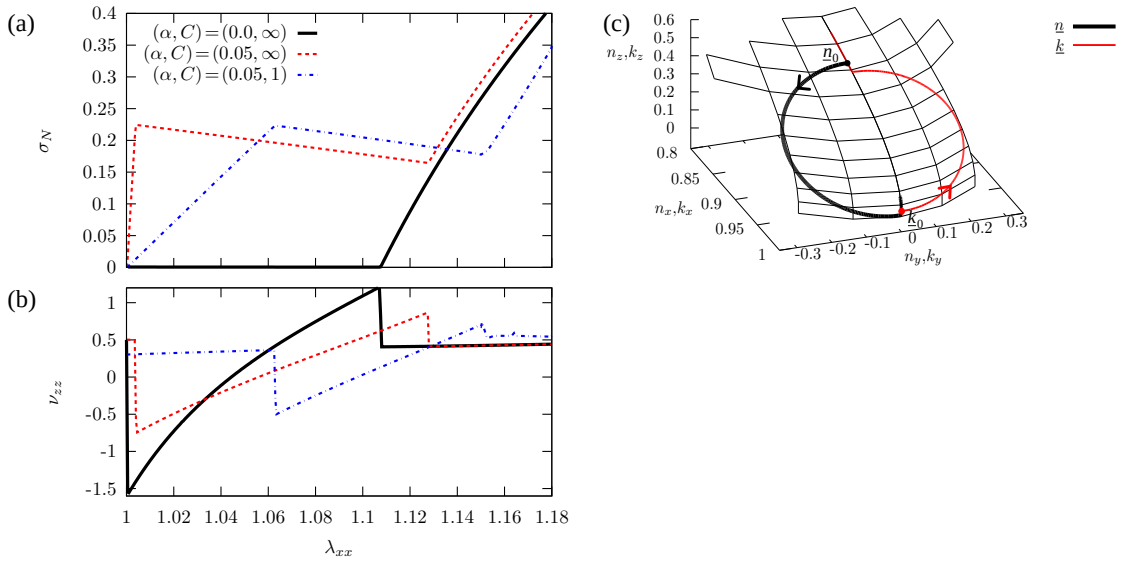

Figure 2.9: (a) The stress-strain response for a semisoft Sm-C elastomer stretched parallel to the layer normal. The model parameters are $B/\mu = 60$, $r = 2$, and $\theta_0 = 0.5$, and the values of (α, c) shown in the figure. (b) The corresponding IPRs for the stress-strain curves. (c) Director and layer normal reorientation for $(\alpha, c) = (0.05, \infty)$.

The stress-strain response is shown in figure 2.9(a) for various values of the semi-soft parameter α. For $c \to \infty$ the first part of the stress-strain curve is determined by the smectic layer modulus B. The semi-soft term prevents the rotation of the director, and the layer spacing increases. Once the force required to increase the layer spacing is comparable to that required to rotate the director the semi-soft mode begins. The stress-strain curve has negative slope once director rotation starts.

As explained in figure 2.2 there is a negative incremental Poisson's ratio in this geometry as the director rotates around the layer normal into the direction perpendicular to the stretch axis. The IPR is shown in figure 2.9(b). The lateral expansion, combined with the free energy expression for the semi-soft elasticity, results in the negative stiffness. For larger values of α the Poisson's ratio becomes less negative.

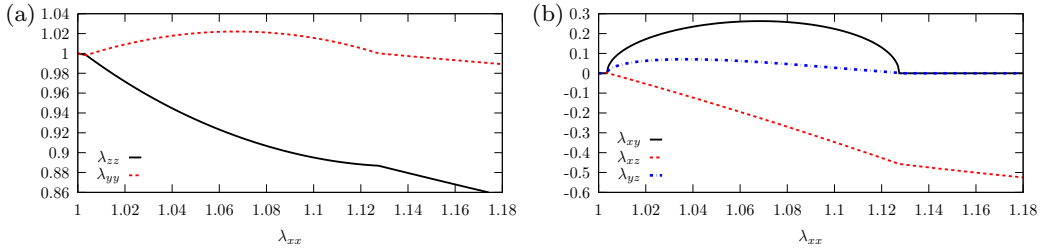

Figure 2.10: (a) The diagonal and (b) shear components of the deformation tensor when stretching parallel to the layer normal, for parameter values of $(\alpha, B/\mu, c, \theta_0, r) = (0.05{,}60{,}\infty{,}0.5{,}2)$.

The rotation of the layer normal and director is illustrated in figure 2.9(c) for the case of a fixed tilt angle, and the corresponding deformations are shown in figure 2.10. The expansion of the sample in the y direction is clearly visible at the onset of rotation, as are the usual shear components that accompany a soft mode. For finite values of c the deformation becomes more complicated; before

the threshold the director rotates towards the layer normal and the sample shears, which itself results in movement of the layer normal. There is both an increase in the threshold to the start of rotation, and a reduction in the amplitude of the semi-soft deformation. This is because the shearing before director rotation results in rotation of the layer normal, and there is a reduction in the tilt angle before the onset of shearing.

Negative stiffness from the Soft Mode

In the limit of small α the semi-soft term is a small perturbation to the nematic and smectic terms. If the geometry permits soft deformation then to a good approximation the deformation is the smectic-C soft-mode. The soft mode deformations in some geometries result in a negative stiffness when combined with the semi-soft energy term.

The soft-mode for stretching perpendicular to $\underline{k}_0$ and $\underline{n}_0$ is described by equation (1.10). Putting this deformation into the semi-soft energy term curve results in a monotonic stress-strain curve, as shown in figure 2.11(a).

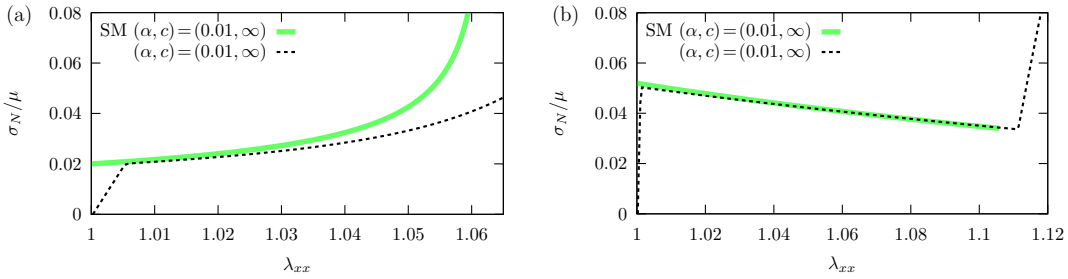

Figure 2.11: (a) The stress-strain response stretching perpendicular to $\underline{k}_0$ and $\underline{n}_0$ for the soft-mode (green) and numerical minimization (black). (b) The stress-strain response stretching parallel to $\underline{k}_0$ for the soft-mode (green) and numerical minimization (black). The parameter values are $(\alpha, B/\mu, c, \theta_0, r) = (0.01, 60, \infty, 0.5, 2)$.

The soft-mode for stretching parallel to $\underline{k}_0$ can be found by a suitable rotation of $\underline{\underline{\lambda}}_{\text{soft}}$. Combining this soft-mode with the semi-soft energy term results in non-monotonic stress-strain curve, see figure 2.11(b). The root cause of the negative stiffness can be investigated with a scalar model.

Scalar model of the negative slope region

The unusual response above for the Sm-C soft mode can be illustrated for a simpler deformation. Consider an elongation with a diagonal deformation matrix of an imposed λ_{xx}, λ_{zz} given by

$$\lambda_{zz} = 1 - A\left(\lambda_{xx} - \frac{3}{2}\right)^2 + \frac{A}{4}, \tag{2.19}$$

with λ_{yy} determined by volume conservation. The parameter A here controls the initial rate of expansion of the material. Its Poisson's ratios are $-A$, and $1 + A$. This is similar to the Sm-C soft mode in illustrated in figure 1.42. The deformation in equation (2.19) can be substituted into a neo-Hookean model of the form,

$$F_{Neo-Hookean} = \tfrac{1}{2}\mu \mathrm{Tr}\left[\underline{\underline{\lambda}} \cdot \underline{\underline{\lambda}}^T\right], \tag{2.20}$$

which is broadly similar to the semi-soft elastic energy term. The resulting stress-strain curve is shown in figure 2.12. It can be seen from this plot that for sufficiently large values of A the stress-strain curve has a negative slope similar to stretching the Sm-C LCE parallel to the layer normal. For some geometries the Poisson's ratio is sufficiently negative to result in a negative stiffness. The configurational entropy of the perpendicular degrees of freedom decreases as the sample expands

resulting in a positive contribution to the stress. Once lateral expansion starts to slow sufficiently there is a weaker contribution to stiffness of the sample from the perpendicular degrees of freedom and the stress starts to drop, which produces a negative slope in the stress-strain response. By tuning the parameter A in the model, the balance between the parallel and perpendicular degrees of freedom can be altered, and the stiffness changed from negative to positive.

This scalar model shows that the negative stiffness is a result of the lateral expansion during the Sm-C soft mode, and not solely due to the form of the semi-soft elastic term.

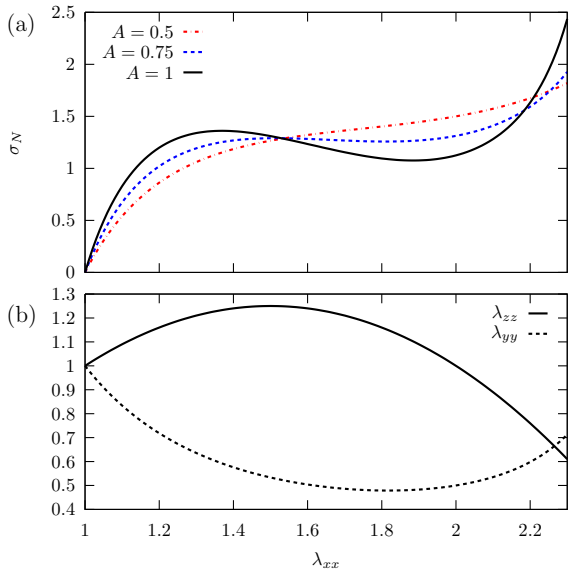

Figure 2.12: For the scalar model of the negative stress strain curve described in the text, (a) shows the stress-strain curves for $A = 0.5, 0.75, 1$, and (b) the deformation components for $A = 1$.

D. Elongation Perpendicular to $\underline{n}_0$, with $\underline{k}_0$ coplanar

Stretching perpendicular to the initial layer normal is illustrated in figure 2.4(d). The results for the numerical calculation of the stress-strain curve for this geometry are shown in figure 2.13(a).

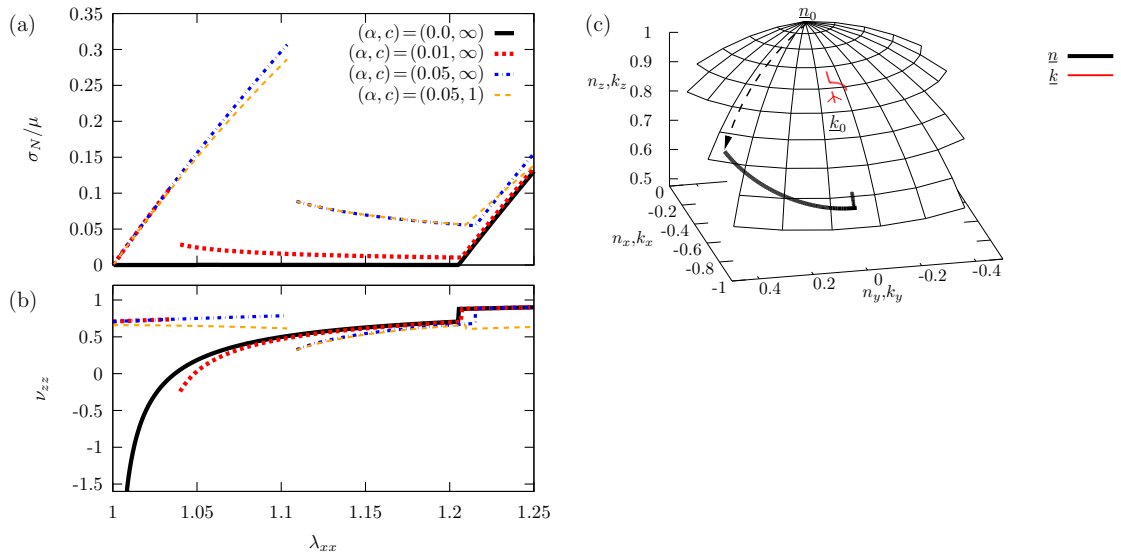

Figure 2.13: (a) The stress-strain response for a semisoft Sm-C elastomer stretched perpendicular to $\underline{n}_0$. The model parameters are $B/\mu = 60$, $r = 2$, and $\theta_0 = 0.5$, and the values of (α, c) shown in the figure. (b) The corresponding IPRs for the stress-strain curves. (c) Director and layer normal reorientation for $(\alpha, c) = (0.05, \infty)$.

This geometry has the remarkable feature that $\nu_{zz} \to -\infty$ when $\alpha \to 0$, as shown in figure 2.13(b). For larger values of α the Poisson's ratio becomes less negative. The jump in the director also causes a discontinuity in the IPR, and a sudden increase in the width of the sample. Note that in this geometry there is a discontinuity in the stress-strain curve, in addition to the negative stiffness. The discontinuity in the stress-strain curve is accompanied by a jump in the director as shown in figure 2.13(c), and the corresponding deformations are shown in figure 2.14.

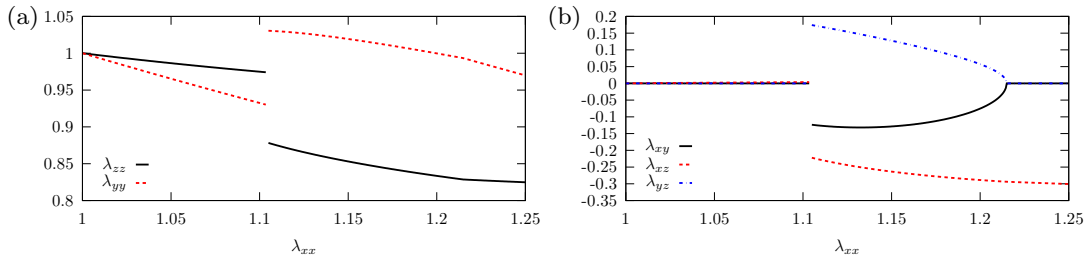

Figure 2.14: (a) The diagonal and (b) shear components of the deformation tensor when stretching perpendicular to the director, for parameter values of $(\alpha, B/\mu, c, \theta_0, r) = (0.05, 60, \infty, 0.5, 2)$.

Intuitively the discontinuity arises because when the director jumps the long axis of the polymer shape tensor jumps towards the elongation direction. Consequently the natural length of the rubber in this direction is increased, so there is corresponding drop in the stress.

The jump in the director can be understood from the properties of the soft mode in this geometry. The first part of the total deformation (until the end of director rotation) can be approximated as a hard deformation where there is no director rotation, followed by a soft mode

$$\underline{\underline{\lambda}} = \underline{\underline{\lambda}}_{\text{soft}} \cdot \underline{\underline{\lambda}}_{\text{hard}}. \tag{2.21}$$

The amplitude of the soft mode in this geometry can be calculated analytically to be

$$\lambda_{xx} = \left(3 + r(7r-2) + 4(r^2-1)\cos 2\theta_0 + (1+(2-3r)r)\cos 4\theta_0\right)^{1/2} / (2\sqrt{2}\rho). \tag{2.22}$$

The hard part of the deformation has only diagonal elements, and an xz shear component.

$$\underline{\underline{\lambda}}_{\text{hard}} = \begin{pmatrix} \lambda_{xx} & 0 & \lambda_{xz} \\ 0 & 1/(\lambda_{xx}\lambda_{zz}) & 0 \\ 0 & 0 & \lambda_{zz} \end{pmatrix}. \tag{2.23}$$

Substituting this into the full free energy density yields an approximate solution to the minimization problem, where the director rotation is assumed to be continuous. The free energy density in this case is shown in figure 2.15.

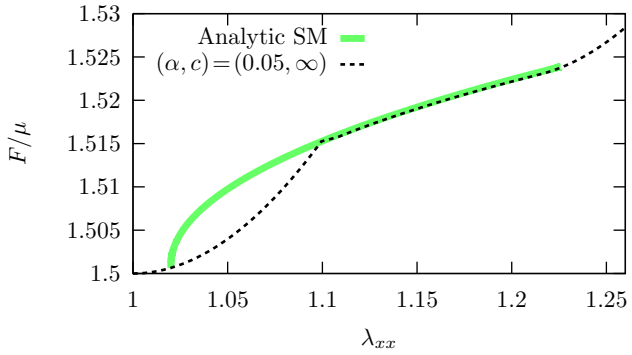

Figure 2.15: The free energy calculated numerically (dashed black), and the free energy trajectory of the semisoft mode with continuous director rotation (thick green) when stretching perpendicular to the director. The parameter values are $(\alpha, B/\mu, c, \theta_0, r) = (0.05{,}60{,}\infty{,}0.5{,}2)$

The analytic solution with continuous director rotation has higher free energy for the first part of the deformation. Hence, the elastomer initially stretches without director rotation. If the director were to start rotating, then the form of the soft mode results in rapid rotation of the director, and an infinite slope in the free energy. However, the rate of increase slows, and eventually the state with a rotated director is lower in free energy than that with a fixed director. At this point the director jumps to the new orientation. There is a discontinuity in the slope of the free energy at this point, or equivalently a jump in the stress.

The energy landscape responsible for the director instability is illustrated in figure 2.16(a).

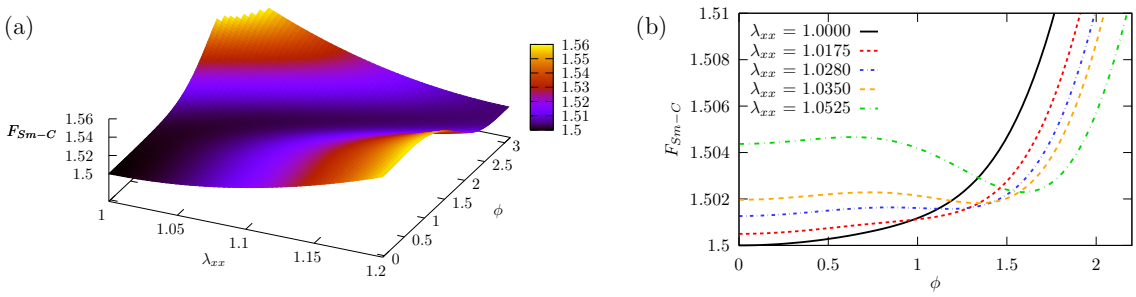

Figure 2.16: (a) F_{Sm-C} versus imposed λ_{xx} and imposed ϕ, for $(\alpha, c) = (0.01, \infty)$. The remaining free variables, λ_{xy}, λ_{xz}, λ_{yz} and λ_{zz}, are minimized over. (b) Cross-sections through the energy landscape at values of constant λ_{xx}.

The transition between the unrotated and rotated director states is similar to a first order phase transition, i.e. a transition occurs when two energy wells become equal in energy. In figure 2.16(b) the depth of the two energy wells becomes equal for $\lambda_{xx} = 1.035$. The results show that the

unrotated state, $\phi = 0$, is always a local energy minimum for any value of imposed λ_{xx} and would therefore be metastable for all values of λ_{xx}. A more realistic description of the transition would consider the scale of energy fluctuations relative to the energy barrier to director rotation.

The gradient of this energy landscape with respect to ϕ is shown in figure 2.17(a). The contour of $\frac{\partial F_{Sm-C}}{\partial \phi} = 0$ is plotted figure 2.17(b). The contour plot shows that at a critical value of λ_{xx} there is a bifurcation point. Points on the top half of the bifurcated curve have minimal values of energy, whereas points on the bottom have maximal values of energy.

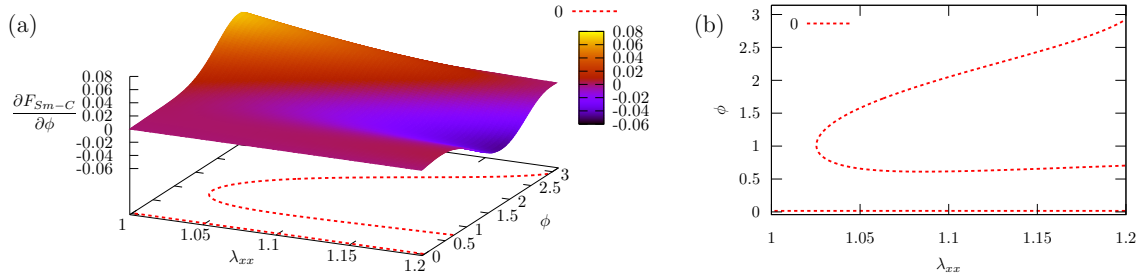

Figure 2.17: (a) $\frac{\partial F_{Sm-C}}{\partial \phi}$ versus λ_{xx} and ϕ, for (α,c) = (0.01,∞). (b) Contour of $\frac{\partial F_{Sm-C}}{\partial \phi} = 0$.

The director instability is not solely a result of the semi-soft energy term, but again is a result of the shape of the soft mode, combined with a general semi-soft elasticity term. These calculations are based on an equilibrium model of a Sm-C elastomer. In practice kinetic terms, such as viscosity would smooth out the sharp jump demonstrated here.

Scalar Model Describing Stress Discontinuity

The semi-soft behaviour of Sm-C elastomers is characterised by two deformation modes; before the onset of director rotation, and afterwards. A scalar model that exhibits the same behaviour when stretching perpendicular to the director can be developed based on representing each of these deformation modes as a spring, and deforming the two springs in series. The total strain is the sum of two deformation modes corresponding to keeping a fixed director ϵ_{U}, and rotating the director ϵ_{SM}

$$\epsilon_{\mathrm{T}} = \epsilon_{\mathrm{U}} + \epsilon_{\mathrm{SM}}. \tag{2.24}$$

The two modes of deformation have different energy penalties, the first arises from a simple uniaxial deformation, so in a neo-Hookean energy model will result in a free energy term of the form

$$F_{\mathrm{U}} = \tfrac{1}{2} K_1 \epsilon_{\mathrm{U}}^2, \tag{2.25}$$

where K_1 corresponds to the shear modulus of the rubber. The second arises from the soft mode, which has a singular edge in the contraction of the rubber as it is stretched. The zz component in the soft mode is initially of the form $\lambda_{zz} = 1/(1 + (\lambda_{xx} - 1)^{\beta})$ (where here $\lambda_{xx} - 1 = \epsilon_{\mathrm{SM}}$. When this is put into the neo-Hookean free energy, it results in free energy terms to leading order in ϵ_{SM} of the form

$$F_{\mathrm{SM}} = \tfrac{1}{2} K_2 \epsilon_{\mathrm{SM}}^{\beta} \tag{2.26}$$

where K_2 is the corresponding shear modulus for this mode. In the case of the semi-soft Sm-C elastomer, this term arises because of the rapid rotation of the director during the start of the soft mode.

The total free energy is then

$$F_{\mathrm{T}} = \tfrac{1}{2} K (\epsilon_{\mathrm{T}} - \epsilon_{\mathrm{SM}})^2 + \tfrac{1}{2} K_2 \epsilon_{\mathrm{SM}}^{\beta}, \tag{2.27}$$

where first spring in this system is hookean, and the second is non-linear, being infinitely stiff at zero strain for $0 < \beta < 1$, but softening rapidly as strain increases. This should be minimized over

ϵ_{SM} to determine the distribution of strain between the two springs. It can be solved analytically for $\beta = 0.5$. The behaviour of this model is illustrated in figure 2.18(a). For small β this system has a discontinuity in the stress-strain curve, but as β is increased the stress-strain response becomes continuous.

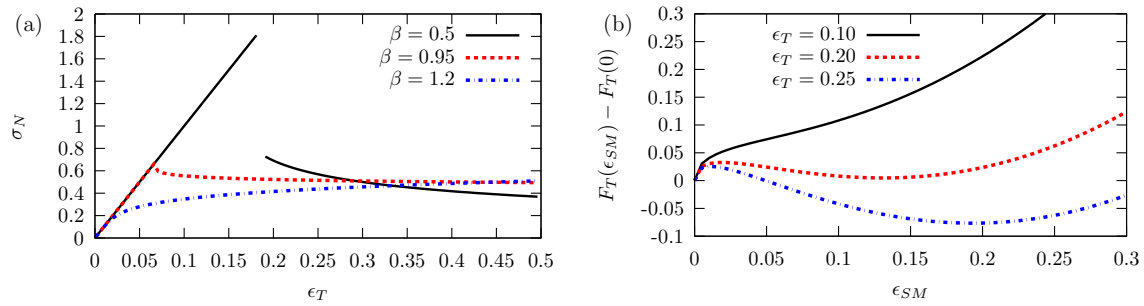

Figure 2.18: (a) An illustration of a discontinuous stress-strain curve for the scalar model described in the text, (b) the free energy as a function of the variable ϵ_{SM} for fixed total strain values. Here $K_1 = 10$ and $K_2 = 1$.

The free energy as a function of ϵ_{SM} is illustrated in figure 2.18(b). For small values of ϵ_T there is only one minimum at $\epsilon_{\mathrm{SM}} = 0$, corresponding to no strain of the second spring. However, as the total strain increases, the second mode of deformation becomes activated and there is a minimum for larger values of ϵ_{SM}. Since there is a barrier between the two minima, the transition is first order, so there is a jump in the equilibrium value of ϵ_{SM}. For larger values of β the phase transition becomes continuous, and the stress-strain curve no longer exhibits a jump.

This behaviour is analogous to that of the semi-soft Sm-C elastomer as the free energy exhibits a discontinuity when stretched perpendicular to the director (where the soft mode has a singular edge). Larger values of β correspond to stretching at a larger angle to the director, where the soft mode does not have such a rapid rotation of the director, and a corresponding sharp drop in the lateral dimension. If the angle between the director and the elongation direction is large enough, then the stress-strain response becomes continuous.

E. Elongation at an angle ψ to $\underline{k}_0$

Stretching at an angle ψ to the initial layer normal is illustrated in figure 2.4(e). The numerical solution of stress-strain curve associated with this geometry is shown in 2.19(a).

The stress-strain curve is continuous in this geometry, but again has a pronounced negative slope. There is a negative IPR of ~ -1.5 that is roughly independent of the semi-soft parameter, see 2.19(b). The rotations of the director and layer normal are shown in figure 2.19(c), with the accompanying deformations shown in figure 2.20.

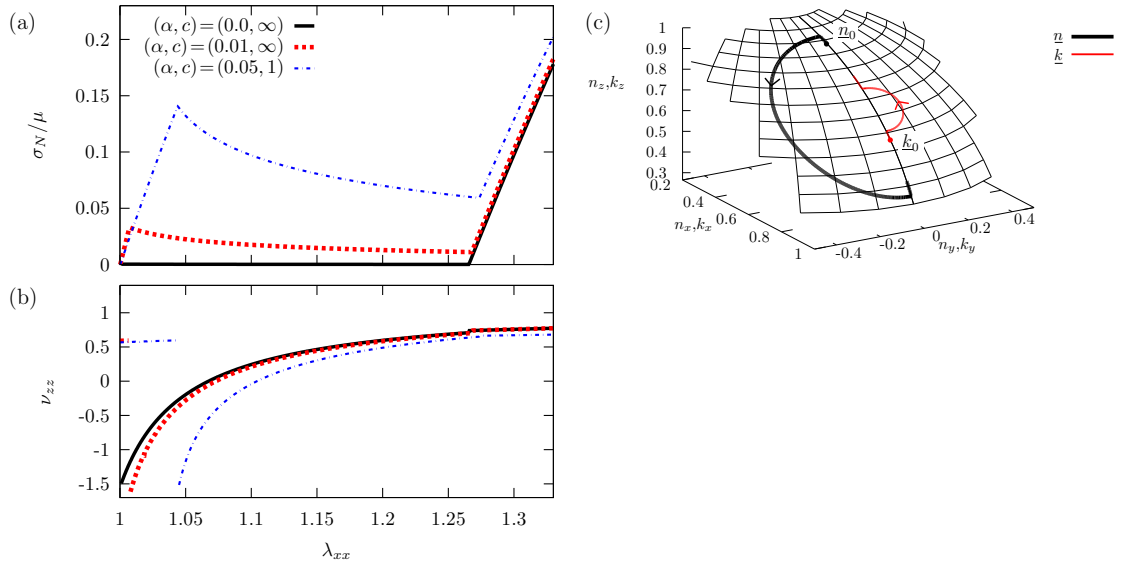

Figure 2.19: (a) The stress-strain response for a semisoft Sm-C elastomer stretched at an angle $\psi = 0.65$ radians to $\underline{k}_0$. The model parameters are $B/\mu = 60$, $r = 2$, and $\theta_0 = 0.5$, and the values of (α, c) shown in the figure. (b) The corresponding IPRs for the stress-strain curves. (c) Director and layer normal reorientation for $(\alpha, c) = (0.05, \infty)$.

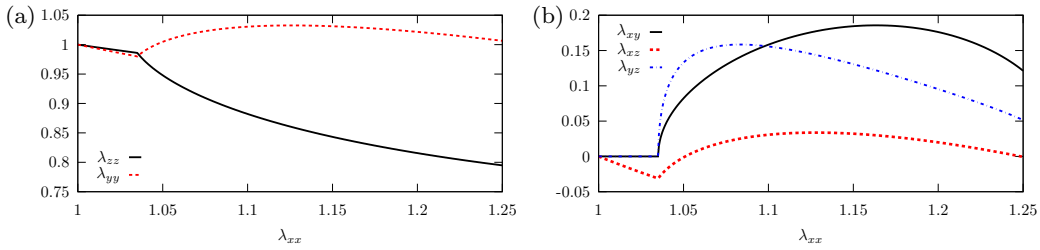

Figure 2.20: (a) The diagonal and (b) shear components of the deformation tensor when stretching at an angle $\psi = 0.65$ radians to $\underline{k}_0$, for parameter values of $(\alpha, B/\mu, c, \theta_0, r) = (0.05, 60, \infty, 0.5, 2)$.

2.3 Discussion

Soft deformations in nematic LCEs are only possible in clamped samples with the formation of microstructure. This has been shown by detailed X-ray experiments [78], and by numerical study [68, 69], and is a result of the non-convex energy of nematic LCEs [79]. The characteristic stress-strain response of Sm-A elastomers [19] also exhibits microstructure if the sample is clamped during stretching [80]. The clamps required in experimental investigation of the Sm-C samples considered here would result in microstructure formation, and some changes to the stress-strain response of the material.

The deformations (b-d) shown in figure 2.4 would not be soft when made with clamped boundary conditions, even without the semi-soft elastic term. This is because no microstructure can be constructed from the soft deformations that is compatible with the boundary conditions, due to the shear components in the Sm-C soft mode [65]. However, the properties of a long sheet of Sm-C LCE may approximate this behaviour as the centre of the sample could deform without rigid boundary conditions. The final deformation shown in figure 2.4(e) can be performed with clamped boundary conditions in the soft case. In the semi-soft case the sample starts to shear before the onset of rotation, which is not compatible with clamped boundaries, so in experiment it may be even stiffer initially due to this additional constraint on its deformation.

The maximum lateral expansion can be deduced from the soft mode presented in equation 1.10.

The shear components are transformed, through a rotation, into an elongation. At $\phi = \pi/2$ the maximum lateral expansion occurs (in the y direction for the geometry considered here), and has a value of $\sqrt{r/\rho}$.

There is currently no experimental work reporting mechanical testing on Sm-C monodomains. Whilst it is anticipated that these monodomains should exhibit soft elasticity, the addition of the semi-soft elasticity term to the model suggests that any soft effects may be difficult to observe for large semi-soft parameter α. When stretching perpendicular to both the layer normal and the director, the semi-soft term may prevent any stress plateau being observed, instead only a shoulder is visible in the stress-strain response.

Imposed Stress

The region of negative slope in the constitutive models reported here is typically explained by a Maxwell Construction. Similar behaviour occurs in the Van der Waals gas model which has a region of negative slope in the pressure-volume curve, where there is a two phase region consisting of a mixture of the liquid and gas phases. In solids the two deformations on either side of the instability must be compatible to form a mixture [63]. The system should then disproportionate, adopting a mixture of the two deformations to achieve the externally imposed strain. The first order type phase transition seen in the example stretching perpendicular to the layer normal can result in hysteretic behaviour as the system jumps from one energy well to another. The rate of the deformation in comparison to the sample relaxation times may also result in hysteresis [81].

The non-monotonic stress-strain curve shown in figure 2.21 is unstable if stress is imposed, as a spontaneous increase in length occurs once the stress reaches a critical value σ_c. If the deformations in the two stable regions are compatible, then the critical stress is determined by an equal area construction, i.e. $A_1 = A_2$.

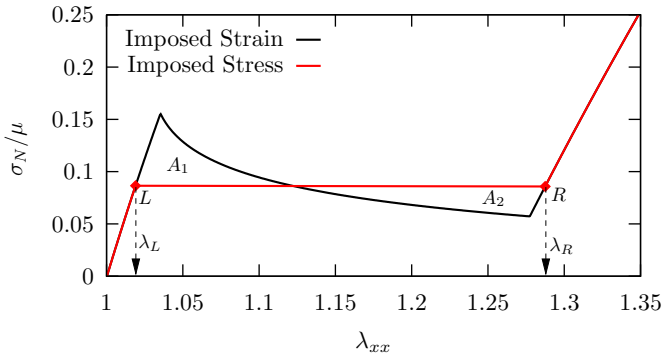

Figure 2.21: Nominal Stress versus λ_{xx}, for $r = 2$, and $B/\mu = 60$ and α=0.05, for a stretch at an angle $\psi = 0.65$ radians to $\underline{k}_0$.

This is because the points L and R in figure 2.21 must satisfy,

$$F_L - \sigma_c\lambda_L = F_R - \sigma_c\lambda_R \implies F_R - F_L = \sigma_c(\lambda_R - \lambda_L).$$

$F_R - F_L$ is the area under the stress-strain curve between L and R. The term $\sigma_c(\lambda_R - \lambda_L)$ is the rectangular area under the stress plateau. For these two terms to be equal the area of the stress-strain curve above the plateau, A_1, must equal the area of the stress-strain curve beneath the plateau, A_2, therefore $A_1 = A_2$.

Computationally a fixed stress, σ, can be imposed using the Lagrange multiplier method, i.e.

$$\underset{\lambda_{xx},\lambda_{xy},\lambda_{yz},\lambda_{xz},\lambda_{zz},\underline{n}}{\text{Minimize}} \quad F_{Sm-C} - \sigma\lambda_{xx}$$
$$\implies \frac{\partial F_{Sm-C}}{\partial \lambda_{xx}} - \sigma = 0.$$

Pseudo-monodomains

Although only the deformations of monodomains have been considered here, the results inform model predictions for polydomains. Polydomains are difficult to model because of the requirement of ensuring that adjacent domains deform in a compatible way. A simplifying approximation used to model a polydomain is to assume that it consists of an array of monodomains that deform at the imposed external strain, but are independent from each other. If the pseudo-monodomain shown in figure 1.9 is stretched in the x direction, then the deformation component λ_{yy} averaged over all the domains is illustrated in figure 2.22 for 50 domains.

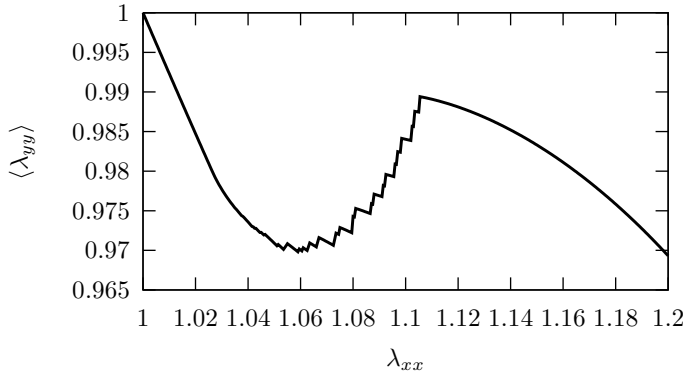

Figure 2.22: The average value of λ_{yy} for 50 domains in a pseudo-monodomain illustrated in figure 1.9 as a function of λ_{xx}, i.e. stretching perpendicular to $\underline{n}_0$. All domains are assumed to experience the same strain and deform independently. Model parameters are $(\alpha, B/\mu, c, \theta_0, r) =$ (0.05,60,∞,0.5,2).

This figure shows that there is a negative IPR as the director in each of the domains jumps causing them to expand. The curve illustrated here is jagged because the alignment of each domain jumps at a slightly different threshold. The expansion of the film thickness, and the energy loss as a result of the jump in the director orientation in this geometry may be observable in experiments on pseudo-monodomains [15, 39]. Ren *et al.* also observed that a pseudo-monodomain stretched perpendicular to the director underwent necking when the strain exceeded 30% [39]. The larger values of deformation reported in experiments before the knee in the stress-strain curve point to a much larger value of α than in the illustrative plot in figure 2.22.

A similar model for a pseudo-monodomain stretched parallel to the director would result in a stiffness $\sim \mu$. However in the experiments of Sánchez-Ferrer *et al.* the observed stiffness is $\sim B$ [15]. This might indicate that the domain structure is confining the available shears, resulting in a much stiffer response.

The features of the smectic-C model described here would be present in a wide range of models that have soft modes of nematic elastomers but incorporate the constraint on the director to remain at a fixed angle to the layer normal. However, validation of these models await either experimental work on mechanical testing of Sm-C monodomains, or theoretical work on pseudo-monodomains to link up with existing mechanical experiments on pseudo-mododomains.

Biaxial Semi-softness Term

The form of the soft mode results in non-monotonic stress-strain curves for the semi-soft energy term as well as for generic rubber energies. However biaxial Sm-C systems might have energy terms of a different form that return the stress-strain curve to monotonicity.

In order to search for these additional terms we can consider the compositional fluctuations model of a biaxial LCE. Although compositional fluctuations are an unlikely physical explanation of how semi-softness really occurs the model has been very successful because the energy it predicts is of

a very general and correct form. The full derivation of the biaxial semi-soft term is included as Appendix B.

For a biaxial tensor with mean chain anisotropies $< r >$ and $< p >$ the semi-softness term is,

$$F_{ss} \sim \left(< \frac{1}{r} > - \frac{1}{< r >} \right) < \mathrm{Tr} \left[\underline{\underline{\lambda}} \cdot \left(\left(1 + \frac{< p >}{2} \right) \underline{m}_0 \, \underline{m}_0^T + \left(1 - \frac{< p >}{2} \right) \underline{k}_0 \, \underline{k}_0^T \right) \cdot \underline{\underline{\lambda}}^T \cdot \underline{n} \, \underline{n}^T \right] >$$
$$+ \left(< \frac{1}{1 + \frac{p}{2}} > - \frac{1}{1 + \frac{<p>}{2}} \right) < \mathrm{Tr} \left[\underline{\underline{\lambda}} \cdot (< r > \underline{n}_0 \, \underline{n}_0^T + 2 \underline{k}_0 \, \underline{k}_0^T) \cdot \underline{\underline{\lambda}}^T \cdot \underline{m} \, \underline{m}^T \right] >$$
$$+ \left(< \frac{1}{1 - \frac{p}{2}} > - \frac{1}{1 - \frac{<p>}{2}} \right) < \mathrm{Tr} \left[\underline{\underline{\lambda}} \cdot (< r > \underline{n}_0 \, \underline{n}_0^T + 2 \underline{m}_0 \, \underline{m}_0^T) \cdot \underline{\underline{\lambda}}^T \cdot \underline{k} \, \underline{k}^T \right] >, \qquad (2.28)$$

where the initial axes of the biaxial shape tensor are in the $\underline{n}_0$, $\underline{m}_0$ and $\underline{k}_0$ directions.

The factors $\left(< \frac{1}{r} > - \frac{1}{<r>} \right)$, $\left(< \frac{1}{1+\frac{p}{2}} > - \frac{1}{1+\frac{<p>}{2}} \right)$ and $\left(< \frac{1}{1-\frac{p}{2}} > - \frac{1}{1-\frac{<p>}{2}} \right)$ are positive.

Only the term weighted by $\left(< \frac{1}{r} > - \frac{1}{<r>} \right)$ results in a monotonic stress-strain curve.

2.4 Conclusion

This numerical study has investigated the mechanical response of a monodomain Sm-C LCE model, with the inclusion of a semi-soft elastic term to describe imperfections in the elastomer. As result of the negative incremental Poisson's ratio inherent in the soft modes of a Sm-C monodomain, the mechanical properties of a semi-soft monodomain are unusual. When stretching perpendicular to the layer normal and the director, the response is reminiscent of a nematic elastomer. The layer normal does not reorient in this stretch, and a finite force is required to deform the LCE and initiate director rotation. However, the stress plateau is less well defined for larger values of semi-soft parameter α; it is reduced to a shoulder in the stress-strain response. This is at variance to the nematic case where the plateau in the stress-strain response remains, even in the limit of large α.

When stretching parallel to the layer normal the elastomer again exhibits a threshold to director rotation. The initial modulus of the stretch is predicted to be the smectic modulus B provided the tilt modulus $\to \infty$. Once director rotation has started the elastomer has a negative incremental Poisson's ratio, and a negative stiffness. The negative stiffness is a consequence of the Sm-C soft mode deformations and the form of the semi-softness term. The rotation of the director causes the sample thickness to expand and then contract. A negative incremental Poisson's ratio of up to $\nu \sim -1.5$ has been found for typical model parameters. The lateral expansion arises because the director rotates in a direction perpendicular to the stretch axis due to the constraint of the layer normal. This more detailed understanding of monodomain deformations of Sm-C elastomers might prove useful in understanding recent mechanical and piezoelectric experiments on polydomain Sm-C elastomers.

When stretching perpendicular to the director with the layer normal coplanar, an instability in the director orientation is predicted. The director jumps from an unrotated state to a rotated state at a threshold strain. The semi-soft term provides an energy barrier to director rotation, so the threshold strain increases with increasing values of the semi-soft parameter. The jump in director orientation causes a discontinuity in the stress-strain curve, i.e. a dramatic decrease in stress once the director has rotated. Unfortunately the metastability of the unrotated state in this transition is not meaningfully predicted by the model, i.e. it is determined to be metastable at any extension.

When stretching parallel to the director the stress-strain response is monotonic and the stiffness is indicative of the rubber modulus $\sim \mu$. The layer normal rotates away from the stretch axis, and the director follows due to the constraint of the tilt angle. Unlike the behaviour observed in nematic elastomers the director is not predicted to align with the stretch axis at large strains.

Chapter 3

Smectic-A Quasi-Convex Energy

This chapter contains a brief introduction to the concepts of convexity, followed by a discussion of the quasi-convexified form of the Adams-Warner smectic-A energy. The process of quasi-convexification is elucidated by considering the toy case of a 2D smectic-A material, for which the laminate microstructure can be calculated explicitly.

An additional energy term is introduced to model the effects of deforming post-buckled smectic-A layers, finite chain-extensibility and entanglements. The quasi-convexified form of the Adams-Warner energy combined with this additional term forms the basis of the numerical calculations in chapter 5. To improve understanding of this model a few uniform deformations are considered, including stretching parallel and perpendicular to the layer normal.

3.1 Types of Convexity

For an elastic medium any equilibrium configuration corresponds to a stationary point of its free energy; the equilibrium is stable or metastable at a minimum, and unstable at a maximum. The general criteria for an elastic medium to always be stable is that its energy is convex. An energy surface is convex if the entire surface lies above all tangent planes to the surface [82]. In the mathematical analysis of microstructure it has proven useful to introduce some alternative conceptions of convexity. An introduction to these is given here, based on lectures notes by Stefan Müller [83].

Convex Functions

A scalar function is convex if the line segment drawn between two arbitrary points on the energy surface, A and B, always lies level with or above the energy surface, as illustrated in figure 3.1.

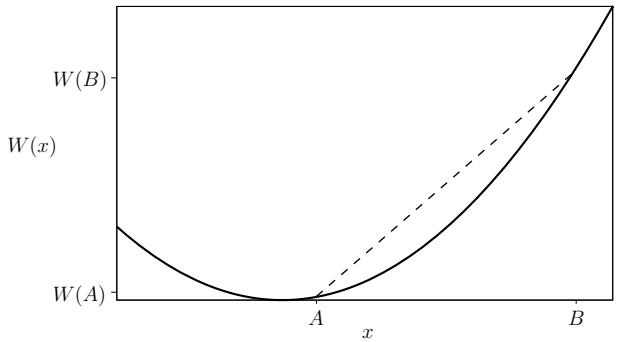

Figure 3.1: The solid curve is a convex function $W(x)$. The dotted line shows a line segment between two points, A and B. For a convex function the line segment always lies level with or above the energy surface for any choice of A and B.

The x-coordinate of points between $x = A$ to $x = B$ can be parameterised by λ, where $0 < \lambda < 1$. The height of the energy surface for a given λ value is $W(\lambda A + (1-\lambda)B)$, whereas the height of the line segment is $\lambda W(A) + (1-\lambda)W(B)$. Using these results the definition of convexity can be restated;

A scalar function $W(x)$ is convex if,

$$W(\lambda A + (1-\lambda)B) \leq \lambda W(A) + (1-\lambda)W(B) \qquad \forall A, B \text{ and } 0 < \lambda < 1. \tag{3.1}$$

This scalar definition of convexity can be extended to the case of functions depending on matrices. For the case of a matrix, $\underline{\underline{F}}$, having $m \times n$ components, i.e. $\underline{\underline{F}} \in \underline{\underline{M}}^{m\times n}$, then a function $W(\underline{\underline{F}})$ is convex if,

$$W(\lambda \underline{\underline{A}} + (1-\lambda)\underline{\underline{B}}) \leq \lambda W(\underline{\underline{A}}) + (1-\lambda)W(\underline{\underline{B}}) \qquad \forall \underline{\underline{A}}, \underline{\underline{B}} \in \underline{\underline{M}}^{m\times n} \text{ and } 0 < \lambda < 1. \tag{3.2}$$

Polyconvex Functions

The concept of polyconvexity arises as a generalisation of convexity. A function $W(\underline{\underline{F}})$ is polyconvex if it can be written as a convex function of the minors of $\underline{\underline{F}}$,

$$W(\underline{\underline{F}}) = W_{convex}(\underline{\underline{\mathscr{M}}}(\underline{\underline{F}})), \tag{3.3}$$

where W_{convex} is a convex function and the vector $\underline{\underline{\mathscr{M}}}(\underline{\underline{F}})$ contains the minors of $\underline{\underline{F}}$ as its elements. Polyconvexity is a weaker condition than convexity; convexity $\implies$ polyconvexity, but polyconvexity $\not\Longrightarrow$ convexity.

Quasi-convex Functions

A function is quasi-convex if spatial variations in $\underline{\underline{F}}$ do not result in a more optimally minimized energy. In elastic solids, where the energy is a function of the deformation gradient $\underline{\underline{F}}$, the condition of quasi-convexity corresponds to stability against microstructure formation, as only affine deformations are energy minimizers. A material energy $W(\underline{\underline{F}})$ is quasi-convex if

$$\int_\Omega W(\underline{\underline{F}})dx \leq \int_\Omega W(\underline{\underline{F}} + \nabla \underline{y}(x))dx \quad \forall \underline{y},$$

provided the integral on the right hand side exists. The $\nabla \underline{y}(x)$ term is a spatial gradient included in the deformation. The displacement $\underline{y}(x)$ must be sufficiently smooth to have a well-defined first derivative on region Ω. The overall deformation must still satisfy any boundary conditions specified on region Ω.

For an energy function that is not quasi-convex it is possible to construct the quasi-convexified form of the energy by minimising it over all microstructures that respect boundary conditions. This requires the displacement term, $\underline{y}(x)$, be zero on the region boundary, $\partial\Omega$. The quasi-convex envelope of an energy $W(\underline{\underline{F}})$ is given by

$$W_{qc}(\underline{\underline{F}}) = \inf_{\underline{y}} \left\{ \frac{1}{|\Omega|} \int_\Omega W(\underline{\underline{F}} + \nabla \underline{y}(x))dx \ : \ \underline{y}(x) = 0 \quad \text{on } \partial\Omega \right\}. \tag{3.4}$$

Quasi-convexity is of central importance to microstructure formation, but unfortunately it is very difficult to determine the quasi-convexity of arbitrary functions. The condition of quasi-convexity is weaker than that of polyconvexity; polyconvexity $\implies$ quasi-convexity, but quasiconvexity $\not\Longrightarrow$ polyconvexity.

Rank-one Convex Functions

A simple laminate consists of alternating bands of two different deformation gradients, $\underline{\underline{A}}$ and $\underline{\underline{B}}$, as illustrated in figure 3.2.

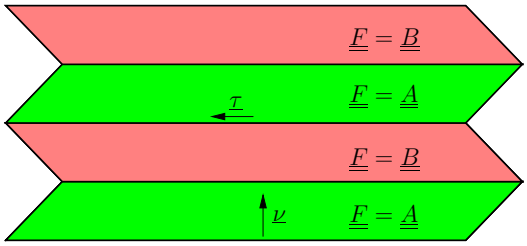

Figure 3.2: Illustration of a simple laminate, composed in equal-parts of deformations $\underline{\underline{A}}$ and $\underline{\underline{B}}$. The vectors, $\underline{\nu}$ and $\underline{\tau}$, are normal and parallel to the laminate interfaces respectively.

In order to maintain the continuity of material along interfaces the deformations must satisfy,

$$\underline{\underline{A}} \cdot \underline{\tau} = \underline{\underline{B}} \cdot \underline{\tau}, \tag{3.5}$$

where $\underline{\tau}$ is a vector parallel to the laminate interfaces. To satisfy this condition the two deformations must be rank-one connected, and so can be written as,

$$\underline{\underline{B}} - \underline{\underline{A}} = \underline{a} \otimes \underline{\nu}, \tag{3.6}$$

where $\underline{\nu}$ is a vector normal to the laminate interfaces.

A function is rank-one convex if it is convex along line segments connecting two matrices $\underline{\underline{A}}$ and $\underline{\underline{B}}$ that are themselves rank-one connected, i.e. $W(\underline{\underline{F}})$ is rank-one convex if

$$W(\lambda \underline{\underline{A}} + (1-\lambda)\underline{\underline{B}}) \leq \lambda W(\underline{\underline{A}}) + (1-\lambda) W(\underline{\underline{B}}) \tag{3.7}$$
$$\forall \underline{\underline{A}}, \underline{\underline{B}} \in \underline{\underline{M}}^{m \times n} \text{ with } \mathrm{rank}(\underline{\underline{B}} - \underline{\underline{A}}) = 1 \text{ and } 0 < \lambda < 1.$$

Rank-one convexity is a weaker condition than quasi-convexity; quasi-convexity $\implies$ rank-one convexity. For a matrix $\underline{\underline{F}} \in \underline{\underline{M}}^{m \times n}$ then it is known that rank-one convexity $\not\Longrightarrow$ quasi-convexity for the case $m \geq 2$ and $n \geq 3$ [84].

3.2 Smectic-A Monodomain Model

The Adams-Warner model of smectic-A elastomer has nematic and smectic contributions [23],

$$F_{\text{smectic-}A} = \underbrace{\frac{1}{2}\mu \mathrm{Tr}\left[\underline{\underline{\lambda}} \cdot \underline{\underline{\ell}}_0 \cdot \underline{\underline{\lambda}}^T \cdot \underline{\underline{\ell}}^{-1}\right]}_{F_{nematic}} + \underbrace{\frac{1}{2} B \left(\frac{d}{d_0} - 1\right)^2}_{F_{smectic}}, \tag{3.8}$$

where μ is the rubber shear modulus, B is the smectic modulus and $\frac{d}{d_0}$ is the change in the layer spacing. The initial polymer step length tensor, for a polymer anisotropy of r in the $\underline{n}_0$ direction, is $\underline{\underline{\ell}}_0 = \underline{\underline{\delta}} + (r-1)\underline{n}_0 \underline{n}_0^T$. The target state step length tensor is $\underline{\underline{\ell}}^{-1} = \underline{\underline{\delta}} + (\frac{1}{r} - 1)\underline{n}\,\underline{n}^T$.

The Adams-Warner model takes the layers to deform like embedded planes, which constrains the layer normal and layer spacing so that,

$$\underline{n} = \frac{\mathrm{cof}\,\underline{\underline{\lambda}} \cdot \underline{n}_0}{|\mathrm{cof}\,\underline{\underline{\lambda}} \cdot \underline{n}_0|}, \tag{3.9}$$

$$\frac{d}{d_0} = \frac{1}{|\text{cof}\,\underline{\underline{\lambda}} \cdot \underline{n}_0|}, \tag{3.10}$$

where the deformation gradient, $\underline{\underline{\lambda}}$, has the smectic-$A$ state as its reference state, and $\underline{\underline{\lambda}}$ is volume conserving, i.e. $\det \underline{\underline{\lambda}} = 1$.

The Adams-Warner energy can be rewritten using the high-temperature isotropic state as the reference configuration. The deformations relative to this reference state are given by $\underline{\underline{F}}$,

$$\underline{\underline{F}} = \underline{\underline{\lambda}} \cdot \underline{\underline{\ell}}_0{}^{1/2} r^{-1/6}. \tag{3.11}$$

The deformation $\underline{\underline{F}}$ corresponds to taking the high-temperature isotropic sample, cooling it to the smectic-A state, and then performing the deformation, $\underline{\underline{\lambda}}$, in the smectic state. Upon cooling to the smectic-A state a volume conserving deformation, $\underline{\underline{\ell}}_0{}^{1/2} r^{-1/6}$, spontaneously occurs. The Adams-Warner energy written in terms of $\underline{\underline{F}}$ was shown in reference [80] to be,

$$F_{\text{smectic-}A} = \frac{1}{2}\mu r^{1/3}\left(\text{Tr}\left[\underline{\underline{F}} \cdot \underline{\underline{F}}^T\right] + kq^2\left(\frac{q}{|\text{cof}\,\underline{\underline{F}} \cdot \underline{n}_0|} - 1\right)^2\right), \tag{3.12}$$

where the constants q and k are given by,

$$q = r^{-1/3}\left(1 + \frac{\mu}{B}(1 - r)\right) \tag{3.13}$$

$$k = \frac{B}{\mu r^{2/3} q^3}. \tag{3.14}$$

Experimentally the layers are much stiffer than the rubber, i.e. $k \gg 1$, so $|\text{cof}\,\underline{\underline{F}} \cdot \underline{n}_0| \approx q$ should always hold. The squared term in (3.12) can therefore be expanded around $(|\text{cof}\,\underline{\underline{F}} \cdot \underline{n}_0| - q)$ yielding,

$$F_{\text{smectic-}A} = \frac{1}{2}\mu r^{1/3}\left(\text{Tr}\left[\underline{\underline{F}} \cdot \underline{\underline{F}}^T\right] + k(|\text{cof}\,\underline{\underline{F}} \cdot \underline{n}_0| - q)^2) + \mathcal{O}(|\text{cof}\,\underline{\underline{F}} \cdot \underline{n}_0| - q)^3\right), \tag{3.15}$$

Approximating the Adams-Warner energy by keeping only the leading order term, and dividing through by $\frac{1}{2}\mu r^{1/3}$ gives the dimensionless energy,

$$W(\underline{\underline{F}}) = \text{Tr}\left[\underline{\underline{F}} \cdot \underline{\underline{F}}^T\right] + k(|\text{cof}\,\underline{\underline{F}} \cdot \underline{n}_0| - q)^2. \tag{3.16}$$

3.3 Smectic-A Quasi-Convexification in 2D

The quasi-convex envelope of an energy is the minimization of the energy over all possible microstructures, assuming that microstructure become infinitely fine. A simple example of quasi-convexification can be given for the 2D smectic-A energy. Taking equation (3.16) and setting $q = 1$ yields the 3D smectic-A energy as

$$W(\underline{\underline{F}}) = \begin{cases} |\underline{\underline{F}}|^2 + k(|\text{cof}\,\underline{\underline{F}} \cdot \underline{n}_0| - 1)^2 & \text{if } \det \underline{\underline{F}} = 1 \\ \\ \infty & \text{else.} \end{cases} \tag{3.17}$$

The 2D smectic-A energy can found by restricting $\underline{\underline{F}}$ to the form,

$$\underline{\underline{F}} = \left(\begin{array}{cc|c} & \underline{\underline{G}} & \begin{matrix}0\\0\end{matrix} \\ \hline 0 & 0 & 1 \end{array}\right), \text{where } \underline{\underline{G}} = \begin{pmatrix} F_{11} & F_{12} \\ F_{21} & F_{22} \end{pmatrix}. \tag{3.18}$$

The direction $\underline{n}_0$ can be taken as $\underline{e}_1$ without a loss of generality, so the $|\text{cof}\,\underline{\underline{F}}\cdot\underline{n}_0|$ term becomes,

$$|\text{cof}\,\underline{\underline{F}}\,\underline{e}_1| = |\underline{\underline{F}}\,\underline{e}_2 \times \underline{\underline{F}}\,\underline{e}_3| = |\underline{\underline{F}}\,\underline{e}_2 \times \underline{e}_3| = |\underline{\underline{G}}\,\underline{e}_2|. \tag{3.19}$$

The term $|\underline{\underline{F}}|^2$ in (3.17) can be expanded out,

$$|\underline{\underline{F}}|^2 = |\underline{\underline{F}}\,\underline{e}_1|^2 + |\underline{\underline{F}}\,\underline{e}_2|^2 + |\underline{\underline{F}}\,\underline{e}_3|^2 = |\underline{\underline{G}}\,\underline{e}_1|^2 + |\underline{\underline{G}}\,\underline{e}_2|^2 + 1. \tag{3.20}$$

Substituting (3.20) and (3.19) into (3.17) and neglecting the constant term yields the 2D smectic-A energy,

$$W_{2D}(\underline{\underline{G}}) = |\underline{\underline{G}}\,\underline{e}_1|^2 + |\underline{\underline{G}}\,\underline{e}_2|^2 + k(|\underline{\underline{G}}\,\underline{e}_2| - 1)^2. \tag{3.21}$$

Constructing the Quasi-Convex Envelope of the 2D Smectic-A Energy

It is useful to consider the convexity of the different parts of the 2D smectic-A energy,

$$W_{2D}(\underline{\underline{G}}) = \underbrace{|\underline{\underline{G}}\,\underline{e}_1|^2}_{\text{convex}} + \underbrace{|\underline{\underline{G}}\,\underline{e}_2|^2 + k(|\underline{\underline{G}}\,\underline{e}_2| - 1)^2}_{\psi(|\underline{\underline{G}}\,\underline{e}_2|),\ \text{non-convex}}, \tag{3.22}$$

$$\text{where } \psi(|\underline{\underline{G}}\,\underline{e}_2|) = |\underline{\underline{G}}\,\underline{e}_2|^2 + k(|\underline{\underline{G}}\,\underline{e}_2| - 1)^2.$$

The term, $|\underline{\underline{G}}\,\underline{e}_1|^2$, is a convex function. Whereas the term, $\psi(|\underline{\underline{G}}\,\underline{e}_2|)$, is not a convex function. The global minimum of $\psi(|\underline{\underline{G}}\,\underline{e}_2|)$ is $\frac{k}{k+1}$, which occurs at deformations satisfying $|\underline{\underline{G}}\,\underline{e}_2| = \frac{k}{k+1}$, as shown in figure 3.3.

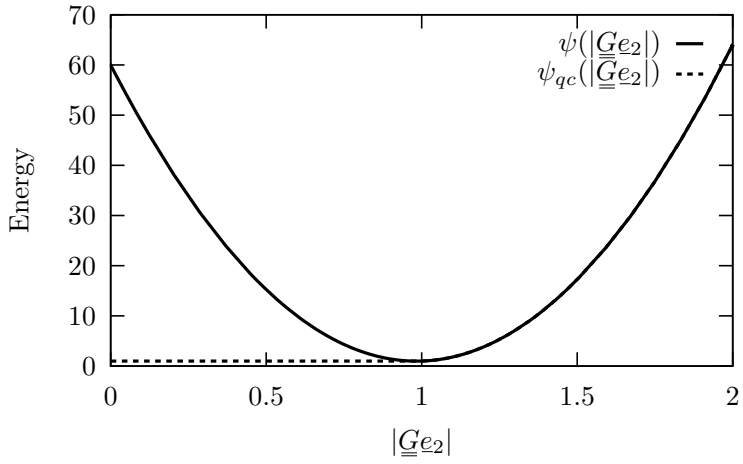

Figure 3.3: The function, $\psi(|\underline{\underline{G}}\,\underline{e}_2|)$, and its quasi-convex envelope, $\psi_{qc}(|\underline{\underline{G}}\,\underline{e}_2|)$, are shown for $k = 60$. ψ has a minimum located at $|\underline{\underline{G}}\,\underline{e}_2| = \frac{k}{k+1}$ with an energy of $\frac{k}{k+1}$. The function, ψ_{qc}, lies lower than ψ in the region $|\underline{\underline{G}}\,\underline{e}_2| < \frac{k}{k+1}$ where $\psi_{qc} = \frac{k}{k+1}$.

If the deformation, $\underline{\underline{G}}$, is taken to be upper-triangular and incompressible, i.e.

$$\underline{\underline{G}} = \begin{pmatrix} G_{11} & G_{12} \\ 0 & \dfrac{1}{G_{11}} \end{pmatrix}, \tag{3.23}$$

then the energy landscape of $\psi(|\underline{\underline{G}}\,\underline{e}_2|)$ has the double-well form shown in figure 3.4.

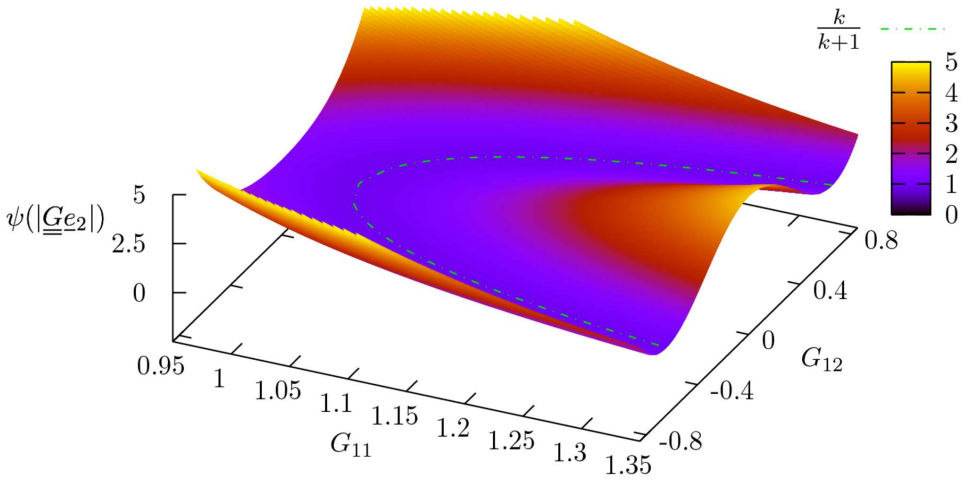

Figure 3.4: The function $\psi(|\underline{\underline{G}}\,\underline{e}_2|)$ versus G_{11} and G_{12}, for $k = 60$. The dotted green line is a contour line of the global minimum $\psi(|\underline{\underline{G}}\,\underline{e}_2|) = \frac{k}{k+1}$, which corresponds to $|\underline{\underline{G}}\,\underline{e}_2| = \frac{k}{k+1}$.

The region of figure 3.4 enclosed by the dotted green-line corresponds to $|\underline{\underline{G}}\,\underline{e}_2| < \frac{k}{k+1}$. Within this region the formation of a simple laminate microstructure is energetically favourable. This microstructure flattens the energy in this region to a constant value of $\frac{k}{k+1}$, see figure 3.5.

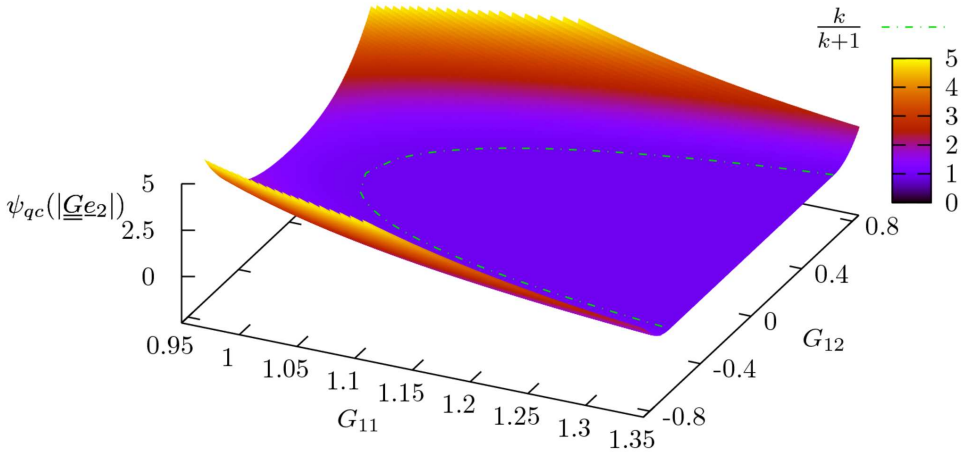

Figure 3.5: The quasi-convex envelope, $\psi_{qc}(|\underline{\underline{G}}\,\underline{e}_2|)$, versus G_{11} and G_{12}, for $k = 60$.

An expression for the quasi-convex envelope of $W_{2D}(\underline{\underline{G}})$ can be found by minimizing the energy over a first order laminate microstucture consisting of two oppositely sheared regions. The deformations in the positively and negatively sheared regions are given by,

$$\underline{\underline{G}}_{\pm} = \underline{\underline{G}}(\underline{\underline{I}} + s_{\pm}\,\underline{e}_1 \otimes \underline{e}_2). \tag{3.24}$$

The deformations, $\underline{\underline{G}}_{+}$ and $\underline{\underline{G}}_{-}$, are rank-one connected as,

$$\underline{\underline{G}}_{+} - \underline{\underline{G}}_{-} = (s_{+} - s_{-})(\underline{\underline{G}} \cdot \underline{e}_1) \otimes \underline{e}_2, \tag{3.25}$$

has the same form as equation (3.6), with the normal to the laminate interface being $\underline{e}_2$.

The proportion of the microstructure composed of the positively sheared deformation is denoted α, where $0 < \alpha < 1$, and the remaining $(1-\alpha)$ is negatively sheared. The average deformation in the microstructure must correspond to the imposed macroscopic deformation, which implies that,

$$\alpha \underline{\underline{G}}_+ + (1-\alpha)\underline{\underline{G}}_- = \underline{\underline{G}}. \tag{3.26}$$

The 2D smectic-A energy for the deformation $\underline{\underline{G}}_\pm$ is,

$$W_{2D}(\underline{\underline{G}}_\pm) = |\underline{\underline{G}}_\pm \, \underline{e}_1|^2 + |\underline{\underline{G}}_\pm \, \underline{e}_2|^2 + k(|\underline{\underline{G}}_\pm \, \underline{e}_2| - 1)^2. \tag{3.27}$$

The terms $|\underline{\underline{G}}_\pm \, \underline{e}_1|$ and $|\underline{\underline{G}}_\pm \, \underline{e}_2|$ simplify as follows,

$$|\underline{\underline{G}}_\pm \, \underline{e}_1| = |\underline{\underline{G}}(\underline{\underline{I}} + s_\pm \, \underline{e}_1 \otimes \underline{e}_2) \, \underline{e}_1| = |\underline{\underline{G}} \, \underline{e}_1|, \tag{3.28}$$

$$|\underline{\underline{G}}_\pm \, \underline{e}_2| = |\underline{\underline{G}}(\underline{\underline{I}} + s_\pm \, \underline{e}_1 \otimes \underline{e}_2) \, \underline{e}_2| = |\underline{\underline{G}} \, \underline{e}_2 + s_\pm \, \underline{\underline{G}} \, \underline{e}_1|. \tag{3.29}$$

Substituting (3.28) and (3.29) into (3.27) yields the energy,

$$W_{2D}(\underline{\underline{G}}_\pm) = |\underline{\underline{G}} \, \underline{e}_1|^2 + |\underline{\underline{G}} \, \underline{e}_2 + s_\pm \, \underline{\underline{G}} \, \underline{e}_1|^2 + k(|\underline{\underline{G}} \, \underline{e}_2 + s_\pm \, \underline{\underline{G}} \, \underline{e}_1| - 1)^2. \tag{3.30}$$

The non-convex part of equation (3.30) can be rewritten by substituting $t = |\underline{\underline{G}} \, \underline{e}_2 + s_\pm \, \underline{\underline{G}} \, \underline{e}_1|$,

$$\psi(t) = t^2 + k(t-1)^2. \tag{3.31}$$

The value of t is set such that the energy $\psi(t)$ is minimized, which corresponds to

$$t = \frac{k}{k+1}, \tag{3.32}$$

or equivalently,

$$|\underline{\underline{G}} \, \underline{e}_2 + s_\pm \, \underline{\underline{G}} \, \underline{e}_1|^2 = \left(\frac{k}{k+1}\right)^2. \tag{3.33}$$

This is simply a quadratic equation for s_+ and s_-,

$$s_\pm^2 \, |\underline{\underline{G}} \, \underline{e}_1|^2 + 2 s_\pm \, (\underline{\underline{G}} \, \underline{e}_1) \cdot (\underline{\underline{G}} \, \underline{e}_2) + |\underline{\underline{G}} \, \underline{e}_2|^2 = \left(\frac{k}{k+1}\right)^2, \tag{3.34}$$

with solutions,

$$s_\pm = \frac{-2\underline{\underline{G}} \, \underline{e}_1 \cdot \underline{\underline{G}} \, \underline{e}_2 \pm \sqrt{4(\underline{\underline{G}} \, \underline{e}_1 \cdot \underline{\underline{G}} \, \underline{e}_2)^2 - 4|\underline{\underline{G}} \, \underline{e}_1|^2 (|\underline{\underline{G}} \, \underline{e}_2|^2 - \left(\frac{k}{k+1}\right)^2)}}{2|\underline{\underline{G}} \, \underline{e}_1|^2}. \tag{3.35}$$

The expression for the quasi-convex envelope of $W_{2D}(\underline{\underline{G}})$ is,

$$W_{qc}(\underline{\underline{G}}) = \begin{cases} |\underline{\underline{G}} \, \underline{e}_1|^2 + \psi_{qc}(|\underline{\underline{G}} \, \underline{e}_2|) & \text{if } \det \underline{\underline{G}} = 1 \\ \\ \infty & \text{else} \end{cases} \tag{3.36}$$

$$\text{where } \psi_{qc}(|\underline{\underline{G}} \, \underline{e}_2|) = \begin{cases} |\underline{\underline{G}} \, \underline{e}_2|^2 + k(|\underline{\underline{G}} \, \underline{e}_2| - 1)^2 & |\underline{\underline{G}} \, \underline{e}_2| \geq \dfrac{k}{k+1} \quad \text{Anisotropic Solid} \\ \\ \dfrac{k}{k+1} & |\underline{\underline{G}} \, \underline{e}_2| \leq \dfrac{k}{k+1} \quad \text{Unidirectional Buckling} \end{cases} \tag{3.37}$$

The energy has two phases; a phase without microstructure where the material behaves like an anisotropic solid, and a phase of simple laminates corresponding to unidirectionally buckled layers. In figure 3.5 the two phases are separated by the dotted green line, with the flat region corresponding to unidirectional buckling.

Laminates in 2D

The proportion of positively sheared laminates, α, within the microstructure is found by rearrangement of equation (3.26),

$$\alpha = -\frac{s_-}{s_+ - s_-}, \tag{3.38}$$

where s_+ and s_- are related to the laminate deformations by $\underline{\underline{G}}_\pm = \underline{\underline{G}}(\underline{\underline{I}} + s_\pm \underline{e}_1 \otimes \underline{e}_2)$. The knowledge of $\underline{\underline{G}}_\pm$ allows the microstructure to be reconstructed, however the absolute length-scale of the microstructure is not accessible from this analysis.

The microstructure formed when stretching parallel to the director is illustrated in figure 3.6, where the uniaxial deformation takes the form,

$$\underline{\underline{G}} = \begin{pmatrix} \lambda & 0 \\ 0 & 1/\lambda \end{pmatrix}. \tag{3.39}$$

When stretching parallel to the director there is initially a threshold to microstructure formation. Above the threshold solutions for the shear components $s_\pm(\lambda)$ appear; these solutions are equal in magnitude but opposite in sign, so the laminate pairs appear in equal proportions, i.e. $\alpha = \frac{1}{2}$.

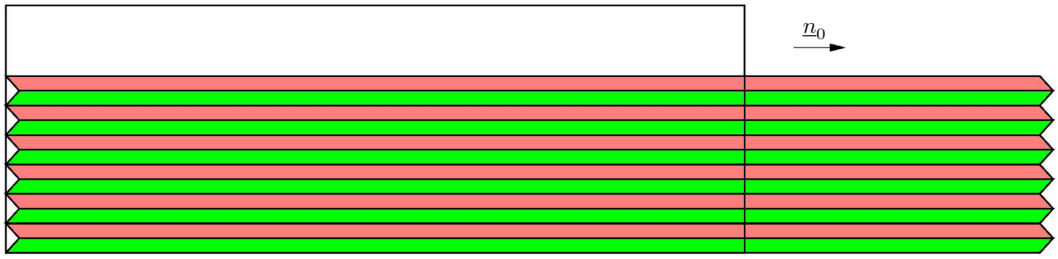

Figure 3.6: Laminate microstructure for $\lambda = 1.4$ parallel to $\underline{n}_0$. The shears are $s_+ = 0.466$ and $s_- = -0.466$, yielding $\alpha = 0.5$. Hence positively sheared laminates (green) fill the same area as negatively sheared laminates (red). The empty rectangle shows the undeformed sample size.

When stretching at an angle to the director there is initially a threshold to microstructure formation. The shear components $s_\pm(\lambda)$, are in general no longer equal and opposite, so α is a function of strain. The case of stretching at 20° to $\underline{n}_0$ is illustrated in figure 3.7. Note that the laminate interfaces rotate with strain, and are not in general along the $\underline{n}_0$ direction.

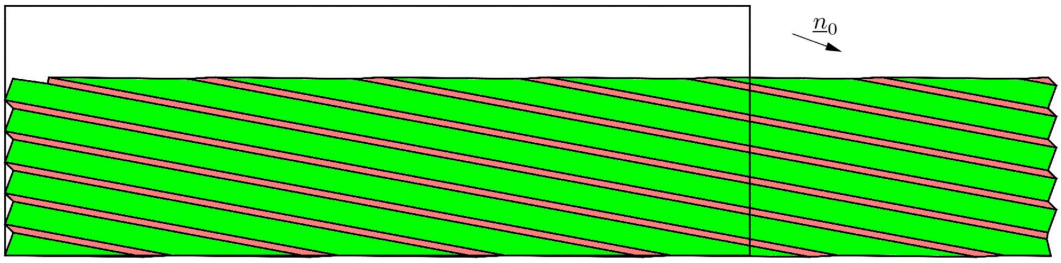

Figure 3.7: Laminate microstructure for $\lambda = 1.4$ at 20° to $\underline{n}_0$. The shears are $s_+ = 0.199$ and $s_- = -0.720$, yielding $\alpha = 0.783$. Hence positively sheared laminates (green) fill greater area than negatively sheared laminates (red).

3.4 Smectic-A Quasi-Convex Energy in 3D

Constructing the quasi-convex envelope in three dimensions is a more complicated task, as higher order laminates are required not just simple laminates. An analytic expression for the quasiconvex envelope of equation (3.16) was derived by Adams, Conti, DeSimone & Dolzmann in reference [80]. The results of this paper are summarised here.

It is useful to introduce the largest singular value of $\underline{\underline{F}}$ denoted by $\lambda_{\max}(\underline{\underline{F}})$. The singular values of $\underline{\underline{F}}$ are the square-roots of the eigenvalues of $\underline{\underline{F}}^T\underline{\underline{F}}$, i.e.

$$\lambda_{\max}(\underline{\underline{F}}) = \sup\left\{|\underline{\underline{F}}\cdot\underline{e}| : \underline{e}\in\mathbb{R}^3, |\underline{e}|=1\right\}. \tag{3.40}$$

The expression for $W_{qc}(\underline{\underline{F}})$ can be written in terms of two convex functions of $\underline{\underline{F}}$,

$$b = \lambda_{\max}(\underline{\underline{F}}\cdot\underline{\underline{P}})^2, \tag{3.41}$$

$$d = |\mathrm{cof}\,\underline{\underline{F}}\cdot\underline{n_0}|, \tag{3.42}$$

where the matrix $\underline{\underline{P}} = \underline{\underline{\delta}} - \underline{n_0}\underline{n_0}^T$ projects out the $\underline{n_0}$ component.

The functions, b and d, have important physical interpretations. For example taking $\underline{n_0} = \underline{x}$ and a deformation of the form,

$$\underline{\underline{F}} = \begin{pmatrix} \lambda_1 & 0 & 0 \\ 0 & \lambda_2 & 0 \\ 0 & 0 & \lambda_3 \end{pmatrix}, \tag{3.43}$$

results in $d = 1/\lambda_1$ and b is the square of the largest of λ_2 and λ_3, i.e. the deformation component parallel to $\underline{n_0}$ is $1/d$ and the square of the largest deformation perpendicular to $\underline{n_0}$ is b.

The expression for $W_{qc}(\underline{\underline{F}})$ is

$$W_{qc}(\underline{\underline{F}}) = \begin{cases} |\underline{\underline{F}}\cdot\underline{n_0}|^2 + f(b,d) & \text{if } \det\underline{\underline{F}} = 1 \\ \\ \infty & \text{else} \end{cases} \tag{3.44}$$

$$\text{where } f(b,d) = \begin{cases} b + \dfrac{d^2}{b} + k(d-q)^2 & d \geq \dfrac{kqb}{kb+1} & \text{Anisotropic Solid} \\ \\ b + \dfrac{kq^2}{qb+1} & \begin{array}{c} b \geq q - \dfrac{1}{k} \\ \text{and} \\ d \leq \dfrac{kqb}{kb+1} \end{array} & \text{Unidirectional Buckling} \\ \\ 2q - \dfrac{1}{k} & b \leq q - \dfrac{1}{k} & \text{Bidirectional Buckling} \end{cases} \tag{3.45}$$

The energy has three phases; a phase without microstructure (anisotropic solid), a phase of simple laminates (unidirectionally buckled layers) and a phase of higher order laminates (bidirectionally buckled layers). The higher order laminates consist of mixtures of multiple simple laminate pairings, which causes the layers to buckle in more than one direction.

$W_{qc}(\underline{\underline{F}})$ is a coarse grained model energy of a smectic-A elastomer that takes into account the formation of microstructure, without resolving the fine-scale oscillations in the deformation gradient.

Equilibrium

To compare with experimental results it is convenient to work with deformations relative to the low temperature equilibrium smectic-A state. The system undergoes a volume conserving uniaxial deformation as it is cooled from the isotropic state to the smectic state. This uniaxial deformation along the layer normal minimizes the total free energy $W_{qc}(\underline{\underline{F}})$. Taking $\underline{n}_0 = \underline{x}$ the uniaxial deformation is,

$$\underline{\underline{F}}_0 = \begin{pmatrix} 1/\lambda_0^2 & 0 & 0 \\ 0 & \lambda_0 & 0 \\ 0 & 0 & \lambda_0 \end{pmatrix}. \tag{3.46}$$

Substituting this into equation (3.44) and minimising with respect to λ_0 yields the equation,

$$\frac{d}{d\lambda_0}\left[k(\lambda_0^2 - q)^2 + 2\lambda_0^2 + \lambda_0^{-4}\right] = 0. \tag{3.47}$$

The value of λ_0 found by solving (3.47) can be used to convert deformations to start from the smectic-A state as follows

$$\underline{\underline{F}} = \underline{\underline{\lambda}} \cdot \underline{\underline{F}}_0 \tag{3.48}$$

Here $\underline{\underline{F}}$ is a deformation defined with respect to the high-temperature isotropic state, and $\underline{\underline{\lambda}}$ is a deformation defined with respect to the smectic-A state, see figure 3.8

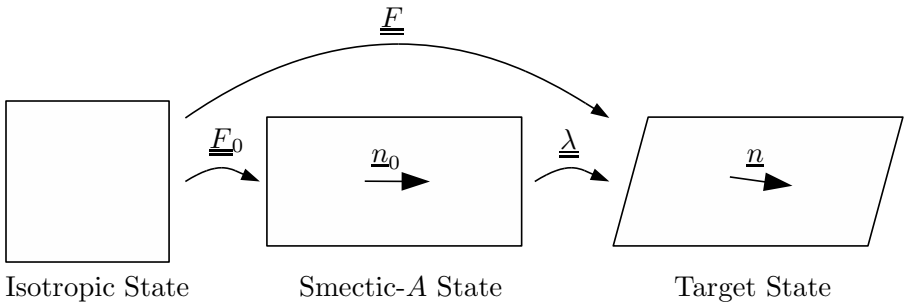

Figure 3.8: The deformation $\underline{\underline{F}}$ transforms directly between the isotropic state and the target state. This is equivalent to performing $\underline{\underline{F}}_0$, which transforms the isotropic state to the smectic-A state, followed by $\underline{\underline{\lambda}}$, which is a deformation starting from the smectic-A state.

Substituting this transformation back into the free energy the terms b and d are scaled by λ_0^{-2}, and the term $|\underline{\underline{F}} \cdot \underline{n}_0|^2$ is scaled by λ_0^{-4}. It is useful to define the scaled quantities

$$\tilde{b} = b/\lambda_0^2 \tag{3.49}$$

$$\tilde{d} = d/\lambda_0^2 \tag{3.50}$$

to describe b and d transformed to the smectic-A reference state. The total free energy with respect to the smectic-A state is

$$\widetilde{W}_{qc}(\underline{\underline{\lambda}}) = \lambda_0^{-4}|\underline{\underline{\lambda}} \cdot \underline{n}_0|^2 + f(\lambda_0^2\tilde{b}, \lambda_0^2\tilde{d}). \tag{3.51}$$

The phase diagram of the quasiconvex free energy is illustrated in figure 3.9.

The region with $\tilde{d} > \tilde{b}$ is inaccessible due to the incompressibility constraint. In the anisotropic solid (AS) phase the quasiconvex free energy and the microscopic free energy are the same. The energy is not lowered by the formation of microstructure, and the layers in the smectic do not buckle. Hence the small angle X-ray scattering pattern should show just one orientation of the layer normal. In the unidirectional buckling (UB) phase the energy is minimized by the formation

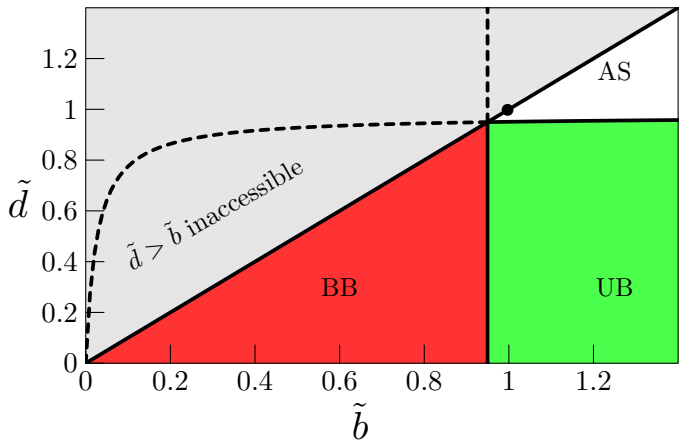

Figure 3.9: The phase diagram of the smectic-A LCE quasiconvex energy indicating the anisotropic solid (AS), unidirectional buckling (UB) and bidirectional buckling (BB) phases. The phase of the deformation is determined by $\tilde{b}$ and $\tilde{d}$ given in equations (3.49) and (3.50). The smectic-A equilibrium point is marked by a black circle.

of a simple laminate [80]. There are two deformation gradients $\underline{\underline{\lambda}}_A$ and $\underline{\underline{\lambda}}_B$ that are rank one connected, and whose suitably weighted average produces the macroscopic deformation. The small angle X-ray scattering pattern should contain two orientations of the layer normal corresponding to the regions of $\underline{\underline{\lambda}}_A$ and $\underline{\underline{\lambda}}_B$. There should be no reduction in X-ray scattering intensity if the beam is normal to the plane in which the laminate forms.

In the bidirectional buckling (BB) phase there is no simple laminate that can achieve the optimal energy. A higher order laminate must be formed [80], which contains an average of several different deformation gradients. Physically buckling of the smectic layers in more than one direction is possible, and it is expected that the small angle X-ray scattering pattern will show a loss of intensity, indicating that some smectic layers are rotated out of the scattering plane.

3.5 Smectic layer buckling, finite extensibility and entanglements

The quasi-convex free energy of equation (3.44) is formulated on the assumption that an infinitely fine microstructure can be formed at no energy cost. In practice terms involving gradients of the deformation, arising through the Frank elastic cost of gradients in the director will give rise to an interfacial energy cost. Deformations perpendicular to the layer normal will distort the buckled layers changing the interfacial energy.

The Adams-Warner model also makes the assumption of a Gaussian phantom chain network model, which neglects effects such as the finite extensibility of polymer chains, and chain entanglements. Several theoretical approaches have been developed to better describe bulk rubber under the influence of these effects [85, 86].

$\widetilde{W}_{qc}$ is independent of $\tilde{b}$ and $\tilde{d}$ in the BB phase, which means there is no energy penalty for deforming the bidirectionally buckled layers in directions perpendicular to $\underline{n}_0$. Consequently the model does not reproduce the Poisson's ratios of $(\frac{1}{2}, \frac{1}{2})$ that occur post-buckling when stretching parallel to $\underline{n}_0$. The Poisson's ratio of $(\frac{1}{2}, \frac{1}{2})$ were observed experimentally by Nishikawa *et al.* [19], and can be observed in figure 1.11. Motivated by the above theoretical considerations, and to recover the experimentally observed Poisson's ratio an additional (convex) term will be included in the model. This term physical relates to the non-Gaussian nature of the polymer chains, and the deformation of the buckled layers. The magnitude of this additional term arising from deforming the buckled layers can be estimated through dimensional analysis.

Mooney-Rivlin Term

To account for non-Gaussian effects, the deformation of buckled layers, and recover the experimentally observed Poisson's ratios in a simple way, a Mooney-Rivlin type term will be included in the energy. This Mooney-Rivlin term is proportional to the second invariant of the Cauchy-Green strain tensor $\underline{\underline{C}} = \underline{\underline{\lambda}}^T \cdot \underline{\underline{\lambda}}$ [87, 88],

$$\widetilde{W}_{MR}(\underline{\underline{\lambda}}) = \tfrac{1}{2} c_{MR}(\mathrm{Tr}[\underline{\underline{C}}]^2 - \mathrm{Tr}[\underline{\underline{C}} \cdot \underline{\underline{C}}]). \tag{3.52}$$

Note that the Mooney-Rivlin model for bulk rubber is overly simplistic in assuming that the derivatives of the energy with respect to the first and second invariants (denoted A_1 and A_2 respectively), $\frac{\partial W}{\partial A_1}$ and $\frac{\partial W}{\partial A_2}$, are constants. The model does not realistically describe the uniaxial or biaxial stretching of even isotropic rubbers [85, 89, 90]. Consequently the values of coefficients fitted to experiments are likely to be only approximate.

The total free energy is

$$\widetilde{W}_{\mathrm{tot}} = \widetilde{W}_{qc} + \widetilde{W}_{MR}, \tag{3.53}$$

which is an altogether polyconvex function as both terms are individually polyconvex [91]. It can be shown by constructing a one-dimensional example that the quasiconvex envelope of the sum of two functions is not in general equal to the sum of their quasiconvex envelopes. If we were to add the Mooney-Rivlin term to the nonconvex free energy of equation (3.16) then the quasiconvex envelope of their sum differs from $\widetilde{W}_{\mathrm{tot}}$ in equation (3.53). The small shift in the energy wells will not alter the qualitative features of the numerical results here, so we will neglect this change.

The terms $\widetilde{W}_{MR}$ and $\widetilde{W}_{qc}$ are both minimal at $\underline{\underline{\lambda}} = \underline{\underline{\delta}}$, so the equilibrium point of $\widetilde{W}_{\mathrm{tot}}$ is located at $\underline{\underline{\lambda}} = \underline{\underline{\delta}}$, as desired. The term $\widetilde{W}_{MR}$ acts to equalise the Poisson's ratios, which can be seen by substituting the deformation

$$\underline{\underline{\lambda}} = \begin{pmatrix} 1 & 0 & 0 \\ 0 & \lambda & 0 \\ 0 & 0 & \frac{1}{\lambda} \end{pmatrix} \tag{3.54}$$

into equation (3.52) yielding the following

$$\widetilde{W}_{MR}(\underline{\underline{\lambda}}) = 3c_{MR} + 4c_{MR}(\lambda - 1)^2 + \mathcal{O}(\lambda - 1)^3. \tag{3.55}$$

This expression is minimized when the deformations in the two transverse directions are equal.

Note that this additional term affects all the phases, not just the BB phase. However it is not the dominant free energy term in the AS and UB phases, so does not alter the physics of the model there.

Estimating the coefficient of the Mooney-Rivlin term

The stiffness associated with changing the buckling wavelength of the layers can be estimated by using a similar calculation to that of Ref. [56] by Finkelmann *et al.*.

Consider the free energy of a single interface between two regions of opposite shear. Taking $\underline{n}_0 = \underline{x}$ then the deformation gradient tensor in the two regions is of the form,

$$\underline{\underline{\lambda}} = \begin{pmatrix} \lambda_{xx} & 0 & \lambda_{xz} \\ 0 & \frac{1}{\lambda_{xx}\lambda_{zz}} & 0 \\ 0 & 0 & \lambda_{zz} \end{pmatrix}. \tag{3.56}$$

Using equations (3.9) and (3.10) this deformation results in the following expression for the layer spacing and director orientation

$$\frac{d}{d_0} = \frac{\lambda_{xx}\lambda_{zz}}{\sqrt{\lambda_{xx}^2 + \lambda_{xz}^2}}, \tag{3.57}$$

$$\underline{n} = \left(\frac{\lambda_{zz}}{\sqrt{\lambda_{xx}^2 + \lambda_{xz}^2}}, 0, -\frac{\lambda_{xz}}{\sqrt{\lambda_{xx}^2 + \lambda_{xz}^2}} \right). \tag{3.58}$$

The orientation of the layer normal can be written as $\underline{n} = (\cos\theta, 0, \sin\theta)$, where $\tan\theta = -\lambda_{xz}/\lambda_{zz}$. Substituting these expressions into the Adams-Warner energy of equation (3.8) gives

$$f = \tfrac{1}{2}\mu \left[\lambda_{zz}^2 + \frac{1}{\lambda_{zz}^2 \lambda_{xx}^2} + \lambda_{zz}^2 \tan^2\theta + (\cos^2\theta + r\sin^2\theta)\lambda_{xx}^2 + \frac{B}{\mu}(\lambda_{xx}\cos\theta - 1)^2 \right]. \tag{3.59}$$

This equation can be minimized over λ_{zz}^2, resulting in $\lambda_{zz}^2 = \cos\theta/\lambda_{xx}$. Substituting this back into the free energy reduces it to

$$f = \tfrac{1}{2}\mu \left[\frac{2}{\lambda_{xx}\cos\theta} + \lambda_{xx}^2(\cos^2\theta + r\sin^2\theta) + \frac{B}{\mu}(\lambda_{xx}\cos\theta - 1)^2 \right]. \tag{3.60}$$

Expanding for small θ up to quartic order, corresponding to small rotations of the layer normal, produces the following expression

$$f = \tfrac{1}{2}\mu \left[p_0 - p_2\theta^2 + \tfrac{1}{3}p_4\theta^4 \right] \tag{3.61}$$

$$p_0 = \frac{2}{\lambda_{xx}} + \lambda_{xx}^2 + \frac{B}{\mu}(\lambda_{xx} - 1)^2 \tag{3.62}$$

$$p_2 = -\frac{1}{\lambda_{xx}} + \lambda_{xx}^2(r-1) + \frac{B}{\mu}(\lambda_{xx}^2 - \lambda_{xx}) \tag{3.63}$$

$$p_4 = \frac{1}{4}\frac{B}{\mu}\lambda_{xx}(4\lambda_{xx} - 1) + \frac{5}{4\lambda_{xx}} + (1-r)\lambda_{xx}^2. \tag{3.64}$$

In addition to the rubber elastic energy, calculation of the interface energy requires a Frank elastic energy. For simplicity the one constant approximation can be made, i.e. splay, twist and bend are penalized by the same constant. For the sample shown in figure 3.10 of size $L_x \times L_y \times L_z$, the total free energy is

$$F = L_x L_y \int_0^{L_z} dz \left(\tfrac{1}{2}\mu \left[p_0 - p_2\theta^2 + \tfrac{1}{3}p_4\theta^4 \right] + \tfrac{1}{2}K\theta'^2 \right). \tag{3.65}$$

It is convenient to convert distance to a dimensionless quantity using $\xi = \sqrt{\frac{K}{\mu}}$ and to denote $t = z/\xi$. The free energy becomes

$$F = L_x L_y \sqrt{\frac{K}{\mu}} \int_0^{\mathcal{L}} dt \left(\tfrac{1}{2}\mu \left[p_0 - p_2\theta^2 + \tfrac{1}{3}p_4\theta^4 \right] + \tfrac{1}{2}\dot{\theta}^2 \right), \tag{3.66}$$

where $L_z = \mathcal{L}\xi$. Minimizing this integral produces the following Euler-Lagrange equation

$$\ddot{\theta} = -p_2\theta + \tfrac{2}{3}p_4\theta^3. \tag{3.67}$$

Far away from the interface the director is in the energy minimum where

$$\theta^2 = \theta_0^2 = \frac{3p_2}{2p_4}. \tag{3.68}$$

The first integral of the Euler-Lagrange equation is given by

$$\tfrac{1}{2}\dot{\theta}^2 = -\tfrac{1}{2}p_2\theta^2 + \tfrac{1}{6}p_4\theta^4 + \tfrac{1}{2}p_2\theta_0^2 - \tfrac{1}{6}p_4\theta_0^4. \tag{3.69}$$

The first integral can be used to substitute for the $\dot{\theta}$ term in the free energy. Subtracting from F the free energy of the uniform state with $\theta = \theta_0$ gives the free energy of the interface,

$$F_{\text{int}} = L_x L_y \sqrt{K\mu} \int_0^{\mathcal{L}} dt \left[-p_2(\theta^2 - \theta_0^2) + \tfrac{1}{3}p_4(\theta^4 - \theta_0^4) \right],$$

$$= \sqrt{2K\mu}\,\frac{p_2^{3/2}}{p_4}L_xL_y. \tag{3.70}$$

The wavelength of the layer buckling, and hence the stiffness of the buckled layers can be estimated as follows. The sample can be divided into three regions, as shown in figure 3.10.

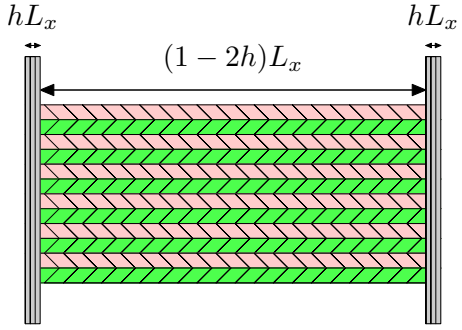

Figure 3.10: To estimate the length scale of the layer buckling it is assumed that the sample divides into three regions as shown. The end regions do not contain buckled layers, whereas the central region does.

The end regions near the clamps are too constrained to buckle, so contain layers with a fixed layer normal ($\theta = 0$), and hence have free energy density

$$F_U = F_{\theta=0} = \frac{\mu}{2}p_0(\lambda_1), \tag{3.71}$$

where λ_1 is the zz component of the deformation in this region. The central region contains smectic layers with tilt angle θ_0, so has free energy density

$$F_R = F_{\theta=\theta_0} = \frac{\mu}{2}\left(p_0(\lambda_2) - \frac{3}{8}\frac{p_2(\lambda_2)^2}{p_4(\lambda_2)}\right), \tag{3.72}$$

where λ_2 is the xx component of the deformation in this region. If the end regions are of order hL_x which in turn is comparable to the wavelength of the layer buckling, then the number of interfaces in the bulk is $\frac{L_z}{hL_x}$. Since the elongation of the sample is performed by imposing a stress σ, that does work in extending the sample, the total free energy of the system is

$$\begin{aligned} F_T = (1-2h)\frac{\mu}{2}\left(p_0(\lambda_2) - \frac{3}{8}\frac{p_2(\lambda_2)^2}{p_4(\lambda_2)}\right)V + h\mu p_0(\lambda_1)V \\ - \sigma\left(2h\lambda_1 + (1-2h)\lambda_2\right)V + F_{\rm int}\frac{L_z}{hL_x}, \end{aligned} \tag{3.73}$$

where $V = L_xL_yL_Z$ is the volume of the sample.

Minimising F_T over h yields the following optimal value,

$$h^{*2} = F_{\rm int}\frac{L_z}{L_xV} \times \frac{1}{\frac{3}{4}\frac{\mu}{2}\frac{p_2^2(\lambda_2)}{p_4(\lambda_2)} + \sigma(\lambda_2-\lambda_1) + \mu(p_0(\lambda_1)-p_0(\lambda_2))}. \tag{3.74}$$

To estimate the stiffness corresponding to changing the buckling wavelength it is useful to denote $h = \gamma h^*$. Substituting this into equation (3.73) and taking the second derivative with respect to γ yields the stiffness of the sample associated with changing the buckling wavelength,

$$Y = \frac{1}{2}\left.\frac{\partial^2 F_T}{\partial\gamma^2}\right|_{\gamma=1} = \frac{F_{\rm int}}{Vh^*L_x}. \tag{3.75}$$

Assuming that $B \gg \mu$ so that $\lambda_1 \approx 1$, simplifies the result to,

$$Y \approx B\sqrt{\sqrt{\frac{K}{B}}\frac{1}{L_x}f(\lambda)}, \tag{3.76}$$

where $f(\lambda)$ is a function of the deformation applied.

As expected the buckled layer modulus goes to zero when $K = 0$.

The stiffness given in equation (3.76) provides an estimate of the magnitude of c_{MR}. It must be divided by $\frac{1}{2}\mu r^{1/3}$ to render it in the same dimensionless units as the smectic-A energy, i.e.

$$c_{MR} \sim \frac{2B}{\mu r^{1/3}} \sqrt{\sqrt{\frac{K}{B}} \frac{1}{L_x}}. \tag{3.77}$$

Alternative Terms

Many possible energy terms, which act to equalise the Poisson's ratio, were considered before arriving at the Mooney-Rivlin term. The additional term should not change the equilibrium point of the model, which rules out simply adding a small multiple of $\tilde{b}$. Also the additional term should only be significant within the BB phase, which rules out terms involving higher powers of $\tilde{b}$.

It is often helpful, when a system has a single anisotropy direction $\underline{n}_0$, to write the energies in terms of the invariants of the Cauchy-Green strain tensor $\underline{\underline{C}} = \underline{\underline{\lambda}}^T \cdot \underline{\underline{\lambda}}$,

$$A_1 = \mathrm{Tr}[\underline{\underline{C}}] \tag{3.78}$$

$$A_2 = \tfrac{1}{2}(\mathrm{Tr}[\underline{\underline{C}}]^2 - \mathrm{Tr}[\underline{\underline{C}} \cdot \underline{\underline{C}}]) \tag{3.79}$$

$$A_3 = \det[\underline{\underline{C}}] \tag{3.80}$$

$$A_4 = \underline{n}_0 \cdot \underline{\underline{C}} \cdot \underline{n}_0 \tag{3.81}$$

$$A_5 = \underline{n}_0 \cdot \underline{\underline{C}} \cdot \underline{\underline{C}} \cdot \underline{n}_0. \tag{3.82}$$

The parameters, $\tilde{b}$ and $\tilde{d}$, can also be rewritten in terms of the invariants. This is done by putting a general form of $\underline{\underline{C}}$ into the definitions of the $\tilde{b}$, $\tilde{d}$ and the invariants; substitution then yields,

$$\tilde{b} = \frac{A_1 - A_4 + \sqrt{(A_1 + A_4)^2 - 4(A_2 + A_5)}}{2} \tag{3.83}$$

$$\tilde{d} = \sqrt{A_2 + A_5 - A_1 A_4}. \tag{3.84}$$

The term, $(A_1 + A_4)^2 - 4(A_2 + A_5)$, which is contained within the square root term of $\tilde{b}$, acts to penalise unequal Poisson's ratios, and may seem a good choice for the additional term. However it does not satisfy the requirement of being polyconvex given the constraint of incompressibility. It is quite difficult to find functions that satisfy this condition, as polyconvex terms can become non-convex when restricted to incompressible deformations, e.g. $A_4 + 2\tilde{b}$ is polyconvex, but graphical plotting shows that it is no longer polyconvex under the constraint of incompressibility.

A function can be proven to be polyconvex by evaluating the second derivatives of the function, and showing that the function always has a positive curvature [91]. This can be performed for the Mooney-Rivlin term by writing it as a function of principal elongations,

$$\widetilde{W}_{MR} = \tfrac{1}{2} c_{MR}(\lambda_1\lambda_2 + \lambda_1\lambda_3 + \lambda_2\lambda_3). \tag{3.85}$$

The incompressibility constraint can be expressed as,

$$\lambda_1\lambda_2\lambda_3 = 1. \tag{3.86}$$

Substituting the constraint into the Mooney-Rivlin term gives,

$$\widetilde{W}_{MR} = \tfrac{1}{2} c_{MR}(\frac{1}{\lambda_3} + \frac{1}{\lambda_2} + \lambda_2\lambda_3). \tag{3.87}$$

The second derivatives of the Mooney-Rivlin term are,

$$\frac{\partial^2 \widetilde{W}_{MR}}{\partial \lambda_2^2} = \frac{c_{MR}}{\lambda_2^3}, \qquad \frac{\partial^2 \widetilde{W}_{MR}}{\partial \lambda_3^2} = \frac{c_{MR}}{\lambda_3^3}, \qquad \frac{\partial^2 \widetilde{W}_{MR}}{\partial \lambda_2 \partial \lambda_3} = \tfrac{1}{2} c_{MR}, \tag{3.88}$$

which are all positive provided that $c_{MR}, \lambda_2, \lambda_3 > 0$.

3.6 Uniform Deformations of the Smectic-A model

In order to increase understanding of the energy $\widetilde{W}_{\text{tot}}$ it is useful to consider a few uniform deformations. Throughout this section the layer normal is taken to be initially aligned with the $\underline{x}$ direction, i.e. $\underline{n}_0 = \underline{x}$.

Elongation parallel to the layer normal

An elongation parallel to the layer normal is described by

$$\underline{\underline{\lambda}}_{\parallel} = \begin{pmatrix} \lambda & 0 & 0 \\ 0 & \frac{1}{\lambda^\gamma} & 0 \\ 0 & 0 & \frac{1}{\lambda^{1-\gamma}} \end{pmatrix}, \tag{3.89}$$

where the parameter γ determines the Poisson's ratio of the deformation. A value of $\gamma = \frac{1}{2}$ gives isotropic behaviour in the directions perpendicular to the $\underline{n}_0$. A value of $\gamma = 1$ gives the anisotropic Poisson's ratios of $(1, 0)$.

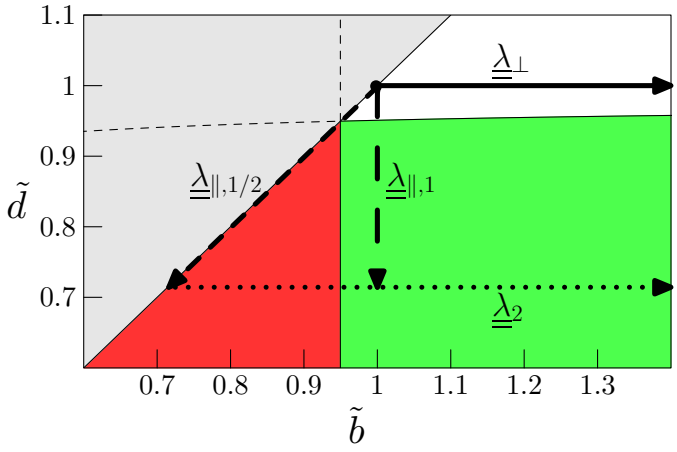

Figure 3.11: Paths traversed in $\tilde{b}$ and $\tilde{d}$ on stretching parallel to $\underline{n}_0$ with $\gamma = \frac{1}{2}$ (short dashed-line) and $\gamma = 1$ (long dashed-line). The deformations $\underline{\underline{\lambda}}_{\perp}$ (solid-line) and $\underline{\underline{\lambda}}_{2}$ (dotted-line) are both stretching perpendicular to $\underline{n}_0$, with the latter performed after an initial parallel stretch.

Figure 3.11 shows that when stretching parallel to $\underline{n}_0$ with $\gamma = \frac{1}{2}$ (labelled $\underline{\underline{\lambda}}_{\parallel,1/2}$) the elastomer deformation follows the line $\tilde{b} = \tilde{d}$. The system crosses from the AS to BB phase at the threshold strain,

$$\lambda_{\text{th}} = \lambda_0^2 (q - 1/k)^{-1}. \tag{3.90}$$

By contrast when stretching parallel to $\underline{n}_0$ with $\gamma = 1$ (labelled $\underline{\underline{\lambda}}_{\parallel,1}$ in figure 3.11) the deformation follows the line of constant $\tilde{b}$. The system crosses from AS to UB phase, at $\lambda = (1 + k\lambda_0^2)/kq$. The nominal stress denoted σ_N, and measured in units of $\frac{1}{2}\mu r^{1/3}$ can be calculated by differentiating the scaled free energy $\widetilde{W}_{\text{tot}}$ with respect to λ. The nominal stress shows a dramatic reduction

when the elastomer crosses into the microstructured phases BB or UB. For example on the $\gamma = \frac{1}{2}$ trajectory the elastic modulus when the deformation begins is

$$k\frac{\lambda_0^4}{\lambda_{\text{th}}} + \frac{4}{\lambda_0^4} + 6c_{MR}. \tag{3.91}$$

This is dominated by the smectic layer modulus encoded in $k \gg 1$. After the threshold at λ_{th} the modulus drops to

$$\frac{2}{\lambda_0^4} + \frac{6}{\lambda_{\text{th}}^4}c_{MR}, \tag{3.92}$$

i.e. it is reduced by a factor of approximately k, as illustrated in figure 3.12.

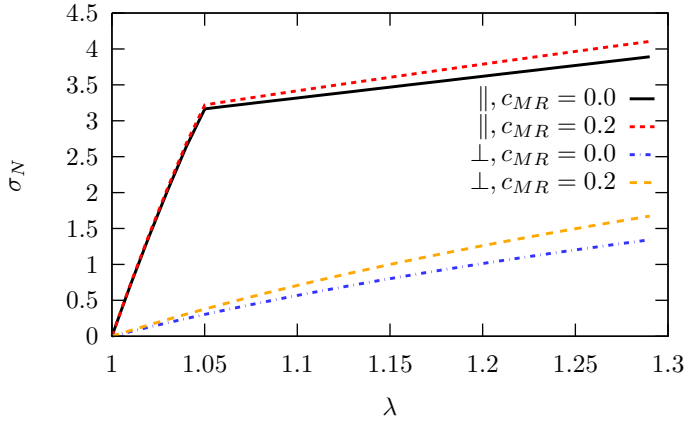

Figure 3.12: The nominal stress σ_N as a function of deformation λ for deformations parallel to $\underline{n}_0$ with $\gamma = \frac{1}{2}$, and perpendicular to $\underline{n}_0$.

Elongation perpendicular to the layer normal

An elongation perpendicular to the layer normal, $\underline{n}_0$, with Poisson's ratios of $(1, 0)$, is described by

$$\underline{\underline{\lambda}}_\perp = \begin{pmatrix} 1 & 0 & 0 \\ 0 & \lambda & 0 \\ 0 & 0 & \frac{1}{\lambda} \end{pmatrix}. \tag{3.93}$$

The trajectory of this deformation is along a line of constant $\tilde{d}$, as shown in figure 3.11 (labelled $\underline{\underline{\lambda}}_\perp$). The elastic modulus in this case is,

$$8\lambda_0^2 + 8c_{MR}. \tag{3.94}$$

The nominal stress σ_N for this geometry is illustrated in figure 3.12. There is no threshold in stress-strain curve, and no microstructure forms in this deformation geometry.

Two step deformation

A two stage deformation process first stretching parallel to the director by a factor of λ_1, and then perpendicular to it by a factor λ_2, defined in equation (3.95), can be used to experimentally determine the constant c_{MR}.

$$\underline{\underline{\lambda}}_2 = \begin{pmatrix} 1 & 0 & 0 \\ 0 & \lambda_2 & 0 \\ 0 & 0 & \frac{1}{\lambda_2} \end{pmatrix} \cdot \begin{pmatrix} \lambda_1 & 0 & 0 \\ 0 & \frac{1}{\sqrt{\lambda_1}} & 0 \\ 0 & 0 & \frac{1}{\sqrt{\lambda_1}} \end{pmatrix}, \tag{3.95}$$

The trajectory of this deformation is illustrated in figure 3.11. The first stage follows $\underline{\underline{\lambda}}_{\parallel,1/2}$, and the second stage is labelled $\underline{\underline{\lambda}}_2$. The first stage of deformation proceeds the system moves along the line $\tilde{b} = \tilde{d}$, thus crossing from the AS to BB phase. During the second deformation stage the system moves along a line of constant $\tilde{d}$, crossing from the BB to UB phase. The nominal stress during the second stage is shown in figure 3.13. If c_{MR} is zero then the deformation is perfectly soft within the BB phase. This is an intrinsic property of $\widetilde{W}_{qc}$ which is altered by the addition of $\widetilde{W}_{MR}$. Physically this reflects the fact that there is an energetic cost to deform buckled layers, which rules out perfectly soft deformation.

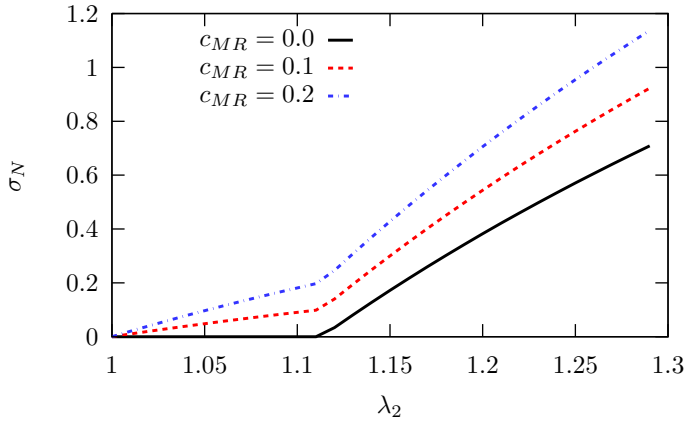

Figure 3.13: Nominal stress as a function of deformation λ_2 during the two stage deformation. The first stage is a deformation parallel to $\underline{n}_0$ of $\lambda_1 = 1.4$, followed by the perpendicular elongation λ_2.

At the start of the λ_2 deformation the elastic modulus is given by,

$$8c_{MR}\lambda_1, \tag{3.96}$$

i.e. it is entirely due to the additional Mooney-Rivlin type term, so can be used to experimentally measure this additional constant. Once the trajectory of the deformation enters the UB phase the stiffness increases to

$$8q + 8/(qk^2) - 16/k + 8c_{MR}\lambda_1. \tag{3.97}$$

Elongation at an angle to the layer normal

Elongation of the elastomer at an angle θ to the layer normal can be represented by the deformation

$$\underline{\underline{\lambda}}_\theta = \begin{pmatrix} \lambda & 0 & 0 \\ 0 & \frac{1}{\sqrt{\lambda}} & 0 \\ 0 & 0 & \frac{1}{\sqrt{\lambda}} \end{pmatrix} \cdot \begin{pmatrix} \cos\theta & 0 & -\sin\theta \\ 0 & 1 & 0 \\ \sin\theta & 0 & \cos\theta \end{pmatrix}. \tag{3.98}$$

Two trajectories for this type of deformation are shown on the phase diagram in figure 3.14 for $\theta = 0.3$ and 0.4 radians.

Elongation at an angle to the layer normal results in a rapid rotation of the layer normal away from the stretch axis. The lowest free energy of the system for larger rotation angles is in the UB phase, as illustrated by the trajectory of the deformation.

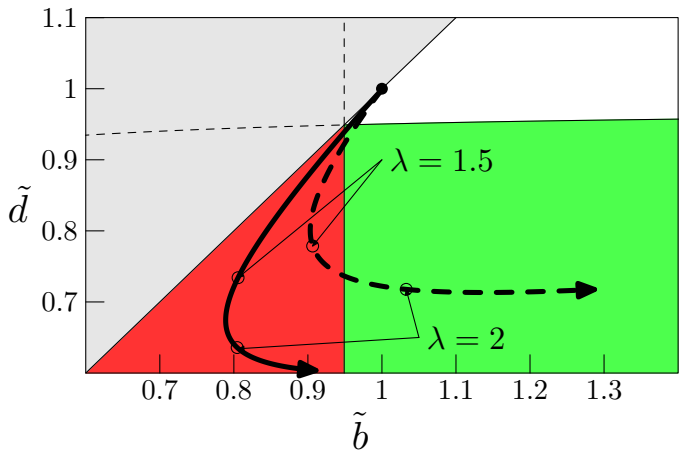

Figure 3.14: The trajectories on the phase diagram for elongations at an angle of $\theta = 0.3$ radians (solid line) and $\theta = 0.4$ radians (dashed line) to $\underline{n}_0$. The maximum deformation shown in each case corresponds to $\lambda = 2.5$.

3.7 Summary

In this chapter we introduced the concept of quasi-convexity. A function is quasi-convex if spatial variations in the deformation do not result in a more optimally minimized energy. The quasi-convex envelope of an energy can be found by minimizing it over all possible microstructures, assuming that the microstructure can form infinitely finely. An example of this process was given for the simple case of a 2D smectic-A energy, where the laminate microstructure can be calculated explicitly.

The quasi-convexified form of the Adams-Warner smectic-A energy was derived by Adams, Conti, DeSimone & Dolzmann in reference [80]. This energy is divided into three phases. In the phase where no microstructure forms the layers are unbuckled, and the material behaves like an asymmetric solid (AS). In the phase with simple laminate microstructure the layers are unidirectionally buckled (UB), and in the phase with higher order microstructure the layers are bidirectionally buckled (BB).

When stretching parallel to $\underline{n}_0$ the experimentally observed Poisson's ratios post-buckling are $(\frac{1}{2}, \frac{1}{2})$. Unfortunately the quasi-convexified energy has no energy penalty for deforming bidirectionally buckled layers in directions perpendicular to $\underline{n}_0$, so the model fails to reproduce the experimental Poisson's ratio. An additional energy term is required to model the deformation of post-buckled smectic-A layers, as well as the non-Gaussian nature of polymer chains. Hence a Mooney-Rivlin type term is included in the model. This term is added to all regions of the energy, but only significantly influences behaviour within the BB region. A Mooney-Rivlin term added to the quasi-convexified form of the Adams-Warner energy is an altogether polyconvex function, which is used as a finite element material model in chapter 5.

Chapter 4

Review of Finite Element Models of LCE

This chapter contains a short introduction to the methodology of finite element modelling, and its mathematical foundations. A one dimensional example of finite element analysis is given, and its generalisation to the three dimensional case is described. There is then a literature review of previous finite element work studying soft and semi-soft nematic elastomers. A numerical study of smectic-A elastomer is undertaken in chapter 5.

4.1 Introduction to the Finite Element Method

The finite element method is a numerical method for finding approximate solutions to system of differential equations with specified boundary conditions. The method subdivides the continuous geometries of complex objects into a discrete mesh. The method has gained widespread engineering usage, with applications to fields such as structural mechanics, heat flow, electrostatics and fluid mechanics.

The static deformation of an elastic solid can be solved using finite element analysis. Typically a set of steps are performed;

- A computer model of the solid geometry is created, then subdivided into a mesh of elements.
- Boundary conditions are specified as displacement constraints on nodes or surfaces.
- A constitutive equation for the material stress-strain behaviour is specified.
- A scheme to control the size of intermediate steps must be chosen.
- When the job is run a numerical solver finds solutions to a system of force balance equations.

The final solution corresponds to force equilibrium existing at every node (within a specified tolerance).

Mathematical Foundation of the Finite Element Method

We now give a 1D example of the finite element method in solving a second-order differential equations of the form

$$-\frac{d}{dx}\left(p(x)\frac{du(x)}{dx}\right)+r(x)u(x)=f(x), \tag{4.1}$$

where the variable x parameterises the position in one-dimensional space [92]. The domain of the problem is restricted to the region $a<x<b$. The physical interpretation of $u(x)$ is dependent on the nature of problem. In the case of heat conduction $u(x)$ represents temperature and in the case of elasticity it represents displacement. Boundary conditions are typically enforced at the ends of a finite element domain, e.g. $u(a)=A$ and $u(b)=B$. Physically such conditions might correspond to an imposed displacement or temperature.

A boundary condition of the form $u(a) = A$ is termed a Dirichlet condition. A condition on the first derivative is termed a Neumann condition, e.g. an imposed heat flow $\frac{du}{dx}|_{x=a} = A$. Commonly a mixture of these boundary conditions apply in finite element problems.

An elastic cylinder deformed axisymmetrically can be modelled as problem of 1D elasticity. If the cylinder has cross-sectional area $A(x)$ and is subject to an external axial force per unit length $f(x)$, then balance of forces gives

$$\frac{d}{dx}\left(\sigma(x)A(x)\right) = f(x). \tag{4.2}$$

The constitutive relation for a Hookean elastic material takes the form $\sigma(x) = \mathrm{E}\epsilon(x)$, where $\sigma(x)$ is stress, $\epsilon(x)$ is strain and E is the modulus. The strain can be written as the gradient of displacement $\epsilon = \frac{du}{dx}$, which yields a second order equation

$$\mathrm{E}\frac{d}{dx}\left(\frac{du(x)}{dx}A(x)\right) = f(x). \tag{4.3}$$

The domain is then divided up into a finite number of elements, see figure 4.1. Only displacements at the nodes are recorded, and interpolation is used to approximate displacements of points between nodes. A 1D element with two nodes per element uses linear interpolation, and a quadratic interpolation scheme would require three nodes per element.

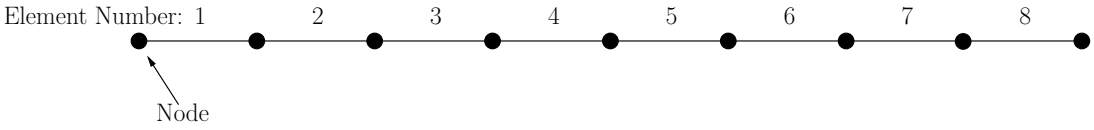

Figure 4.1: A finite element domain sub-divided into 8 linear elements with 9 nodes.

On each element a piecewise polynomial function is defined to approximate the true displacement solution, as shown in figure 4.2. Each piecewise region starts and ends at a node.

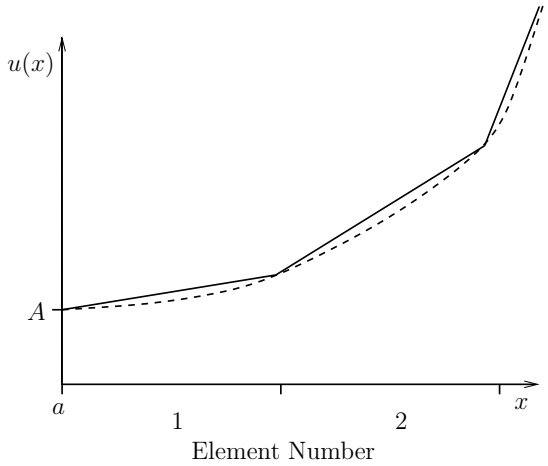

Figure 4.2: Linear basis functions are shown approximating the true solution (dotted-line). Basis functions must always satisfy the boundary conditions.

Two ways to construct approximate solutions exist (i) the *Rayleigh-Ritz method* and (ii) the *Galerkin method*. In most cases the approximate solutions found using these methods can be made arbitrarily close to the true solution, by making the finite element mesh increasingly fine.

It is possible to find the true displacement solution, $u(x)$, by starting with a trial function $u^{trial}(x)$ that it defined such that it always satisfies the boundary conditions. Then the fitness of the trial function is improved by tuning its free parameters. The Rayleigh-Ritz method requires that second

order differential equation can be restated in the following quadratic variational form

$$\mathcal{J}(u^{trial}(x)) = \int_a^b \frac{1}{2}\left(p(x)\left(\frac{du^{trial}(x)}{dx}\right)^2 + r(x)u^{trial}(x)^2\right) - f(x)u^{trial}(x)\,dx. \tag{4.4}$$

The Rayleigh-Ritz principle states that the true solution $u(x)$ is the function that successfully minimizes the functional $\mathcal{J}(\,\cdot\,)$. The Rayleigh-Ritz method is to obtain an approximation to the true solution by finding the trial function that minimizes the functional $\mathcal{J}(u^{trial}(x))$.

If the second order differential equation includes a first order term, i.e. $\frac{du}{dx}$, then it may not be possible rewrite it in the required variational form. For this reason the Galerkin method has a broader applicability than the Rayleigh-Ritz method.

The Galerkin principle states that the true solution $u(x)$ satisfies the weak formulation of the problem, i.e.

$$\int_a^b p(x)\frac{du(x)}{dx}\frac{dv(x)}{dx} + r(x)u(x)v(x)\,dx = \int_a^b f(x)v(x)\,dx \quad \forall v(x) \text{ satisfying the BCs } v(a) = 0 \;\&\; v(b) = 0 \tag{4.5}$$

where the function $v(x)$ is any function that is continuous over the domain $a < x < b$ and satisfies $v(a) = 0$ and $v(b) = 0$. The functions $v(x)$ and $u(x)$ are both required to have well-defined first derivatives. The Galerkin method to obtain an approximation to the true solution is to replace $u(x)$ in equation (4.5) with a discretised function $u^G(x)$. The discrete function $u^G(x)$ is a weighted sum of the Galerkin basis functions ψ_i,

$$u^G(x) = \psi_0 + \sum_{j=1}^{n-1} u_j\psi_j, \tag{4.6}$$

and the correct choice of the u_j will successfully approximate the true solution. The lowest Galerkin basis function ψ_0 is a linear interpolation between the boundary conditions $u(a) = A$ and $u(b) = B$. The higher ψ_j are commonly chosen to be linear splines defined piecewise over the elements, as shown in figure 4.3. For a domain subdivided into n elements there are $(n-1)$ linear splines functions.

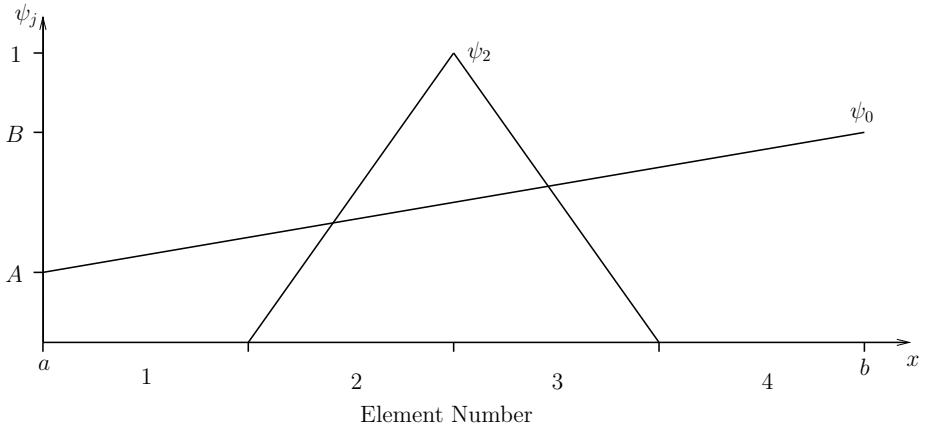

Figure 4.3: The lowest Galerkin basis function ψ_0 interpolates between the boundary conditions. The basis function ψ_2 is only non-zero on elements 2 and 3.

The Galerkin principle of equation (4.5) can be written more succinctly as,

$$\mathcal{A}(u(x), v(x)) = \langle f(x), v(x)\rangle \quad \forall v(x) \text{ satisfying BCs}, \tag{4.7}$$

where $\mathcal{A}(\,\cdot\,,\,\cdot\,)$ is a functional form and $\langle f(x), v(x)\rangle$ denotes the inner product of $f(x)$ and $v(x)$ over the domain $a < x < b$.

Any choice of the function $v(x)$ can be made provided the boundary conditions are satisfied, i.e. $v(a) = 0$ and $v(b) = 0$. Thus the arbitrary function $v(x)$ can be approximated by a weighted sum of the higher Galerkin basis functions

$$v(x) \approx \sum_{i=1}^{n-1} \beta_i \psi_i. \tag{4.8}$$

Thus following the Galerkin method and discretising equation (4.7) gives,

$$\mathcal{A}(u^G(x), \sum_{i=1}^{n-1} \beta_i \psi_i) = \langle f(x), \sum_{i=1}^{n-1} \beta_i \psi_i \rangle \ , \tag{4.9}$$

which as the β_i are arbitrary is equivalent to the following set of $(n-1)$ equations

$$\mathcal{A}(u^G(x), \psi_i) = \langle f(x), \psi_i \rangle \ \text{ for } 1 < i < n-1. \tag{4.10}$$

Writing out the discrete function $u^G(x)$ in terms of its expansion yields

$$\mathcal{A}(\psi_0 + \sum_{j=1}^{n-1} u_j \psi_j, \psi_i) = \langle f(x), \psi_i \rangle \ \text{ for } 1 < i < n-1. \tag{4.11}$$

Using the property that $\mathcal{A}(\,\cdot\,,\,\cdot\,)$ is a bilinear function gives

$$\sum_{j=1}^{n-1} \mathcal{A}(\psi_j, \psi_i) u_j = \langle f(x), \psi_i \rangle - \mathcal{A}(\psi_0, \psi_i) \ \text{ for } 1 < i < n-1, \tag{4.12}$$

or equivalently in matrix form

$$\sum_{j=1}^{n-1} -K_{ij} u_j = f_i \ \text{ for } 1 < i < n-1, \tag{4.13}$$

where $K_{ij} = -\mathcal{A}(\psi_j, \psi_i)$ and $f_i = \langle f(x), \psi_i \rangle - \mathcal{A}(\psi_0, \psi_i)$. The components of the matrix K_{ij} and the vector f_i can be computed by evaluating the integrals using numerical integration. The system of equations can then be solved using matrix methods to yield the coefficients u_j, which describe the approximate solution.

Generalisation to Three Dimensions

In three dimensional problems the solution to a set of differential equations is sought over a volume domain Ω, and the boundary conditions are specified on the surface of the volume $\partial\Omega$. Provided the differential equations are linear the system of equations can be represented as,

$$\mathcal{L}u(x, y, z) + b = 0 \text{ on } \Omega, \tag{4.14}$$

$$\mathcal{M}u(x, y, z) + t = 0 \text{ on } \partial\Omega, \tag{4.15}$$

where $u(x, y, z)$ is a scalar or vector representing the function sought, e.g. temperature or displacement [93].

The next step of finite element analysis is to subdivide the three dimensional volume domain into a mesh of elements. The most commonly used elements in three dimensions are tetrahedral or brick shaped, see figure 4.4. Elements using linear interpolation only have nodes situated at their corners, whereas a higher order element has additional nodes located along its edges.

Once a mesh is defined then the function $u(x, y, z)$ can be approximated by an expansion in terms of the corresponding basis functions, i.e.

$$u(x, y, z) \approx \psi_0 + \sum_{j=1}^{n-1} u_j \psi_j. \tag{4.16}$$

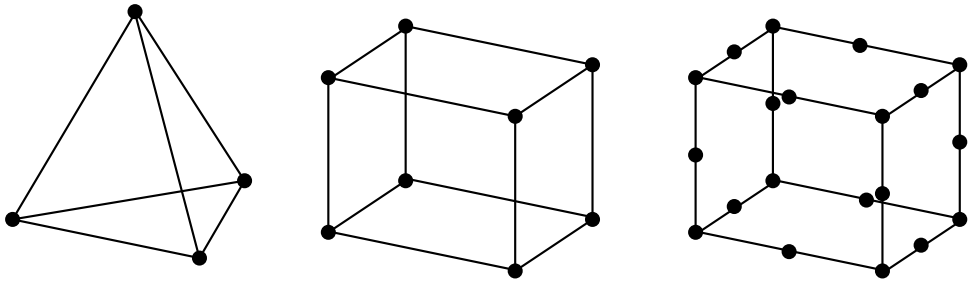

Figure 4.4: (left) A 4-node linear tetrahedral element. (middle) An 8-node linear brick element. (right) A 20-node quadratic brick element.

Following the Galerkin method then yields a system of equations which have the same form as the one dimensional case, i.e.

$$K_{ij}u_j + f_i = 0, \tag{4.17}$$

In order to obtain the coefficients of the matrix K_{ij} it is necessary to use numerical integration to compute an integral over the volume of each element. Typically the Gaussian quadrature method is used, which approximates an integral of a function as a weighted sum of the function values at n points in the integral domain. If the function being integrated is a polynomial of order $2n - 1$ then the method computes the integral exactly [94]. The material response is calculated at the integration points of the Gaussian quadrature method; the displacements and stresses are then extrapolated from the integration points out to the element nodes.

Elements can be formulated to either use full-integration or reduced-integration. A fully-integrated element has enough integration points to compute its integrals exactly, provided that the element is in a regular configuration, which for a linear brick element means the sides must be parallel and meet at 90°. For a linear element to be fully-integrated two integration points are required for each dimension of the element, so a three dimensional brick element has eight integration points, see figure 4.5. A reduced-integration element typically only has one integration point, which has the advantage that it reduces the number of equations to be solved and therefore speeds up computation. However this speed-up comes at the cost of the reduced accuracy of the achieved solution. Reduced-integration linear elements can suffer from the anomalous deformation mode known as hourglassing, where rectangular elements deform into an hourglass shape at zero energy cost [95]. This deformation is non-physical, and should be prevented by adding artificial stiffness.

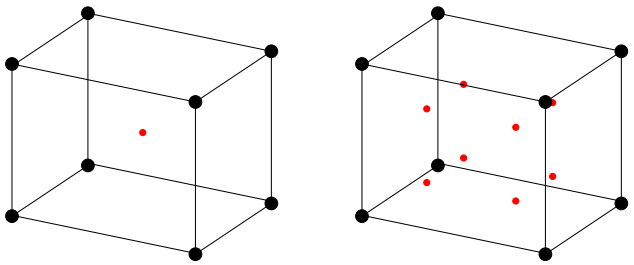

Figure 4.5: (left) A reduced-integration 8-node linear brick element has a single central integration point (marked in red). (right) A fully-integrated 8-node linear brick element has eight integration points located throughout its volume.

Different element types have different strengths and weaknesses; the choice of element should reflect the nature of the problem at hand. Incompressible and near-incompressible materials tend to cause problems with elements based solely on the standard displacement description of elasticity [93]. Fully incompressible materials require an element with a hybrid formulation, where an additional hydrostatic pressure term is introduced to enforce incompressibility. Nearly incompressible materials can be modelled by reduced-integration elements without using a hybrid formulation.

Quadratic elements are superior to linear elements at describing stress concentrations, provided that severe distortions do not occur [96]. They are also better suited to modelling complex geometries, such as curved surfaces, and bending deformations. A fully-integrated linear brick element can not accurately represent a bending deformation, which causes an excessive stiffness in bending termed shear-locking. However quadratic elements can suffer from an excessive stiffness termed mesh locking when deformed incompressibly, which linear elements are immune from.

Accurate results can only be achieved if the finite element domain is meshed sufficiently finely. To demonstrate that results are accurate the simulation should be repeated using finer and finer meshes, until the results are seen to converge. Finer meshes increase the computation time, but overly coarse meshes will produce inaccurate results. The choice of element type affects the rate of mesh convergence, for example linear tetrahedral elements converge slowly towards the true solution and are therefore best avoided.

Finite element analysis can be performed either statically or dynamically. In static analysis the path between the initial and final state of the system is parameterised by dividing it into many increments. For example in a solid mechanics problem the applied deformation is increased at each increment, until at the final increment the full deformation is achieved. At the beginning of each increment the stiffness matrix, K_{ij}, from equation (4.17) is computed. The solution is then found by applying Newton's method (or a similar procedure) to solve the matrix equations to within a specified tolerance. The solution from one increment is used as the initial estimate of the solution at the next increment. If the estimate lies within the radius of convergence to the solution then Newton's method will successfully find the solution. Decreasing the increment size tends to improve convergence, however in problems with material or geometric instabilities convergence is not guaranteed.

In dynamic analysis the progress of the solution is parameterised by a time variable. The deformation is computed by advancing from one time increment to the next using the laws of motion. The equilibrium configuration at each time increment is not sought and the stiffness matrix is never computed. In the limit of sufficiently slow kinematics the dynamic solution will correspond to the static case. Dynamic analysis is commonly used to compute wave solutions and in situations where a static analysis does not converge.

The finite element method has been used to model the deformation of LCE in realistic stretching geometries; predicting the spatial distribution of microstructure as well as stress-strain curves. The next section is a review of the literature of LCE modelling using the finite element method.

4.2 Finite Element Models of Nematic LCE

The elastic energetic cost of deforming a nematic elastomer was proposed by Bladon, Terentjev and Warner [52] to take the form;

$$F_{nematic} = \frac{1}{2}\mu \mathrm{Tr}\left[\underline{\underline{\lambda}} \cdot \underline{\underline{\ell}}_0 \cdot \underline{\underline{\lambda}}^T \cdot \underline{\underline{\ell}}^{-1}\right]. \tag{4.18}$$

This energy permits perfectly soft deformations via rotations of the director. Also the energy is not convex, which motivates the formation of microstructure as a means of lowering the energy. This is consistent with the experimental observation of an induced stripe microstructure in nematic elastomers, as shown in figure 4.6(a).

In the stripe pattern the director is rotated oppositely in neighbouring stripes. The rotation is caused by the simple shear present in each stripe, which is either positive or negative and alternates between stripes. Stripe formation can occur locally even when the stretching geometry prohibits the global shearing of the sample. In reality striped deformations are not perfectly soft, and to account for this theoretical models may include a semi-softness term, which penalizes director rotation.

When a nematic elastomer is stretched perpendicular to its initial director a striped texture forms in the bulk of the sample, see the middle frame of figure 4.7. In the immediate vicinity of the clamps the shears necessary to form a stripe are restricted by the clamping conditions. This causes a thin

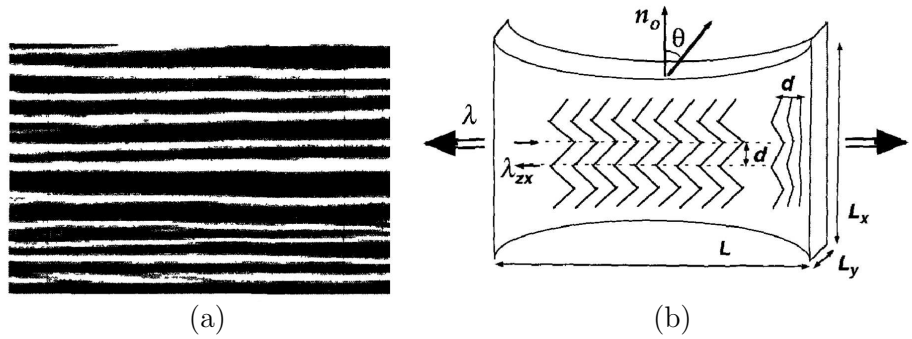

(a) (b)

Figure 4.6: (a) Stripe domain texture observed using polarizing microscopy by Kundler and Finkelmann [54]. The characteristic width of domains is $\sim 15\mu$m. (b) Geometry of stretching.

region without microstructure to occur near the clamped edges, as illustrated in figure 4.6(b). The width of these regions is of order the characteristic microstructure size, so they are difficult to observe without magnification.

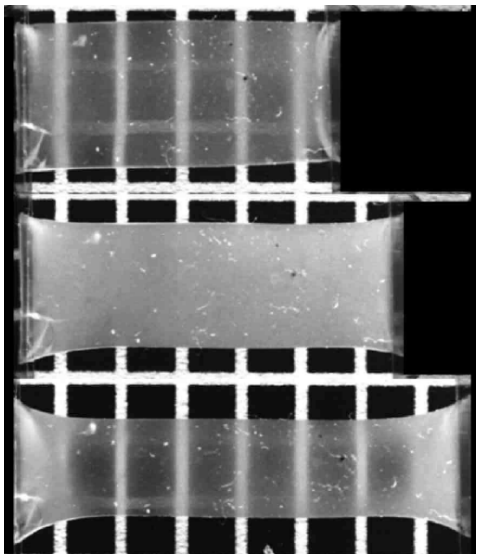

Figure 4.7: The spatial distribution of microstructure in a monodomain nematic elastomer, stretched perpendicular to the initial director, as seen by direct observation. (top) The undeformed state, $\lambda = 1$. (middle) A strain of $\lambda \approx 1.2$ exceeds the strain threshold to director rotation. (bottom) A strain of $\lambda \approx 1.4$ exceeds the strain required to fully rotate the director [60].

At large strains the stripe texture disappears from the bulk of the sample, as seen in the bottom frame of figure 4.7. The stripe texture clears once the directors in the stripes become fully aligned with the stretch axis. However a complicated pattern of microstructure still persists near the clamped edges. The shape of the deformed sample near the clamps is intrinsically related to the distribution of microstructure in this region. An experimental study by Zubarev *et al.* demonstrates that the spatial distributions of microstructure is dependent on the length to width aspect ratio of the sample [78]. The higher the aspect ratio the less impact the clamping conditions have on the bulk of the sample. This means that with all other parameters equal a higher aspect ratio sample will be slighter softer than a low aspect ratio sample.

In the literature quasi-convexified nematic energies have been used to construct finite element material models of soft and semi-soft nematic elastomers. These models allow the spatial distribution

of microstructure to be studied in realistic stretching geometries, i.e. with clamped edges. The models are static models, as they contain no dynamic terms. Models based on quasi-convex energies are coarse-grained, as they do not resolve the fine scale of the microstructure. For a simulation to resolve the microstructure the energy model would require a term that penalizes spatial gradients in the director, and the finite element mesh would need to be at an extremely fine scale.

Soft Nematic Quasi-Convex Energy

The nematic free energy can be rewritten with the isotropic state as the reference configuration rather than the nematic phase,

$$W(\underline{\underline{F}}) = \begin{cases} \lambda_1^2 + \lambda_2^2 + a\lambda_3^2 - 3a^{1/3} & \text{if } \det\underline{\underline{F}} = 1 \\ +\infty & \text{else} \end{cases} \tag{4.19}$$

where $\lambda_1(\underline{\underline{F}}) \leq \lambda_2(\underline{\underline{F}}) \leq \lambda_3(\underline{\underline{F}})$ are the ordered singular values of deformation gradient, $\underline{\underline{F}}$, and the multiplicative factor of μ has been neglected. The parameter a characterises the extent of the uniaxial deformation that occurs on transition from the isotropic to the nematic state, this deformation has the same form as equation (3.46) with $\lambda_0 = a^{1/6}$, and in terms of the polymer anisotropy $\lambda_0 = r^{-1/6}$.

The quasi-convex envelope of the nematic energy was derived by DeSimone and Dolzmann (2002) [97] to be,

$$W_{qc}(\underline{\underline{F}}) = \begin{cases} 0 & \text{if } \lambda_1 > a^{1/6} \\ W(\underline{\underline{F}}) & \text{if } a^{1/2}\lambda_3^2\lambda_1 > 1 \\ \lambda_1^2 + 2a^{1/2}\lambda_1^{-1} - 3a^{1/3} & \text{else} \end{cases} \tag{4.20}$$

where the deformation gradient is volume conserving, i.e. $\det\underline{\underline{F}} = 1$.

Conti, DeSimone, Dolzmann (2002) used W_{qc} plus a neo-Hookean perturbation as the finite element material model [68]. The perturbation term is necessary because multiple possible deformation states exist when $W_{qc} = 0$. A small perturbation term splits the degeneracy, and was shown quantitatively to not change the results. Because the perturbation term is small it is not necessary to consider its effects on the quasi-convex envelope. The model allows the study of loading experiments in realistic geometries, i.e. with clamped boundaries. Numerical simulations were performed on a quarter-sample using a non-uniform 2D mesh of 800 elements and a reverse loading path.

The quasi-convexified energy predicts three phases (i) liquid-like microstructure (ii) smectic-like microstructure (iii) no microstructure. Liquid-like microstructure deforms perfectly softly, i.e. at no energy cost. Smectic-like microstructure is soft when sheared in-plane but solid when stretched in-plane. The phase with no microstructure is not soft, i.e. it is a rubbery solid.

The predicted distribution of microstructure when stretching perpendicular to the initial director is shown in figure 4.8. At a stretch of 1.46 the bulk of the sample forms no microstructure, as the director has fully re-oriented to become parallel to the stretch axis. In the central region of the clamps a small region of microstructure exists, which is smectic-like and therefore transmits stress. This microstructure exists at the clamp because no contraction in the width direction is possible, so the deformation is largest in the thickness direction, which can be accommodated by a smectic microstructure.

Semisoft Nematic Quasi-Convex Energy

The model of Verwey, Terentjev and Warner [55] introduces an additional semisoftness term to describe non-ideal nematic elastomers,

$$F_{VTW} = \underbrace{\frac{1}{2}\mu \mathrm{Tr}[\underline{\underline{\lambda}} \cdot \underline{\underline{\ell}}_0 \cdot \underline{\underline{\lambda}}^T \cdot \underline{\underline{\ell}}^{-1}]}_{F_{nematic}} + \underbrace{\frac{1}{2}\mu_{ss} \mathrm{Tr}[\underline{\underline{\lambda}} \cdot (\underline{\underline{\delta}} - \underline{n}_0 \underline{n}_0^T) \cdot \underline{\underline{\lambda}}^T \cdot \underline{n}\,\underline{n}^T]}_{F_{semisoft}}. \tag{4.21}$$

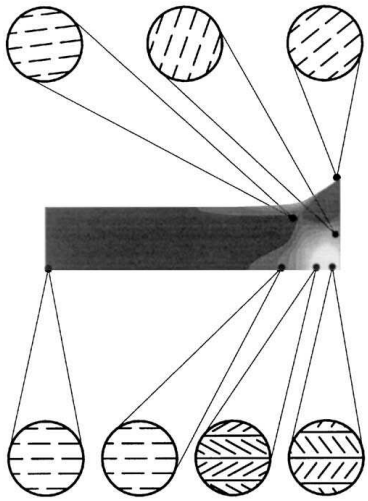

Figure 4.8: Spatial microstructure distribution at a stretch of 1.46 perpendicular to the initial director. Darkly shaded regions correspond to the absence of microstructure, whereas lightly shaded regions correspond to liquid or smectic-like microstructure. The enlarged pictures show possible constructions of the microstructure, with director orientations shown by short lines.

Conti *et al.* (2002) transformed equation (4.21) using an affine change of coordinates, so that the reference configuration is the isotropic state giving,

$$F_{VTW} = |\underline{\underline{F}}|^2 - \alpha|\underline{\underline{F}}^T\underline{n}|^2 - \beta|\underline{\underline{F}}\underline{n}_0|^2, \tag{4.22}$$

where $\underline{\underline{F}}$ is the deformation gradient measured in the isotropic reference state. The term α, where $0 < \alpha < 1$, describes the coupling between the nematic ordering and strain. The term β is the degree of semisoftness in the elastomer; the case $\beta = 0$ is a soft elastomer.

Conti *et al.* then derived the thin film limit version of equation (4.22) to be,

$$F_{VTW} = |\underline{\underline{F}}|^2 + \frac{1}{\det^2\underline{\underline{F}}} - \alpha|\underline{\underline{F}}^T\underline{n}|^2 - \beta|\underline{\underline{F}}\underline{n}_0|^2. \tag{4.23}$$

Minimizing equation (4.23) over $\underline{n}$ gives,

$$F_{VTW} = \lambda_1^2 + (1-\alpha)\lambda_2^2 + \frac{1}{\lambda_1^2\lambda_2^2} - \beta|\underline{\underline{F}}\underline{n}_0|^2, \tag{4.24}$$

where λ_1 and λ_2 are the ordered singular values of $\underline{\underline{F}}$ ($\lambda_1 \leq \lambda_2$).

The quasi-convexified form of (4.24) was shown to be,

$$W_{qc} = \beta|\underline{\underline{F}}\underline{n}_0^{\perp}|^2 + \frac{1}{\det^2\underline{\underline{F}}} + \begin{cases} (1-\beta)\left(\det^2\underline{\underline{F}}/\lambda_2^2(\underline{\underline{F}}) + a\lambda_2^2(\underline{\underline{F}})\right) & \text{if } \det\underline{\underline{F}} \leq a^{1/2}\lambda_2^2(\underline{\underline{F}}) \quad \text{Hard} \\ 2a^{1/2}(1-\beta)\det\underline{\underline{F}} & \text{if } \det\underline{\underline{F}} \geq a^{1/2}\lambda_2^2(\underline{\underline{F}}) \quad \text{Soft,} \end{cases} \tag{4.25}$$

where the parameter $a = 1 - \frac{\alpha}{1-\beta}$ and $\underline{n}_0^{\perp}$ is a unit vector perpendicular to $\underline{n}_0$.

The energy of equation (4.25), with $\det\underline{\underline{F}} = 1$ enforced, was used as the constitutive equation in a finite element model of semisoft nematic elastomer sheets. Numerical simulations were performed on a triangular 2D mesh. Stretching was performed perpendicular to the initial director with rigid clamping conditions. The force curves stretching perpendicular to $\underline{n}_0$ are initially stiff, as shown in figure 4.9.

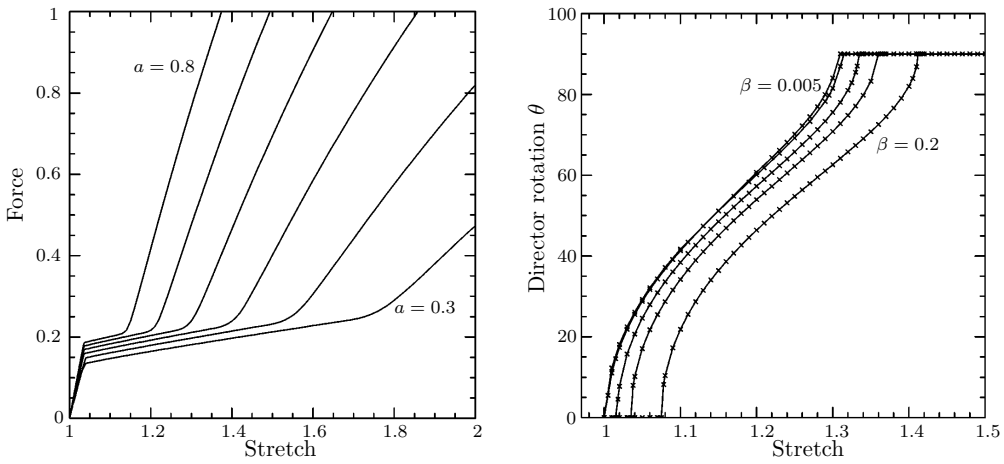

Figure 4.9: (left) Force verus strain, stretching perpendicular to the initial director for parameters $\beta = 0.1$, $r = 3$ and $a = 0.8, 0.7, 0.6, 0.5, 0.4, 0.3$. (right) Director rotation at the centre of the sample versus stretch, for $\beta = 0.005, 0.01, 0.05, 0.1, 0.2$ and $a = 0.5$ [69].

A threshold strain of a few percent is required to reach the semisoft plateau. The plateau corresponds to the rotation of the director, see figure 4.9. The length of the semi-soft plateau decreases with increasing a. At large strains the director becomes fully aligned with the stretch axis, and the deformation becomes stiffer.

Dynamic model of Nematic Elastomers

Mbanga *et al.* (2010) studied the formation of stripes using a dynamic finite element model [98]. A sample of dimensions $1.5\,\text{mm} \times 0.5\,\text{mm} \times 50\,\mu\text{m}$ was uniformly meshed with 78000 tetrahedral elements, with each element possessing a director orientation, $\underline{n}$. All the directors are initially oriented in the $\underline{n}_0$ direction, which is perpendicular to the stretch axis.

The material model consists of the energy of isotropic elastic solid, a kinetic energy term and nematic terms. The nematic ordering is described by the $\underline{\underline{Q}}$-tensor, $\underline{\underline{Q}}_{ij} = \frac{1}{2}S(3\underline{n}_i\underline{n}_j - \underline{\underline{\delta}}_{ij})$, where the order parameter S is taken as 1. The strain is written in terms of the Green-Lagrange tensor, $\underline{\underline{\epsilon}}_{ij} = \frac{1}{2}\left(\underline{\underline{u}}_{ij}\underline{\underline{u}}_{ji} + \underline{\underline{u}}_{ki}\underline{\underline{u}}_{kj}\right)$. The total nematic energy of an elastomer, divided into p elements of volume V_p, takes the form

$$W_{nematic} = \underbrace{\sum_p V_p \frac{1}{2}\underline{\underline{C}}_{ijkl}\underline{\underline{\epsilon}}_{ij}\underline{\underline{\epsilon}}_{kl}}_{\text{isotropic solid}} + \underbrace{\sum_p V_p \frac{1}{2}\underline{\rho}_i\underline{v}_i{}^2}_{\text{kinetic energy}} + \underbrace{\sum_p V_p\left(-\alpha\underline{\underline{\epsilon}}_{ij}(\underline{\underline{Q}}^p_{ij} - \underline{\underline{Q}}^0_{ij})\right)}_{\text{coupling strain to nematic order}} + \underbrace{\sum_p V_p\beta(\underline{\underline{Q}}^p_{ij} - \underline{\underline{Q}}^0_{ij})^2}_{\text{preference for initial ordering}} + \underbrace{\sum_{<p,q>}\gamma(\underline{\underline{Q}}^p_{ij} - \underline{\underline{Q}}^q_{ij})^2}_{\text{penalize }\Delta\underline{\underline{Q}}\text{ between nearest neighbours}}. \tag{4.26}$$

The nematic ordering and strain are coupled by the α parameter. The β parameter penalizes deviations in $\underline{\underline{Q}}_{ij}$ from its state during cross-linking. Gradients in $\underline{\underline{Q}}_{ij}$ are penalized by the γ parameter. Parameter values were chosen as $\mu = 5.7 \times 10^5\,\text{Pa}$, bulk modulus $B_r = 2.8 \times 10^7\,\text{Pa}$, $\alpha = \mu$, $\beta = 0.3\mu$, and $\gamma = 10^7\,\text{J}$.

This model is dynamic, as it includes a kinetic energy term dependent on the material velocity. An internal damping force was included in the model, which acts along the line between two nodes and is proportional to their strain rate.

The spatial distribution of microstructure is shown in figure 4.10. At a strain of 10% the microstructure can be seen to form on a length-scale much larger than is experimentally observed. At 50% strain the bulk of the sample is free from microstructure, as the director has rotated parallel to the stretch axis. The director partially rotates in regions near the clamps. These results are qualitatively similar to the semi-soft simulations of Conti *et al.* (2002).

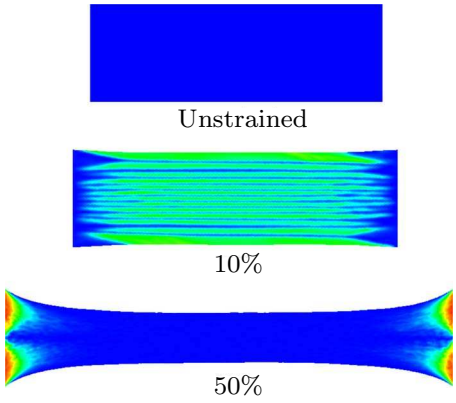

Figure 4.10: Director orientations stretching perpendicular to $\underline{n}_0$ at strains of $0\%, 10\%$ and 50%. Regions with a director oriented at $0°$ or $90°$ to $\underline{n}_0$ are shown dark blue. Regions with a director oriented at $\pm 45°$ to $\underline{n}_0$ are shaded red.

Chapter 5

Finite Element Modelling of Monodomain Smectic-A LCE

In this chapter the deformation of monodomain smectic-A elastomer is investigated for the case of a rectangular sheet stretched between two clamps, with the initial layer normal oriented in the plane of the sheet. The finite element model makes predictions about the spatial distribution of microstructure and stress-strain behaviour, which can be related to the experimental literature. The angle of the stretch axis relative to the initial layer normal is varied between 0° and 90°, and the predicted microstructure patterns are highly amenable to future experimental verification. It is also interesting to simulate samples with different length to width aspect ratios, and to examine the combined influence of aspect ratio and stretching angle.

5.1 Background

In smectic-A liquid crystals the layers are unstable to a buckling instability when strained parallel to the layer normal [11]. Models of layered materials, containing free energy penalties for layer curvature and layer dilation, exhibit layer buckling [99]. The models predict that at the buckling threshold strain the layer modulation in a single direction is degenerate with bidirectional modulation. At larger strain this degeneracy is removed and bidirectional modulation of the layers, as illustrated in figure 5.1, is lower in energy.

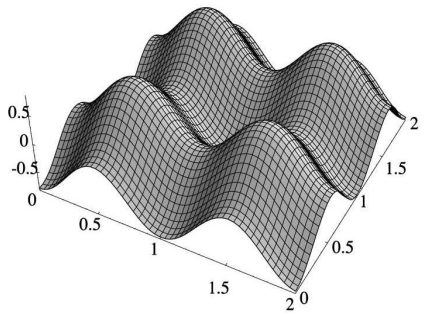

Figure 5.1: The vertical displacements of an initially flat layer are sinusoidal for a strain just above the buckling threshold in smectic-A liquid crystal [99]. The bidirectional buckling favours the formation of square periodic cells; only four cells are depicted here. Increasing the strain causes the cell size to grow and the buckling pattern becomes increasingly zigzag shaped.

This theory of bidirectional buckling is consistent with experiments on liquid smectics, where two directions of buckling are observed in X-ray scattering patterns [100]. The smectic layer modulus in liquid crystals is typically $\sim 10^7$ Pa. Layer buckling is relaxed away in liquid smectics by the

propagation of dislocations into the layers that relieve the strain. In the smectic-A elastomer samples investigated by Nishikawa *et al.* the buckling of layers is not relaxed away by the propagation of defects. However samples with highly defective layer structures behave differently to the largely defect-free samples of Nishikawa *et al.* [25].

Nishikawa *et al.* reported that on stretching perpendicular to the layer normal the sample remains transparent, and has Poisson's ratios of $(0, 1)$ [21]. This indicates that the the deformation is accommodated within the layers. The modulus is of order $\mu \sim 10^5\,\mathrm{Pa}$ for this deformation. On stretching parallel to the layer normal the sample is initially much stiffer, having the modulus B, and Poisson's ratios of $(\frac{1}{2}, \frac{1}{2})$. The elastic modulus drops sharply to $\sim \mu$ above a threshold strain of a few percent, where the elastomer becomes cloudy [19]. The X-ray scattering pattern indicates that the layers are buckled, and the reduction in X-ray intensity shows that the modulation is in more than one direction as layers tilt out of the X-ray scattering plane.

It should be possible to distinguish unidirectional buckling from bidirectional buckling by viewing the sample between a crossed polariser-analyser pair. The optical axis in smectic-A elastomer is parallel to the director, so the simple laminates associated with unidirectional layer buckling will appear as light and dark striped domains, much like nematic elastomer stripes. In bidirectional buckling the director varies rapidly in both buckling directions, so will always be bright when viewed between the polariser-analyser. Unbuckled regions will appear dark when the polariser (or analyser) is parallel to the optical axis, and have maximum brightness when the polariser is at 45° to the optical axis. It is anticipated that both types of buckling will appear opaque to the naked eye, similar to striped domains in nematic elastomers (see Refs. [56, 78], and Fig. 8.10 of [60]).

The finite element material model used in this work is based on a coarse grained smectic-A free energy, so does not resolve the microstructure. To accurately model the microscopic length scale on which buckling occurs requires the inclusion of spatial gradient terms, for example those arising from Frank elastic energy. This approach would be highly computationally expensive and is not pursued here. Instead the coarse grained free energy model is used to model realistic geometries of tensile loading that have been studied experimentally.

5.2 Finite Element Material Model

The total free energy $\widetilde{W}_{tot}$, introduced in equation (3.53) of chapter 3, is

$$\widetilde{W}_{tot}(\underline{\underline{\lambda}}) = \begin{cases} \lambda_0^{-4}|\underline{\underline{\lambda}}\cdot\underline{n}_0|^2 + f(\lambda_0^2\tilde{b}, \lambda_0^2\tilde{d}) + \widetilde{W}_{MR} & \det\underline{\underline{\lambda}} = 1 \\ \\ \infty & \text{else} \end{cases} \tag{5.1}$$

$$\text{where } f(\lambda_0^2\tilde{b}, \lambda_0^2\tilde{d}) = \begin{cases} b + \dfrac{d^2}{b} + k(d-q)^2 & d \geq \dfrac{kqb}{kb+1} & \text{AS} \\ \\ b + \dfrac{kq^2}{kb+1} & \begin{array}{c} b \geq q - \dfrac{1}{k} \\ \text{and} \\ d \leq \dfrac{kqb}{kb+1} \end{array} & \text{UB} \\ \\ 2q - \dfrac{1}{k} & b \leq q - \dfrac{1}{k} & \text{BB} \end{cases} \tag{5.2}$$

It is useful to express $\widetilde{W}_{tot}$ in terms of the invariants of the Cauchy-Green tensor, $\underline{\underline{C}} = \underline{\underline{\lambda}}^T \cdot \underline{\underline{\lambda}}$. The term $\lambda_0^{-4}|\underline{\underline{\lambda}}\cdot\underline{n}_0|^2$ is simply $\lambda_0^{-4}A_4$. The parameters $\tilde{b}$ and $\tilde{d}$ are,

$$\tilde{b} = \frac{A_1 - A_4 + \sqrt{(A_1+A_4)^2 - 4(A_2+A_5)}}{2}, \tag{5.3}$$

$$\tilde{d} = \sqrt{A_2 + A_5 - A_1A_4}, \tag{5.4}$$

and the Mooney-Rivlin term is,

$$\widetilde{W}_{MR}(\underline{\underline{\lambda}}) = c_{MR} A_2. \tag{5.5}$$

Some care must be taken in treating these expressions numerically. Firstly in equation (5.3) the two terms $(A_1 + A_4)^2$ and $4(A_2 + A_5)$ are typically close together. This subtractive cancellation can lead to large numerical errors. Secondly the derivatives of the free energy are required to compute the stresses in the material. Differentiating the square root expression in equation (5.3) gives an expression that diverges when $(A_1 + A_4)^2 = 4(A_2 + A_5)$. It is useful to smooth the divergence in this expression by adding a small value $\epsilon \sim 10^{-5}$ to the contents of the square root.

The material energy, $\widetilde{W}_{\text{tot}}(\underline{\underline{\lambda}})$, was implemented in the commercial finite element code `Abaqus 6.10` [96] by writing a `UANISOHYPER_INV` subroutine for the standard implicit integration scheme. The numerical method in this routine is based on previous work implementing invariant based elasticity [101, 102]. Incompressibility is enforced within this code by specifying `type=incompressible` in the material definition in the input file. The anisotropy parameter `local directions=1` is specified, with the local direction defined as $\underline{n}_0$. The Fortran code for the material routine is included in Appendix C, along with an example input file.

Rigid clamping boundary conditions were used on the end faces of the elastomer. In `Abaqus` these constraints are implemented as pinned displacement boundary conditions, e.g. `U1=0.64,U2=0` and `U3=0` at the mobile clamp. Experimentally an alternative to rigid clamping is to secure the ends of the elastomer with tape, which allows a contraction in thickness of the elastomer at the clamp. Simulations using tape-like boundary conditions produce very similar stress-strain curves to rigid clamping with a slight difference in microstructure near the clamps.

The elastomer was deformed by moving one of the clamps to achieve a total deformation of $\lambda = 1.4$, with the step size increment constant at 5×10^{-3}.

Model Parameters

The material parameters are chosen to be similar to values found by Nishikawa *et al.* [19, 21]. The parameters listed in Table 5.1 describe the smectic layer modulus B, the rubber shear modulus μ, and a polymer anisotropy r appropriate for a prolate side chain LCP. Equations (3.13),(3.14) and (3.47) can then be used to find q, k and λ_0.

Parameter (symbol)	Value
B	$3.6 \times 10^6\,\text{Pa}$
μ	$10^5\,\text{Pa}$
r	1.95
K	$10^{-11}\,\text{N}$
λ_0	0.895
k	48.43
q	0.780
c_{MR}	0.14

Table 5.1: Smectic-A Model Parameters

Equation (3.90) gives the threshold strain to bidirectional buckling for a stretch parallel to $\underline{n}_0$ as $\lambda_{\text{th}} = \lambda_0^2(q - 1/k)^{-1}$, for these values $\lambda_{\text{th}} = 1.053$.

Following the work of Nishikawa *et al.* [19] the sample will initially be taken as a rectangular cuboid of dimensions $1.6\,\text{cm} \times 1.0\,\text{cm} \times 500\,\mu\text{m}$. The value of the layer buckling term, c_{MR}, can then be estimated by examining the effect of c_{MR} when stretching parallel to $\underline{n}_0$. The width of the middle of the sample W was measured as a function of deformation. Figure 5.2 shows that if $c_{MR} = 0$ then the incremental Poisson's ratios are $(1, 0)$ above the threshold, which is inconsistent

with experimental findings [19]. Whereas a value of $c_{MR} = 0.14$ successfully approximates the deformed state shown in figure 1.11.

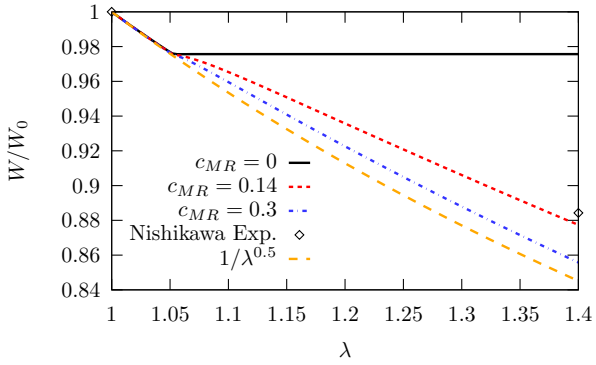

Figure 5.2: Deformation across the width of the sample as a function of the deformation applied parallel to $\underline{n}_0$.

A similar value of the Mooney-Rivlin coefficient can be estimated from equation (3.77) with $L_x \sim 1\,\text{cm}$ and $K = 10^{-11}\,\text{N}$. This is also broadly consistent with the work of Stannarius *et al.*, who performed mechanical experiments on smectic-A LCE balloons and found that Mooney-Rivlin coefficients in the range $0 < c_{MR} < 0.1$ could fit their experimental data [44].

Mesh Verification

Initial tests of the `UANISOHYPER_INV` subroutine were conducted on a single C3D8H (8-node linear brick hybrid) element. These showed that the model is correctly equilibriated, as no stresses are present at zero deformation. When stretching parallel to $\underline{n}_0$ the expected stress-strain curve was reproduced. Integration points undergo a transition from the AS to BB phase at the correct threshold strain.

The subroutine was then tested with C3D8RH (reduced-integration) and C3D20H (twenty-node) elements and it was confirmed that the results were independent of the element-type.

The thin film was represented using uniform meshes with between 800 ($40 \times 20 \times 1$) and $32,000$ ($200 \times 160 \times 1$) elements. These meshes were observed to achieve equivalent results. Computations were also performed using biased meshes, which achieved stress solutions within 0.5% of uniform meshes. Equivalent results were also obtained with thicker meshes ($100 \times 50 \times 5$).

The results presented in the following sections were obtained using a rectangularly uniform mesh of 5000 ($100 \times 50 \times 1$) C3D8H elements.

5.3 Tensile Deformation of Smectic-A Elastomer Sheets

Elongation parallel and perpendicular to the director

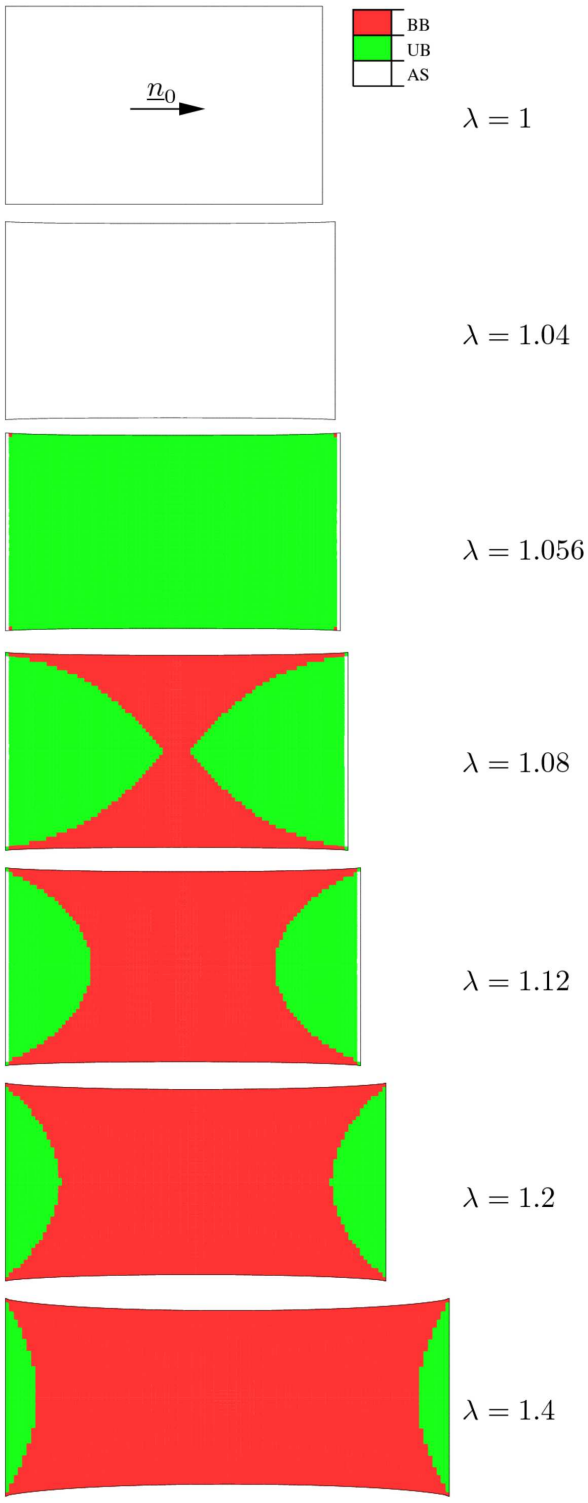

Figure 5.3: Spatial distribution of microstructure stretching parallel to $\underline{n}_0$, at strains of $\lambda = 1$, 1.04, 1.056, 1.08, 1.12, 1.2 and 1.4. Sample dimensions are 1.6 cm $\times$ 1.0 cm $\times$ 500 μm.

The spatial distribution of phase of the sample is shown in figure 5.3. At a strain of $\lambda = 1.04$ the sample is beneath the buckling threshold $\lambda_{\text{th}} \sim 1.053$, so no microstructure forms. Just above the buckling threshold, at $\lambda = 1.056$, almost the whole sample is in the UB phase. Then at higher strains the bulk of the sample moves to the BB phase, with the UB phase persisting only in the vicinity of the clamps. The material near the clamps is constrained in a way that prevents isotropic deformation, meaning it tends to form UB microstructure rather than BB microstructure. The shape of the deformed sample is similar to that of the isotropic neo-Hookean elastomer shown in figure 5.5(c), which means the Poisson's ratios post-buckling are $(\frac{1}{2}, \frac{1}{2})$.

The stress-strain curve for deformation parallel to $\underline{n}_0$ is shown in figure 5.4. This curve, obtained from finite element modelling, is in agreement with the stress-strain curve obtained for a uniform deformation shown in figure 3.12.

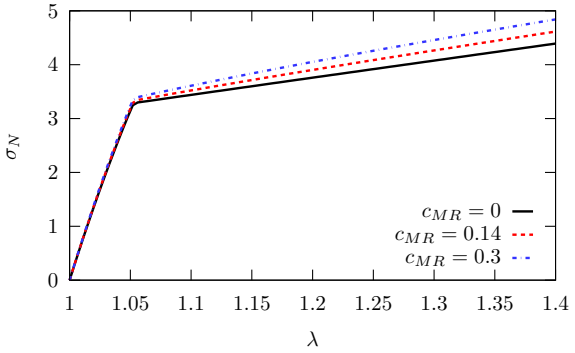

Figure 5.4: Nominal stress stretching parallel to $\underline{n}_0$, for different values of c_{MR}.

On stretching the sample perpendicular to $\underline{n}_0$ no buckled microstructure forms, as shown in figure 5.5(b). This behaviour is consistent with the uniform deformation case shown in figure 3.11. The layer spacing is constant and the sample deforms with Poisson's ratios of $(1, 0)$.

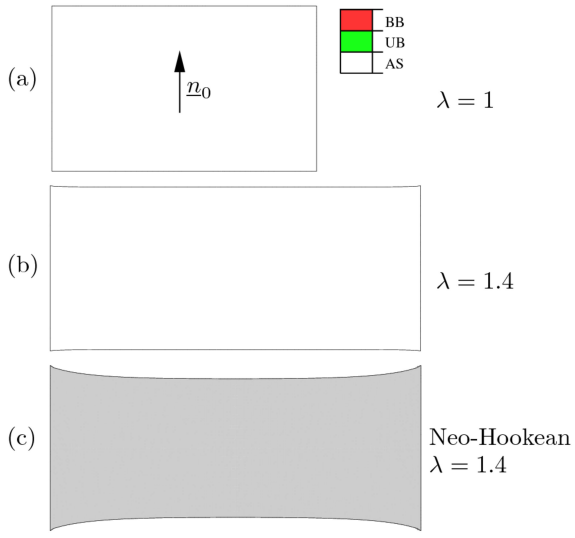

Figure 5.5: Microstructure distribution when stretching smectic-A elastomer perpendicular to $\underline{n}_0$, shown at (a) $\lambda = 1$ and (b) $\lambda = 1.4$. For comparison (c) shows an isotropic neo-Hookean sample, with free energy $W(\underline{\underline{\lambda}}) = C_1(A_1 - 3) + \frac{1}{D_1}(A_3 - 1)^2$, where $C_1 = 2$ and $D_1 = 10^{-6}$.

Elongation at an arbitrary angle to the director

The stress-strain behaviour for elongations at various angles to $\underline{n}_0$ are shown in figure 5.6 for an elastomer with the same aspect ratio as those of Nishikawa *et al.*

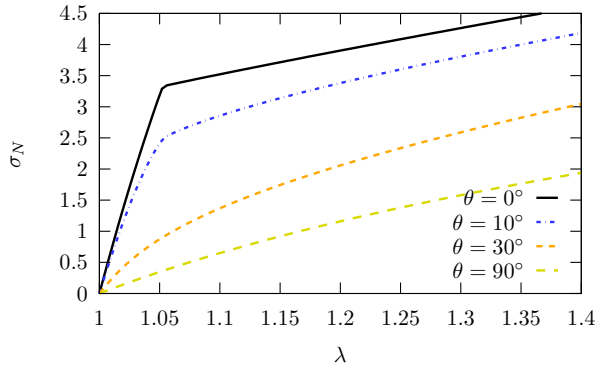

Figure 5.6: The nominal stress as a function of deformation, where $\underline{n}_0$ is oriented in the plane of the film at an angle θ to the elongation axis.

For elongations within $\sim 10°$ of $\underline{n}_0$ the stress-strain curve still resembles that of the parallel case. However for elongations at $\sim 20°$ and above there is no longer a well defined threshold transition to a lower modulus. The corresponding spatial distribution of microstructure for elongations at various angles to $\underline{n}_0$ are shown in figure 5.7.

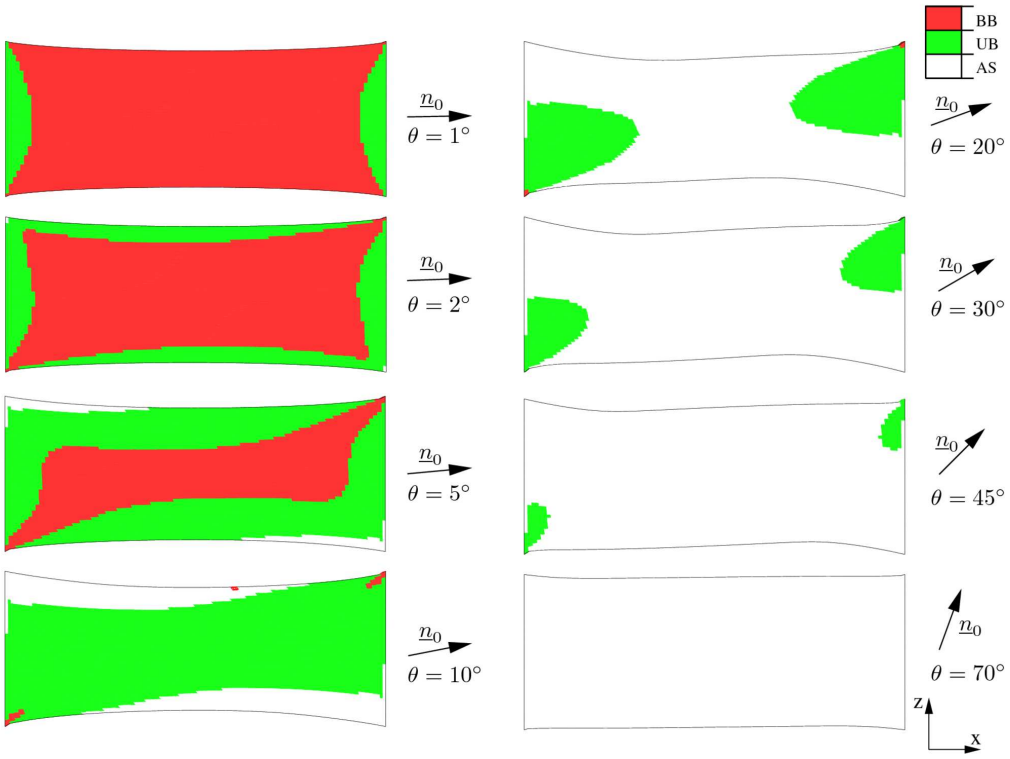

Figure 5.7: Microstructure distribution for elongations at 1°, 2°, 5°, 10°, 20°, 30°, 45° and 70° to $\underline{n}_0$, shown at a deformation of 1.4. The sample dimensions are 1.6 cm × 1.0 cm × 500 μm

These results show that elongations at an angle within $\sim 1°$ of $\underline{n}_0$ result in the BB phase forming in the bulk of the sample, with UB phase at the clamps. At a stretching angle of 2° the UB phase

forms at the free edges of the sample. The formation of UB microstructure is accompanied by λ_{xz} shears present in these regions of the sample. Note that for angles above $\sim 20°$ there is no percolation of the strip of the UB phase across the sample. This coincides with the disappearance of the threshold in the stress-strain response.

The stretching of a sample at a 5° inclination to the director will now be examined in more depth; the spatial distribution of microstructure is shown in figure 5.8 for various strains.

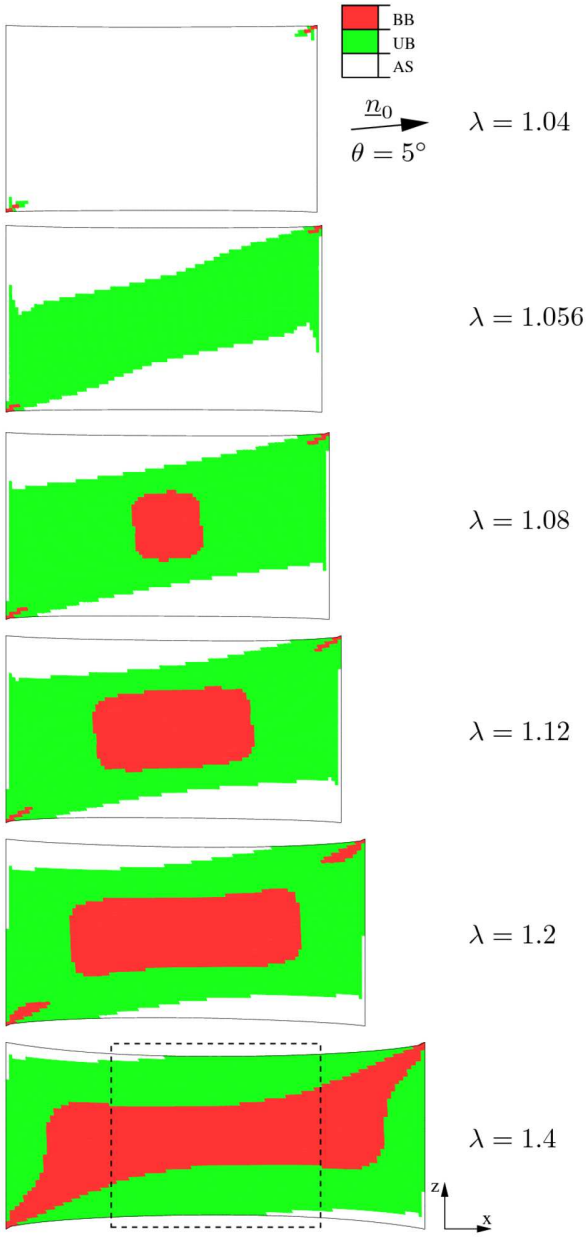

Figure 5.8: Microstructure distribution when stretching at 5° to $\underline{n}_0$ at strains of 1.04, 1.056, 1.08, 1.12, 1.2 and 1.4. The dashed region is explored in more detailed in Fig. 5.9.

At the threshold strain the sample clearly forms a stripe of UB phase, which runs between opposite corners of the elastomer. Due to the clamping conditions the material along the stripe is being stretched roughly parallel to the initial director, which causes a transition to the UB phase. At high strains the central region of the elastomer undergoes a transition to the BB phase, whereas the free edges of the sample are largely in the UB phase.

The spatial phase distribution is closely related to the spatial shear strain distribution, as shown in figures 5.9(a) and (b). Only the weakly sheared, central area of the sample is in the BB phase. Strong shears result in a transition from the BB to UB phase. For an imposed deformation of $\lambda_{xx} = 1.4$ the transition occurs at a $\lambda_{xz} \sim 0.4$, which is equivalent to an engineering shear strain of $\gamma_{xz} = (\lambda_{xz} + \lambda_{zx})/2 \sim 0.2$. The γ_{xy} and γ_{yz} shears are practically zero for the region shown.

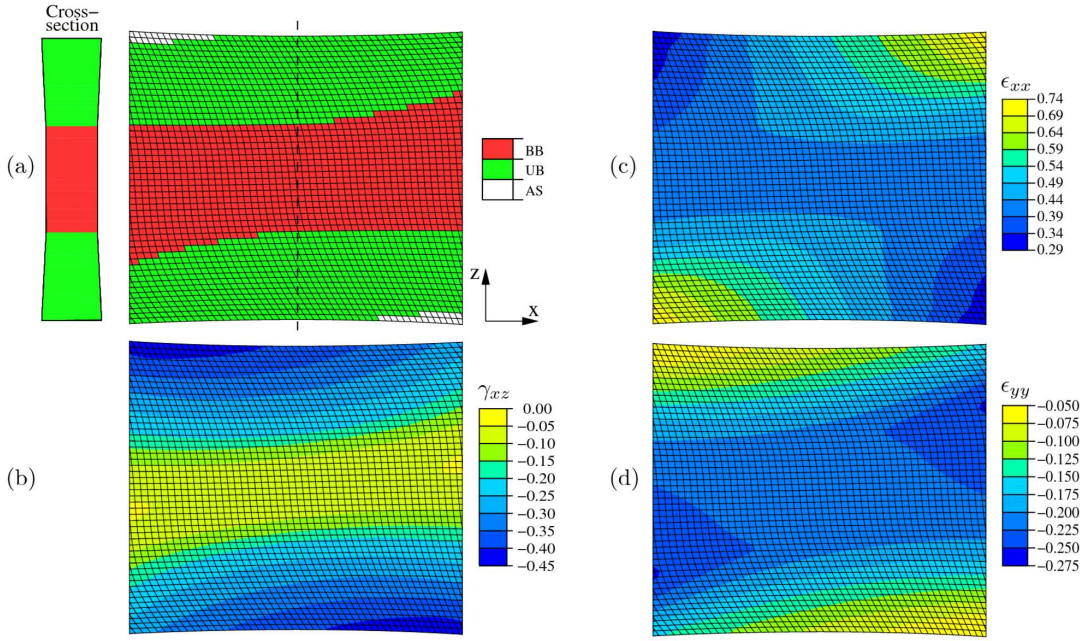

Figure 5.9: (a) Spatial microstructure distribution, the thickness of the cross-section has been exaggerated by a factor of 4 for clarity. (b) γ_{xz} engineering shear strain, (c) ϵ_{xx} engineering strain and (d) ϵ_{yy} engineering strain for the dashed region of figure 5.8.

The strains, ϵ_{xx} and ϵ_{yy}, are distributed inhomogeneously, as shown in figures 5.9(c) and (d). The ϵ_{xx} strain is lower near regions without any microstructure. The ϵ_{yy} strain represents the thickness of the sample. The regions of the sample in the BB phase have a near uniform thickness and are thinner than regions in the UB phase. It is interesting to analyse the $(\tilde{b},\tilde{d})$ values of elements located along the dashed line of figure 5.9(a), as plotted in figure 5.10.

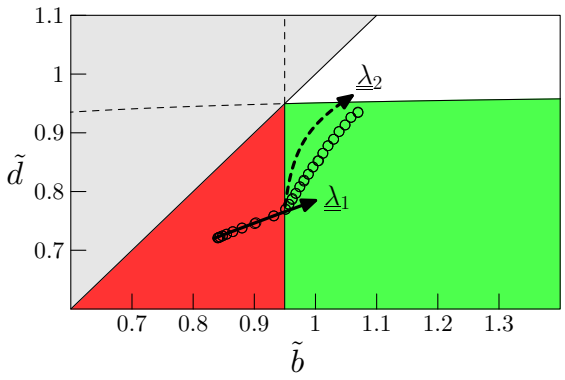

Figure 5.10: The phase of elements on the dashed line of figure 5.9 (i) is shown in $(\tilde{b}, \tilde{d})$ space. The trajectory $\underline{\underline{\lambda}}_1$ is a deformation, of the form equation (5.6), with $\gamma = 0.73$, $\theta = 5°$, $\lambda_1 = 1.4$, and $\lambda_{xz} = 0$ to 0.4. Trajectory $\underline{\underline{\lambda}}_2$ is a deformation with $\gamma = 0.1$, $\theta = 5°$, $\lambda_1 = 1.4$ and $\lambda_{xz} = 0.4$ to 0.7.

It is possible to understand the distribution of elements in phase space, shown in figure 5.10, by

considering a uniform deformation at an angle θ to $\underline{n}_0$ consisting of an elongation with a variable Poisson's ratio, and a λ_{xz} shear,

$$\underline{\underline{\lambda}} = \begin{pmatrix} \lambda_1 & 0 & \lambda_{xz} \\ 0 & \frac{1}{\lambda_1^{\gamma}} & 0 \\ 0 & 0 & \frac{1}{\lambda_1^{\gamma-1}} \end{pmatrix} \cdot \begin{pmatrix} \cos\theta & 0 & -\sin\theta \\ 0 & 1 & 0 \\ \sin\theta & 0 & \cos\theta \end{pmatrix}. \tag{5.6}$$

Elements at the centre of the dashed line of figure 5.9 are in the BB phase, and have almost zero shear strain. Moving away from the centre of the sample, in either direction, the elements are subjected to an increased amount of shear, which is illustrated by the trajectory labelled $\underline{\underline{\lambda}}_1$ in figure 5.10. It is the additional shearing that drives the transition from the BB into the UB phase. Once the UB phase is reached the thickness of the sample increases. This is because the UB phase consists of buckling in only one direction, and is therefore thicker in the direction perpendicular to the plane in which the microstructure laminates are formed. Moving towards the free edges of the sample the increasing shear nearly causes a transition from the UB to AS phase, as illustrated by the trajectory $\underline{\underline{\lambda}}_2$ in figure 5.10.

Aspect Ratio

So far only samples with the aspect ratio of 1.6 have been investigated. Other work on smectic-A elastomers has used different sample aspect ratios such as Komp *et al.* [25], where the sample dimensions were 2 cm × 0.4 cm × 100 μm, i.e. an aspect ratio of 5. It is therefore interesting to study samples with different length to width ratios, at constant film thickness. Figure 5.11 shows that varying the aspect ratio alters the stress-strain curves obtained when stretching at a small angle to $\underline{n}_0$, but produces the same stress strain curves when stretching parallel to $\underline{n}_0$.

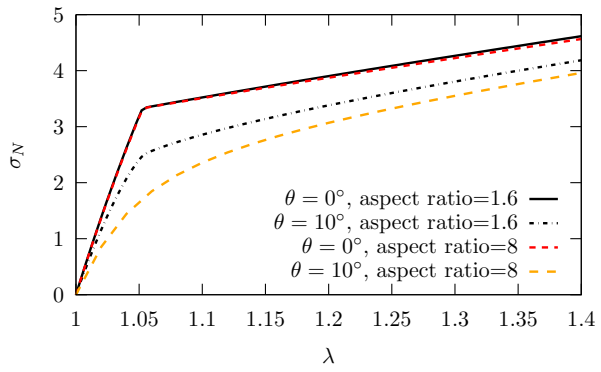

Figure 5.11: Nominal stress as a function of deformation for elongation at 0° and 10° to $\underline{n}_0$, for aspect ratios of 1.6 and 8.

The spatial microstructure distribution is highly sensitive to the aspect ratio. Figure 5.12 shows the microstructure distribution in a sample with an aspect ratio of 8.

When compared to figure 5.7, where the aspect ratio is 1.6, it can be seen that the larger aspect sample reverts to the AS phase for smaller angles of inclination of the deformation to the layer normal. Qualitatively this is because a smaller fraction of the sample is taken up by the end region near the clamps as the aspect ratio increases. Hence the layer normal is less constrained in its rotation by these end regions, and can adopt the lowest energy orientation rotated away from the elongation axis. For the aspect ratio of 8 an inclination of as little as 2° results in the sample forming the UB phase rather than the BB phase. This may make it difficult to experimentally observe BB microstructure in high aspect ratios samples by stretching parallel to $\underline{n}_0$. The sensitivity of the microstructure to the deformation direction is increased for larger values of B/μ.

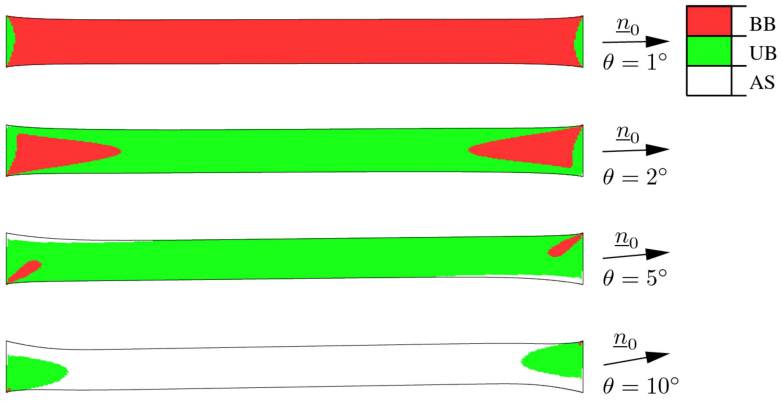

Figure 5.12: Microstructure distribution when stretching at 1°, 2°, 5° and 10° to $\underline{n}_0$ at a strain of 0.4. The sample dimensions are 8.0 cm × 1.0 cm × 500 μm, which is an aspect ratio of 8.

The microstructure distribution in a sample with an aspect ratio of 0.8 is shown in figure 5.13. These patterns are similar to those of a sample with an aspect ratio of 1.6, except that at low aspect ratio the UB phase near the clamps occupies a greater proportion of the elastomer.

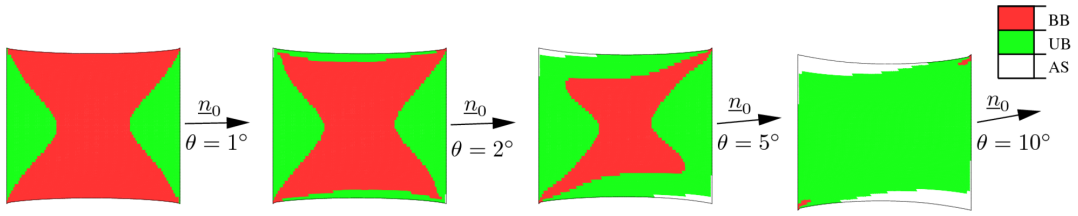

Figure 5.13: Microstructure distribution when stretching at 1°, 2°, 5° and 10° to $\underline{n}_0$ at a strain of 0.4. The sample dimensions are 0.8 cm × 1.0 cm × 500 μm, which is an aspect ratio of 0.8.

The effects of aspect ratio are summarised in figure 5.14, which shows the phase present in the centre of the sample for various aspect ratios and stretching angles. The lowest aspect ratio forms UB phase for all stretching angles 0°-10°, as the effect of the clamps dominate the whole sample.

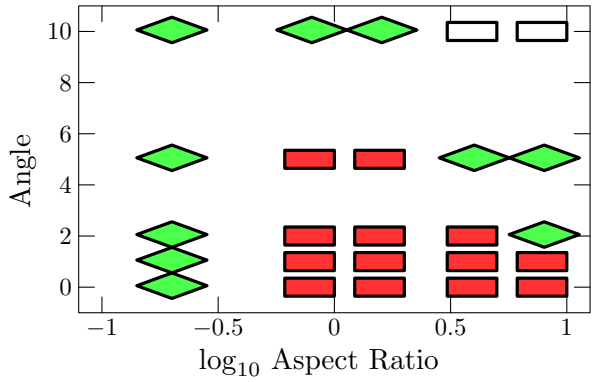

Figure 5.14: The phase found in the centre of the sample at a deformation of $\lambda = 1.4$, for various aspect ratios and stretching angles relative to $\underline{n}_0$.

At high aspect ratios the effect of the clamps on the centre of the sample diminishes and the BB phase forms for very small angles. However a small deviation from stretching parallel to the layer normal results in the formation of the UB phase. Experimental studies on higher aspect ratio sam-

ples [25] show no opacity when stretching parallel to the layer normal. A possible explanation for this behaviour is that the layer normal is slightly misaligned with the stretch direction. However in order for the AS phase to occupy the bulk of the sample it would require a significant misalignment, greater than 5°. Also a large misalignment would create a significant, near-uniform γ_{xz} shear in the bulk of the sample, which would rotate the layer normal in the x-z plane. Whereas the X-ray scattering data indicates that the layer normal does not reorient in the plane of the film .

It is also possible to vary the thickness of the sample at a constant length to width ratio. This was investigated by modelling samples between 10 times thicker and thinner than previously considered. These results reproduce qualitatively similar microstructure distributions and stress-strain curves, which demonstrates that the achieved results are largely independent of the sample thickness.

5.4 Conclusions

The stretching of monodomain smectic-A elastomer sheets was studied numerically using the free energy model, described in chapter 3. The model consists of the coarse grained smectic-A energy, derived in reference [80], augmented with a Mooney-Rivlin term to account for the energy of deforming buckled layers. This model is successful in reproducing the experimentally observed Poisson's ratios post-buckling. The magnitude of the Mooney-Rivlin term can be measured experimentally by a two step deformation process; first deforming the elastomer parallel to the layer normal, then deforming perpendicular to this direction. The modulus of the elastomer during this second step indicates the magnitude of c_{MR}.

A sample with dimensions and material parameters similar to those of Nishikawa *et al.* was investigated. When elongated parallel to $\underline{n}_0$ the majority of the sample is predicted to form a bidirectionally buckled microstructure, except at the clamps where unidirectional microstructure is expected. Experimentally these microstructural differences should be distinguishable using X-ray scattering patterns or polariser-analyser pair. When elongated at a small inclination to the layer normal the phase of the sample is sensitive to the aspect ratio of the sample. For small aspect ratios the bidirectionally buckled phase persists to large angles. For large aspect ratios no buckled phase is observed in the bulk of the sample for small inclination angles.

Some experimental studies on side chain smectic-A elastomers show that the sample remains optically transparent on stretching [25]. A small or large misalignment of the layer normal with the stretch direction is not consistent with the behaviour found in the model. However, a 3D X-ray scattering experiment that resolves spatially different regions of the smectic film would provide a useful comparison with the model presented here.

Chapter 6

Summary

Modelling semi-soft Smectic-C Elastomer

The aim of this work was to investigate the mechanical response of a smectic-C model, with an additional semi-softness term included. Semi-soft elasticity is expected in smectic-C elastomers, as like nematic elastomers the perfectly soft behaviour predicted for rotations of the polymer anisotropy will be destroyed by non-idealities. The inclusion of semi-softness significantly alters the mechanical response, and results in unusual behaviour such as negative stiffness. The model of monodomain smectic-C elastomer includes energy contributions from nematic, semi-soft and smectic layer elasticity terms, and a penalty for changing the tilt angle. The stress-strain responses for uniform deformations were calculated using an energy minimization routine.

When stretching parallel to the layer normal the rotation of the director in the Sm-C soft mode causes the sample thickness to expand and then contract. A negative incremental Poisson's ratio of up to $\nu \sim -1.5$ has been found for typical model parameters. The semi-soft parameter α delays director rotation, and the initial stiffness will reflect the smectic modulus provided the tilt modulus $c \to \infty$. Once director rotation has started the elastomer has a negative incremental Poisson's ratio, and a negative stiffness. The negative stiffness is a consequence of the Sm-C soft mode deformations and the form of the semi-softness term.

When stretching perpendicular to the layer normal and the director, the response is reminiscent of a semi-soft nematic elastomer, as the director rotates towards the stretch axis once a threshold strain is reached and the layers do not reorient. The stress-strain curve shows a semi-soft plateau, which becomes less well defined for larger values of semi-soft parameter α.

When stretching perpendicular to the director with the layer normal coplanar, an instability in the director orientation is predicted. The director jumps from an unrotated state to a rotated state at a threshold strain. The semi-soft term provides an energy barrier to director rotation, so the threshold strain increases with increasing values of the semi-soft parameter. The jump in director orientation causes a discontinuity in the stress-strain curve, i.e. a dramatic decrease in stress once the director has rotated.

When stretching parallel to the director the stress-strain response is monotonic and the stiffness is indicative of the rubber modulus. The layer normal rotates away from the stretch axis, and the director follows due to the constraint of the tilt angle.

Modelling realistic deformations of smectic-A elastomer

The deformation of monodomain smectic-A elastomer sheets was modelled under realistic clamping conditions using finite element analysis. The motivation for this work was to improve the understanding of the buckling instability that occurs when stretching parallel to the director, as observed by Nishikawa *et al.* [19]. The model is used to predict the spatial distribution of buckled microstructure, and investigate the combined effects of sample aspect ratio and varying the angle of the stretch relative to the director.

The constitutive model used was the coarse grained smectic-A energy [80], augmented with an additional Mooney-Rivlin term to account for the energy of deforming buckled layers. The additional term is necessary to reproduce the experimentally observed Poisson's ratios post-buckling. The magnitude of the Mooney-Rivlin term c_{MR} can be measured experimentally by a two step deformation process; first deforming the elastomer parallel to the layer normal, then deforming perpendicular to this direction. The modulus of the elastomer during this second step indicates the magnitude of c_{MR}.

A sample with dimensions and material parameters similar to those of Nishikawa *et al.* was investigated. When elongated parallel to $\underline{n}_0$ the majority of the sample is predicted to form a bidirectionally buckled microstructure, except at the clamps where unidirectional microstructure is expected. Experimentally these microstructural differences should be distinguishable using X-ray scattering patterns or polariser-analyser pair. When elongated at a small inclination to $\underline{n}_0$ the phase of the sample is sensitive to the aspect ratio of the sample. For small aspect ratios the bidirectionally buckled phase persists to large angles. For large aspect ratios no buckled phase is observed in the bulk of the sample for small inclination angles.

Some experimental studies on side chain smectic-A elastomers show that the sample remains optically transparent on stretching [25]. Conceivably this could be caused by a misalignment of the director with the stretch direction, however the results of this study do not support this. An alternative constitutive model is required to describe smectic-A elastomers where the smectic layers are not strongly coupled to the rubber matrix [25, 28, 38].

6.1 Further Work

Modelling pseudo-monodomain Smectic-C Elastomer

The work presented here needs to be extended if it is to meet with the existing experiments on smectic-C pseudo-monodomains. This would require modelling the domain microstructure present in a pseudo-monodomain. A possible simplification is to ignore the compatibility of the domains and calculate the stiffness of a representative sample of domains stretched in parallel and in series. These approximations are known as the Taylor and Sachs bounds and correspond to the stiffest and softest behaviours possible [103, 104], as explained in Appendix D. However these bounds are only valid for materials with positive stiffness, and semi-soft Sm-C elastomer is negatively stiff in many geometries.

Another option would be to resolve how neighbouring domains constrain each other in a small region of a Sm-C microstructure, i.e. by simulating a few domains using the finite element method. The averaged behaviour of the microstructure could then be extrapolated to model a macroscopic sample. Unfortunately the quasi-convex envelope of the smectic-C energy is not yet known, so there is currently no constitutive model suitable for finite element modelling Sm-C elastomer.

Modelling interfaces in Smectic-A elastomer

The buckled microstructure of smectic-A elastomers includes a large number of interfaces between regions with differently oriented directors, and each interface has an energetic cost due to the Frank elasticity. The behaviour of the post-buckled microstructure is influenced by the interfacial energy cost, as well as the rubbery elasticity. The interfacial energy could be incorporated into existing smectic-A models by adding the Frank elasticity splay term,

$$F = \frac{1}{2}K(\nabla \cdot \underline{n})^2 + F_{Sm-A}.$$

The complexity of this model could be reduced by considering a two dimensional case. Minimizing this energy would result in equations for the director orientation profile. The time-dependence of microstructure formation could also be be probed, as the displacement $\underline{u}$ responds in a viscous way to the forces, i.e

$$\frac{\partial \underline{u}}{\partial t} = -\frac{\delta F}{\delta \underline{u}}.$$

Layer creation in monodomain Smectic-A elastomer

A number of smectic-A samples exhibit a stress-strain threshold, but do not show evidence of a buckling instability [25, 28, 38]. Komp *et al.* suggest that new smectic layers are created upon extension in their side-chain system [25]. Kramer *et al.* argue that the defective layer structure causes the breakdown of layers under strain. Beyer *et al.* associate the instability with the unfolding of hairpin chains in their main-chain system [38]. These behaviours are all similar, in as much as they imply that mesogens can leave the smectic layer they start in. Currently the experimental evidence indicating that mesogens jump between layers in elastomer is indirect, but layer formation is observed in Sm-A liquid crystals [11]. It may similarly be possible to directly observe the propagation of layer defects in elastomers using optical microscopy.

A simple model of these systems is to assume that the energetic cost of layer creation is linear in strain ϵ. The creation of new layers would stretch the polymer chain backbone, so the associated stiffness is likely to be comparable to the rubber modulus. The energetic cost of layer stretching is $\sim \frac{1}{2}B\epsilon^2$. Interestingly this model results in a stress-strain threshold behaviour when stretching parallel to the layer normal. At low strains it is energetically cheapest to deform by layer stretching, but above a threshold layer creation becomes favourable, see figure 6.1

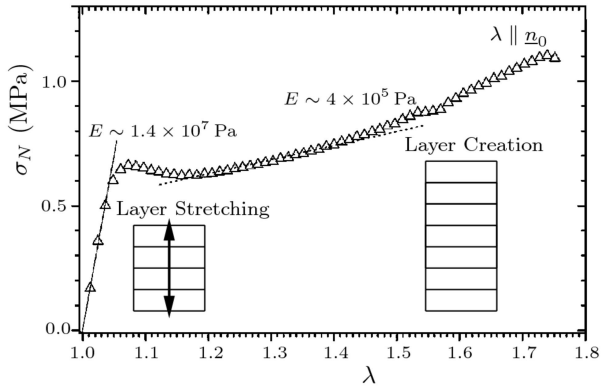

Figure 6.1: The stess-strain curve for the Sm-A monodomain of Komp *et al.* [25], with layer stretching and layer creation deformation modes illustrated.

Modelling non-embedded layer reorientation

Experiments on main chain smectic-C polydomains indicate that the layers do not deform like embedded planes, as the layer normals do not rotate away from the stretch axis at high strain [33, 34]. Instead these samples reorient to form a pseudo-monodomain, with the director parallel to the stretch axis. The layers in these systems appear to have an additional freedom, which might be expected if the deformation mode does not preserve the smectic layers, e.g. hairpin unfolding in main-chain systems or layer creation in highly defective samples.

Sánchez-Ferrer *et al.* observe that a pseudo-monodomain stretched perpendicular to the director reorients to form a pseudo-monodomain with the director parallel to the stretch axis once $\lambda > 6$ [15]. The corresponding modulus is rubbery, indicating a fixed layer spacing. A tentative explanation is that the deformation mode creates additional layers, which permits the layer normals to rotate towards the stretch axis. This freedom allows the layer normals to be maintained at the tilt angle relative to the stretch axis, so that the director is aligned with the stretch direction. Currently there is no quantitative model of non-embedded layers. The layer normal orientation would be dependent on the proportion of created layers, and the deformation matrix.

Appendix A

Smectic-C Energy Minimization Routine

A Fortran 90 program to minimize the semi-soft smectic-C energy is given here. In this program the tilt angle is taken as fixed and not minimized over. The minimization is performed by a subroutine `simann`, which implements the simulated annealing algorithm described by Goffe *et al.* [75]. The code for the `simann` subroutine is not included here, as it is identical in function to the original implementation. Suitable minimization control parameters for successful minimization are T = 1.0, RT = 0.95, NS = 20, NT = 10 and MAXEVL = 800000.

```
!%%%%%%%%%%%%%%%%%%%%%%%%%%%%%%%%%%%%%%%%%%%%%%%%%%%%%%%%%%%%%%%%%
!%                  Define the global variables                  %
!%%%%%%%%%%%%%%%%%%%%%%%%%%%%%%%%%%%%%%%%%%%%%%%%%%%%%%%%%%%%%%%%%
module globvars
implicit none
integer, parameter :: SP = kind(1.0d0)
integer, parameter :: WP = kind(1.0d0)

! The reduced smectic modulus B/mu is bmod, the tilt modulus is cmod,
! and the semi-soft parameter is alpha.
! The initial tilt angle is q0, the tilt angle is qangle,
! and the polymer anisotropy is ranist. The imposed lxx strain is limp.
! The initial orientation of n and k are (nx0,ny0,nz0) and (k0x, k0y, k0z).
! The nematic, smectic, semisoft and tilt energies are fnem, fsm, fss, ftilt.
real (kind = WP) :: bmod, cmod, alpha, q0, qangle, ranist,&
& limp, nx0, ny0, nz0, k0x, k0y, k0z, fnem, fsm, fss, ftilt
end module globvars

module function
use globvars
implicit none
contains

!%%%%%%%%%%%%%%%%%%%%%%%%%%%%%%%%%%%%%%%%%%%%%%%%%%%%%%%%%%%%%%%%%
!%           Functions to return the smectic-C energy            %
!%%%%%%%%%%%%%%%%%%%%%%%%%%%%%%%%%%%%%%%%%%%%%%%%%%%%%%%%%%%%%%%%%
function fnemenergy(k0x, k0y, k0z, nx0, ny0, nz0, nx, ny, nz, lxx, lxy, lxz, lyz, lzz)
real (SP) :: fnemenergy
real (SP) , intent(in) :: k0x, k0y, k0z, nx0, ny0, nz0, nx, ny, nz, lxx, lxy, lxz, lyz, lzz
      fnemenergy = (lzz**2*(1 + nz**2*(-1 + 1/ranist))*(1 + nz0**2*(-1 + ranist)) + &
& (ny*nz*(lxx*lyz*lzz + nz0*(ny0 + lxx*lyz*lzz*nz0)*(-1 + ranist))*(-1 + 1/ranist))/lxx - &
& ((lxx**2*(1 + nx0**2*(-1 + ranist)) + lxy**2*(1 + ny0**2*(-1 + ranist)) + &
& lxz**2*(1 + nz0**2*(-1 + ranist)) + 2*lxy*lxz*ny0*nz0*(-1 + ranist) + &
& 2*lxx*nx0*(lxy*ny0 + lxz*nz0)*(-1 + ranist))*(nx**2*(-1 + ranist) - ranist))/ranist - &
& ((1 + lxx**2*lyz**2*lzz**2*(1 + nz0**2*(-1 + ranist)) + ny0**2*(-1 + ranist) + &
& 2*lxx*lyz*lzz*ny0*nz0*(-1 + ranist))*(ny**2*(-1 + ranist) - ranist))/&
& (lxx**2*lzz**2*ranist) + (2*nx*ny*(-lxy - lxx*lyz*lzz*(lxz + nz0*&
& (lxx*nx0 + lxy*ny0 + lxz*nz0)*(-1 + ranist)) - ny0*(lxx*nx0 + lxy*ny0 + lxz*nz0)*&
& (-1 + ranist))*(-1 + ranist))/(lxx*lzz*ranist) - (2*lzz*nx*nz*(lxz + nz0*&
& (lxx*nx0 + lxy*ny0 + lxz*nz0)*(-1 + ranist))*(-1 + ranist))/ranist - (ny*nz*&
& (lxx*lyz*lzz + nz0*(ny0 + lxx*lyz*lzz*nz0)*(-1 + ranist))*(-1 + ranist))/(lxx*ranist))/2.
end function fnemenergy

function fssenergy(k0x, k0y, k0z, nx0, ny0, nz0, nx, ny, nz, lxx, lxy, lxz, lyz, lzz)
real (SP) :: fssenergy
```

```
real (SP) , intent(in) :: k0x, k0y, k0z, nx0, ny0, nz0, nx, ny, nz, lxx, lxy, lxz, lyz, lzz
      fssenergy = -(alpha*(ny**2*(-1 + (ny0 + lxx*lyz*lzz*(-1 + nz0))*&
&  (ny0 + lxx*lyz*lzz*(1 + nz0))) + &
&  lxx**2*lzz**2*(lzz**2*nz**2*(-1 + nz0**2) + &
&  2*lzz*nx*nz*(lxx*nx0*nz0 + lxy*ny0*nz0 + lxz*(-1 + nz0**2)) + &
&  nx**2*(lxx**2*(-1 + nx0**2) + lxy**2*(-1 + ny0**2) + &
&  2*lxy*lxz*ny0*nz0 + 2*lxx*nx0*(lxy*ny0 + lxz*nz0) + &
&  lxz**2*(-1 + nz0**2))) + &
&  2*lxx*lzz*ny*(lzz*nz*(ny0*nz0 + lxx*lyz*lzz*(-1 + nz0**2)) + &
&  nx*(-lxy + ny0*(lxx*nx0 + lxy*ny0 + lxz*nz0) + &
&  lxx*lyz*lzz*(-lxz + nz0*(lxx*nx0 + lxy*ny0 + lxz*nz0))))))/&
&  (2.*lxx**2*lzz**2)
end function fssenergy

function fsmenergy(k0x, k0y, k0z, lxx, lxy, lxz, lyz, lzz)
real (SP) :: fsmenergy
real (SP) , intent(in) :: k0x, k0y, k0z, lxx, lxy, lxz, lyz, lzz
      fsmenergy =  (bmod*(-1 + 1/&
& Sqrt(k0x**2/lxx**2 + (k0y*lxx*lzz - k0x*lxy*lzz)**2 + &
& (k0y*lxx*lyz + (k0x*lxz - lxx*(k0z + k0x*lxy*lyz*lzz))/&
& (lxx*lzz))**2))**2)/2.
end function fsmenergy

function ftiltenergy(q0, qangle)
real (SP) :: ftiltenergy
real (SP) , intent(in) :: q0, qangle
      ftiltenergy =  (cmod*(cos(q0)**2 - cos(qangle)**2)**2)/2.
end function ftiltenergy

!%%%%%%%%%%%%%%%%%%%%%%%%%%%%%%%%%%%%%%%%%%%%%%%%%%%%%%%%%%%%%%%%%
!%         Subroutine that recieves the point xc from simann     %
!%                  and returns the Smectic-C energy             %
!%%%%%%%%%%%%%%%%%%%%%%%%%%%%%%%%%%%%%%%%%%%%%%%%%%%%%%%%%%%%%%%%%
      SUBROUTINE FCN(n,xc,funct)
integer, intent(in) :: n
real (SP), intent(in) :: xc(n)
real (SP) ftotal, funct
real (SP) :: fnem, fsm, fss
real (SP) :: k1, k2, k3, c1, c2, c3, lxx, lxy, lxz, lyz, lzz, p, nx, ny, nz

    call conv_vars(xc, lxy, lxz, lyz, lzz, p)

lxx = limp

k1 = kx(lxx, lxy, lxz, lyz, lzz)
k2 = ky(lxx, lxy, lxz, lyz, lzz)
k3 = kz(lxx, lxy, lxz, lyz, lzz)

c1 = cx(k1, k2, k3, p)
c2 = cy(k1, k2, k3, p)
c3 = cz(k1, k2, k3, p)

nx = k1* cos(q0) + c1 * sin(q0)
ny = k2* cos(q0) + c2 * sin(q0)
nz = k3* cos(q0) + c3 * sin(q0)

fnem = fnemenergy(k0x, k0y, k0z, nx0, ny0, nz0, nx, ny, nz, lxx, lxy, lxz, lyz, lzz)
fss = fssenergy(k0x, k0y, k0z, nx0, ny0, nz0, nx, ny, nz, lxx, lxy, lxz, lyz, lzz)
fsm = fsmenergy(k0x, k0y, k0z, lxx, lxy, lxz, lyz, lzz)

ftotal = fnem + fsm + fss
funct = 1.0/ftotal

RETURN
      END Subroutine

!%%%%%%%%%%%%%%%%%%%%%%%%%%%%%%%%%%%%%%%%%%%%%%%%%%%%%%%%%%%%%%%%
!%         Subroutine to convert the parameters x(:) from       %
!%            the range [0,1] into physical variables.          %
!%%%%%%%%%%%%%%%%%%%%%%%%%%%%%%%%%%%%%%%%%%%%%%%%%%%%%%%%%%%%%%%%
      subroutine conv_vars(x, lxy, lxz, lyz, lzz, p)
real(SP), intent(in) :: x(:)
```

```
real(SP), intent(out) ::  lxy, lxz, lyz, lzz, p

lxy = (x(1)-0.5)*3
lxz = (x(2)-0.5)*3
lyz = (x(3)-0.5)*3
lzz =  0.5+x(4)
p =    0.0+x(5)*2*3.141592

      end subroutine conv_vars

!%%%%%%%%%%%%%%%%%%%%%%%%%%%%%%%%%%%%%%%%%%%%%%%%%%%%%%%%%%%%%%%%%
!%               Functions to return the values of the           %
!%                  layer normal and director                    %
!%%%%%%%%%%%%%%%%%%%%%%%%%%%%%%%%%%%%%%%%%%%%%%%%%%%%%%%%%%%%%%%%%
function cx(k1, k2, k3, p)
real (SP) :: cx
real (SP) , intent(in) :: k1, k2, k3, p
      cx =  - ( Sqrt(k2**2 + k3**2)*Cos(p) )
end function cx

function cy(k1, k2, k3, p)
real (SP) :: cy
real (SP) , intent(in) :: k1, k2, k3, p
      cy = - (  -((k1*k2*Cos(p))/Sqrt(k2**2 + k3**2)) + &
     &  Sqrt(1 - k2**2)*Sqrt(-(k3**2/((-1 + k2**2)*(k2**2 + k3**2))))*Sin(p)   )
end function cy

function cz(k1, k2, k3, p)
real (SP) :: cz
real (SP) , intent(in) :: k1, k2, k3, p
      cz =  - (  -((k1*k3*Cos(p))/Sqrt(k2**2 + k3**2)) - &
     &  (k2*Sqrt(1 - k2**2)*Sqrt(-(k3**2/((-1 + k2**2)*(k2**2 + k3**2))))*Sin(p))/&
     &   k3)
end function cz

function kx(lxx, lxy, lxz, lyz, lzz)
real (SP) :: kx
real (SP), intent(in) :: lxx, lxy, lxz, lyz, lzz
kx =      k0x/(lxx*Sqrt(k0x**2/lxx**2 + (k0y*lxx*lzz - k0x*lxy*lzz)**2 + &
     &      (k0y*lxx*lyz + (k0x*lxz - lxx*(k0z + k0x*lxy*lyz*lzz))/(lxx*lzz))**2))
end function kx

function ky(lxx, lxy, lxz, lyz, lzz)
real (SP) :: ky
real (SP), intent(in) :: lxx, lxy, lxz, lyz, lzz
ky =         ((k0y*lxx - k0x*lxy)*lzz)/&
     &  Sqrt(k0x**2/lxx**2 + (k0y*lxx*lzz - k0x*lxy*lzz)**2 + &
     &    (k0y*lxx*lyz + (k0x*lxz - lxx*(k0z + k0x*lxy*lyz*lzz))/(lxx*lzz))**2)
end function ky

function kz(lxx, lxy, lxz, lyz, lzz)
real (SP) :: kz
real (SP), intent(in) :: lxx, lxy, lxz, lyz, lzz
kz =     (-(k0x*lxz) + lxx*(k0z + (-(k0y*lxx) + k0x*lxy)*lyz*lzz))/&
     &  (lxx*lzz*Sqrt(k0x**2/lxx**2 + (k0y*lxx*lzz - k0x*lxy*lzz)**2 + &
     &      (k0y*lxx*lyz + (k0x*lxz - lxx*(k0z + k0x*lxy*lyz*lzz))/(lxx*lzz))**2))
end function kz

end module function

!%%%%%%%%%%%%%%%%%%%%%%%%%%%%%%%%%%%%%%%%%%%%%%%%%%%%%%%%%%%%%%%%%
!%            Minimize the Smectic-C Semisoft Energy             %
!%              for the case of a fixed tilt angle               %
!%%%%%%%%%%%%%%%%%%%%%%%%%%%%%%%%%%%%%%%%%%%%%%%%%%%%%%%%%%%%%%%%%
program main
use globvars
use function
implicit none

! Define the variables used in the program.
integer, parameter :: n=5       ! n is the number of variables to be minimized over.
real (SP) ::f, fold, xc(n)      ! f is the energy, xc(n) are the optimised variables on the range [0,1].
```

```
integer :: i, STEPS

real (SP) :: c1, c2, c3, k1, k2, k3, nx, ny, nz
real (SP) :: straininc                    ! the increment of imposed strain.
real(SP) :: lxx, lxy, lxz, lyz, lzz, p    ! the  strain tensor components and the director rotation angle.

! Define the material parameters
bmod = 60
ranist = 2
q0 = 0.50
alpha =  0.05

! Define the initial layer normal and director
k0x = cos(q0)
k0y = 0.
k0z = sin(q0)

nx0 = 1.
ny0 = 0.
nz0 = 0.

! Open a file to store the data in
open (unit=110, file='paran0_B=60_alpha=0.05.dat', status= 'OLD',ACCESS="SEQUENTIAL")

fold = 1.5

straininc = 0.001
STEPS =  400

do i = 0, STEPS-1
   limp = 1. + i*straininc

! Find the energy minimum at the imposed strain by calling simann.
   call simann(limp, f, xc)
! Convert the array xc into physical variables.
   call conv_vars(xc, lxy, lxz, lyz, lzz, p)

      lxx = limp
      k1 = kx(lxx, lxy, lxz, lyz, lzz)
      k2 = ky(lxx, lxy, lxz, lyz, lzz)
      k3 = kz(lxx, lxy, lxz, lyz, lzz)

      c1 = cx(k1, k2, k3, p)
      c2 = cy(k1, k2, k3, p)
      c3 = cz(k1, k2, k3, p)

      nx = k1* cos(q0) + c1 * sin(q0)
      ny = k2* cos(q0) + c2 * sin(q0)
      nz = k3* cos(q0) + c3 * sin(q0)

fnem = fnemenergy(k0x, k0y, k0z, nx0, ny0, nz0, nx, ny, nz, lxx, lxy, lxz, lyz, lzz)
fss = fssenergy(k0x, k0y, k0z, nx0, ny0, nz0, nx, ny, nz, lxx, lxy, lxz, lyz, lzz)
fsm = fsmenergy(k0x, k0y, k0z, lxx, lxy, lxz, lyz, lzz)

20 format(E20.5,1X, E20.5,1X, E20.5,1X, E20.5,1X, E20.5,1X, E20.5,1X, &
         &E20.5,1X, E20.5,1X, E20.5,1X, F11.6,2X, F11.6,2X,E20.5,1X,&
         &E20.5,1X,E20.5,1X,E20.5,1X,E20.5,1X,E20.5,1X, E20.5,1X,E20.5 &
         &,1X,E20.5,1X)

write(110,20)  limp, lxy, lxz, lyz, 1/(limp*lzz), lzz, nx, ny, nz, f, (f-fold)/straininc,&
& nx**2+ny**2+nz**2, nx*k1+ny*k2+nz*k3, k1, k2, k3, fnem, fsm, fss, p

fold = f
enddo

end program main
```

Appendix B

Compositional Fluctuations Model of Biaxial LCE

A biaxial LCE has different polymer anisotropy tensor lengths in the two directions perpendicular to the director, see figure B.1.

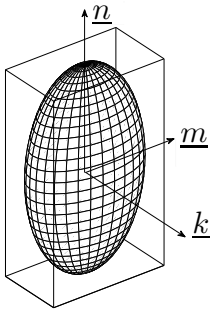

Figure B.1: The biaxial shape ellipsoid has semi-axis length $\sqrt{1-\frac{p}{2}}$ in direction $\underline{k}$ and semi-axis length $\sqrt{1+\frac{p}{2}}$ in direction $\underline{m}$.

We can write down the biaxial anisotropy step-length tensor, $\underline{\underline{\ell}}_0$, and its inverse, $\underline{\underline{\ell}}^{-1}$,

$$\underline{\underline{\ell}}_0 = \underline{\underline{\delta}} + (< r > -1)\underline{n}_0\,\underline{n}_0^T + \frac{< p >}{2}\underline{m}_0\,\underline{m}_0^T - \frac{< p >}{2}\underline{k}_0\,\underline{k}_0^T, \tag{B.1}$$

$$\underline{\underline{\ell}}^{-1} = \frac{1}{< r >}\underline{n}\,\underline{n}^T + \frac{1}{1+\frac{<p>}{2}}\underline{m}\,\underline{m}^T + \frac{1}{1-\frac{<p>}{2}}\underline{k}\,\underline{k}^T, \tag{B.2}$$

where $< r >$ and $< p >$ are the mean chain anisotropies.

Now consider the step-length tensors of only the ν^{th} polymer chain. The simplest model takes $r^{(\nu)}$ and $p^{(\nu)}$ as independent of each other,

$$\underline{\underline{\ell}}_0^{(\nu)} = \underline{\underline{\delta}} + (r^{(\nu)} - 1)\underline{n}_0\,\underline{n}_0^T + \frac{p^{(\nu)}}{2}\underline{m}_0\,\underline{m}_0^T - \frac{p^{(\nu)}}{2}\underline{k}_0\,\underline{k}_0^T, \tag{B.3}$$

$$\underline{\underline{\ell}}^{-1(\nu)} = \frac{1}{r^{(\nu)}}\underline{n}\,\underline{n}^T + \frac{1}{1+\frac{p^{(\nu)}}{2}}\underline{m}\,\underline{m}^T + \frac{1}{1-\frac{p^{(\nu)}}{2}}\underline{k}\,\underline{k}^T. \tag{B.4}$$

The step-length tensors for the ν^{th} polymer chain can also be written as,

$$\begin{aligned}\underline{\underline{\ell}}_0^{(\nu)} = &\underbrace{\underline{\underline{\delta}} + (< r > -1)\underline{n}_0\,\underline{n}_0^T + \frac{< p >}{2}\underline{m}_0\,\underline{m}_0^T - \frac{< p >}{2}\underline{k}_0\,\underline{k}_0^T}_{\underline{\underline{\ell}}_0} \\ &+ (r^{(\nu)} - < r >)\underline{n}_0\,\underline{n}_0^T + \left(\frac{p^{(\nu)}}{2} - \frac{< p >}{2}\right)\underline{m}_0\,\underline{m}_0^T + \left(-\frac{p^{(\nu)}}{2} + \frac{< p >}{2}\right)\underline{k}_0\,\underline{k}_0^T,\end{aligned} \tag{B.5}$$

$$\begin{aligned}\underline{\underline{\ell}}^{-1(\nu)} = &\underbrace{\frac{1}{< r >}\underline{n}\,\underline{n}^T + \frac{1}{1+\frac{<p>}{2}}\underline{m}\,\underline{m}^T + \frac{1}{1-\frac{<p>}{2}}\underline{k}\,\underline{k}^T}_{\underline{\underline{\ell}}^{-1}} \\ &+ \left(\frac{1}{r^{(\nu)}} - \frac{1}{< r >}\right)\underline{n}\,\underline{n}^T + \left(\frac{1}{1+\frac{p^{(\nu)}}{2}} - \frac{1}{1+\frac{<p>}{2}}\right)\underline{m}\,\underline{m}^T + \left(\frac{1}{1-\frac{p^{(\nu)}}{2}} - \frac{1}{1-\frac{<p>}{2}}\right)\underline{k}\,\underline{k}^T.\end{aligned} \tag{B.6}$$

The free energy density is the average over all polymer chains,

$$F_{el} \sim < \mathrm{Tr}[\underline{\underline{\lambda}} \cdot \underline{\underline{\ell}}_0^{(\nu)} \cdot \underline{\underline{\lambda}}^T \cdot \underline{\underline{\ell}}^{-1(\nu)}] >_\nu . \tag{B.7}$$

So the free energy density can be written as,

$$\begin{aligned}F_{el} \sim < \mathrm{Tr}[\underline{\underline{\lambda}} \cdot (\underline{\underline{\ell}}_0 + (r^{(\nu)} - < r >)\underline{n}_0\,\underline{n}_0^T + \left(\frac{p^{(\nu)}}{2} - \frac{< p >}{2}\right)\underline{m}_0\,\underline{m}_0^T + \left(-\frac{p^{(\nu)}}{2} + \frac{< p >}{2}\right)\underline{k}_0\,\underline{k}_0^T) \cdot \\ \underline{\underline{\lambda}}^T \cdot (\underline{\underline{\ell}}^{-1} + \left(\frac{1}{r^{(\nu)}} - \frac{1}{< r >}\right)\underline{n}\,\underline{n}^T + \left(\frac{1}{1+\frac{p^{(\nu)}}{2}} - \frac{1}{1+\frac{<p>}{2}}\right)\underline{m}\,\underline{m}^T + \left(\frac{1}{1-\frac{p^{(\nu)}}{2}} - \frac{1}{1-\frac{<p>}{2}}\right)\underline{k}\,\underline{k}^T)] >_\nu .\end{aligned} \tag{B.8}$$

Expanding out this expression for the free energy density leads to 16 terms.

$$F_{el} \sim < \mathrm{Tr}[\underline{\underline{\lambda}} \cdot \underline{\underline{\ell}}_0 \cdot \underline{\underline{\lambda}}^T \cdot \underline{\underline{\ell}}^{-1}] >_\nu \tag{1}$$

$$+ < \mathrm{Tr}[\underline{\underline{\lambda}} \cdot (r^{(\nu)} - < r >)\underline{n}_0\,\underline{n}_0^T \cdot \underline{\underline{\lambda}}^T \cdot \underline{\underline{\ell}}^{-1}] >_\nu \tag{2}$$

$$+ < \mathrm{Tr}[\underline{\underline{\lambda}} \cdot \left(\frac{p^{(\nu)}}{2} - \frac{< p >}{2}\right)\underline{m}_0\,\underline{m}_0^T \cdot \underline{\underline{\lambda}}^T \cdot \underline{\underline{\ell}}^{-1}] >_\nu \tag{3}$$

$$+ < \mathrm{Tr}[\underline{\underline{\lambda}} \cdot \left(-\frac{p^{(\nu)}}{2} + \frac{< p >}{2}\right)\underline{k}_0\,\underline{k}_0^T \cdot \underline{\underline{\lambda}}^T \cdot \underline{\underline{\ell}}^{-1}] >_\nu \tag{4}$$

$$+ < \mathrm{Tr}[\underline{\underline{\lambda}} \cdot \underline{\underline{\ell}}_0 \cdot \underline{\underline{\lambda}}^T \cdot \left(\frac{1}{r^{(\nu)}} - \frac{1}{< r >}\right)\underline{n}\,\underline{n}^T] >_\nu \tag{5}$$

$$+ < \mathrm{Tr}[\underline{\underline{\lambda}} \cdot (r^{(\nu)} - < r >)\underline{n}_0\,\underline{n}_0^T \cdot \underline{\underline{\lambda}}^T \cdot \left(\frac{1}{r^{(\nu)}} - \frac{1}{< r >}\right)\underline{n}\,\underline{n}^T] >_\nu \tag{6}$$

$$+ < \mathrm{Tr}[\underline{\underline{\lambda}} \cdot \left(\frac{p^{(\nu)}}{2} - \frac{< p >}{2}\right)\underline{m}_0\,\underline{m}_0^T \cdot \underline{\underline{\lambda}}^T \cdot \left(\frac{1}{r^{(\nu)}} - \frac{1}{< r >}\right)\underline{n}\,\underline{n}^T] >_\nu \tag{7}$$

$$+ < \mathrm{Tr}[\underline{\underline{\lambda}} \cdot \left(-\frac{p^{(\nu)}}{2} + \frac{< p >}{2}\right)\underline{k}_0\,\underline{k}_0^T \cdot \underline{\underline{\lambda}}^T \cdot \left(\frac{1}{r^{(\nu)}} - \frac{1}{< r >}\right)\underline{n}\,\underline{n}^T] >_\nu \tag{8}$$

$$+ < \mathrm{Tr}[\underline{\underline{\lambda}} \cdot \underline{\underline{\ell}}_0 \cdot \underline{\underline{\lambda}}^T \cdot \left(\frac{1}{1+\frac{p^{(\nu)}}{2}} - \frac{1}{1+\frac{<p>}{2}}\right)\underline{m}\,\underline{m}^T] >_\nu \tag{9}$$

$$+ < \mathrm{Tr}[\underline{\underline{\lambda}} \cdot (r^{(\nu)} - < r >)\underline{n}_0\,\underline{n}_0^T \cdot \underline{\underline{\lambda}}^T \cdot \left(\frac{1}{1+\frac{p^{(\nu)}}{2}} - \frac{1}{1+\frac{<p>}{2}}\right)\underline{m}\,\underline{m}^T] >_\nu \tag{10}$$

$$+ < \mathrm{Tr}[\underline{\underline{\lambda}} \cdot \left(\frac{p^{(\nu)}}{2} - \frac{< p >}{2}\right)\underline{m}_0\,\underline{m}_0^T \cdot \underline{\underline{\lambda}}^T \cdot \left(\frac{1}{1+\frac{p^{(\nu)}}{2}} - \frac{1}{1+\frac{<p>}{2}}\right)\underline{m}\,\underline{m}^T] >_\nu \tag{11}$$

$$+ < \mathrm{Tr}[\underline{\underline{\lambda}} \cdot \left(-\frac{p^{(\nu)}}{2} + \frac{< p >}{2}\right)\underline{k}_0\,\underline{k}_0^T \cdot \underline{\underline{\lambda}}^T \cdot \left(\frac{1}{1+\frac{p^{(\nu)}}{2}} - \frac{1}{1+\frac{<p>}{2}}\right)\underline{m}\,\underline{m}^T] >_\nu \tag{12}$$

$$+ < \mathrm{Tr}[\underline{\underline{\lambda}} \cdot \underline{\underline{\ell}}_0 \cdot \underline{\underline{\lambda}}^T \cdot \left(\frac{1}{1 - \frac{p^{(\nu)}}{2}} - \frac{1}{1 - \frac{<p>}{2}} \right) \underline{k}\,\underline{k}^T] >_\nu \tag{13}$$

$$+ < \mathrm{Tr}[\underline{\underline{\lambda}} \cdot (r^{(\nu)} - < r >) \underline{n}_0\,\underline{n}_0^T \cdot \underline{\underline{\lambda}}^T \cdot \left(\frac{1}{1 - \frac{p^{(\nu)}}{2}} - \frac{1}{1 - \frac{<p>}{2}} \right) \underline{k}\,\underline{k}^T] >_\nu \tag{14}$$

$$+ < \mathrm{Tr}[\underline{\underline{\lambda}} \cdot \left(\frac{p^{(\nu)}}{2} - \frac{< p >}{2} \right) \underline{m}_0\,\underline{m}_0^T \cdot \underline{\underline{\lambda}}^T \cdot \left(\frac{1}{1 - \frac{p^{(\nu)}}{2}} - \frac{1}{1 - \frac{<p>}{2}} \right) \underline{k}\,\underline{k}^T] >_\nu \tag{15}$$

$$+ < \mathrm{Tr}[\underline{\underline{\lambda}} \cdot \left(-\frac{p^{(\nu)}}{2} + \frac{< p >}{2} \right) \underline{k}_0\,\underline{k}_0^T \cdot \underline{\underline{\lambda}}^T \cdot \left(\frac{1}{1 - \frac{p^{(\nu)}}{2}} - \frac{1}{1 - \frac{<p>}{2}} \right) \underline{k}\,\underline{k}^T] >_\nu \tag{16}$$ (B.9)

Terms (2), (3), (4), (7), (8), (10), (14) average to zero (assuming $r^{(\nu)}$ and $p^{(\nu)}$ are independent variables).

Group together terms (5) + (6) =

$$\left(< \frac{1}{r} > - \frac{1}{< r >} \right) < \mathrm{Tr}[\underline{\underline{\lambda}} \cdot (\underline{\underline{\delta}} - \underline{n}_0\,\underline{n}_0^T + \frac{< p >}{2} \underline{m}_0\,\underline{m}_0^T - \frac{< p >}{2} \underline{k}_0\,\underline{k}_0^T) \cdot \underline{\underline{\lambda}}^T \cdot \underline{n}\,\underline{n}^T] > .$$

Group together terms (9) + (11) + (12) =

$$+ \left(< \frac{1}{1 + \frac{p}{2}} > - \frac{1}{1 + \frac{<p>}{2}} \right) < \mathrm{Tr}[\underline{\underline{\lambda}} \cdot (\underline{\underline{\delta}} + (< r > -1) \underline{n}_0\,\underline{n}_0^T + \frac{< p >}{2} \underline{m}_0\,\underline{m}_0^T - \frac{< p >}{2} \underline{k}_0\,\underline{k}_0^T) \cdot \underline{\underline{\lambda}}^T \cdot \underline{m}\,\underline{m}^T] >$$
$$+ \left(1 - < \frac{1}{1 + \frac{p}{2}} > (1 + \frac{< p >}{2}) \right) < \mathrm{Tr}[\underline{\underline{\lambda}} \cdot \underline{m}_0\,\underline{m}_0^T \cdot \underline{\underline{\lambda}}^T \cdot \underline{m}\,\underline{m}^T] >$$
$$- \left(1 - < \frac{1}{1 + \frac{p}{2}} > (1 + \frac{< p >}{2}) \right) < \mathrm{Tr}[\underline{\underline{\lambda}} \cdot \underline{k}_0\,\underline{k}_0^T \cdot \underline{\underline{\lambda}}^T \cdot \underline{m}\,\underline{m}^T] >$$
$$= < \mathrm{Tr}[\underline{\underline{\lambda}} \cdot (\underline{\underline{\delta}} \left(< \frac{1}{1 + \frac{p}{2}} > - \frac{1}{1 + \frac{<p>}{2}} \right) + (< r > -1) \left(< \frac{1}{1 + \frac{p}{2}} > - \frac{1}{1 + \frac{<p>}{2}} \right) \underline{n}_0\,\underline{n}_0^T$$
$$+ \left(1 - < \frac{1}{1 + \frac{p}{2}} > - \frac{< p >}{2} \frac{1}{1 + \frac{<p>}{2}} \right) \underline{m}_0\,\underline{m}_0^T - \left(1 - < \frac{1}{1 + \frac{p}{2}} > - \frac{< p >}{2} \frac{1}{1 + \frac{<p>}{2}} \right) \underline{k}_0\,\underline{k}_0^T) \cdot \underline{\underline{\lambda}}^T \cdot \underline{m}\,\underline{m}^T] > .$$

Group together terms (13) + (15) + (16) =

$$+ \left(< \frac{1}{1 - \frac{p}{2}} > - \frac{1}{1 - \frac{<p>}{2}} \right) < \mathrm{Tr}[\underline{\underline{\lambda}} \cdot (\underline{\underline{\delta}} + (< r > -1) \underline{n}_0\,\underline{n}_0^T + \frac{< p >}{2} \underline{m}_0\,\underline{m}_0^T - \frac{< p >}{2} \underline{k}_0\,\underline{k}_0^T) \cdot \underline{\underline{\lambda}}^T \cdot \underline{k}\,\underline{k}^T] >$$
$$- \left(1 - < \frac{1}{1 - \frac{p}{2}} > (1 - \frac{< p >}{2} \right) < \mathrm{Tr}[\underline{\underline{\lambda}} \cdot \underline{m}_0\,\underline{m}_0^T \cdot \underline{\underline{\lambda}}^T \cdot \underline{k}\,\underline{k}^T] >$$
$$+ \left(1 - < \frac{1}{1 - \frac{p}{2}} > (1 - \frac{< p >}{2} \right) < \mathrm{Tr}[\underline{\underline{\lambda}} \cdot \underline{k}_0\,\underline{k}_0^T \cdot \underline{\underline{\lambda}}^T \cdot \underline{k}\,\underline{k}^T] >$$
$$= < \mathrm{Tr}[\underline{\underline{\lambda}} \cdot (\underline{\underline{\delta}} \left(< \frac{1}{1 - \frac{p}{2}} > - \frac{1}{1 - \frac{<p>}{2}} \right) + (< r > -1) \left(< \frac{1}{1 - \frac{p}{2}} > - \frac{1}{1 - \frac{<p>}{2}} \right) \underline{n}_0\,\underline{n}_0^T$$
$$- \left(1 - < \frac{1}{1 - \frac{p}{2}} > + \frac{< p >}{2} \frac{1}{1 - \frac{<p>}{2}} \right) \underline{m}_0\,\underline{m}_0^T + \left(1 - < \frac{1}{1 - \frac{p}{2}} > + \frac{< p >}{2} \frac{1}{1 - \frac{<p>}{2}} \right) \underline{k}_0\,\underline{k}_0^T) \cdot \underline{\underline{\lambda}}^T \cdot \underline{k}\,\underline{k}^T] > .$$

Altogether the free energy density is,

$$F_{el} \sim < \mathrm{Tr}[\underline{\underline{\lambda}} \cdot \underline{\underline{\ell}}_0 \cdot \underline{\underline{\lambda}}^T \cdot \underline{\underline{\ell}}^{-1}] >$$
$$+ \left(< \frac{1}{r} > - \frac{1}{< r >} \right) < \mathrm{Tr}[\underline{\underline{\lambda}} \cdot (\underline{\underline{\delta}} - \underline{n}_0\,\underline{n}_0^T + \frac{< p >}{2} \underline{m}_0\,\underline{m}_0^T - \frac{< p >}{2} \underline{k}_0\,\underline{k}_0^T) \cdot \underline{\underline{\lambda}}^T \cdot \underline{n}\,\underline{n}^T] >$$

$$
\begin{aligned}
&+ < \mathrm{Tr}[\underline{\underline{\lambda}} \cdot (\underline{\underline{\delta}} \left(< \frac{1}{1+\frac{p}{2}} > - \frac{1}{1+\frac{<p>}{2}} \right) + (< r > -1) \left(< \frac{1}{1+\frac{p}{2}} > - \frac{1}{1+\frac{<p>}{2}} \right) \underline{n}_0 \, \underline{n}_0^T \\
&+ \left(\frac{1}{1+\frac{<p>}{2}} - < \frac{1}{1+\frac{p}{2}} > \right) \underline{m}_0 \, \underline{m}_0^T - \left(\frac{1}{1+\frac{<p>}{2}} - < \frac{1}{1+\frac{p}{2}} > \right) \underline{k}_0 \, \underline{k}_0^T) \cdot \underline{\underline{\lambda}}^T \cdot \underline{m} \, \underline{m}^T] > \\
&+ < \mathrm{Tr}[\underline{\underline{\lambda}} \cdot (\underline{\underline{\delta}} \left(< \frac{1}{1-\frac{p}{2}} > - \frac{1}{1-\frac{<p>}{2}} \right) + (< r > -1) \left(< \frac{1}{1-\frac{p}{2}} > - \frac{1}{1-\frac{<p>}{2}} \right) \underline{n}_0 \, \underline{n}_0^T \\
&- \left(\frac{1}{1-\frac{<p>}{2}} - < \frac{1}{1-\frac{p}{2}} > \right) \underline{m}_0 \, \underline{m}_0^T + \left(\frac{1}{1-\frac{<p>}{2}} - < \frac{1}{1-\frac{p}{2}} > \right) \underline{k}_0 \, \underline{k}_0^T) \cdot \underline{\underline{\lambda}}^T \cdot \underline{k} \, \underline{k}^T] > .
\end{aligned}
\tag{B.10}
$$

In finality the biaxial semi-softness term is,

$$
\begin{aligned}
F_{ss} \sim &\left(< \frac{1}{r} > - \frac{1}{< r >} \right) < \mathrm{Tr}[\underline{\underline{\lambda}} \cdot (\left(1 + \frac{< p >}{2} \right) \underline{m}_0 \, \underline{m}_0^T + \left(1 - \frac{< p >}{2} \right) \underline{k}_0 \, \underline{k}_0^T) \cdot \underline{\underline{\lambda}}^T \cdot \underline{n} \, \underline{n}^T] > \\
&+ \left(< \frac{1}{1+\frac{p}{2}} > - \frac{1}{1+\frac{<p>}{2}} \right) < \mathrm{Tr}[\underline{\underline{\lambda}} \cdot (< r > \underline{n}_0 \, \underline{n}_0^T + 2 \underline{k}_0 \, \underline{k}_0^T) \cdot \underline{\underline{\lambda}}^T \cdot \underline{m} \, \underline{m}^T] > \\
&+ \left(< \frac{1}{1-\frac{p}{2}} > - \frac{1}{1-\frac{<p>}{2}} \right) < \mathrm{Tr}[\underline{\underline{\lambda}} \cdot (< r > \underline{n}_0 \, \underline{n}_0^T + 2 \underline{m}_0 \, \underline{m}_0^T) \cdot \underline{\underline{\lambda}}^T \cdot \underline{k} \, \underline{k}^T] > .
\end{aligned}
\tag{B.11}
$$

If we had assumed that $r^{(\nu)}$ and $p^{(\nu)}$ were not independent then the terms in F_{ss} would still all be present, but weighted by different factors.

Due to the convexity of $\frac{1}{r}$ the factor $\left(< \frac{1}{r} > - \frac{1}{<r>} \right)$ is positive.

The factors $\left(< \frac{1}{1+\frac{p}{2}} > - \frac{1}{1+\frac{<p>}{2}} \right)$ and $\left(< \frac{1}{1-\frac{p}{2}} > - \frac{1}{1-\frac{<p>}{2}} \right)$ are also positive.

Appendix C

Smectic-A Finite Element Material Routine

The smectic-A elastomer material model encoded as a user subroutine, uanisohyper_smecticA.f, is given here. An example input file, smecticA.inp, is also included. Using `Abaqus 6.10` the simulation can be run from the command-line with,

```
"/scratch/Commands/abaqus job=SmA input=smecticA.inp user=uanisohyper_smecticA.f".
```

The input file specifies the case of stretching of a unit cube of smectic-A elastomer between rigid clamps. The geometry of the stretch is as follows. Two nodes, A at (0,0,0) and B at (1,1,1), are defined at corners of the unit cube. The "x=0" and "x=1" faces of the cube are rigidly kinematically constrained to nodes A and B respectively. During the stretching step node A is stationary, whereas node B is displaced a distance of 0.64 in the x-direction; stretching the cube the in x-direction. The cube is meshed with only two C3D8H elements; the faces of the elements meet on the x=0.5 plane.

The material, `UANISO_SMA`, is defined to use the invariant formulation of anisotropic hyperelasticity, i.e. it calls a `UANISOHYPER_INV` user subroutine. It is important that incompressibility is enforced, as the smectic-A model requires this. The material is specified with one anisotropy direction, corresponding to the initial layer normal direction. The orientation of the anisotropy direction, ori-1, is given here as the x-direction. The material parameters are $r = 2.0$, $B/\mu = 60.0$ and $c_{MR} = 0.14$.

The parameter, depvar=7, sets the number of components held by the SDV array. Nodal forces and displacements are output to the output database file, as well as engineering strains, stresses and the contents of the SDV array.

Example input file: smecticA.inp

```
*Heading
*Preprint, echo=NO, model=NO, history=NO, contact=NO
**
** PARTS
**
*Part, name=Elastomer
*Node
      1,          0.5,           0.,           0.
      2,          0.5,           0.,           1.
      3,           0.,           0.,           1.
      4,           0.,           0.,           0.
      5,          0.5,           1.,           1.
      6,           0.,           1.,           1.
      7,           0.,           1.,           0.
      8,          0.5,           1.,           0.
      9,           1.,           1.,           1.
     10,           1.,           0.,           1.
```

```
     11,           1.,           0.,           0.
     12,           1.,           1.,           0.
*Element, type=C3D8H
1, 8, 5, 6, 7, 1, 2, 3, 4
2,  5,  2,  1,  8,  9, 10, 11, 12
*Nset, nset=A
 4,
*Nset, nset=B
 9,
*Nset, nset=All, generate
  1,  12,   1
*Elset, elset=All
 1, 2
*Elset, elset="_x=0_S5", internal
 1,
*Surface, type=ELEMENT, name="x=0"
"_x=0_S5", S5
*Elset, elset="_x=1_S2", internal
 2,
*Surface, type=ELEMENT, name="x=1"
"_x=1_S2", S2
*orientation,name=ori-1,local directions=1
 1.0,0.0,0.0,0.0,1.0,0.0
 3,0.0
 1,0,0
** Section: Section-1
*solid section, elset=All, material=UANISO_SMA,orientation=ori-1
1.
*End Part
**
** ASSEMBLY
**
*Assembly, name=Assembly
**
*Instance, name=Elastomer-1, part=Elastomer
*End Instance
**
*Node
      1,           0.,           0.,           0.
*Node
      2,           1.,           1.,           1.
** Constraint: A_to_x=0
*Coupling, constraint name="A_to_x=0", ref node=Elastomer-1.A, surface=Elastomer-1."x=0"
*Kinematic
** Constraint: B_to_x=1
*Coupling, constraint name="B_to_x=1", ref node=Elastomer-1.B, surface=Elastomer-1."x=1"
*Kinematic
*End Assembly
**
** MATERIALS
**
*material,name=UANISO_SMA
*anisotropic hyperelastic,user,formulation=invariant, local directions=1,type=incompressible,properties=3
2.0,60.0,0.14
*DEPVAR
7
** ----------------------------------------------------------------
**
** STEP: Stretch
**
*Step, name=Stretch, nlgeom=YES, inc=400
*Static
0.01, 1., 1e-05, 0.01
**
** BOUNDARY CONDITIONS
**
** Name: Fix_A Type: Displacement/Rotation
*Boundary
Elastomer-1.A, 1, 1
Elastomer-1.A, 2, 2
Elastomer-1.A, 3, 3
Elastomer-1.A, 4, 4
```

```
Elastomer-1.A, 5, 5
Elastomer-1.A, 6, 6
** Name: Move_B Type: Displacement/Rotation
*Boundary
Elastomer-1.B, 1, 1, 0.64
Elastomer-1.B, 2, 2
Elastomer-1.B, 3, 3
Elastomer-1.B, 4, 4
Elastomer-1.B, 5, 5
Elastomer-1.B, 6, 6
**
** OUTPUT REQUESTS
**
*Restart, write, frequency=0
**
** FIELD OUTPUT: F-Output-1
**
*Output, field
*Node Output
RF, U
*Element Output, directions=YES
NE, S, SDV
**
** HISTORY OUTPUT: H-Output-1
**
*Output, history
*Energy Output
ALLAE,
*End Step
```

Smectic-A Elastomer Material Subroutine: uanisohyper_smecticA.f

```
c This material model encodes the smectic-A elastomer energy, of theorem 1.2. in
c "Relaxation of some transversally isotropic energies and applications to smectic-A elastomers" (2007).
c An additional energy term, cmu*Ainv(2), has been included to
c account for the energy of deforming post-buckled layers.
c The energy is written in terms of five invariants, Ainv(1) to Ainv(5).
c The parameter b is defined with a small epsilon parameter included
c inside the square root term, to avoid subtractive cancellation errors.
c The routine must be used with incompressiblity enforced on the input file.
      subroutine uanisohyper_inv (ainv, ua, zeta, nfibers, ninv,
     $     ui1, ui2, ui3, temp, noel, cmname, incmpflag, ihybflag,
     $     numstatev, statev, numfieldv, fieldv, fieldvinc,
     $     numprops, props)

      include 'aba_param.inc'

      character*80 cmname, CHARV
      dimension ua(2), ainv(ninv), ui1(ninv),
     $     ui2(ninv*(ninv+1)/2), ui3(ninv*(ninv+1)/2),
     $     statev(numstatev), fieldv(numfieldv),
     $     fieldvinc(numfieldv),props(numprops),
     $     INTV(ninv),REALV(ninv)

c     ainv: invariants
c     ua  : energies ua(1): utot, ua(2); udev
c     ui1 : dUdI
c     ui2 : d2U/dIdJ
c     ui3 : not used for regular elements; for hybrid define d3U/dJ3

      parameter ( half = 0.5d0,
     *            zero = 0.d0,
     *            one  = 1.d0,
     *            two  = 2.d0,
     *            three= 3.d0,
     *            four = 4.d0,
     *            five = 5.d0,
     *            six  = 6.d0,
     *            twt4 = 24.d0,
     *            index_I1 = 1,
```

```
     *           index_I2 = 2,
     *           index_J  = 3  )
      DOUBLE PRECISION k, r, d0, Bmu, lambda, Cmu, Q, t
      Integer noel

c The material parameter values are read in here.
c r is the polymer anisotropy
c Bmu is B divided by mu
c Cmu the Mooney-Rivlin coefficient
      r   = props(1)
      Bmu = props(2)
      Cmu = props(3)

      rI1 = ainv(index_I1)
      rI2 = ainv(index_I2)
      rJ  = ainv(index_J )

      rI1m3 = rI1 - three
      rI2m3 = rI2 - three
      rJm1  = rJ  - one
c Calculate the value of k.
      k = (Bmu**4*r**0.3333333333333333)/(1 + Bmu - r)**3
c Calculate the value of the initial layer spacing q.
      d0  =  (one + (one - r)/Bmu)/r**0.3333333333333333
c Calculate the value of lambda_0
      lambda =    Sqrt(d0/4. - 1/(4.*k) +
     -   Sqrt((1 - d0*k)**2/(4.*k**2) -
     -      (4*2**0.3333333333333333)/
     -       (-27 + 54*d0*k - 27*d0**2*k**2 +
     -          Sqrt(6912*k**3 + 729*(1 - d0*k)**4))**
     -        0.3333333333333333 +
     -      (-27 + 54*d0*k - 27*d0**2*k**2 +
     -          Sqrt(6912*k**3 + 729*(1 - d0*k)**4))**
     -        0.3333333333333333/
     -       (3.*2**0.3333333333333333*k))/2. +
     -   Sqrt((1 - d0*k)**2/(2.*k**2) +
     -      (4*2**0.3333333333333333)/
     -       (-27 + 54*d0*k - 27*d0**2*k**2 +
     -          Sqrt(6912*k**3 + 729*(1 - d0*k)**4))**
     -        0.3333333333333333 -
     -      (-27 + 54*d0*k - 27*d0**2*k**2 +
     -          Sqrt(6912*k**3 + 729*(1 - d0*k)**4))**
     -        0.3333333333333333/
     -       (3.*2**0.3333333333333333*k) -
     -      (1 - d0*k)**3/
     -       (4.*k**3*Sqrt((1 - d0*k)**2/(4.*k**2) -
     -           (4*2**0.3333333333333333)/
     -            (-27 + 54*d0*k - 27*d0**2*k**2 +
     -               Sqrt(6912*k**3 + 729*(1 - d0*k)**4))**
     -             0.3333333333333333 +
     -           (-27 + 54*d0*k - 27*d0**2*k**2 +
     -               Sqrt(6912*k**3 + 729*(1 - d0*k)**4))**
     -             0.3333333333333333/
     -            (3.*2**0.3333333333333333*k))))/2.)
c The parameter t is defined here to be (lambda_0)**-6,
c It is used to rescale the energy; changing its equilibrium point.
      t= lambda**(-6.0)
c      Values of parameters during intermediate analysis steps can be output to the .msg file, e.g.
c      REALV(1) = b
c      REALV(2) = d
c      INTV(1) = noel
c      CALL STDB_ABQERR(1," %R %R %I #b,d,noel",INTV,REALV,CHARV)

c     The Epsilon parameter inside the square-root term of b is called Epslo1.
      Epslo1 = 1.D-5
c     The invariant terms inside the square-root term of b are called Q.
c     It is important to ensure Q is positive.
      Q = (Ainv(1)+Ainv(4))**2 - 4*(Ainv(2)+Ainv(5))
      Q = Max(0.0,Q)

c     Here b and d represent the high temperature b and d values, i.e. these are not btilde and dtilde
      b =  (Sqrt(epslo1 + Q) + Ainv(1) - Ainv(4))/
```

```
     - (2.*t**0.3333333333333333)
c
      d = ((Ainv(2) - Ainv(1)*Ainv(4) + Ainv(5)))**0.5/
     - t**0.3333333333333333

c     Test if the point is inside the asymmetric solid region (AS)
      IF(d.GE.k*b*d0/(k*b+1)) THEN
c     STATEV(1) outputs the region of the energy, AS=1, UB=2, BB=3.
      STATEV(1)=1.00000

c     ua(2) represents the AS energy
      ua(2)= b + d**2/b + (d - d0)**2*k +
     - t**0.6666666666666666*Ainv(4)
      ua(2)= ua(2) + Cmu*Ainv(2)

c     ui1 contains the first derivatives of the AS energy
      ui1(1) = (1 - (4*Ainv(4))/(Sqrt(epslo1 + Q) +
     -     Ainv(1) - Ainv(4)) +
     -    (Ainv(1) + Ainv(4))/Sqrt(epslo1 + Q) -
     -    (4*(1 + (Ainv(1) + Ainv(4))/Sqrt(epslo1 + Q))*
     -       (Ainv(2) - Ainv(1)*Ainv(4) + Ainv(5)))/
     -     (Sqrt(epslo1 + Q) + Ainv(1) - Ainv(4))**2 +
     -    2*k*Ainv(4)*(-t**(-0.3333333333333333) +
     -       d0/Sqrt(Ainv(2) - Ainv(1)*Ainv(4) + Ainv(5))))/
     -  (2.*t**0.3333333333333333)
c
      ui1(2) = ((epslo1 + Q - Ainv(1)**2 + 4*Ainv(2) -
     -     2*Ainv(1)*Ainv(4) -
     -       Ainv(4)**2 + 4*Ainv(5))/
     -     (Sqrt(epslo1 + Q)*
     -       (Sqrt(epslo1 + Q) + Ainv(1) - Ainv(4))**2) +
     -    k*(t**(-0.3333333333333333) -
     -       d0/Sqrt(Ainv(2) - Ainv(1)*Ainv(4) + Ainv(5))))/
     -  t**0.3333333333333333
c
      ui1(3) = zero
c
      ui1(4) =         (-1 + 2*t - (4*Ainv(1))/
     -     (Sqrt(epslo1 + Q) + Ainv(1) - Ainv(4)) +
     -    (Ainv(1) + Ainv(4))/Sqrt(epslo1 + Q) -
     -    (4*(-1 + (Ainv(1) + Ainv(4))/Sqrt(epslo1 + Q))*
     -       (Ainv(2) - Ainv(1)*Ainv(4) + Ainv(5)))/
     -     (Sqrt(epslo1 + Q) + Ainv(1) - Ainv(4))**2 +
     -    2*k*Ainv(1)*(-t**(-0.3333333333333333) +
     -       d0/Sqrt(Ainv(2) - Ainv(1)*Ainv(4) + Ainv(5))))/
     -  (2.*t**0.3333333333333333)
c
      ui1(5) = ((epslo1 + Q - Ainv(1)**2 + 4*Ainv(2) -
     -     2*Ainv(1)*Ainv(4) -
     -       Ainv(4)**2 + 4*Ainv(5))/
     -     (Sqrt(epslo1 + Q)*
     -       (Sqrt(epslo1 + Q) + Ainv(1) - Ainv(4))**2) +
     -    k*(t**(-0.3333333333333333) -
     -       d0/Sqrt(Ainv(2) - Ainv(1)*Ainv(4) + Ainv(5))))/
     -  t**0.3333333333333333
c
      ui1(1)= ui1(1)
c
      ui1(2)= ui1(2) + Cmu
c
      ui1(3)= ui1(3)
c
      ui1(4)= ui1(4)
c
      ui1(5)= ui1(5)
c     ui2 contains the second  derivatives
      ui2(1) =          ((8*t**0.3333333333333333*Ainv(4)*
     -       (1 + (Ainv(1) + Ainv(4))/Sqrt(epslo1 + Q)))/
     -     (Sqrt(epslo1 + Q) + Ainv(1) - Ainv(4))**2 +
     -    (t**0.3333333333333333*
     -       (epslo1 + Q - (Ainv(1) + Ainv(4))**2))/
     -     (epslo1 + Q)**1.5 +
```

```
     -    (4*t**0.3333333333333333*
     -       (epslo1 + Q - (Ainv(1) + Ainv(4))**2)*
     -       (-Ainv(2) + Ainv(1)*Ainv(4) - Ainv(5)))/
     -     ((epslo1 + Q)**1.5*
     -       (Sqrt(epslo1 + Q) + Ainv(1) - Ainv(4))**2) +
     -    (k*Ainv(4)**2)/(Ainv(2) - Ainv(1)*Ainv(4) + Ainv(5)) +
     -    (8*t**0.3333333333333333*
     -       (1 + (Ainv(1) + Ainv(4))/Sqrt(epslo1 + Q))**2*
     -       (Ainv(2) - Ainv(1)*Ainv(4) + Ainv(5)))/
     -     (Sqrt(epslo1 + Q) + Ainv(1) - Ainv(4))**3 -
     -    (k*Ainv(4)**2*(-(d0*t**0.3333333333333333) +
     -         Sqrt(Ainv(2) - Ainv(1)*Ainv(4) + Ainv(5))))/
     -     (Ainv(2) - Ainv(1)*Ainv(4) + Ainv(5))**1.5)/
     -  (2.*t**0.6666666666666666)
c
      ui2(2) =         ((-8*t**0.3333333333333333*Ainv(4))/
     -     (Sqrt(epslo1 + Q)*
     -       (Sqrt(epslo1 + Q) + Ainv(1) - Ainv(4))**2) +
     -    (2*t**0.3333333333333333*(Ainv(1) + Ainv(4)))/
     -     (epslo1 + Q)**1.5 -
     -    (4*t**0.3333333333333333*
     -       (1 + (Ainv(1) + Ainv(4))/Sqrt(epslo1 + Q)))/
     -     (Sqrt(epslo1 + Q) + Ainv(1) - Ainv(4))**2 +
     -    (16*t**0.3333333333333333*
     -       (Sqrt(epslo1 + Q) + Ainv(1) + Ainv(4))*
     -       (-Ainv(2) + Ainv(1)*Ainv(4) - Ainv(5)))/
     -     ((epslo1 + Q)*(Sqrt(epslo1 + Q) + Ainv(1) - Ainv(4))**
     -        3) - (k*Ainv(4))/
     -     (Ainv(2) - Ainv(1)*Ainv(4) + Ainv(5)) -
     -    (8*t**0.3333333333333333*(Ainv(1) + Ainv(4))*
     -       (Ainv(2) - Ainv(1)*Ainv(4) + Ainv(5)))/
     -     ((epslo1 + Q)**1.5*
     -       (Sqrt(epslo1 + Q) + Ainv(1) - Ainv(4))**2) +
     -    (k*Ainv(4)*(-(d0*t**0.3333333333333333) +
     -         Sqrt(Ainv(2) - Ainv(1)*Ainv(4) + Ainv(5))))/
     -     (Ainv(2) - Ainv(1)*Ainv(4) + Ainv(5))**1.5)/
     -  (2.*t**0.6666666666666666)
c
      ui2(4) =  zero
c
      ui2(7) =         ((-4*t**0.3333333333333333)/
     -     (Sqrt(epslo1 + Q) + Ainv(1) - Ainv(4)) +
     -    (4*t**0.3333333333333333*Ainv(4)*
     -       (-1 + (Ainv(1) + Ainv(4))/Sqrt(epslo1 + Q)))/
     -     (Sqrt(epslo1 + Q) + Ainv(1) - Ainv(4))**2 +
     -    (4*t**0.3333333333333333*Ainv(1)*
     -       (1 + (Ainv(1) + Ainv(4))/Sqrt(epslo1 + Q)))/
     -     (Sqrt(epslo1 + Q) + Ainv(1) - Ainv(4))**2 +
     -    (t**0.3333333333333333*
     -       (epslo1 + Q - (Ainv(1) + Ainv(4))**2))/
     -     (epslo1 + Q)**1.5 +
     -    (4*t**0.3333333333333333*
     -       (epslo1 + Q - (Ainv(1) + Ainv(4))**2)*
     -       (-Ainv(2) + Ainv(1)*Ainv(4) - Ainv(5)))/
     -     ((epslo1 + Q)**1.5*
     -       (Sqrt(epslo1 + Q) + Ainv(1) - Ainv(4))**2) +
     -    (k*Ainv(1)*Ainv(4))/
     -     (Ainv(2) - Ainv(1)*Ainv(4) + Ainv(5)) +
     -    (8*t**0.3333333333333333*
     -       (-1 + (Ainv(1) + Ainv(4))/Sqrt(epslo1 + Q))*
     -       (1 + (Ainv(1) + Ainv(4))/Sqrt(epslo1 + Q))*
     -       (Ainv(2) - Ainv(1)*Ainv(4) + Ainv(5)))/
     -     (Sqrt(epslo1 + Q) + Ainv(1) - Ainv(4))**3 +
     -    2*k*(-1 + (d0*t**0.3333333333333333)/
     -        Sqrt(Ainv(2) - Ainv(1)*Ainv(4) + Ainv(5))) -
     -    (k*Ainv(1)*Ainv(4)*
     -       (-(d0*t**0.3333333333333333) +
     -         Sqrt(Ainv(2) - Ainv(1)*Ainv(4) + Ainv(5))))/
     -     (Ainv(2) - Ainv(1)*Ainv(4) + Ainv(5))**1.5)/
     -  (2.*t**0.6666666666666666)
c
      ui2(11) =         ((-8*t**0.3333333333333333*Ainv(4))/
```

```
     -     (Sqrt(epslo1 + Q)*
     -       (Sqrt(epslo1 + Q) + Ainv(1) - Ainv(4))**2) +
     -    (2*t**0.3333333333333333*(Ainv(1) + Ainv(4)))/
     -     (epslo1 + Q)**1.5 -
     -    (4*t**0.3333333333333333*
     -       (1 + (Ainv(1) + Ainv(4))/Sqrt(epslo1 + Q)))/
     -     (Sqrt(epslo1 + Q) + Ainv(1) - Ainv(4))**2 +
     -    (16*t**0.3333333333333333*
     -       (Sqrt(epslo1 + Q) + Ainv(1) + Ainv(4))*
     -       (-Ainv(2) + Ainv(1)*Ainv(4) - Ainv(5)))/
     -     ((epslo1 + Q)*(Sqrt(epslo1 + Q) + Ainv(1) - Ainv(4))**
     -        3) - (k*Ainv(4))/
     -     (Ainv(2) - Ainv(1)*Ainv(4) + Ainv(5)) -
     -    (8*t**0.3333333333333333*(Ainv(1) + Ainv(4))*
     -       (Ainv(2) - Ainv(1)*Ainv(4) + Ainv(5)))/
     -     ((epslo1 + Q)**1.5*
     -       (Sqrt(epslo1 + Q) + Ainv(1) - Ainv(4))**2) +
     -    (k*Ainv(4)*(-(d0*t**0.3333333333333333) +
     -         Sqrt(Ainv(2) - Ainv(1)*Ainv(4) + Ainv(5))))/
     -     (Ainv(2) - Ainv(1)*Ainv(4) + Ainv(5))**1.5)/
     -  (2.*t**0.6666666666666666)
c
      ui2(3) = ((d0*k)/(Ainv(2) - Ainv(1)*Ainv(4) + Ainv(5))**1.5 -
     -    4/(epslo1 + (Ainv(1) + Ainv(4))**2 -
     -        4*(Ainv(2) + Ainv(5)))**1.5 +
     -    (32*(Ainv(2) - Ainv(1)*Ainv(4) + Ainv(5)))/
     -     ((epslo1 + (Ainv(1) + Ainv(4))**2 -
     -         4*(Ainv(2) + Ainv(5)))*
     -       (Ainv(1) - Ainv(4) +
     -          Sqrt(epslo1 + (Ainv(1) + Ainv(4))**2 -
     -            4*(Ainv(2) + Ainv(5))))**3) +
     -    (16*(Ainv(2) - Ainv(1)*Ainv(4) + Ainv(5)))/
     -     ((epslo1 + (Ainv(1) + Ainv(4))**2 -
     -          4*(Ainv(2) + Ainv(5)))**1.5*
     -       (Ainv(1) - Ainv(4) +
     -          Sqrt(epslo1 + (Ainv(1) + Ainv(4))**2 -
     -            4*(Ainv(2) + Ainv(5))))**2) +
     -    16/(Sqrt(epslo1 + (Ainv(1) + Ainv(4))**2 -
     -         4*(Ainv(2) + Ainv(5)))*
     -       (Ainv(1) - Ainv(4) +
     -          Sqrt(epslo1 + (Ainv(1) + Ainv(4))**2 -
     -            4*(Ainv(2) + Ainv(5))))**2))/
     -  (2.*t**0.3333333333333333)
c
      ui2(5) = zero
c
      ui2(8) =         ((-8*t**0.3333333333333333*Ainv(1))/
     -     (Sqrt(epslo1 + Q)*
     -       (Sqrt(epslo1 + Q) + Ainv(1) - Ainv(4))**2) +
     -    (2*t**0.3333333333333333*(Ainv(1) + Ainv(4)))/
     -     (epslo1 + Q)**1.5 -
     -    (4*t**0.3333333333333333*
     -       (-1 + (Ainv(1) + Ainv(4))/Sqrt(epslo1 + Q)))/
     -     (Sqrt(epslo1 + Q) + Ainv(1) - Ainv(4))**2 -
     -    (k*Ainv(1))/(Ainv(2) - Ainv(1)*Ainv(4) + Ainv(5)) -
     -    (8*t**0.3333333333333333*(Ainv(1) + Ainv(4))*
     -       (Ainv(2) - Ainv(1)*Ainv(4) + Ainv(5)))/
     -     ((epslo1 + Q)**1.5*
     -       (Sqrt(epslo1 + Q) + Ainv(1) - Ainv(4))**2) -
     -    (16*t**0.3333333333333333*
     -       (-1 + (Ainv(1) + Ainv(4))/Sqrt(epslo1 + Q))*
     -       (Ainv(2) - Ainv(1)*Ainv(4) + Ainv(5)))/
     -     (Sqrt(epslo1 + Q)*
     -       (Sqrt(epslo1 + Q) + Ainv(1) - Ainv(4))**3) +
     -    (k*Ainv(1)*(-(d0*t**0.3333333333333333) +
     -         Sqrt(Ainv(2) - Ainv(1)*Ainv(4) + Ainv(5))))/
     -     (Ainv(2) - Ainv(1)*Ainv(4) + Ainv(5))**1.5)/
     -  (2.*t**0.6666666666666666)
c
      ui2(12) =          (-4/(epslo1 + Q)**1.5 +
     -    16/
     -     (Sqrt(epslo1 + Q)*
```

```
     -       (Sqrt(epslo1 + Q) + Ainv(1) - Ainv(4))**2) +
     -    (d0*k)/(Ainv(2) - Ainv(1)*Ainv(4) + Ainv(5))**1.5 +
     -    (32*(Ainv(2) - Ainv(1)*Ainv(4) + Ainv(5)))/
     -     ((epslo1 + Q)*(Sqrt(epslo1 + Q) + Ainv(1) -
     -         Ainv(4))**3) +
     -    (16*(Ainv(2) - Ainv(1)*Ainv(4) + Ainv(5)))/
     -     ((epslo1 + Q)**1.5*
     -       (Sqrt(epslo1 + Q) + Ainv(1) - Ainv(4))**2))/
     -  (2.*t**0.3333333333333333)
c
      ui2(6) = zero
c
      ui2(9) = zero
c
      ui2(13) = zero
c
      ui2(10) =         ((8*t**0.3333333333333333*Ainv(1)*
     -       (-1 + (Ainv(1) + Ainv(4))/Sqrt(epslo1 + Q))))/
     -     (Sqrt(epslo1 + Q) + Ainv(1) - Ainv(4))**2 +
     -    (t**0.3333333333333333*
     -       (epslo1 + Q - (Ainv(1) + Ainv(4))**2))/
     -     (epslo1 + Q)**1.5 +
     -    (4*t**0.3333333333333333*
     -       (epslo1 + Q - (Ainv(1) + Ainv(4))**2)*
     -       (-Ainv(2) + Ainv(1)*Ainv(4) - Ainv(5)))/
     -     ((epslo1 + Q)**1.5*
     -       (Sqrt(epslo1 + Q) + Ainv(1) - Ainv(4))**2) +
     -    (k*Ainv(1)**2)/
     -     (Ainv(2) - Ainv(1)*Ainv(4) + Ainv(5)) +
     -    (8*t**0.3333333333333333*
     -       (-1 + (Ainv(1) + Ainv(4))/Sqrt(epslo1 + Q))**2*
     -       (Ainv(2) - Ainv(1)*Ainv(4) + Ainv(5)))/
     -     (Sqrt(epslo1 + Q) + Ainv(1) - Ainv(4))**3 -
     -    (k*Ainv(1)**2*(-(d0*t**0.3333333333333333) +
     -         Sqrt(Ainv(2) - Ainv(1)*Ainv(4) + Ainv(5))))/
     -     (Ainv(2) - Ainv(1)*Ainv(4) + Ainv(5))**1.5)/
     -  (2.*t**0.6666666666666666)
c
      ui2(14) =          ((-8*t**0.3333333333333333*Ainv(1))/
     -     (Sqrt(epslo1 + Q)*
     -       (Sqrt(epslo1 + Q) + Ainv(1) - Ainv(4))**2) +
     -    (2*t**0.3333333333333333*(Ainv(1) + Ainv(4)))/
     -     (epslo1 + Q)**1.5 -
     -    (4*t**0.3333333333333333*
     -       (-1 + (Ainv(1) + Ainv(4))/Sqrt(epslo1 + Q)))/
     -     (Sqrt(epslo1 + Q) + Ainv(1) - Ainv(4))**2 -
     -    (k*Ainv(1))/(Ainv(2) - Ainv(1)*Ainv(4) + Ainv(5)) -
     -    (8*t**0.3333333333333333*(Ainv(1) + Ainv(4))*
     -       (Ainv(2) - Ainv(1)*Ainv(4) + Ainv(5)))/
     -     ((epslo1 + Q)**1.5*
     -       (Sqrt(epslo1 + Q) + Ainv(1) - Ainv(4))**2) -
     -    (16*t**0.3333333333333333*
     -       (-1 + (Ainv(1) + Ainv(4))/Sqrt(epslo1 + Q))*
     -       (Ainv(2) - Ainv(1)*Ainv(4) + Ainv(5)))/
     -     (Sqrt(epslo1 + Q)*
     -       (Sqrt(epslo1 + Q) + Ainv(1) - Ainv(4))**3) +
     -    (k*Ainv(1)*(-(d0*t**0.3333333333333333) +
     -         Sqrt(Ainv(2) - Ainv(1)*Ainv(4) + Ainv(5))))/
     -     (Ainv(2) - Ainv(1)*Ainv(4) + Ainv(5))**1.5)/
     -  (2.*t**0.6666666666666666)
c
      ui2(15) =         (-4/(epslo1 + Q)**1.5 +
     -    16/
     -     (Sqrt(epslo1 + Q)*
     -       (Sqrt(epslo1 + Q) + Ainv(1) - Ainv(4))**2) +
     -    (d0*k)/(Ainv(2) - Ainv(1)*Ainv(4) + Ainv(5))**1.5 +
     -    (32*(Ainv(2) - Ainv(1)*Ainv(4) + Ainv(5)))/
     -     ((epslo1 + Q)*(Sqrt(epslo1 + Q) + Ainv(1) -
     -         Ainv(4))**3) +
     -    (16*(Ainv(2) - Ainv(1)*Ainv(4) + Ainv(5)))/
     -     ((epslo1 + Q)**1.5*
     -       (Sqrt(epslo1 + Q) + Ainv(1) - Ainv(4))**2))/
```

```
     -  (2.*t**0.3333333333333333)
c
      ui2(1) = ui2(1)
c
      ui2(2) = ui2(2)
c
      ui2(4) = ui2(4)
c
      ui2(7) = ui2(7)
c
      ui2(11) = ui2(11)
c
      ui2(3) = ui2(3)
c
      ui2(5) = ui2(5)
c
      ui2(8) = ui2(8)
c
      ui2(12) = ui2(12)
c
      ui2(6) = ui2(6)
c
      ui2(9) = ui2(9)
c
      ui2(13) = ui2(13)
c
      ui2(10) = ui2(10)
c
      ui2(14) = ui2(14)
c
      ui2(15) = ui2(15)
c
c     Test to see material is in the UB region of the energy
      else if(b.GE.d0-(one/k)) THEN
      STATEV(1)=2.00000
c     This is the UB region energy
      ua(2)=         b + (d0**2*k)/(1 + b*k) +
     -  Ainv(4)*t**0.6666666666666666
      ua(2)= ua(2) + Cmu*Ainv(2)

c     First Derivatives
      ui1(1) =         ((1 - (d0**2*k**2)/
     -       (1 + (k*(Sqrt(epslo1 + Q) + Ainv(1) - Ainv(4)))/
     -           (2.*t**0.3333333333333333))**2)*
     -    (1 + (Ainv(1) + Ainv(4))/Sqrt(epslo1 + Q)))/
     -  (2.*t**0.3333333333333333)
c
      ui1(2) =         (-1 + (d0**2*k**2)/
     -     (1 + (k*(Sqrt(epslo1 + Q) + Ainv(1) - Ainv(4)))/
     -         (2.*t**0.3333333333333333))**2)/
     -  (Sqrt(epslo1 + Q)*t**0.3333333333333333)
c
      ui1(3) = zero
c
      ui1(4) = (-1 + 2*t + (Ainv(1) + Ainv(4))/Sqrt(epslo1 + Q) -
     -    (d0**2*k**2*(-1 +
     -         (Ainv(1) + Ainv(4))/Sqrt(epslo1 + Q)))/
     -     (1 + (k*(Sqrt(epslo1 + Q) + Ainv(1) - Ainv(4)))/
     -         (2.*t**0.3333333333333333))**2)/
     -  (2.*t**0.3333333333333333)
c
      ui1(5) =         (-1 + (d0**2*k**2)/
     -     (1 + (k*(Sqrt(epslo1 + Q) + Ainv(1) - Ainv(4)))/
     -         (2.*t**0.3333333333333333))**2)/
     -  (Sqrt(epslo1 + Q)*t**0.3333333333333333)
c
      ui1(1)= ui1(1)
c
      ui1(2)= ui1(2) + Cmu
c
      ui1(3)= ui1(3)
c
```

```
      ui1(4)= ui1(4)
c
      ui1(5)= ui1(5)
c     Second  Derivatives
      ui2(1) = ((d0**2*k**3*(1 + (Ainv(1) + Ainv(4))/
     - Sqrt(epslo1 + Q))**
     -        2)/
     -     (1 + (k*(Sqrt(epslo1 + Q) + Ainv(1) - Ainv(4)))/
     -         (2.*t**0.3333333333333333))**3 +
     -    (t**0.3333333333333333*
     -       (epslo1 + Q - (Ainv(1) + Ainv(4))**2))/
     -     (epslo1 + Q)**1.5 -
     -    (4*d0**2*k**2*t*(epslo1 + Q - (Ainv(1) + Ainv(4))**2))/
     -     ((epslo1 + Q)**1.5*
     -       (2*t**0.3333333333333333 +
     -          k*(Sqrt(epslo1 + Q) + Ainv(1) - Ainv(4)))**2))/
     -  (2.*t**0.6666666666666666)
c
      ui2(2) = (t**0.3333333333333333*(Ainv(1) + Ainv(4)) -
     -    (4*d0**2*k**2*t*(Ainv(1) + Ainv(4)))/
     -     (2*t**0.3333333333333333 +
     -        k*(Sqrt(epslo1 + Q) + Ainv(1) - Ainv(4)))**2 -
     -    (8*d0**2*k**3*Sqrt(epslo1 + Q)*t*
     -       (Sqrt(epslo1 + Q) + Ainv(1) + Ainv(4)))/
     -     (2*t**0.3333333333333333 +
     -        k*(Sqrt(epslo1 + Q) + Ainv(1) - Ainv(4)))**3)/
     -  ((epslo1 + Q)**1.5*t**0.6666666666666666)
c
      ui2(4) = zero
c
      ui2(7) = ((d0**2*k**3*(-1 + (Ainv(1) + Ainv(4))/
     - Sqrt(epslo1 + Q))*
     -       (1 + (Ainv(1) + Ainv(4))/Sqrt(epslo1 + Q)))/
     -     (1 + (k*(Sqrt(epslo1 + Q) + Ainv(1) - Ainv(4)))/
     -        (2.*t**0.3333333333333333))**3 +
     -    (t**0.3333333333333333*
     -       (epslo1 + Q - (Ainv(1) + Ainv(4))**2))/
     -     (epslo1 + Q)**1.5 -
     -    (4*d0**2*k**2*t*(epslo1 + Q - (Ainv(1) + Ainv(4))**2))/
     -     ((epslo1 + Q)**1.5*
     -       (2*t**0.3333333333333333 +
     -          k*(Sqrt(epslo1 + Q) + Ainv(1) - Ainv(4)))**2))/
     -  (2.*t**0.6666666666666666)
c
      ui2(11) = (t**0.3333333333333333*(Ainv(1) + Ainv(4)) -
     -    (4*d0**2*k**2*t*(Ainv(1) + Ainv(4)))/
     -     (2*t**0.3333333333333333 +
     -        k*(Sqrt(epslo1 + Q) + Ainv(1) - Ainv(4)))**2 -
     -    (8*d0**2*k**3*Sqrt(epslo1 + Q)*t*
     -       (Sqrt(epslo1 + Q) + Ainv(1) + Ainv(4)))/
     -     (2*t**0.3333333333333333 +
     -        k*(Sqrt(epslo1 + Q) + Ainv(1) - Ainv(4)))**3)/
     -  ((epslo1 + Q)**1.5*t**0.6666666666666666)
c
      ui2(3) =         (2*(-1 + (4*d0**2*k**2*t**0.6666666666666666*
     -         (2*t**0.3333333333333333 +
     -           k*(3*Sqrt(epslo1 + Q) + Ainv(1) - Ainv(4))))/
     -       (2*t**0.3333333333333333 +
     -          k*(Sqrt(epslo1 + Q) + Ainv(1) - Ainv(4)))**3))/
     -  ((epslo1 + Q)**1.5*t**0.3333333333333333)
c
      ui2(5) = zero
c
      ui2(8) =         (t**0.3333333333333333*(Ainv(1) + Ainv(4)) -
     -    (4*d0**2*k**2*t*(Ainv(1) + Ainv(4)))/
     -     (2*t**0.3333333333333333 +
     -        k*(Sqrt(epslo1 + Q) + Ainv(1) - Ainv(4)))**2 -
     -    (d0**2*k**3*(epslo1 + Q)*
     -       (-1 + (Ainv(1) + Ainv(4))/Sqrt(epslo1 + Q)))/
     -     (1 + (k*(Sqrt(epslo1 + Q) + Ainv(1) - Ainv(4)))/
     -        (2.*t**0.3333333333333333))**3)/
     -  ((epslo1 + Q)**1.5*t**0.6666666666666666)
```

```
c
      ui2(12) =  (2*(-1 + (4*d0**2*k**2*t**0.6666666666666666*
     -         (2*t**0.3333333333333333 +
     -           k*(3*Sqrt(epslo1 + Q) + Ainv(1) - Ainv(4))))/
     -       (2*t**0.3333333333333333 +
     -          k*(Sqrt(epslo1 + Q) + Ainv(1) - Ainv(4)))**3))/
     -  ((epslo1 + Q)**1.5*t**0.3333333333333333)
c
      ui2(6) = zero
c
      ui2(9) = zero
c
      ui2(13) = zero
c
      ui2(10) = ((d0**2*k**3*(-1 + (Ainv(1) + Ainv(4))/
     -  Sqrt(epslo1 + Q))**
     -        2)/
     -     (1 + (k*(Sqrt(epslo1 + Q) + Ainv(1) - Ainv(4)))/
     -         (2.*t**0.3333333333333333))**3 +
     -    (t**0.3333333333333333*
     -       (epslo1 + Q - (Ainv(1) + Ainv(4))**2))/
     -     (epslo1 + Q)**1.5 -
     -    (4*d0**2*k**2*t*(epslo1 + Q - (Ainv(1) + Ainv(4))**2))/
     -     ((epslo1 + Q)**1.5*
     -       (2*t**0.3333333333333333 +
     -          k*(Sqrt(epslo1 + Q) + Ainv(1) - Ainv(4)))**2))/
     -  (2.*t**0.6666666666666666)
c
      ui2(14) =  (t**0.3333333333333333*(Ainv(1) + Ainv(4)) -
     -    (4*d0**2*k**2*t*(Ainv(1) + Ainv(4)))/
     -     (2*t**0.3333333333333333 +
     -        k*(Sqrt(epslo1 + Q) + Ainv(1) - Ainv(4)))**2 -
     -    (d0**2*k**3*(epslo1 + Q)*
     -       (-1 + (Ainv(1) + Ainv(4))/Sqrt(epslo1 + Q)))/
     -     (1 + (k*(Sqrt(epslo1 + Q) + Ainv(1) - Ainv(4)))/
     -         (2.*t**0.3333333333333333))**3)/
     -  ((epslo1 + Q)**1.5*t**0.6666666666666666)
c
      ui2(15) =  (2*(-1 + (4*d0**2*k**2*t**0.6666666666666666*
     -         (2*t**0.3333333333333333 +
     -           k*(3*Sqrt(epslo1 + Q) + Ainv(1) - Ainv(4))))/
     -       (2*t**0.3333333333333333 +
     -          k*(Sqrt(epslo1 + Q) + Ainv(1) - Ainv(4)))**3))/
     -  ((epslo1 + Q)**1.5*t**0.3333333333333333)
c
      ui2(1) = ui2(1)
c
      ui2(2) = ui2(2)
c
      ui2(4) = ui2(4)
c
      ui2(7) = ui2(7)
c
      ui2(11) = ui2(11)
c
      ui2(3) = ui2(3)
c
      ui2(5) = ui2(5)
c
      ui2(8) = ui2(8)
c
      ui2(12) = ui2(12)
c
      ui2(6) = ui2(6)
c
      ui2(9) = ui2(9)
c
      ui2(13) = ui2(13)
c
      ui2(10) = ui2(10)
c
      ui2(14) = ui2(14)
```

```
c
      ui2(15) = ui2(15)
c
c     If the material was not in the AS or UB regions then it must be in the BB region.
      else
      STATEV(1)=3.00000
c     This is the BB region energy.
      ua(2)= 2*d0 - 1/k + Ainv(4)*t**0.6666666666666666
      ua(2)= ua(2) + Cmu*Ainv(2)

c     First Derivatives
      ui1(1) = zero
c
      ui1(2) = zero
c
      ui1(3) = zero
c
      ui1(4) = t**0.6666666666666666
c
      ui1(5) = zero
c
      ui1(1)= ui1(1)
c
      ui1(2)= ui1(2) + Cmu
c
      ui1(3)= ui1(3)
c
      ui1(4)= ui1(4)
c
      ui1(5)= ui1(5)
c     Second  Derivatives
      ui2(1) = zero
c
      ui2(2) = zero
c
      ui2(4) = zero
c
      ui2(7) = zero
c
      ui2(11) = zero
c
      ui2(3) = zero
c
      ui2(5) = zero
c
      ui2(8) = zero
c
      ui2(12) = zero
c
      ui2(6) = zero
c
      ui2(9) = zero
c
      ui2(13) = zero
c
      ui2(10) = zero
c
      ui2(14) = zero
c
      ui2(15) = zero
c
      ui2(1) = ui2(1)
c
      ui2(2) = ui2(2)
c
      ui2(4) = ui2(4)
c
      ui2(7) = ui2(7)
c
      ui2(11) = ui2(11)
c
      ui2(3) = ui2(3)
```

```
c
      ui2(5) = ui2(5)
c
      ui2(8) = ui2(8)
c
      ui2(12) = ui2(12)
c
      ui2(6) = ui2(6)
c
      ui2(9) = ui2(9)
c
      ui2(13) = ui2(13)
c
      ui2(10) = ui2(10)
c
      ui2(14) = ui2(14)
c
      ui2(15) = ui2(15)

      End if

c     It is helpful to output a few solution dependent variables, e.g. k,t,b,d.
c     Ainv(3) is a useful way to check that incompressibility is enforced.
      STATEV(2)=Ainv(3)
      STATEV(3)=k
      STATEV(4)=t
      STATEV(5)=b
      STATEV(6)=d
      STATEV(7)=Sqrt(epslo1 + (Ainv(1) +
     - Ainv(4))**2 - 4*(Ainv(2) + Ainv(5)))
      return
      end
```

Appendix D

Smectic-C Elastomer Polydomain Model

The uniaxial stretching and shear experiments of Sánchez-Ferrer and Finkelmann were performed on smectic-C, main-chain LCE with a domain microstructure. The pseudo-monodomain samples studied have a uniform director $\underline{n}_0 = \underline{z}$ and a conical distribution of layer normals arranged at an angle θ_0 to $\underline{n}_0$, see figure D.1.

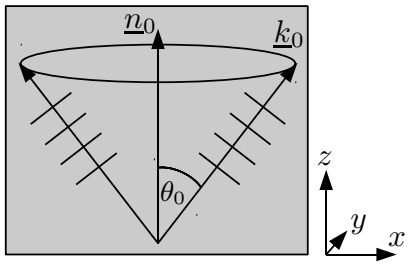

Figure D.1: Initial conical distribution of layer normals around the director.

The microstructure complicates the calculation of the stiffness of polydomain samples; as it would require modelling of the internal boundary structure.

It is possible to obtain a maximum and minimum bound on the stiffness of a polydomain by considering the Taylor and Sachs bounds respectively [103, 104]. These bounds work by ignoring the compatibility of the domain microstructure. The true behaviour of the sample should lie somewhere between the Taylor and Sachs regimes.

Taylor and Sachs Bounds

The Taylor bound is an upper bound to the stiffness of a polydomain sample; the monodomains are removed from the polydomain structure and strained in parallel between two plates, see figure D.2. The stiffest domains dictate the stiffness in a parallel arrangement, and this gives an upper limit for the energy required to deform a polydomain sample.

The Sachs bound is a lower bound to the stiffness of a polydomain sample; the monodomains are removed from the polydomain structure and strained in series, see figure D.3. It is only the softest domains that dictate the overall deformation, giving a low energy bound.

A computational simulation could set bounds on the mechanical properties of a smectic-C LCE polydomain sample under uniaxial deformation. The x-ray scattering patterns could then be calculated to allow experimental comparison.

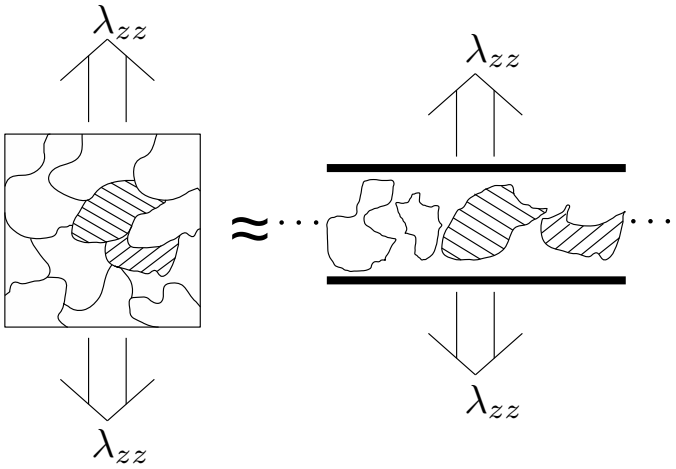

Figure D.2: A representation of the Taylor bound approximation; all domains experience the same strain. Two domains are shown with their smectic layering included.

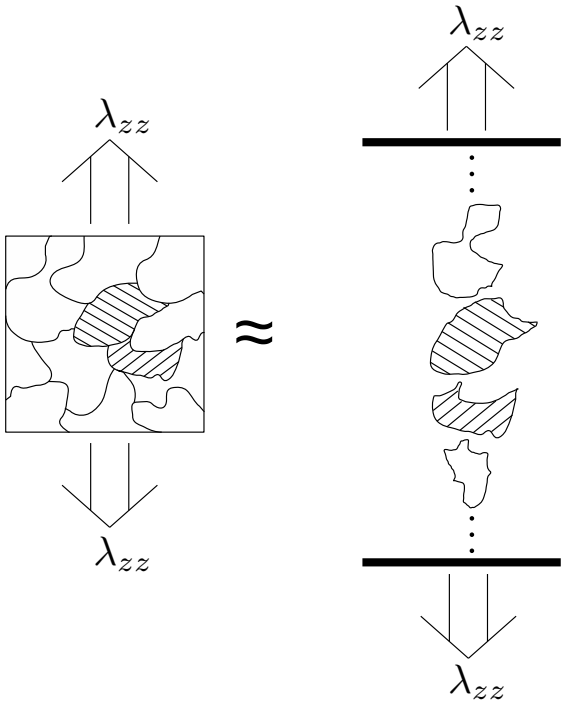

Figure D.3: A representation of the Sachs bound approximation; all domains experience the same external stress.

Bibliography

[1] S. Chandrasekhar, B. K. Sadashiva, and K. A. Suresh. Liquid crystals of disc-like molecules. *Pramana*, 9(5):471–480, 1977.

[2] G. Friedel. The mesomorphic states of matter. *Ann. Phys*, 18:273–474, 1922.

[3] S. Chandrasekhar. *Liquid Crystals*. Cambridge University Press, 1992.

[4] R. B. Meyer, L. Liebert, L. Strzelecki, and P. Keller. Ferroelectric liquid crystals. *J. Physique Lett.*, 36(3):69–71, 1975.

[5] D. W. Berreman. Solid surface shape and the alignment of an adjacent nematic liquid crystal. *Phys. Rev. Lett.*, 28:1683–1686, Jun 1972.

[6] F. C. Frank. I. Liquid crystals. on the theory of liquid crystals. *Discussions of the Faraday Society*, 25:19–28, 1958.

[7] M Delaye, R Ribotta, and G Durand. Buckling instability of the layers in a smectic-A liquid crystal. *Physics Letters A*, 44(2):139–140, 1973.

[8] P. S. Pershan. Dislocation effects in smectic-A liquid crystals. *Journal of Applied Physics*, 45(4):1590–1604, 1974.

[9] P. G. De Gennes. Conjectures sur l'etat smectique. *Le Journal de Physique Colloques*, 30(C4):C4–65, 1969.

[10] R. Bartolino and G. Durand. Plasticity in a smectic-A liquid crystal. *Phys. Rev. Lett.*, 39:1346–1349, Nov 1977.

[11] N. A. Clark and R. B. Meyer. Strain-induced instability of monodomain smectic-A and cholesteric liquid crystals. *Applied Physics Letters*, 22(10):493–494, 1973.

[12] S. J. Singer. Layer buckling in smectic-A liquid crystals and two-dimensional stripe phases. *Phys. Rev. E*, 48:2796–2804, Oct 1993.

[13] G. Cordoyiannis, A. Sánchez-Ferrer, H. Finkelmann, B. Rožic, S. Žumer, and Z. Kutnjak. Thermal study of the isotropic to smectic-C phase transition in main-chain liquid crystalline elastomers. *Liquid Crystals*, 37:349–353, 2010.

[14] B. Donnio, H. Wermter, and H. Finkelmann. A simple and versatile synthetic route for the preparation of main-chain, liquid-crystalline elastomers. *Macromolecules*, 33(21):7724–7729, 2000.

[15] A. Sánchez-Ferrer and H. Finkelmann. Uniaxial and shear deformations in smectic-C main-chain liquid-crystalline elastomers. *Macromolecules*, 41:970–980, 2008.

[16] E. P. Obraztsov, A. S. Muresan, B. I. Ostrovskii, and W. H. de Jeu. Road to disorder in smectic elastomers. *Phys. Rev. E*, 77(2):021706, Feb 2008.

[17] W. H. de Jeu, E. P. Obraztsov, B. I. Ostrovskii, W. Ren, P. McMullan, A. C. Griffin, A. Sánchez-Ferrer, and H. Finkelmann. Order and strain in main-chain smectic liquid-crystalline polymers and elastomers. *The European Physical Journal E: Soft Matter and Biological Physics*, 24:399–409, 2007.

[18] J. Küpfer and H. Finkelmann. Nematic liquid single crystal elastomers. *Die Makromolekulare Chemie, Rapid Communications*, 12(12):717–726, 1991.

[19] E. Nishikawa and H. Finkelmann. Smectic-*A* liquid single crystal elastomers strain induced break-down of smectic layers. *Macromolecular Chemistry and Physics*, 200(2):312–322, 1999.

[20] P. Heinze and H. Finkelmann. Shear deformation and ferroelectricity in chiral SmC* main-chain elastomers. *Macromolecules*, 43:6655–6665, 2010.

[21] E. Nishikawa, H. Finkelmann, and H. R. Brand. Smectic-*A* liquid single crystal elastomers showing macroscopic in-plane fluidity. *Macromolecular rapid communications*, 18(2):65–71, 1997.

[22] K. Semmler and H. Finkelmann. Mechanical field orientation of chiral smectic-*C* polymer networks. *Macromolecular Chemistry and Physics*, 196(10):3197–3208, 1995.

[23] J. M. Adams and M. Warner. Elasticity of smectic-*A* elastomers. *Phys. Rev. E*, 71(2):021708, Feb 2005.

[24] C. M. Spillmann, J. H. Konnert, J. M. Adams, J. R. Deschamps, J. Naciri, and B. R. Ratna. Strain analysis of a chiral smectic-*A* elastomer. *Phys. Rev. E*, 82(3):031705, Sep 2010.

[25] A. Komp and H. Finkelmann. A new type of macroscopically oriented smectic-*A* liquid crystal elastomer. *Macromolecular Rapid Communications*, 28:5562, 2007.

[26] D. Kramer and H. Finkelmann. Breakdown of layering in frustrated smectic-*A* elastomers. *Macromolecular Rapid Communications*, 28:2318–2324, 2007.

[27] W. H. de Jeu, B. I. Ostrovskii, D. Kramer, and H. Finkelmann. Random disorder and the smectic-nematic transition in liquid-crystalline elastomers. *Phys. Rev. E*, 83:041703, Apr 2011.

[28] D. Kramer and H. Finkelmann. Shear-induced tilt in smectic-*A* elastomers. *Phys. Rev. E*, 78(2):021704, Aug 2008.

[29] P. Beyer, E. M. Terentjev, and R. Zentel. Monodomain liquid crystal main chain elastomers by photocrosslinking. *Macromolecular Rapid Communications*, 28(14):1485–1490, Jul 2007.

[30] R. Ishige, K. Osada, H. Tagawa, H. Hiwano, M. Tokita, and J. Wantanabe. Elongation behaviour of main-chain smectic liquid crystalline elastomers. *Macromolecules*, 41:7566–7570, 2008.

[31] C. Ortiz, M. Wagner, N. Bhargava, C. K. Ober, and E. J. Kramer. Deformation of a polydomain, smectic liquid crystalline elastomer. *Macromolecules*, 31(24):8531–8539, 1998.

[32] J. M. Adams and M. Warner. Hairpin rubber elasticity. *Eur. Phys. J. E*, 16:97–107, 2005.

[33] H. P. Patil, D. M. Lentz, and R. C. Hedden. Necking instability during polydomain-monodomain transition in a smectic main-chain elastomer. *Macromolecules*, 42(10):3525–3531, 2009.

[34] A. Sánchez-Ferrer and H. Finkelmann. Polydomain-Monodomain orientational process in smectic-*C* main-chain liquid-crystalline elastomers. *Macromolecular Rapid Communications*, 32(3):309–315, 2011.

[35] Semmler K. and Finkelmann H. Orientation of a chiral smectic-*C* elastomer by mechanical fields. *Polymers for Advanced Technologies*, 5:231–235, 1994.

[36] K. Hiraoka and H. Finkelmann. Uniform alignment of chiral smectic-*C* elastomers induced by mechanical shear field. *Macromolecular Rapid Communications*, 22:456–460, 2001.

[37] K. Hiraoka, W. Sagano, T. Nose, and H Finkelmann. Biaxial shape memory effect exhibited by monodomain chiral smectic-*C* elastomers. *Macromolecules*, 38:7352–7357, 2005.

[38] P. Beyer, E. M. Terentjev, and R. Zentel. Strain analysis of a chiral smectic-A elastomer. *Macromolecular Rapid Communications*, 28:1485–1490, 2007.

[39] W. Ren, P. J. McMullan, and A. C. Griffin. Poisson's ratio of monodomain liquid crystalline elastomers. *Macromolecular Chemistry and Physics*, 209:1896–1899, 2008.

[40] W. Ren, P. J. McMullan, and A. C. Griffin. Stress-strain behavior in main chain liquid crystalline elastomers: effect of crosslinking density and transverse rod incorporation on "poisson's ratio". *Phys. Status Solidi B*, 9:2124, 2009.

[41] D Tabor. The bulk modulus of rubber. *Polymer*, 35(13):2759–2763, 1994.

[42] H. Schüring, R. Stannarius, C. Tolksdorf, and R. Zentel. Liquid crystal elastomer balloons. *Macromolecules*, 34(12):3962–3972, 2001.

[43] R Stannarius, R Köhler, M Rössle, and R Zentel. Study of smectic elastomer films under uniaxial stress. *Liquid crystals*, 31(7):895–906, 2004.

[44] R. Stannarius, R. Köhler, U. Dietrich, M. Lösche, C. Tolksdorf, and R. Zentel. Structure and elastic properties of smectic liquid crystalline elastomer films. *Phys. Rev. E*, 65:041707, Apr 2002.

[45] R. Stannarius, V. Aksenov, J. Bläsing, A. Krost, M. Rössle, and R. Zentel. Mechanical manipulation of molecular lattice parameters in smectic elastomers. *Phys. Chem. Chem. Phys.*, 8:2293–2298, 2006.

[46] C. Ohm, M. Brehmer, and R. Zentel. Liquid crystalline elastomers as actuators and sensors. *Advanced Materials*, 22(31):3366–3387, 2010.

[47] I. A. Rousseau and P. T. Mather. Shape memory effect exhibited by smectic-C liquid crystalline elastomers. *J. Am. Chem. Soc.*, 125:15300–15301, 2003.

[48] S. Garoff and R. B. Meyer. Electroclinic effect at the A-C phase change in a chiral smectic liquid crystal. *Phys. Rev. Lett.*, 38(15):848–851, Apr 1977.

[49] J. M. Adams and M. Warner. Mechanical response of smectic-C elastomers. *Phys. Rev. E*, 77(2):021702, Feb 2008.

[50] K. Hiraoka, M. Kobayashi, R. Kazama, and H. Finkelmann. Electromechanics of monodomain chiral smectic-C elastomer mechanical response to electric stimulation. *Macromolecules*, 42:5600–5604, 2009.

[51] P. T. Mather, X. Luo, and I. A. Rousseau. Shape memory polymer research. *Annual Review of Materials Research*, 39:445–471, 2009.

[52] P. Bladon, E. M. Terentjev, and M. Warner. Transitions and instabilities in liquid crystal elastomers. *Phys. Rev. E*, 47(6):3838–3840, Jun 1993.

[53] G. R. Mitchell, F. J. Davis, and W. Guo. Strain-induced transitions in liquid-crystal elastomers. *Phys. Rev. Lett.*, 71(18):2947–2950, Nov 1993.

[54] I. Kundler and H. Finkelmann. Strain-induced director reorientation in nematic liquid single crystal elastomers. *Macromolecular Rapid Communications*, 16:679–686, 1995.

[55] G. C. Verwey, M. Warner, and E. M. Terentjev. Elastic instability and stripe domains in liquid crystalline elastomers. *J. Phys. II France*, 6(9):1273–1290, 1996.

[56] H. Finkelmann, I. Kundler, E. M. Terentjev, and M. Warner. Critical stripe-domain instability of nematic elastomers. *J. Phys. II France*, 7(8):1059–1069, Aug 1997.

[57] J. Weilepp and H. R. Brand. Director reorientation in nematic-liquid-single-crystal elastomers by external mechanical stress. *Europhys. Lett.*, 34:495–500, 1996.

[58] E. M. Terentjev and M. Warner. Comment on "Director reorientation in nematic liquid-single-crystal elastomers by external mechanical stress". *EPL (Europhysics Letters)*, 37(7):495, 1997.

[59] J. Weilepp and H. R. Brand. Undulation instability in smectic-A liquid single crystal elastomers. *Macromolecular Theory and Simulations*, 7:91–96, 1998.

[60] M. Warner and E. M. Terentjev. *Liquid Crystal Elastomers.* Oxford University Press, Oxford, 2007.

[61] O. Stenull and T. C. Lubensky. Unconventional elasticity in smectic-A elastomers. *Phys. Rev. E*, 76(1):011706, Jul 2007.

[62] O. Stenull, T. C. Lubensky, J. M. Adams, and M. Warner. Smectic-C tilt under shear in smectic-A elastomers. *Phys. Rev. E*, 78(2):021705, 2008.

[63] J. M. Adams, M. Warner, O. Stenull, and T. C. Lubensky. Smectic-A elastomers with weak director anchoring. *Phys. Rev. E*, 78(1):011703, Jul 2008.

[64] J. M. Adams and M. Warner. Soft elasticity in smectic elastomers. *Phys. Rev. E*, 72(1):011703, Jul 2005.

[65] J. Adams, S. Conti, and A. DeSimone. Soft elasticity and microstructure in smectic-C elastomers. *Continuum Mechanics and Thermodynamics*, 18:319–334, 2007.

[66] Y. O. Popov and A. N. Semenov. Nematic ordering in anisotropic elastomers: "Effect of frozen anisotropy". *Eur. Phys. J. B*, 6:245–256, 1998.

[67] J. S. Biggins, E. M. Terentjev, and M. Warner. Semisoft elastic response of nematic elastomers to complex deformations. *Phys. Rev. E*, 78(4):041704, Oct 2008.

[68] S. Conti, A. DeSimone, and G. Dolzmann. Soft elastic response of stretched sheets of nematic elastomers; a numerical study. *Journal of the Mechanics and Physics of Solids*, 50:1431–1451, 2002.

[69] S. Conti, A. DeSimone, and G. Dolzmann. Semisoft elasticity and director reorientation in stretched sheets of nematic elastomers. *Phys. Rev. E*, 66(6):061710, 2002.

[70] W. T. Ren. PhD thesis, Georgia Institute of Technology, 2007.

[71] R. Lakes. Foam structures with a negative poisson's ratio. *Science*, 235:1039, 1987.

[72] http://www.nag.co.uk/numeric/fl/manual/pdf/e04/e04ccf.pdf.

[73] http://www.nag.com/numeric/fn/manual/pdf/c09/c09m04_con_nlin_lsq_fn04.pdf.

[74] http://www.hao.ucar.edu/modeling/pikaia/pikaia.php.

[75] W. Goffe. Simann: A global optimization algorithm using simulated annealing. *Studies in Nonlinear Dynamics & Econometrics*, 1(3):169–176, October 1996.

[76] S. Lecommandoux, L. Noirez, M. F. Achard, A. Brûlet, J. P. Cotton, and F. Hardouin. Backbone conformation study on side-on fixed liquid crystal polymers. *Physica B: Condensed Matter*, 234-236:250–251, 1997.

[77] A. Petelin and M. Čopič. Strain dependence of the nematic fluctuation relaxation in liquid-crystal elastomers. *Phys. Rev. E*, 82(1):011703, Jul 2010.

[78] E. R. Zubarev, S. A. Kuptsov, T. I. Yuranova, R. V. Talroze, and H. Finkelmann. Monodomain liquid crystalline networks: reorientation mechanism from uniform to stripe domains. *Liquid Crystals*, 26(10):1531–1540, 1999.

[79] P. Cesana and A. DeSimone. Quasiconvex envelopes of energies for nematic elastomers in the small strain regime and applications. *Journal of the Mechanics and Physics of Solids*, 59:787–803, 2011.

[80] J. Adams, S. Conti, A. DeSimone, and G. Dolzmann. Relaxation of some transversally isotropic energies and applications to smectic-A elastomers. *Mathematical Models and Methods in Applied Sciences*, 18(01):1–20, 2008.

[81] G. S. Agarwal and S. R. Shenoy. Observability of hysteresis in first-order equilibrium and nonequilibrium phase transitions. *Phys. Rev. A*, 23:2719, 1981.

[82] H. B. Callen. *Thermodynamics & an Introduction to Thermostatistics*. John Wiley & Sons, 1985.

[83] S. Müller. *Variational models for microstructure and phase transitions*. Springer, 1999.

[84] V. Šveràk. Rank-one convexity does not imply quasiconvexity. *Proceedings of the Royal Society of Edinburgh: Section A Mathematics*, 120:185–189, 1992.

[85] L. R. G. Treloar, H. G. Hopkins, R. S. Rivlin, and J. M. Ball. The mechanics of rubber elasticity [and discussions]. *Proceedings of the Royal Society of London. A. Mathematical and Physical Sciences*, 351(1666):301–330, 1976.

[86] R. T. Deam and S. F. Edwards. The theory of rubber elasticity. *Philosophical Transactions of the Royal Society of London. Series A, Mathematical and Physical Sciences*, 280(1296):317–353, 1976.

[87] M. Mooney. A theory of large elastic deformation. *Journal of Applied Physics*, 11(9):582–592, 1940.

[88] R. S. Rivlin. Large elastic deformations of isotropic materials. IV. Further developments of the general theory. *Philosophical Transactions of the Royal Society of London. Series A, Mathematical and Physical Sciences*, 241(835):379–397, 1948.

[89] M. Gottlieb and R. J. Gaylord. Experimental tests of entanglement models of rubber elasticity. 3. Biaxial deformations. *Macromolecules*, 20(1):130–138, 1987.

[90] T. Kawamura, K. Urayama, and S. Kohjiya. Multiaxial deformations of end-linked poly(dimethylsiloxane) networks. 1. Phenomenological approach to strain energy density function. *Macromolecules*, 34(23):8252–8260, 2001.

[91] J. Schröder and P. Neff. Invariant formulation of hyperelastic transverse isotropy based on polyconvex free energy functions. *International Journal of Solids and Structures*, 40:401–445, 2003.

[92] E. Süli and D. F. Mayers. *An introduction to numerical analysis*. Cambridge University Press, Cambridge, 2003.

[93] O. C. Zienkiewicz, R. L. Taylor, and J. Z. Zhu. *Finite Element Method : Its Basis and Fundamentals (6th Edition)*. Butterworth-Heinemann, 2005.

[94] G. H. Golub and J. H. Welsch. Calculation of gauss quadrature rules. Technical report, Stanford, CA, USA, 1967.

[95] D. P. Flanagan and T. Belytschko. A uniform strain hexahedron and quadrilateral with orthogonal hourglass control. *International Journal for Numerical Methods in Engineering*, 17(5):679–706, 1981.

[96] *Abaqus 6.10 User Subroutines Reference Manual 1.1.20, Dassault Systèmes S.A.*, 2010.

[97] A. DeSimone and G. Dolzmann. Macroscopic response of nematic elastomers via relaxation of a class of SO(3)-invariant energies. *Arch. Rational Mech. Anal.*, 161:181–204, 2002.

[98] B. L. Mbanga, F. Ye, J. V. Selinger, and R. L. B. Selinger. Modeling elastic instabilities in nematic elastomers. *Phys. Rev. E*, 82:051701, Nov 2010.

[99] S. J. Singer. Buckling induced by dilative strain in two- and three-dimensional layered materials. *Phys. Rev. E*, 62(3):3736–3746, 2000.

[100] R. Ribotta and G. Durand. Mechanical instabilities of smectic-A liquid crystals under dilative or compressive stresses. *J. Phys. France*, 38(2):179–204, 1977.

[101] J. A. Weiss, B. N. Maker, and S. Govindjee. Finite element implementation of incompressible, transversely isotropic hyperelasticity. *Computer Methods in Applied Mechanics and Engineering*, 135(1-2):107–128, 1996.

[102] M. Kaliske. A formulation of elasticity and viscoelasticity for fibre reinforced material at small and finite strains. *Computer Methods in Applied Mechanics and Engineering*, 185(2-4):225–243, 2000.

[103] G Taylor. Plastic strain in metals. *J. Inst. Metals*, 62:307–324, 1938.

[104] G Sachs. Zur Ableitung einer Fließbedingung. *Z. Verein dt. Ing., 72,*, 72:734–736, 1928.